©Copyright 2024

Christopher Arian

Development and Characterization of a Human Intestinal Organoid Monolayer Model to Predict Oral Drug Disposition

Christopher Arian

A dissertation
submitted in partial fulfillment of the
requirements for the degree of

Doctor of Philosophy

University of Washington
2024

Reading Committee:
Kenneth Thummel, Chair
Edward Kelly
Samuel Arnold

Program Authorized to Offer Degree:
Pharmaceutics

University of Washington

Abstract

Development and Characterization of a Human Intestinal Organoid Monolayer Model to Predict Oral Drug Disposition

Christopher Arian

Chair of the Supervisory Committee:
Dr. Kenneth Thummel
Department of Pharmaceutics

The intestine plays an important role in governing the disposition of orally administered medication, serving important gate-keeping functions that can profoundly impact the systemic blood exposure of such medications. While currently used *in vitro* systems have substantially enhanced our knowledge of intestinal physiology as it relates to drug disposition, they suffer from limitations which often hinders their ability to broadly and accurately predict the fate of orally administered drugs. The use of complex *in vitro* systems, such as the intestinal microphysiological system (MPS) and adult human stem cell-derived intestinal organoids (enteroids), have profoundly expanded our understanding of intestinal development, physiology, and pathology. However, research employing these models for use in the field of pharmaceutical

sciences remains relatively sparse. The projects described in this dissertation proposal seek to develop and characterize an intestinal MPS and a long-term cultured enteroid monolayer model for use in pharmaceutical sciences research.

Chapter 2 describes the development and characterization of an intestinal MPS model cultured with LS180 cells, an immortalized colorectal adenocarcinoma cell line, and primary human umbilical vein endothelial cells (HUVECs). In Chapter 3, the development and biochemical characterization of a long-term cultured human enteroid monolayer model was explored. Chapter 4 provides further characterization of the long-term cultured enteroid monolayer model, utilizing RNA-seq deconvolution methods to determine the cell type proportions present in our differentiated enteroid cultures. In Chapter 5, the utility of the enteroid monolayer model to recapitulate and uncover the mechanisms precipitating a select natural product-drug interaction between goldenseal and metformin is explored.

This work presented in this dissertation suggests that human enteroid monolayers are a promising model to predict orally administered drug disposition for use in preclinical drug development. Additionally, human enteroid monolayers display promise as a screening tool to predict drug-drug and natural product-drug interactions *in vitro* to better inform prescribing clinicians and improve the health and safety of patients.

Table of Contents

List of Figures

List of Tables

ACKNOWLEDGEMENTS

First and foremost, I would like to thank my advisor, Dr. Ken Thummel – his mentorship and support have been pivotal for me throughout my dissertation work, and I would not be where I am today without his guidance. He treats all students with respect and is quick to praise successes and treats non-successes as learning opportunities instead of failures. As an aspiring academic researcher, I couldn't have asked for a better role model.

Additionally, I would like to thank Dr. Ed Kelly, who has served as my co-advisor. Ed stressed that scientific education to younger future scientists is a mandate for working with him and I have embraced this philosophy wholeheartedly. I always felt comfortable going to his office to chat and always felt better about any scientific issues I had after leaving.

I would also like to thank the rest of my doctoral supervisory committee, Dr. Sam Arnold, Dr. Cathy Yeung, and Dr. Beno Freedman for their guidance throughout my dissertation work – particularly Cathy, who holds joint lab meeting with Ed and was a constant uplifting voice throughout my time in graduate school.

I would like to thank the Thummel and Kelly/Yeung lab members for their friendship throughout graduate school. You all made graduate school fun and made it easy for me to go into the lab every day. Thank you for all the conversations (scientific or not), the vent sessions, and the happy hours to keep my spirits high. I would like to particularly thank the Thummel lab manager, Tina Calamia, for being an incredible lab manager – I learned a lot working for you.

To my family and friends, I thank you for always supporting me and being a source of comfort whenever I am feeling down. A special thank you to my mom for sending me care packages with Italian goodies from home so I never forget my roots. A special thank you as well to my former roommate and Pharmaceutics alumnus, Antonio, for being a great friend – there isn't anyone else I'd rather have lived with during the pandemic.

Lastly, I would like to thank my partner, Marelle, for her love and support during the latter stages of my graduate schooling. I am so thankful to have met you during this time – you make me feel like the luckiest person in the world. I am grateful I get to come home to you and our cat Chives. No matter how difficult my day was, seeing you two made everything better. I'm looking forward to a future with you filled with more laughs and smiles.

CHAPTER 1. INTRODUCTION

(Part of this chapter was published as a review article "Gutsy Science: *In vitro* systems of the human intestine to model oral drug disposition" (2021) *Pharmacology and Therapeutics*)

1.1. BACKGROUND

1.1.1. Introduction

In the science of drug development, it is well recognized that the intestine can play a significant role in determining the systemic exposure and pharmacological response of orally-administered drugs. As depicted in **Figure 1.1**, for orally dosed drug to reach the blood circulation, the formulation (e.g. , capsule or tablet) generally must first dissolve in luminal fluid and pass through an epithelial barrier (transcellular pathway) in order to gain access to the splanchnic capillaries in the intimal space of the intestinal mucosa that feed the portal vein. Drug may also pass through the paracellular space between epithelial cells for delivery to lymphatic vessels also in the intimal space, but this is a low efficiency absorptive process reserved for some large and/or polar molecules. When encountering the absorptive epithelial enterocytes, drugs may be subject to active cell influx and efflux processes that facilitate or impede drug absorption, as well as intracellular metabolic biotransformation by both phase I and phase II enzymes. Intact drug that escapes into the portal circulation passes into the liver and, following uptake into its parenchymal cells, is subject to another round of metabolic elimination or biliary excretion or escapes unchanged into systemic blood from which it can exert biological effects. Collectively, the initial intestinal and hepatic biological elimination processes comprise the "first-pass effect" and contribute to incomplete oral drug bioavailability (Rowland et al., 2009). Mathematically, a drug's bioavailability (F) can be described with the following equation:

$$F = F_A * F_G * F_H$$

Where F_A is the net fraction of administered drug absorbed through the intestinal epithelium, F_G is the fraction of absorbed drug that escapes metabolism in the gut, and F_H is the fraction of drug in the portal vein that escapes metabolism or biliary excretion in the liver. The enteric processes that affect F_A and F_G, are important determinants of a drug's oral bioavailability, and as a result, should be accurately characterized during drug development.

1.1.2. Bioavailability components

Processes that influence the "F_A" component of oral bioavailability include "non-intestinal" factors (e.g. dosage form, and a drug's physicochemical properties such as water and lipid solubilities) and/or intestinal processes that relate directly to the intestine's microanatomy/physiology (e.g., apical surface area, luminal fluid composition, integrity of unstirred water layer) and epithelial drug transporter expression profile (Lin and Wong, 2017). Transcellular drug absorption from the intestinal lumen into the portal blood can occur through two general processes: passive mechanisms and transport-mediated mechanisms. Passive processes, largely via transcellular diffusion, are facilitated directly by the small intestine's large surface area of ~32 m^2 (Helander and Fandriks, 2014). This large enteric surface area is a result of extensive mucosal folding, villi that include mucosal epithelia, and the microvilli of the individual epithelial barrier cells. The intestine's microanatomical structures (villi and microvilli) decrease in density from the duodenum to the colon and, thus, influence the drug absorption fraction, the extent to which depends on the predominant site of absorption within the intestine.

Transport-mediated mechanisms can also affect the oral absorption fraction, depending on the drug and its physicochemical properties. Intestinal enterocytes express a multitude of transporters, both cellular influx and efflux, on both the apical and basolateral membranes of the absorptive enterocytes in the gut mucosa (Giacomini et al., 2018). The most well studied of the intestinal efflux transporters, P-glycoprotein (P-gp, *ABCB1*), can reduce the overall absorption of multiple drugs. For example, the area under the curve (AUC) of orally administered digoxin has been shown to have a strong negative correlation to intestinal P-gp levels, and transcriptional induction of intestinal P-gp via rifampin treatment significantly decreases digoxin exposure, likely due to reduced absorption (decreased F_A) in the intestine as a result of increased P-gp levels (Greiner et al., 1999). In addition, P-gp efflux activity can delay the absorption of orally administered drugs. This has been demonstrated by evaluating changes in the rate constant of absorption, k_{abs}, for P-gp substrates in the presence and absence of P-gp inducers and/or inhibitors. For example, the P-gp substrate, cyclosporine, exhibited a substantially decreased or increased k_{abs} when co-administered with a P-gp inducer or inhibitor, respectively (Wacher et al., 1998).

Other intestinal transporters, such as BCRP (*ABCG1*), OATP2B1 (*SLCO2B1*), and OCT1 (*SLC22A1*), are also expressed in relatively high abundance within intestinal mucosal epithelia and can be an important determinant of a drug's oral bioavailability and a source of drug-drug interactions (Shugarts and Benet, 2009; Yu et al., 2017). For example, Chen et al., have demonstrated that OATP2B1 plays an important role in mediating the intestinal absorption of fluvastatin – thus the inhibition of this transporter by known inhibitors, such as the tyrosine kinase inhibitor (TKI) erlotinib, will lead to subtherapeutic plasma and liver concentrations of fluvastatin and subsequent lack of efficacy (Chen et al., 2020). Interestingly, targeting intestinal uptake transporters has emerged as a viable strategy in the drug development process to improve intestinal absorption of polar compounds through the synthesis of a prodrug that is a substrate for intestinal uptake transporters. This concept is illustrated well when comparing the oral bioavailability of the antiviral, acyclovir, to its prodrug, valacyclovir. Through the addition of a

L-valine moiety (valacyclovir), the oral bioavailability of acyclovir (released after hydrolysis of valacyclovir), is improved to >50%, while oral acyclovir has a bioavailability of ~15%. This 3-fold increase in bioavailability of the pharmacologically active molecule has been attributed to enhanced cellular uptake mediated by PEPT1 in the apical membrane, which more readily transports the prodrug due to the addition of the L-valine moiety (Yang and Smith, 2013; Minhas and Newstead, 2019). Similar to the heterogeneity in villi and microvilli density stated above, there is also heterogeneity in the expression pattern of intestinal transporters along the length of the intestine. This non-uniform expression profile can affect a drug's oral bioavailability, depending on the preferred site of its absorption (often determined by drug formulation) and its susceptibility to active influx or efflux transport.

The final enteric process that can affect a drug's oral bioavailability is biotransformation, occurring primarily within the absorptive enterocytes of the gut mucosa. The importance of intestinal epithelial metabolism emerged in the early to mid-90's, when multiple groups showed unequivocally that intestinal metabolism in humans, particularly for high turnover CYP3A substrates could substantially limit a drug's oral bioavailability (Kolars et al., 1991; Paine et al., 1996). In addition, it was shown that CYP3A substrates bear a striking substrate overlap with substrates of the efflux transporter P-gp (Wacher et al., 1995). For some drugs, the efflux transporter may act synergistically with intracellular enzymes to limit a drug's bioavailability by prolonging the drug's residence time within the enterocytes, leading to increased metabolism of parent drug by CYP3A and a subsequent decrease in oral bioavailability (Benet et al., 1996; Cummins et al., 2002). Although an intriguing concept, current cell culture models that lack full *in vivo* physiologic context are poorly suited for testing such a hypothesis.

Along with CYP3A, other drug metabolizing enzymes (DMEs), such as CYP2C9, CYP2C19, SULT1A, and UGT1A, are also present in sufficient abundance in the intestine (compared to the liver) to potentially affect the bioavailability of high intrinsic clearance substrates (Paine et al., 2006; Fritz et al., 2019). Similar to intestinal microvilli and intestinal transporter expression, intestinal DMEs display heterogeneity in their expression along the intestine, with the highest abundance in the proximal jejunum, and that decreases down the intestinal track (Paine et al., 1997; Couto et al., 2020; Li, 2020; Zhang et al., 2020).

An important determinant of the expression of the intestinal DMETs are the nuclear receptors (NRs), which are proteins that when activated (via exogenous and/or endogenous ligands) interact with specific DNA sequences to control the expression of DMET genes, by either up-regulating or down-regulating a given gene product. NR binding of an agonistic ligand imparts a conformational change allowing the NR to drive its cellular response (Olefsky, 2001). The interaction between intestinal NRs and their constitutive and foreign ligands are likely a major determinant of the large inter-individual variability in the intestinal first-pass effect. Accordingly, further characterization of the regulation of intestinal DMETs may lead to improved understanding of the factors contributing to variability in the intestinal first pass effect. Important NRs expressed along the intestine include PXR (pregnane X receptor), farnesoid X receptor (FXR), aryl hydrocarbon receptor (AhR), and vitamin D receptor (VDR) (Thummel et al., 2001; Thummel, 2007). Another factor that can contribute to intraindividual variability in intestinal DMET content is the expression of various coactivators (e.g., steroid receptor 1, SRC1, and nuclear receptor coactivator 6, NCoA6) and corepressors (e.g., nuclear receptor corepressor, NCoR), which can enhance or repress the impact of NR activation via ligand binding, respectively (Rigalli et al., 2021). Strikingly, these coactivators/corepressors can lead to organ specific impacts on the effects of inducers binding to their NRs. For example, tocotrienols, members of the vitamin E family, bind to PXR and induce CYP3A4 in hepatic cell lines but not intestinal lines (Zhou et al., 2004). This phenomenon is explained by the relatively high abundance of the corepressor, NCoR, in the intestinal cell lines, disrupting the impact of tocotrienols on CYP3A4 expression. This data suggests that NCoR plays an important role in mediating tissue-specific DMET regulation of PXR gene targets. Like the expression of DMETs, NR abundance along the intestine can be heterogeneous, with the highest expression of PXR and CAR, for example, seen typically in the proximal small intestine and decreases down the intestinal track (Fritz et al., 2019).

1.1.3. Natural product-drug interactions impacting bioavailability

The effects of intestinal transporters and metabolic enzymes on oral drug bioavailability can be modified by drug-drug (DDI) and natural product-drug interactions (NPDI), potentially impacting drug safety and efficacy. NPDIs are of particular concern to intestinal DMET function, as these interactions take place preferentially in the intestinal mucosa, where exposure concentrations of natural product (NP) are likely greater than that of the blood because of high luminal concentrations and extensive first-pass NP metabolism (conjugation, oxidation and hydrolysis). Additionally, with the sale and use of NPs on the rise, the potential for NPDIs to occur and alter the efficacy/safety of prescribed medication is becoming a significant concern for healthcare professionals (Paine and Roe, 2018; Paine et al., 2018). A classic and clinically important example of an intestinal NPDI is the interaction between cyclosporine (victim drug) and St. John's Wort (perpetrator NP). Cyclosporine is an immunosuppressant used for solid organ transplant patients and is a substrate of both CYP3A4 and P-gp, while St. John's Wort is an herbal supplement and a known CYP3A4 and P-gp inducer, mediated by nuclear receptor (NR) activation (e.g., pregnane-X-receptor, PXR) (Zanger and Schwab, 2013). Co-administration of cyclosporine with St. John's Wort led to sub-therapeutic concentrations of cyclosporine, and subsequent acute transplant rejection (Barone et al., 2000). This example and the growing use of NPs illustrates the importance of predicting and characterizing potential intestinal NPDIs to ensure optimal therapeutic outcomes for patients.

1.1.4. Historical in vitro models of the human intestine

All of the factors mentioned above highlight the importance of the intestine as a gate-keeping organ that can profoundly influence oral drug disposition. Characterizing and predicting a new molecular entity's (NME) metabolism and transport within the intestine is a pivotal step in the drug development process. Drugs with low and variable oral bioavailability are generally de-selected in the drug development process and, ideally, identified at the pre-clinical stage. Unfortunately, traditional *in vitro* systems employed to predict the intestinal first-pass effect and oral bioavailability can be sub-optimal (summarized in **Table 1.1**). These include intact tissue systems, such as Ussing chambers and precision cut intestinal slices (PCIS), which maintain segment specific tissue microanatomy and drug metabolizing enzyme and transport (DMET) expression, but suffer from limited duration of tissue viability and are technically challenging (van de Kerkhof et al., 2007). Other commonly used *in vitro* systems include monolayer cultures of immortalized cell lines, such as Caco-2 and LS180, which represent a relatively inexpensive, technically simple, and high throughput means of assessing intestinal transport and metabolism, respectively. However, these cell systems display disparate transporter and enzyme expression, compared to the normal human intestine, and lack the ability to simultaneously study metabolism and transport phenomena within the same cell line (Sun et al., 2002; Pfrunder et al., 2003). Recent advances in the isolation and cryopreservation of primary human enterocytes have promulgated studies of intestinal metabolism and associated DDIs (Ho et al., 2017; Li et al., 2018), but again the model has limited culture viability, a high cost, and transport activity that remains underexplored.

Along with the aforementioned *in vitro* models above, *in situ* perfusion techniques and in silico predictions have been applied towards the prediction of intestinal drug absorption and metabolism. The Loc-I-Gut technique, first described in the early 1990s, utilizes two latex balloons spaced 10 cm apart in order to occlude short segments of the small intestine to study regional drug perfusion and metabolism (Lennernas et al., 1992). While this is a powerful technique that maintains intestinal physiology, it is infrequently used by academia or the pharmaceutical industry due to the highly invasive nature of the device, ethical concerns and cost (van de Kerkhof et al., 2007).

In an effort to better predict the oral pharmacokinetics of investigational drug candidates before incurring the costs of clinical studies, *in silico* techniques such as physiologically-based pharmacokinetic (PBPK) modeling have been introduced. PBPK models are mathematical constructs that integrate compound-specific parameters – e.g., drug physicochemical properties and drug metabolism and transport parameters derived from incubations with subcellular tissue fractions or recombinantly expressed proteins – with organ physiological properties (e.g., organ blood flow, expression of specific DMETs) in order to predict *in vivo* drug disposition. PBPK models have also been applied towards the prediction of drug-drug/natural product-drug interactions, the prediction of drug disposition in special populations, as well as the assessment of population variability (Lin and Wong, 2017). While this is another powerful experimental technique that is both cost- and time-effective, PBPK models are only as good as the inputted *in vitro* data used to inform the model. Current limitations in the aforementioned *in vitro* experimental systems can lead to misinformed models that will not accurately predict *in vivo* oral drug disposition. Of particular note is the inadequacy of many *in vitro* systems to simultaneously study transport and metabolism processes, processes that may interact in complex ways to reduce oral drug bioavailability.

1.1.5. Emerging complex in vitro models of the human intestine

The limitations of current *in vitro*, *in situ,* and *in silico* models mentioned above highlight the need for a more complete and physiologically relevant model of the human intestine. Over the past decade, there has been growing effort to develop advanced *in vitro* tissue models to overcome past limitations. One such example is the microphysiological system (MPS), which represents a more physiologically and anatomically relevant epithelial cell culture platform than traditional, static cell culture systems, as the MPS incorporates flow of media down a luminal channel, with accompanying shear forces that have been shown to be beneficial for cell viability and function (Chang et al., 2017). The MPS can also be configured to include a parallel vascular-like channel to ensure basolateral "sink" conditions that support vectorial (apical to basolateral) drug transport, as described for a renal epithelial MPS model (Chapron et al., 2020).

Another example of a burgeoning complex *in vitro* system are cultured human organoid, which consists of stem cell-derived, multicellular, 3-dimensional (3D) structures that recapitulate organ function on a much smaller scale but of sufficient complexity to recapitulate important cell-cell interactions and tissue functions (Rossi et al., 2018). Key features of intestinal organoids, or enteroids, are that they can be produced from each segment of the small or large intestine, they maintain the genetic identity of the donor, and they have extremely long culture viability, as they are a self-renewing system (In et al., 2016; Blutt et al., 2017).

The studies described in this dissertation proposal investigate the development and characterization of an intestinal MPS and enteroid monolayer models and applies the latter towards predicting and elucidating the mechanisms of a select NPDI. Work aimed at characterizing an intestinal MPS model populated with LS180 cells is described in chapter 2. Work aimed towards characterizing enteroid monolayers are described in chapter 3 and chapter 4. Finally, the application of intestinal monolayers towards the prediction of a select NPDI impacting oral metformin's absorption precipitated by the herbal supplement, goldenseal, is described in chapter 5.

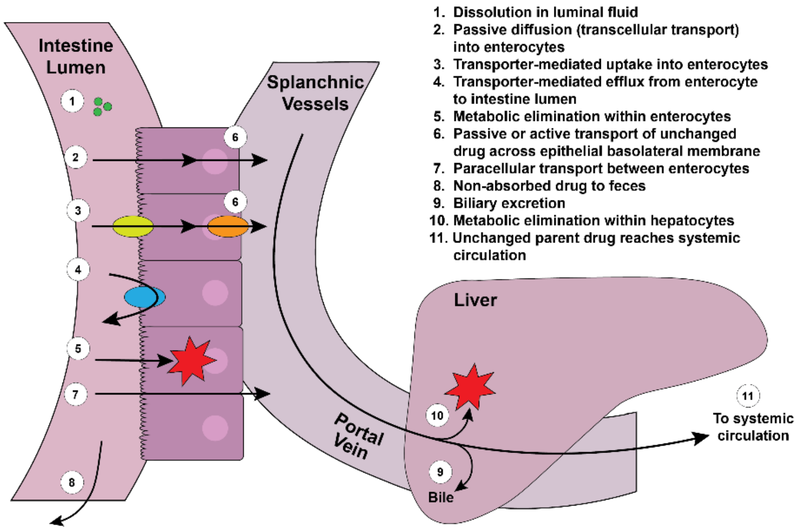

Figure 1.1. The first-pass effect for orally administered drugs and relevant enzymes, transporters, and nuclear receptors expressed in the intestine.

In order for an orally administered drug to reach the systemic blood circulation, there must first be dissolution of the dosage form in the luminal fluid (1) releasing the drug for uptake processes. Absorption of free drug can be transcellular and involve passive (2) or active (3) transport across the apical membrane of the mucosal epithelium. Drug that enters the absorptive enterocytes can be effluxed back into the gut lumen by apical membrane transporters (4), undergo metabolic elimination by phase I and/or phase II drug metabolizing enzymes (5) or be passively or actively transported across the epithelial basolateral membrane (6) for delivery to the splanchnic blood vessels in the intimal space. Of particular note for prodrugs, metabolites can also undergo active transport across the epithelial basolateral membrane for delivery to the splanchnic blood vessels. Absorption from the intestinal lumen can also proceed by diffusion through the paracellular pathway (7) for delivery into splanchnic blood vessels or the lymphatic system. Drug that has undergone luminal degradation in the GI tract (by low pH mediated-degradation or direct degradation by intestinal microbiome enzymes) and/or drug that is not absorbed will continue along the intestinal tract where it will eventually be excreted in the feces (8). Unchanged drug in the splanchnic vessels will be delivered to the liver via the portal vein and then, after uptake into hepatocytes, subjected to either biliary excretion (9) or another round of metabolic elimination within the hepatocytes (10). Drug that is able to escape both the intestine and liver unchanged is then available to the systemic blood circulation (11), where it can reach site(s) of action. An ideal pre-clinical model of drug absorption and the first-pass effect should be able to capture all of these processes.

Table 1.1 – Summary of strengths and weaknesses of historically used *in vitro* systems.

In vitro system	Strengths	Weaknesses
Ussing chamber	- Segment-specific drug transport and metabolic studies[1] - Can assess simultaneous transport and metabolism processes[2]	- Requires access to fresh tissue biopsies[1,3,4] - Limited viability (2-4 hours)[1,3,4]
Precision-cut intestinal slices	- More efficient use of tissue than Ussing chamber[4] - Valuable tool to study first-pass metabolism and DDIs[5]	- Unsuitable for drug permeability (diffusion and active transport) studies[4] - Requires access to fresh tissue biopsies[6] - Limited viability (8-24 hours)[6]
Caco-2 cells	- High throughput model to study intestinal drug absorption[7]	- Lack key DME and NR expression/function[8] - Derived from human colorectal cancer – display disparate DMET expression compared to healthy human adult small intestine[8,9]
LS180 cells	- High throughput model to study intestinal drug metabolism[10]	- Unsuitable for drug transporter studies – cells do not form tight junctions[11] - Derived from human colorectal cancer – display disparate DMET expression compared to healthy human adult small intestine[12]
Primary enterocytes	- Derived from the small intestine of healthy tissue; can be isolated from different regions[13] - Useful tool to study intestinal drug metabolism[13,14]	- Unsuitable for drug transporter studies – cells are cultured in suspension[13] - Limited viability (5-7 days) and cannot be passaged[13]

[1] (Sjöberg et al., 2013), [2] (Michiba et al., 2021), [3] (Kisser et al., 2017), [4] (van de Kerkhof et al., 2007), [5] (Groothuis and de Graaf, 2013), [6] (Li et al., 2016), [7] (Lea, 2015), [8] (Schmiedlin-Ren et al., 1997), [9] (Sun et al., 2002), [10] (Gupta et al., 2008), [11] (Yamaura et al., 2016), [12] (Pfrunder et al., 2003), [13] (Ho et al., 2017), [14] (Li et al., 2020)

1.2. HYPOTHESIS AND SPECIFIC AIMS

A more physiologically relevant *in vitro* model of the human intestine will result in more accurate predictions of the intestinal first pass effect and associated drug-drug/NP-drug interactions.

Specific aim 1: Develop protocols and techniques for culturing intestinal cells (LS180) in the Microfluidic ChipShop MPS and assess DMET/barrier function compared to traditional 2D (Transwell®) culture.

Specific aim 2: Develop intestinal organoid (enteroid) culturing protocol and assess physical and DMET barrier functions for enteroid monolayers in Transwell® culture.

Specific aim 3: Determine cell types present in enteroid monolayer culture and their relative proportions by using publicly available single cell RNA-seq datasets of the *in vivo* human intestine to deconvolute bulk RNA-seq data of enteroid monolayers.

Specific aim 4: Assess the utility of enteroid monolayers to predict and elucidate the mechanisms of a selected natural product-drug interactions precipitated by goldenseal via the inhibition of organic cation transporters impacting metformin's intestinal absorption.

1.3. REFERENCES

Barone GW, Gurley BJ, Ketel BL, Lightfoot ML, and Abul-Ezz SR (2000) Drug interaction between St. John's wort and cyclosporine. *The Annals of pharmacotherapy* **34:**1013-1016.

Benet LZ, Wu C-Y, Hebert MF, and Wacher VJ (1996) Intestinal drug metabolism and antitransport processes: A potential paradigm shift in oral drug delivery. *Journal of Controlled Release* **39:**139-143.

Blutt SE, Broughman JR, Zou W, Zeng XL, Karandikar UC, In J, Zachos NC, Kovbasnjuk O, Donowitz M, and Estes MK (2017) Gastrointestinal microphysiological systems. *Exp Biol Med (Maywood)* **242:**1633-1642.

Chang SY, Voellinger JL, Van Ness KP, Chapron B, Shaffer RM, Neumann T, White CC, Kavanagh TJ, Kelly EJ, and Eaton DL (2017) Characterization of rat or human hepatocytes cultured in microphysiological systems (MPS) to identify hepatotoxicity. *Toxicol In Vitro* **40:**170-183.

Chapron A, Chapron BD, Hailey DW, Chang SY, Imaoka T, Thummel KE, Kelly E, Himmelfarb J, Shen D, and Yeung CK (2020) An Improved Vascularized, Dual-Channel Microphysiological System Facilitates Modeling of Proximal Tubular Solute Secretion. *ACS Pharmacol Transl Sci* **3:**496-508.

Chen M, Hu S, Li Y, Gibson AA, Fu Q, Baker SD, and Sparreboom A (2020) Role of Oatp2b1 in Drug Absorption and Drug-Drug Interactions. *Drug Metab Dispos* **48:**419-425.

Couto N, Al-Majdoub ZM, Gibson S, Davies PJ, Achour B, Harwood MD, Carlson G, Barber J, Rostami-Hodjegan A, and Warhurst G (2020) Quantitative Proteomics of Clinically Relevant Drug-Metabolizing Enzymes and Drug Transporters and Their Intercorrelations in the Human Small Intestine. *Drug Metab Dispos* **48:**245-254.

Cummins CL, Jacobsen W, and Benet LZ (2002) Unmasking the dynamic interplay between intestinal P-glycoprotein and CYP3A4. *J Pharmacol Exp Ther* **300:**1036-1045.

Fritz A, Busch D, Lapczuk J, Ostrowski M, Drozdzik M, and Oswald S (2019) Expression of clinically relevant drug-metabolizing enzymes along the human intestine and their correlation to drug transporters and nuclear receptors: An intra-subject analysis. *Basic Clin Pharmacol Toxicol* **124:**245-255.

Giacomini KM, Galetin A, and Huang SM (2018) The International Transporter Consortium: Summarizing Advances in the Role of Transporters in Drug Development. *Clin Pharmacol Ther* **104:**766-771.

Greiner B, Eichelbaum M, Fritz P, Kreichgauer HP, von Richter O, Zundler J, and Kroemer HK (1999) The role of intestinal P-glycoprotein in the interaction of digoxin and rifampin. *J Clin Invest* **104:**147-153.

Groothuis GM and de Graaf IA (2013) Precision-cut intestinal slices as in vitro tool for studies on drug metabolism. *Curr Drug Metab* **14:**112-119.

Gupta A, Mugundu GM, Desai PB, Thummel KE, and Unadkat JD (2008) Intestinal human colon adenocarcinoma cell line LS180 is an excellent model to study pregnane X receptor, but not constitutive androstane receptor, mediated CYP3A4 and multidrug resistance transporter 1 induction: studies with anti-human immunodeficiency virus protease inhibitors. *Drug Metab Dispos* **36:**1172-1180.

Helander HF and Fandriks L (2014) Surface area of the digestive tract - revisited. *Scand J Gastroenterol* **49:**681-689.

Ho MD, Ring N, Amaral K, Doshi U, and Li AP (2017) Human Enterocytes as an In Vitro Model for the Evaluation of Intestinal Drug Metabolism: Characterization of Drug-Metabolizing Enzyme Activities of Cryopreserved Human Enterocytes from Twenty-Four Donors. *Drug Metab Dispos* **45:**686-691.

In JG, Foulke-Abel J, Estes MK, Zachos NC, Kovbasnjuk O, and Donowitz M (2016) Human mini-guts: new insights into intestinal physiology and host-pathogen interactions. *Nat Rev Gastroenterol Hepatol* **13:**633-642.

Kisser B, Mangelsen E, Wingolf C, Partecke LI, Heidecke CD, Tannergren C, Oswald S, and Keiser M (2017) The Ussing Chamber Assay to Study Drug Metabolism and Transport in the Human Intestine. *Curr Protoc Pharmacol* **77:**7 17 11-17 17 19.

Kolars JC, Awni WM, Merion RM, and Watkins PB (1991) First-pass metabolism of cyclosporin by the gut. *Lancet (London, England)* **338:**1488-1490.

Lea T (2015) Caco-2 Cell Line, in: *The Impact of Food Bioactives on Health: in vitro and ex vivo models* (Verhoeckx K, Cotter P, Lopez-Exposito I, Kleiveland C, Lea T, Mackie A, Requena T, Swiatecka D, and Wichers H eds), pp 103-111, Cham (CH).

Lennernas H, Ahrenstedt O, Hallgren R, Knutson L, Ryde M, and Paalzow LK (1992) Regional jejunal perfusion, a new in vivo approach to study oral drug absorption in man. *Pharm Res* **9:**1243-1251.

Li AP (2020) In vitro human cell-based experimental models for the evaluation of enteric metabolism and drug interaction potential of drugs and natural products. *Drug Metab Dispos*.

Li AP, Alam N, Amaral K, Ho MD, Loretz C, Mitchell W, and Yang Q (2018) Cryopreserved Human Intestinal Mucosal Epithelium: A Novel In Vitro Experimental System for the Evaluation of Enteric Drug Metabolism, Cytochrome P450 Induction, and Enterotoxicity. *Drug Metab Dispos* **46:**1562-1571.

Li AP, Ho MD, Alam N, Mitchell W, Wong S, Yan Z, Kenny JR, and C ECAH (2020) Inter-individual and inter-regional variations in enteric drug metabolizing enzyme activities: Results with cryopreserved human intestinal mucosal epithelia (CHIM) from the small intestines of 14 donors. *Pharmacology research & perspectives* **8:**e00645.

Li M, de Graaf IAM, and Groothuis GMM (2016) Precision-cut intestinal slices: alternative model for drug transport, metabolism, and toxicology research. *Expert Opinion on Drug Metabolism & Toxicology* **12:**175-190.

Lin L and Wong H (2017) Predicting Oral Drug Absorption: Mini Review on Physiologically-Based Pharmacokinetic Models. *Pharmaceutics* **9**.

Michiba K, Maeda K, Kurimori K, Enomoto T, Shimomura O, Takeuchi T, Nishiyama H, Oda T, and Kusuhara H (2021) Characterization of the Human Intestinal Drug Transport with Ussing Chamber System Incorporating Freshly Isolated Human Jejunum. *Drug Metab Dispos* **49:**84-93.

Minhas GS and Newstead S (2019) Structural basis for prodrug recognition by the SLC15 family of proton-coupled peptide transporters. *Proc Natl Acad Sci U S A* **116:**804-809.

Olefsky JM (2001) Nuclear receptor minireview series. *J Biol Chem* **276:**36863-36864.

Paine MF, Hart HL, Ludington SS, Haining RL, Rettie AE, and Zeldin DC (2006) The human intestinal cytochrome P450 "pie". *Drug Metab Dispos* **34:**880-886.

Paine MF, Khalighi M, Fisher JM, Shen DD, Kunze KL, Marsh CL, Perkins JD, and Thummel KE (1997) Characterization of interintestinal and intraintestinal variations in human CYP3A-dependent metabolism. *J Pharmacol Exp Ther* **283:**1552-1562.

Paine MF and Roe AL (2018) "Green Medicine": The Past, Present, and Future of Botanicals. *Clin Pharmacol Ther* **104:**410-415.

Paine MF, Shen DD, Kunze KL, Perkins JD, Marsh CL, McVicar JP, Barr DM, Gillies BS, and Thummel KE (1996) First-pass metabolism of midazolam by the human intestine. *Clin Pharmacol Ther* **60:**14-24.

Paine MF, Shen DD, and McCune JS (2018) Recommended Approaches for Pharmacokinetic Natural Product-Drug Interaction Research: a NaPDI Center Commentary. *Drug Metab Dispos* **46:**1041-1045.

Pfrunder A, Gutmann H, Beglinger C, and Drewe J (2003) Gene expression of CYP3A4, ABC-transporters (MDR1 and MRP1-MRP5) and hPXR in three different human colon carcinoma cell lines. *J Pharm Pharmacol* **55:**59-66.

Rigalli JP, Theile D, Nilles J, and Weiss J (2021) Regulation of PXR Function by Coactivator and Corepressor Proteins: Ligand Binding Is Just the Beginning. *Cells* **10**.

Rossi G, Manfrin A, and Lutolf MP (2018) Progress and potential in organoid research. *Nat Rev Genet* **19:**671-687.

Rowland M, Tozer TN, and Rowland M (2009) *Pharmacokinetics and pharmacodynamics : concepts and clinical applications*. Lippincott William & Wilkins, Philadelphia.

Schmiedlin-Ren P, Thummel KE, Fisher JM, Paine MF, Lown KS, and Watkins PB (1997) Expression of enzymatically active CYP3A4 by Caco-2 cells grown on extracellular matrix-coated permeable supports in the presence of 1alpha,25-dihydroxyvitamin D3. *Mol Pharmacol* **51:**741-754.

Shugarts S and Benet LZ (2009) The role of transporters in the pharmacokinetics of orally administered drugs. *Pharm Res* **26:**2039-2054.

Sjöberg Å, Lutz M, Tannergren C, Wingolf C, Borde A, and Ungell A-L (2013) Comprehensive study on regional human intestinal permeability and prediction of fraction absorbed of drugs using the Ussing chamber technique. *European Journal of Pharmaceutical Sciences* **48:**166-180.

Sun D, Lennernas H, Welage LS, Barnett JL, Landowski CP, Foster D, Fleisher D, Lee KD, and Amidon GL (2002) Comparison of human duodenum and Caco-2 gene expression profiles for 12,000 gene sequences tags and correlation with permeability of 26 drugs. *Pharm Res* **19:**1400-1416.

Thummel KE (2007) Gut instincts: CYP3A4 and intestinal drug metabolism. *J Clin Invest* **117:**3173-3176.

Thummel KE, Brimer C, Yasuda K, Thottassery J, Senn T, Lin Y, Ishizuka H, Kharasch E, Schuetz J, and Schuetz E (2001) Transcriptional control of intestinal cytochrome P-4503A by 1alpha,25-dihydroxy vitamin D3. *Mol Pharmacol* **60:**1399-1406.

van de Kerkhof EG, de Graaf IA, and Groothuis GM (2007) In vitro methods to study intestinal drug metabolism. *Curr Drug Metab* **8:**658-675.

Wacher VJ, Silverman JA, Zhang Y, and Benet LZ (1998) Role of P-glycoprotein and cytochrome P450 3A in limiting oral absorption of peptides and peptidomimetics. *J Pharm Sci* **87:**1322-1330.

Wacher VJ, Wu CY, and Benet LZ (1995) Overlapping substrate specificities and tissue distribution of cytochrome P450 3A and P-glycoprotein: implications for drug delivery and activity in cancer chemotherapy. *Mol Carcinog* **13:**129-134.

Yamaura Y, Chapron BD, Wang Z, Himmelfarb J, and Thummel KE (2016) Functional Comparison of Human Colonic Carcinoma Cell Lines and Primary Small Intestinal Epithelial Cells for Investigations of Intestinal Drug Permeability and First-Pass Metabolism. *Drug Metab Dispos* **44:**329-335.

Yang B and Smith DE (2013) Significance of peptide transporter 1 in the intestinal permeability of valacyclovir in wild-type and PepT1 knockout mice. *Drug Metab Dispos* **41:**608-614.

Yu J, Zhou Z, Tay-Sontheimer J, Levy RH, and Ragueneau-Majlessi I (2017) Intestinal Drug Interactions Mediated by OATPs: A Systematic Review of Preclinical and Clinical Findings. *J Pharm Sci* **106:**2312-2325.

Zanger UM and Schwab M (2013) Cytochrome P450 enzymes in drug metabolism: regulation of gene expression, enzyme activities, and impact of genetic variation. *Pharmacol Ther* **138:**103-141.

Zhang H, Wolford C, Basit A, Li AP, Fan PW, Murray BP, Takahashi RH, Khojasteh SC, Smith BJ, Thummel KE, and Prasad B (2020) Regional Proteomic Quantification of Clinically Relevant Non-Cytochrome P450 Enzymes along the Human Small Intestine. *Drug Metab Dispos* **48:**528-536.

Zhou C, Tabb MM, Sadatrafiei A, Grun F, and Blumberg B (2004) Tocotrienols activate the steroid and xenobiotic receptor, SXR, and selectively regulate expression of its target genes. *Drug Metab Dispos* **32:**1075-1082.

CHAPTER 2. THE DEVELOPMENT OF AN INTESTINAL MICROPHYSIOLOGICAL SYSTEM

(Part of this chapter was published as a review article "Gutsy Science: *In vitro* systems of the human intestine to model oral drug disposition" (2021) *Pharmacology and Therapeutics*)

2.1. INTRODUCTION

Over the past decade, there has been growing interest and progress towards the development of microphysiological systems (MPS) to produce organotypic *in vitro* models that can more accurately recapitulate organ function than traditional *in vitro* methods (Arian et al., 2022). MPS, frequently referred to as "organs-on-a-chip", are microfluidic devices that incorporate one or more cell types and perfused by a directional flow of culture media (Marx et al., 2020). The application of flow, and its associated shear force, facilitates cell polarization, cell viability, and cell function that more closely recapitulates what is seen *in vivo* (Wikswo, 2014; Chang et al., 2017; Trietsch et al., 2017). Some intestinal MPS contain two collagen-coated hollow channels separated by a porous membrane, where the membrane facing surface of one channel is populated with intestinal epithelial cells (epithelial channel) while the other is populated with endothelial cells (vascular channel). This platform design allows researchers to sample both the epithelial and vascular channels, permitting the study of vectorial transport across the intestinal epithelium (Bein et al., 2018). Furthermore, the introduction of drug in the epithelial flow channel produces a more physiologically relevant presentation of drug to the epithelial barrier, and incorporation of a vascular channel can recapitulate the "sink" condition *in vivo*, which facilitates vectorial transport.

Current applications of intestinal MPS for use in pharmaceutical research has employed both Caco-2 cells and human enteroids (Kim et al., 2012; Shim et al., 2017; Kasendra et al., 2020).

The former is of note as MPS populated with Caco-2 cells have demonstrated improved CYP3A4 function compared to traditional, static, cell culture. This is a significant improvement over traditional culture methods as Caco-2 cells are known to have sub-physiologic expression and activity of CYP3A4, likely reflective of their derivation from the colon where CYP3A4 expression is limited. Though MPS culture has improved the physiologic relevance of Caco-2 cells compared to Caco-2 monolayers, there currently are no reports of MPS populated with LS180 cells. Like Caco-2, LS180 cells are an immortalized human epithelial colorectal adenocarcinoma cell line typically cultured on Transwell® filters, allowing for a high throughput assessment of function. Unlike Caco-2, LS180 cells display faster proliferation and less distinct morphological and functional differentiation in culture (Heischmann and Christians, 2018). This allows LS180 monolayers to reach functional maturity in culture after only three days, as opposed to 2-3 weeks for Caco-2. However, in contrast to Caco-2 monolayers, LS180 monolayers do not display tight junction formation in traditional static cell culture, making them a poor model to study transport-mediated and/or passive absorption of drugs in the intestine (Yamaura et al., 2016). This lack of barrier formation is likely a major reason for the absence of studies utilizing LS180 cells cultured in MPS to predict orally administered drug disposition. However, the improvements in CYP3A4 activity demonstrated by Caco-2 cells cultured in MPS suggests that the MPS environment, which incorporates fluid dynamics and associated sheer stress upon the cells, might impart an improvement on the barrier function of LS180 cells.

This chapter explores the utility of a dual-channel MPS – the “Fluidic 480”, produced by Microfluidic ChipShop® (**Figure 2.1**) – cultured with LS180 cells and a primary human umbilical vein endothelial cells (HUVECs), as a model to predict orally administered drug disposition. To achieve this, we assessed global RNA expression via RNA-seq analysis, monolayer barrier function utilizing a paracellular transport probe, and CYP3A activity using midazolam as a selective probe substrate for LS180 cells cultured in MPS versus traditional Transwell® culture™.

2.2. MATERIALS AND METHODS

2.2.1. Chemicals and reagents.

MEM, fetal bovine serum (FBS), Trypsin-EDTA (0.25%), Versene solution, Penicillin-Streptomycin (10,000 U/mL), Dulbecco's phosphate-buffered saline with calcium and magnesium (DPBS^{++}), DPBS without calcium and magnesium, HEPES buffer (1M), and Hanks' Balanced Salt Solution with calcium and magnesium (HBSS^{++}) were purchased from Life Technologies (Carlsbad, CA).Midazolam, midazolam-d_4, 1-OH midazolam, and 1-OH midazolam-d_4 were purchased from Cerilliant (Round Rock, TX). Collagen IV was purchased from Corning (Corning, NY). Atenolol-d_7 was purchased from Cayman Chemical (Ann Arbor MI). Atenolol and sodium bicarbonate were purchased from Sigma-Aldrich (St. Louis, MO). RLT Lysis buffer was purchased from Qiagen (Germantown, MD).

2.2.2. Cell culture maintenance

LS180 cells were maintained in culture as described in a previous report (Arian et al., 2024) with slight adjustments. Briefly, LS180 cells (passages 26-32) were cultured in a T75 flask with MEM supplemented with 2% (v/v) FBS and 1% (v/v) penicillin-streptomycin. After 7 days in culture, cells were washed with warm DPBS (without calcium and magnesium) then incubated with Versene 1x for 5 minutes at room temperature and detached from the flask via gentle tapping of the flask. Suspended cells were then centrifuged at 1200g for 2 minutes. The resulting cell pellet was resuspended in MEM containing 2% FBS and 1% penicillin-streptomycin and passaged at a density of 1:3 to 1:5 and cultured in a fresh T75 flask.

HUVECs (passages 4-7) were maintained as described by Lonza. Briefly, cells were cultured in a T25 or T75 flask with EGM™-2 Endothelial Cell Growth Medium-2 BulletKit™ (Lonza, Switzerland). After 5-7 days in culture, or when cells reached ~80% confluency, cells were washed HEPES buffered saline solution and then incubated with 3 mL trypsin/EDTA (0.25%) for 3 minutes at 37ºC to detach cells from flask. The trypsin solution was then neutralized with 6 mL of defined trypsin inhibitor and the cell suspension was transferred to a 15 mL tube for centrifugation. Cells were centrifuged at 220g for 5 minutes. The resulting cell pellet was resuspended in endothelial cell medium and passaged at a density of 1:3 in a fresh T25 or T75 flask.

2.2.3. MPS preparation

Materials and MPS were prepared one day prior to seeding MPS with LS180 cells and HUVECs. MPS (Fluidic 480, product code 10000739; Microfluidic ChipShop®, Jena, Germany) were placed in cell culture hoods aseptically and subjected to UV light decontamination for 15 minutes to sterilize. Male luer fluid connectors (Product code 10000029; Microfluidic ChipShop®, Jena, Germany) were attached to MPS and the connection point of the MPS and fluid connectors was sealed with medical-grade sealant (Factor II Inc., Pinetop-Lakeside AZ). Plugs (8 per MPS) were prepared via attaching sterile metal couplers (blunt; Instech Lab) to small pieces of C-flex tubing (~3 cm) and half of the plugs were attached to the inlet fluid connectors attached to the MPS and the remaining half were stored in a sterile environment until the day of HUVEC seeding. Collecting vessels (4 per MPS) for washing/cell seeding effluent were prepared by attaching metal couplers to both ends of a small piece of C-flex tubing (~5 cm). One end of the tubing was attached to an amber vial capped with a pre-slit lid and the other end was attached to the outlet fluid connectors attached to the MPS. The prepared MPS were then stored in a sterile environment until the day of cell seeding. The tubing to be connected to the chip when flow is initiated (8 per chip) was then prepared via attaching a metal couplers to one end of a 9 cm piece of C-flex tubing (Cole Parmer, cat. no. 06422-00). These prepared tubing sections were then stored in a sterile environment until the day flow was initiated. On the day of LS180 seeding and HUVEC seeding, MPS chambers were unplugged and the chambers were coated with 100 μg/mL collagen IV and then incubated at 37ºC for 4 hours prior to cell seeding.

2.2.4. MPS and Transwell® culture

For Transwell® culture, LS180 cells were seeded and cultured as described in a previous report (Arian et al., 2024) with slight adjustments. Briefly, cells were passaged as described above. Following centrifugation, the resulting cell pellet was resuspended in MEM containing 2% FBS and 1% penicillin-streptomycin at a density of 167,000 cells/mL (resulting in final seeding density of 500,000 cells/cm^2 in Transwell® culture) as determined by a hemocytometer. A 0.25 mL volume of the cell slurry was plated on a 0.4 μm pore-size Transwell® filter inserts for 24-well plates (catalog no. 3470; Corning Inc., NY) that were coated with 100 μg/mL collagen IV as described above. A 1 mL volume of MEM containing 2% FBS and 1% penicillin-streptomycin was then added to the basolateral chamber. Cells were fed every two days by aspirating apical and basolateral medium and replacing with 0.25 mL and 1 mL of MEM containing 2% FBS and 1% penicillin-streptomycin to the apical and basolateral chambers, respectively. Cells were grown for 7- and 21-days prior to experiments. For experimental conditions that included vitamin D-induction (see CYP3A activity assay section), cells were treated with LS180 media containing 1 nM of $1\alpha,25(OH)_2$ vitamin D_3 at day 5 and day 19 of culture. Cells were treated with vitamin D for 48 hours prior to CYP3A activity assessment.

For MPS culture, LS180 cells were cultured as described above. Following centrifugation, the resulting cell pellet was resuspended in MEM containing 2% FBS and 1% penicillin-streptomycin at a density of 8,800,000 cells/mL (resulting in a final density of 500,000 cells/cm^2 in MPS) as determined by a hemocytometer. MPS were removed from the 37ºC cell incubator and the channels were washed with 3-channel volumes of blank LS180 media via injection with a 1 mL syringe to equilibrate the intestinal (top) channels. A 100 µL volume of the cell suspension was then injected into the intestinal channels. The collecting vessels attached to the intestinal channels were removed and the intestinal channels were occluded with the plugs prepared above. MPS were then placed in a 37ºC overnight to allow LS180 cells to attach.

The following day, HUVEC cells were cultured as described above. Following centrifugation, the resulting cell pellet was resuspended in endothelial cell medium at a density of 9,600,000 cells/mL (resulting in a final density of 500,000 cells/cm^2 in MPS) as determined by a hemocytometer. MPS were removed from the 37ºC cell incubator and the channels were washed with 3-channel volumes of blank endothelial cell medium via injection with a 1 mL syringe to equilibrate the vascular (bottom) channels. A 100 µL volume of the cell suspension was then injected into the vascular channels. The collecting vessels attached to the vascular channels were removed and the vascular channels were occluded with the plugs prepared above. MPS were then inverted upside down to allow HUVECs to attach to the semipermeable membrane adjacent to the LS180 cells to allow for cell-cell contact. Inverted MPS were then placed in a 37ºC overnight to allow HUVECs to attach.

The following day, operational MPS platforms were prepared by placing 8 media reservoirs (Nortis Inc, Bothel WA) per chip (4 inlet, 4 outlet – two inlets/outlets correspond to the intestinal channels and two inlets/outlets correspond to the vascular channel) into a reservoir housing unit.

A 10 mL volume of the appropriate media (LS180 or endothelial cell medium) was added to each inlet reservoir. The C-flex tubing segments prepared in the above section were then attached to the reservoirs and the end containing the metallic blunt was placed in an amber vial capped with a pre-slit lid. The reservoir housing units were then sealed and pressurized and placed into a 37ºC cell incubator and connected to a pneumatic pump (Nortis Inc, Bothel WA) to equilibrate the tubing attached to the inlet reservoirs to remove all air from the tubes. The pump was set to a pressure that corresponded to a flow rate of 1 µL/min. Following equilibration of the inlet tubing segments (~15 minutes), the MPS platform was removed from the 37ºC incubator. The amber vials were removed from the tubing and the tubing was then connected to the MPS, with intestinal channels being connected to inlet reservoirs containing LS180 medium and vascular channels connected to inlet reservoirs containing endothelial cell medium. The connection point of the tubing and the MPS was then sealed with a medical-grade sealant and the MPS platform was returned to the 37ºC incubator. The platform was then connected to the pneumatic pump at a pressure that corresponded to a flow rate of 1 µL/min. Cells were allowed to grow for 7 and 21 days prior to experimentation. Inlet media was replaced and outlet media was aspirated every 3 days.

For experimental conditions that included vitamin D-induction (see CYP3A activity assay section), the intestinal channel was perfused with LS180 media containing 1 nM of $1\alpha,25(OH)_2$ vitamin D_3 at day 5 and day 19 of culture. Cells were treated with vitamin D for 48 hours prior to CYP3A activity assessment.

2.2.5. RNA-seq analysis

RNA-seq analysis was performed as described in a previous report (Arian et al., 2024). Briefly, matched LS180 cells from the same passage and experiment cultured in either Transwell® or

MPS grown for 7- or 21-days were lysed with 0.5 mL of RLT lysis buffer (Qiagen Sciences Inc., Germantown, Maryland) and stored at -80ºC until analysis. Samples were sent to Novogene America (Sacramento, California) where the RNA was isolated and messenger RNA was purified from total RNA using poly-T oligo-attached magnetic beads. mRNA was then fragmented and the first strand cDNA was synthesized using random hexamer primers, followed by second strand cDNA synthesis using dTTP for non-directional library and sequenced by a NovaSeq 6000 system (Illumina, San Diego, CA). Quality of the sequencing data was assessed using fastqc (Andrews, 2010), and then reads were aligned to the Ensembl GRCh38 p12 genome using the HiSat2 aligner (Kim et al., 2019). Counts/gene were generated using the Bioconductor Rsubread (Liao et al., 2019) package. Total aligned reads ranged between 14.5M – 18M per sample. Pathway analysis of the RNA-seq data was performed using the iPathwayGuide software from ADVAITA (Advaita Corporation, Ann Arbor, MI). Genes with FDR <0.05 were used for pathway analysis. Details for the statistical analysis of the RNA-seq data are provided in section 2.2.11.

2.2.6. Transwell® permeability assay

Transwell® culture paracellular permeability was performed as described in (Arian et al., 2024). Briefly, cell monolayers were washed three times with blank apical transport buffer (10 mM HEPES in Hank's balanced salt solution, pH 6.5) and maintained at 37ºC until use. Stock solutions of the atenolol (60 mM in DMSO) was diluted in apical transport buffer to make the dosing solutions (final concentration of 300 µM atenolol, 0.5% DMSO).

A 0.3 mL volume of the dosing solution was added to the filter insert and 0.7 mL of the receiver solution (10 mM HEPES in Hank's balanced salt solution, pH 7.4, containing 0.5% DMSO) was added to the basolateral compartment. Cells were incubated for 90 minutes at 37ºC and the total volume from the apical and basolateral compartment were collected separately and stored at -80ºC until analysis. Atenolol was quantified using liquid chromatography coupled with tandem mass spectrometry on an Agilent 6410 QQQ equipped with a UPLC 1290 system. After thawing and vortexing, 50 μL of basolateral samples and 50 μL of diluted apical samples (diluted 300-fold in blank apical transport buffer) were mixed with 20 μL internal standard (1.25 μM in methanol) and 30 μL of methanol. A series of dilutions of atenolol standards were prepared in methanol and stored at -80ºC. The standard curve was prepared using 10 μL of each stock solution and 50 μL of blank transport buffer mixed with 20 μL of internal standard and 20 μL of methanol. Unknowns and standards were then centrifuged at 20,800*g* for 10 minutes at room temperature, and 75 μL of the supernatant was analyzed by LC/MS-MS. Chromatographic separation was achieved following injection of 5 μL of sample using a Zorbax SB-C18 narrow-bore, 5 μm, 2.1 x 150 mm column using 10 mM ammonium acetate (A) and methanol (B) as a mobile phase. The flow rate was 0.25 mL/min with a gradient as follows: 5% B for 1.5 minutes, then increased to 75% B linearly over 2 minutes, held at 75% for 4.5 minutes, and then equilibrated back to 5% for 4 minutes. The following MRM transitions were monitored: *m/z* 267.3 > 145.0 for atenolol, and *m/z* 274.3 > 145.2 for atenolol-d_7 in the positive ion mode. For both compounds, dwell time was set to 200 ms, collision energy was set to 29 eV, and cell accelerator voltage was set to 4 V. The fragmentor was set to 113 V for atenolol and 127 for atenolol-d_7.

2.2.7. MPS permeability assay

Stock solutions of the atenolol (60 mM in DMSO) was diluted in apical transport buffer to make the dosing solutions (final concentration of 300 μM atenolol, 0.5% DMSO). The intestinal and vascular channels were washed, respectively, with the dosing apical transport buffer containing atenolol and vehicle-matched basolateral transport buffer, for 4 hours at 37ºC at a flow rate of 1 µL/min to equilibrate each channel. Following the 4-hour equilibration period, the outlet reservoirs were aspirated and the MPS platforms were placed back in the 37ºC incubator for an additional 4 hours at a flow rate of 1 µL/min. At the end of the 4-hour period, samples from both the intestinal and vascular reservoirs were collected and were prepared for analysis as described above in section 2.2.7.

2.2.8. Permeability coefficient calculation

The apparent permeability coefficient for atenolol was calculated using the following equation:

$$P_{app} = \frac{dQ}{dt} \cdot \frac{1}{SA \cdot C_0}$$

where dQ/dt is the rate of compound appearance in the vascular channel for MPS or basolateral chamber for Transwell® (pmol/s) under sink conditions, SA is the surface area of the MPS semipermeable membrane or Transwell® insert filter (cm^2), and C_0 is the dosing concentration of compound in the apical compartment.

2.2.9. CYP3A activity assay

CYP3A activity for Transwell® cultured LS180 cells was performed as described in a previous report (Arian et al., 2024). Briefly, monolayers were washed three times with $DPBS^{++}$ maintained at 37ºC until use. A stock solution of midazolam (3 mM) was diluted in LS180 medium (final concentration 8 µM midazolam, 0.27% methanol). $DPBS^{++}$ was then removed, and 0.3 mL of the dosing solution was added to the filter insert and 0.7 mL of LS180 medium (containing 0.27% methanol v/v) was added to the basolateral compartment. Cells were incubated for 60 minutes at 37ºC and the total volume from the apical and basolateral compartment were collected separately and stored at -80ºC until analysis.

For MPS culture, a stock solution of midazolam (3 mM) was diluted in LS180 medium (final concentration 8 μM midazolam, 0.27% methanol) and added to the intestinal channel media. Methanol was added to endothelial cell medium (final concentration of 0.27% methanol v/v). Inlet and outlet reservoirs were aspirated and the appropriate medias were added to the intestinal and vascular inlet reservoirs, respectively. The MPS platform was placed back in the 37°C reservoir and media was flowed at a rate of 1 μL/ min for 24 hours. Following 24 hours, the total medium from the outlet reservoirs of both the intestinal and vascular channels were collected and stored at -80°C for later analysis.

Midazolam and 1-OH midazolam were quantified using liquid chromatography coupled with tandem mass spectrometry on an Agilent 6410 QQQ equipped with a UPLC 1290 system. After thawing and vortexing samples, 200 μL of basolateral sample and 50 μL of apical sample (diluted 4-fold in blank apical buffer to a final volume of 200 μL) was mixed with 250 μL of sodium carbonate buffer (100 mM, pH 11.4) and 20 μL of internal standard (midazolam-d4, 150 ng/mL in methanol). A series of dilutions of midazolam standards were prepared in methanol and stored at -80°C. A standard curve was prepared using 10 μL of each stock solution and 200 μL of blank transport buffer and mixing with 250 μL of sodium carbonate buffer and 20 μL of internal standard. 3 mL of ethyl acetate was then added to the unknown and standard curve samples followed by 20 minutes of shaking and centrifugation at 2000*g* for 20 minutes at room temperature. The top organic layer was then collected and samples were dried using a nitrogen evaporator. Dried samples were then resuspended in 100 μL of 1:1 formic acid solution (0.1% in water): methanol and analyzed via LC/MS-MS. Chromatographic separation following injection of 5 μL sample was achieved using a Zorbax SB-C18 narrow-bore, 5 μm, 2.1 x 150 mm column using 0.1% formic acid in water (A) and methanol (B) as a mobile phase. The flow rate was 0.25

mL/min with a gradient as follows: 50% B for 1 minute, increased to 90% B linearly over 2 minutes, held at 90% for 3 minutes, and then equilibrated back to 50% for 4 minutes. The following MRM transitions were monitored: *m/z* 326.0 > 291.2 for midazolam, and *m/z* 330.0 > 295.0 for midazolam-d_4, *m/z* 342 > 168.1 for 1-OH midazolam, and *m/z* 346 > 168 for 1-OH midazolam-d_4 in the positive ion mode. For midazolam and midazolam-d_4, the dwell time was set to 100 ms, fragmentor was set to 159V, collision energy was set to 28 eV, and cell accelerator voltage was set to 7V. For 1-OH midazolam and 1-OH midazolam-d_4, the dwell time was set to 100 ms and cell accelerator voltage was set to 7 V. Fragmentor and collision energy was set to 143 V and 40 eV for 1-OH midazolam and 153 V and 44 eV for 1-OH midazolam-d_4.

2.2.10. Midazolam first-pass extraction ratio calculation

The midazolam first pass extraction ratio (ER) to assess CYP3A activity was calculated using the following equation (Fisher et al., 1999):

$$ER = \frac{\Sigma(1 - OH\ MDZ)}{\Sigma(1 - OH\ MDZ) + MDZ_{vascular}}$$

where Σ(1-OH MDZ) is the amount of 1-OH midazolam measured in both the intestinal and vascular effluent for MPS or the apical and basolateral chamber for Transwell® (pmol) and $MDZ_{vascular}$ is the amount of unchanged midazolam measured in the vascular effluent for MPS or basolateral chamber for Transwell®. This equation only applies under “sink conditions” – where the concentration of parent midazolam is less than 10% of the dosing concentration of midazolam.

2.2.11. Statistical analysis

RNA-seq statistical analysis was performed as described in a previous report (Arian et al., 2024). Prior to making comparisons, genes with very low expression levels were excluded, based on a mean log counts/million (logCPM) > 0, which reduced the number of genes from just over 70,000 to 13,728 genes. Normalization factors were estimated using the trimmed-mean of M-values (TMM) method (Robinson and Oshlack, 2010), and then comparisons were made between differentiated and undifferentiated cells using a quasi-likelihood F-test (Lun et al., 2016), with a blocking factor to control for sample donor. The analysis was performed using the Bioconductor edgeR package (Robinson et al., 2010). To restrict to those genes with a large change in expression, an additional 20%-fold change criterion was included (e.g., the null hypothesis was specified as Ho: $|\beta| < 1.2$), using the treat function (McCarthy and Smyth, 2009). Differentially expressed genes were selected using a false discovery rate (FDR)<0.05 (Benjamini and Hochberg, 1995). Statistical significance ($\alpha = 0.05$) for the permeability and CYP3A metabolism studies was determined via unpaired t-test. All statistical analysis was performed in RStudio (R. Posit Software, PBC, Boston, MA).

2.3. RESULTS

2.3.1. LS180 MPS versus Transwell® drug transporter expression

The mRNA abundance of various DMET gene products – including phase I and phase II drug metabolizing enzymes, nuclear receptors, transporters, and tight junction proteins – for LS180 cells cultured in MPS and Transwell® at day 7 and day 21 in culture are shown in **Figure 2.2**. Interestingly, drug transporters are the DMET gene products that display the most differentially expressed genes between the two culturing platforms.

2.3.2. Cell monolayer barrier integrity

A comparison of cell monolayer barrier integrity, utilizing the paracellular probe substrate atenolol, for LS180 cells grown in MPS versus Transwell® for 7- and 21-days is shown in **Figure 2.3**. Atenolol permeability was approximately 2-fold lower across LS180 monolayers cultured in MPS than LS180 monolayers in Transwell®, for both time points.

2.3.3. CYP3A activity

A comparison of basal and vitamin-D-induced CYP3A activity, expressed as midazolam first pass extraction ratio, for LS180 cells grown in MPS versus Transwell® is shown in **Figure 2.4**. Midazolam extraction ratio increased following vitamin D treatment for LS180 cells cultured in both platforms and extraction ratios were higher on day-21 in culture, compared to day-7. LS180 cells cultured in MPS had higher midazolam extraction ratios for vitamin D-treated monolayers at day 7 in culture, at approximately 20% for MPS compared to approximately 15% for Transwell®. There was no significant difference for LS180 cells grown on MPS versus Transwell® for basal CYP3A activity at day 7 or for basal and vitamin-D induced CYP3A activity at 21 days in culture.

2.4. DISCUSSION

The development of an intestinal MPS to predict the disposition of orally administered drugs is of high priority for the pharmaceutical industry – exemplified by the recent FDA Modernization Act 2.0, which has authorized the use of alternatives to animal testing in the drug development pipeline (Zushin et al., 2023). These models could provide more informative measures and subsequent predictions of drug absorption and metabolism across the intestinal epithelium than preclinical species or historically used *in vitro* models. Studies in this chapter explore the utility of a dual-channel MPS, the Fluidic 480, populated with LS180 cells in the intestinal chamber and HUVECs in the vascular chamber. We performed RNA-seq analysis of LS180 cells cultured in MPS compared to LS180 cells cultured in static Transwell® culture to assess global changes in gene expression for cells cultured in MPS versus Transwell®. The DMET genes that were most highly impacted by MPS versus Transwell® culture were transporter genes. Moreover, at 21 days in culture the expression of several SLC transporters, such as OATP2B1 and ENT1, were lower in MPS culture while several ABC transporters, such as P-gp and MRP3, were higher in MPS culture. These differences in mRNA expression could reflect that the MPS cultured LS180 cells revert to a colonic phenotype – as expression of ABC transporters is typically higher in the distal intestine, particularly MRP3 which is highly expressed in the human colon (Drozdzik et al., 2014).

We next assessed the barrier integrity of LS180 monolayers in MPS versus Transwell® culture utilizing the probe substrate, atenolol. Results demonstrate that MPS culture resulted in an approximately 2-fold lower atenolol permeability compared to Transwell® culture at both 7- and 21-days in culture. While encouraging, a likely cause for this decreased atenolol permeability is the presence of HUVECs in the vascular chamber, which are known to have high TEER values (>600 Ω*cm^2 for HUVEC versus <30 Ω*cm^2 for LS180) (McRae et al., 2018). RNA-seq results corroborate this hypothesis as there was little change in mRNA expression for tight junction proteins in MPS versus Transwell® culture. While non-physiologic, as the barrier is formed by the endothelial cells as opposed to the intestinal epithelial cells, this system could have utility for the study of passively absorbed compounds – as these compounds would be absorbed via passive diffusion transcellularly or paracellularly. Indeed, the LS180 MPS system could be uniquely suited for the study of passively absorbed compounds that undergo intestinal first-pass metabolism (e.g., some BCS class I drugs), as LS180 cells maintain DME activity. However, this non-physiologic barrier might not be appropriate to recapitulate the drug absorption of compounds that undergo transporter-mediated absorption, as the LS10 and HUVEC cell barriers may not express the relevant intestinal transporters required to model this phenomenon.

We next assessed the CYP3A activity of LS180 cells cultured in MPS and Transwell® using midazolam as a probe substrate. Corroborating previous work from our group, LS180 cells demonstrate increased CYP3A activity following Vitamin D treatment compared to basal conditions at day 7 and day 21 for both MPS and Transwell® culture. Interestingly, LS180 cells cultured in MPS for 7 days had higher CYP3A activity than LS180 cells cultured in Transwell® for 7 days, while there was no difference between the two culture platforms for any other culture conditions. The modest to no change of CYP3A activity between the two culture platforms is corroborated by the RNA-seq results, which show no significant difference in CYP3A expression.

A limitation of this study is that we did not include experiments utilizing Caco-2 cells within our MPS as a positive control. Other groups have shown these cells have displayed an improved CYP3A activity when culture in MPS and these cells could have been utilized as a positive control to assess if the same improved phenotype could be seen in our MPS platform. However, it could be that the intrinsically high CYP3A activity of LS180 cells is high under both Transwell® and MPS culture conditions. Additionally, we did not assess the activity of any transporters in this study. A key finding of the RNA-seq work was that transporters were the DMET genes most impacted by MPS versus Transwell® culture, and that the mRNA phenotype more closely mimicked that of the human colon than the human duodenum. A follow-up study on the activity of these transporters, in particular P-gp, in MPS versus Transwell® could have corroborated the mRNA results. Additionally, this study only assessed CYP3A activity. While CYP3A is the most abundant CYP found within the intestine (Paine et al., 2006), the activity of other DMEs in MPS versus Transwell® would have provided further insight into the physiological relevance of this model.

The absence of substantial differences between LS180 cells cultured in MPS versus Transwell® suggests that this model, cultured with LS180 cells, may not be appropriate for predicting the disposition of orally administered drugs. However, we have developed a high-fidelity protocol with a high success rate (>80% seeding efficiency) – and this high-fidelity culturing protocol, used with more physiologically relevant cells such as human enteroids, could produce a model that may more accurately predict the fate of orally administered drugs. In fact, other groups have demonstrated that human duodenal enteroid monolayers cultured in MPS display phenotypes, such as DMET mRNA and protein expression, that more accurately recapitulates the *in vivo* duodenum compared to other *in vitro* systems (Kim et al., 2012). The remaining chapters of this dissertation will focus on the development and characterization of a human duodenal enteroid monolayer model, cultured on Transwell®. The work presented in this chapter has laid the essential groundwork for culturing enteroid monolayer cells within an MPS, allowing for an accurate and complete comparison between the two Transwell® and MPS culturing systems, in the future.

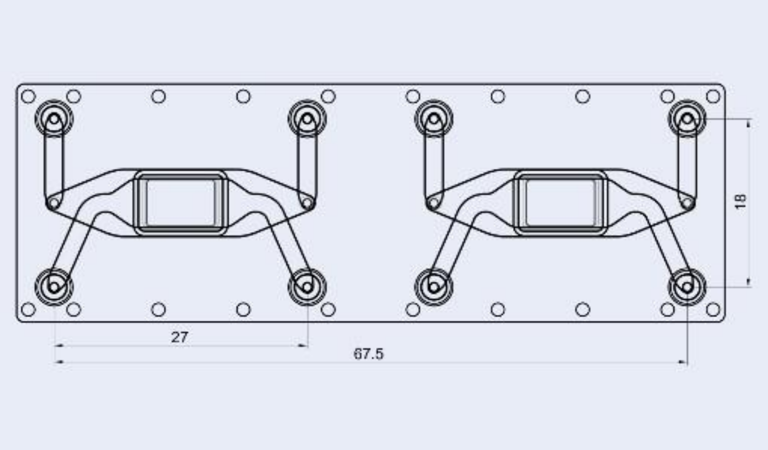

Figure 2.1. CAD diagram of the Microfluidic ChipShop® "Fluidic 480"

Each chip contains two dual-channels, one of which is seeded with endothelial cells and the other with intestinal cells, allowing for the study of vectorial transport.

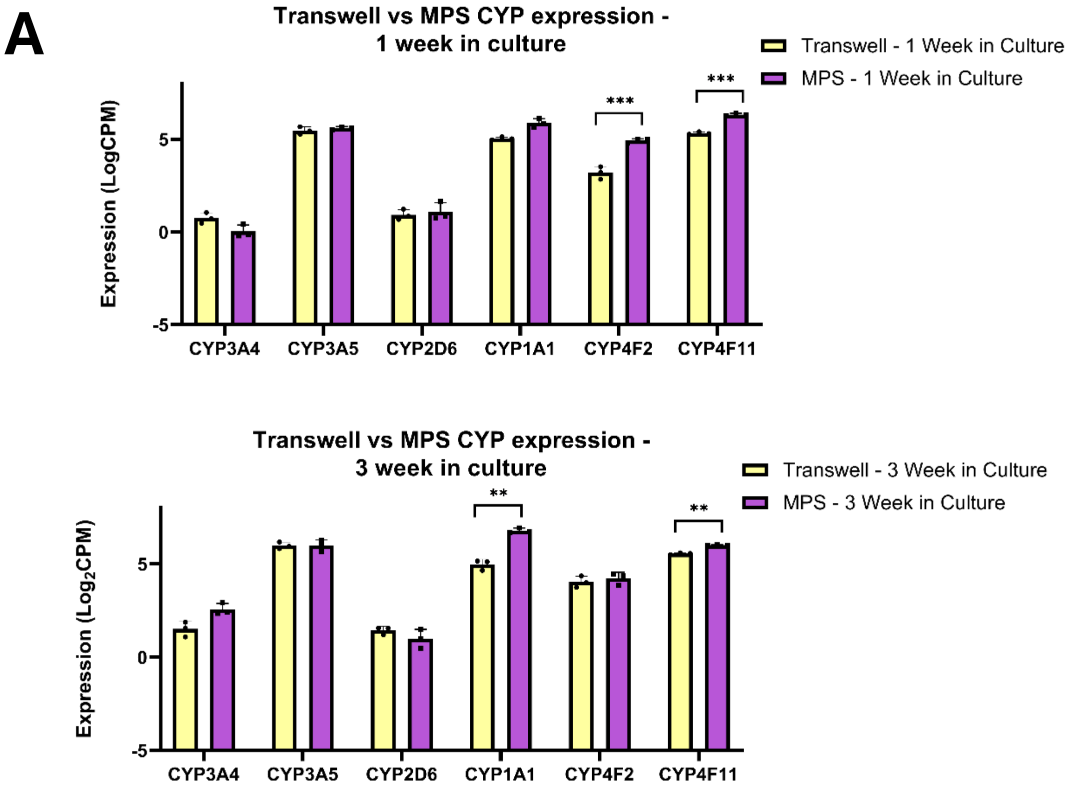
Transwell vs MPS CYP expression - 1 week in culture

Transwell vs MPS CYP expression - 3 week in culture

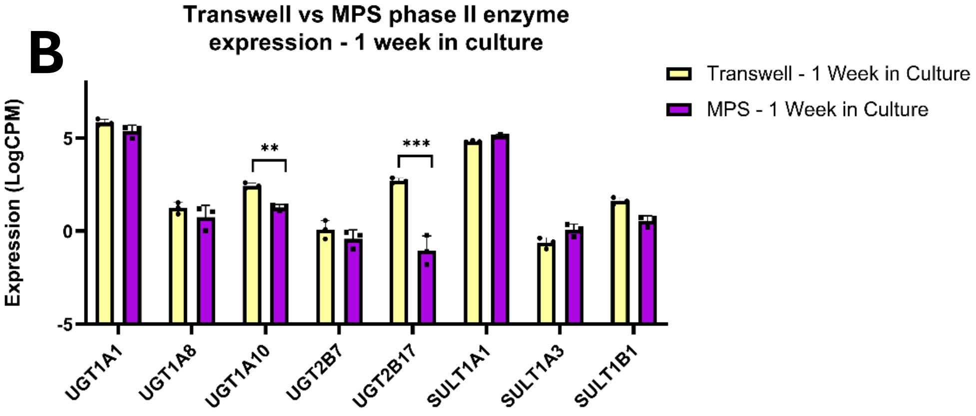
Transwell vs MPS phase II enzyme expression - 1 week in culture

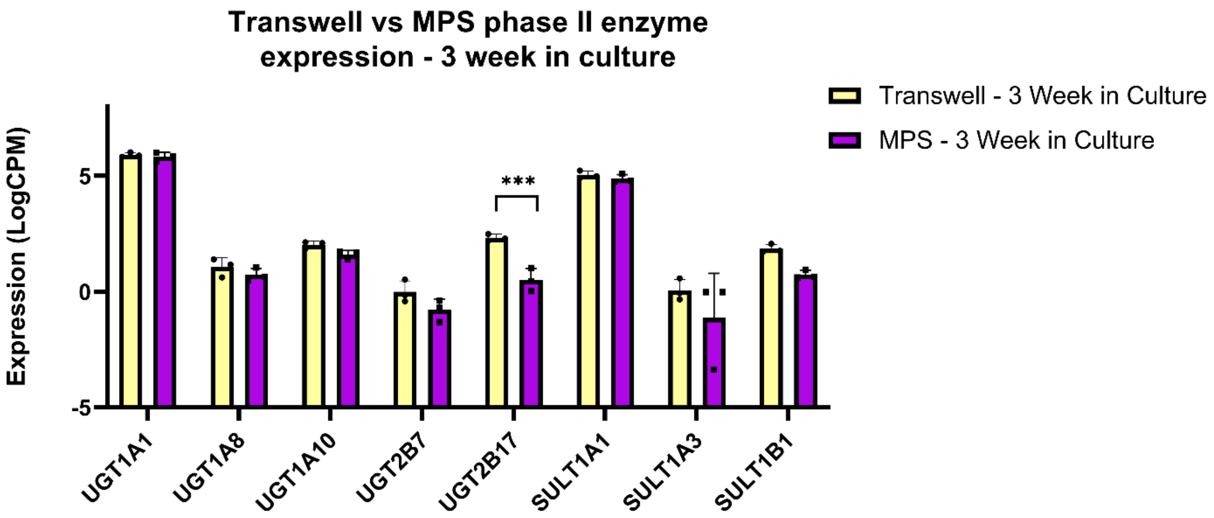
Transwell vs MPS phase II enzyme expression - 3 week in culture
Transwell - 3 Week in Culture
MPS - 3 Week in Culture
Expression (LogCPM)
5
0
-5
***
UGT1A1
UGT1A8
UGT1A10
UGT2B7
UGT2B17
SULT1A1
SULT1A3
SULT1B1

C

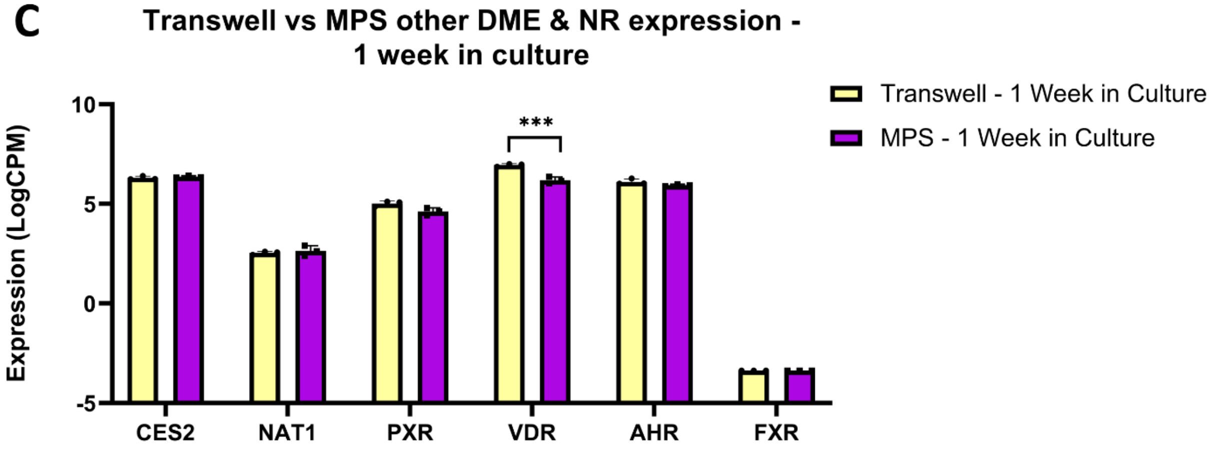
Transwell vs MPS other DME & NR expression - 1 week in culture
Transwell - 1 Week in Culture
MPS - 1 Week in Culture
Expression (LogCPM)
10
5
0
-5
***
CES2
NAT1
PXR
VDR
AHR
FXR

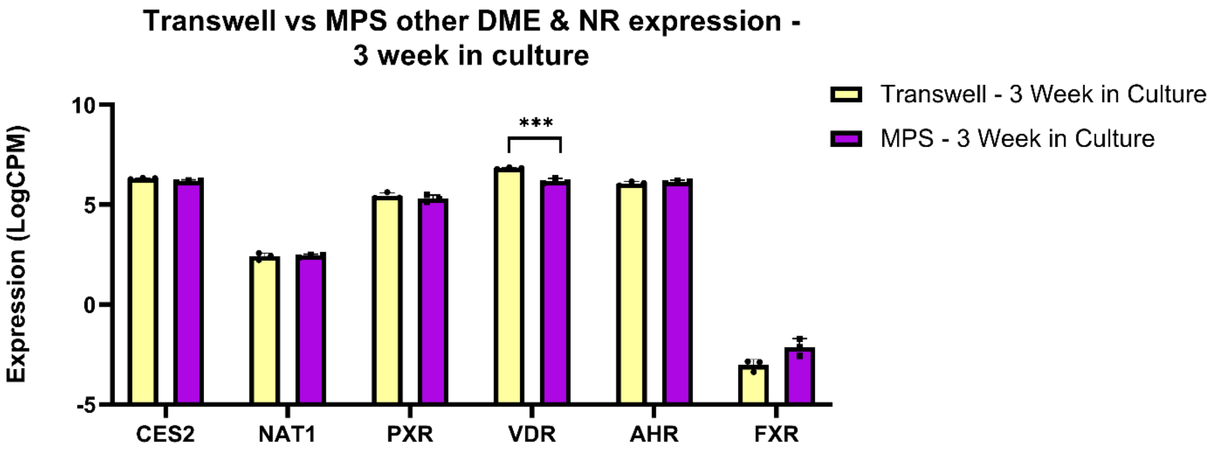
Transwell vs MPS other DME & NR expression - 3 week in culture
Transwell - 3 Week in Culture
MPS - 3 Week in Culture
Expression (LogCPM)
10
5
0
-5
***
CES2
NAT1
PXR
VDR
AHR
FXR

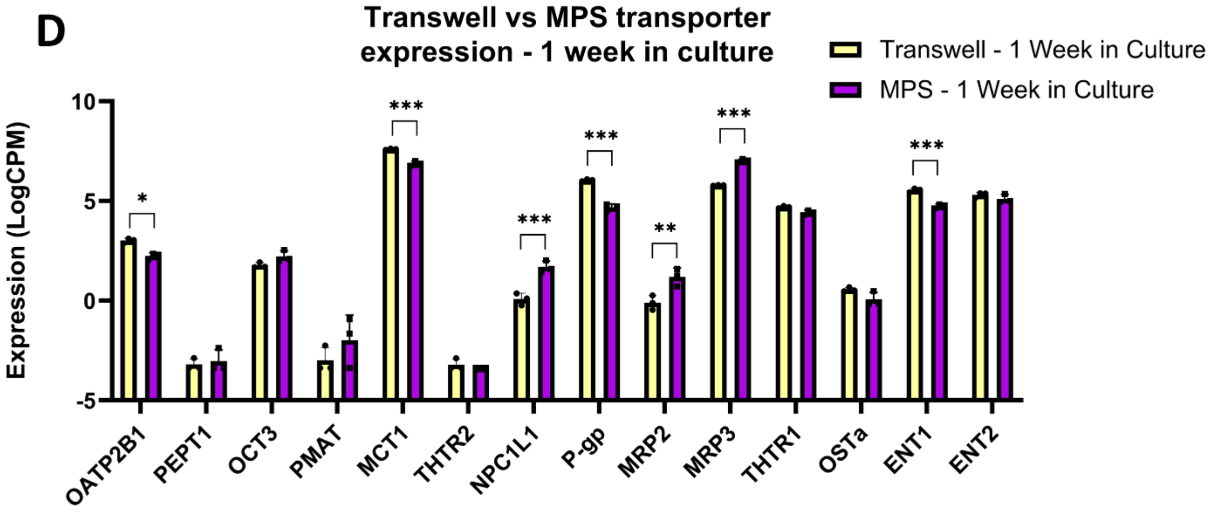
D
Transwell vs MPS transporter expression - 1 week in culture
Transwell - 1 Week in Culture
MPS - 1 Week in Culture
Expression (LogCPM)
10
5
0
-5
*
***
***
***
**
***
***
OATP2B1
PEPT1
OCT3
PMAT
MCT1
THTR2
NPC1L1
P-gp
MRP2
MRP3
THTR1
OSTa
ENT1
ENT2

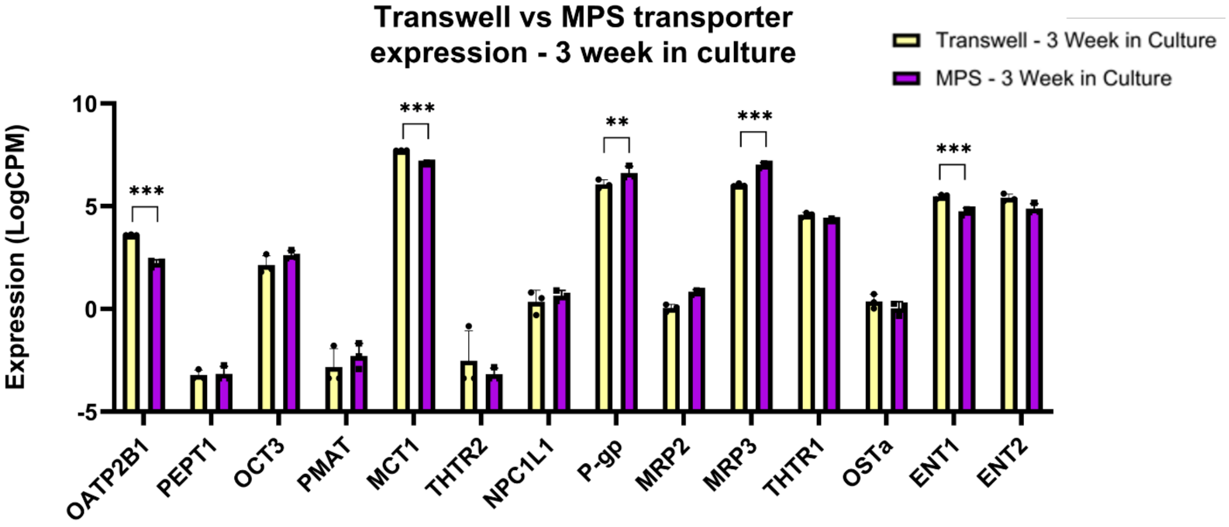
Transwell vs MPS transporter expression - 3 week in culture
Transwell - 3 Week in Culture
MPS - 3 Week in Culture
Expression (LogCPM)
10
5
0
-5
***
***
**
***
***
OATP2B1
PEPT1
OCT3
PMAT
MCT1
THTR2
NPC1L1
P-gp
MRP2
MRP3
THTR1
OSTa
ENT1
ENT2

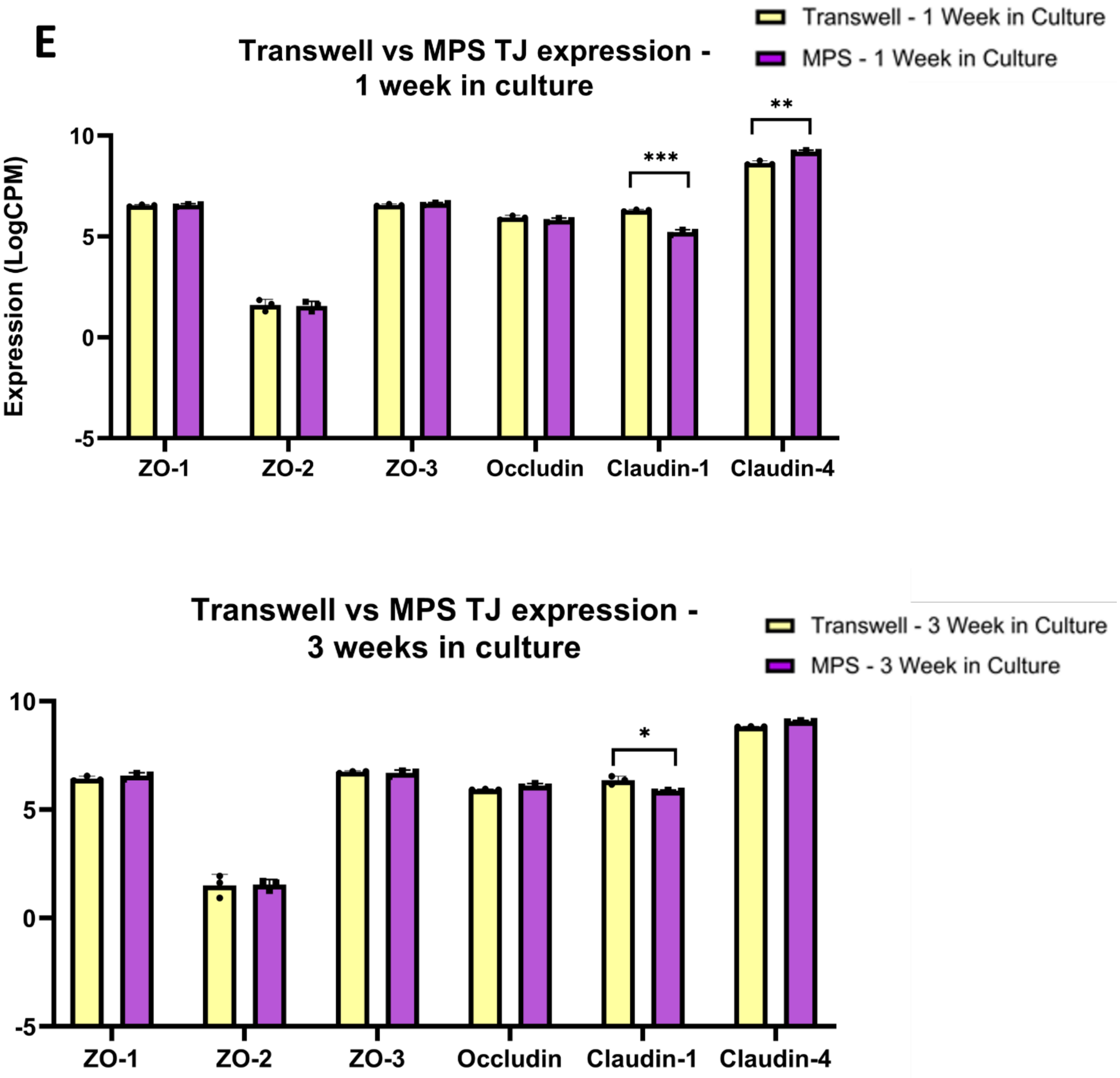

Figure 2.2. RNA-seq analysis of LS180 cells cultured in MPS versus Transwell®

The mRNA expression, expressed as Log_2CPM (counts per million reads) of phase I drug metabolizing enzymes (A), phase II drug metabolizing enzymes (B), other drug metabolizing enzymes and nuclear receptors (C), drug transporters (D), and tight junction proteins (E). Data points represent expression values of individual culture replicates and bars represent means from each condition (n = 3 each). * $P < 0.05$, ** $P < 0.01$, and *** $P < 0.001$.

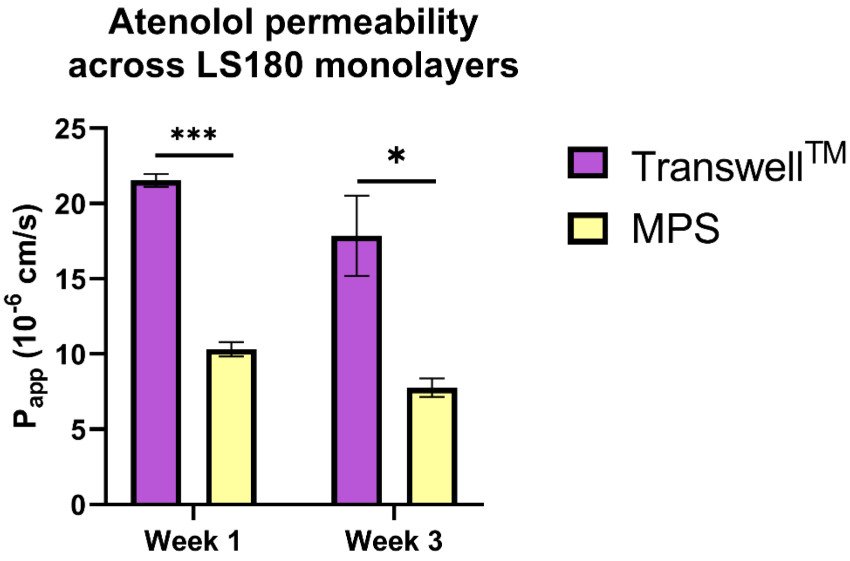

Figure 2.3. Barrier integrity comparison

The permeability of atenolol, expressed as P_{app}, across LS180 monolayer cultured in MPS versus Transwell®. Bars represent the means of 3 culture replicates with standard deviation. * $P < 0.05$ and *** $P < 0.001$.

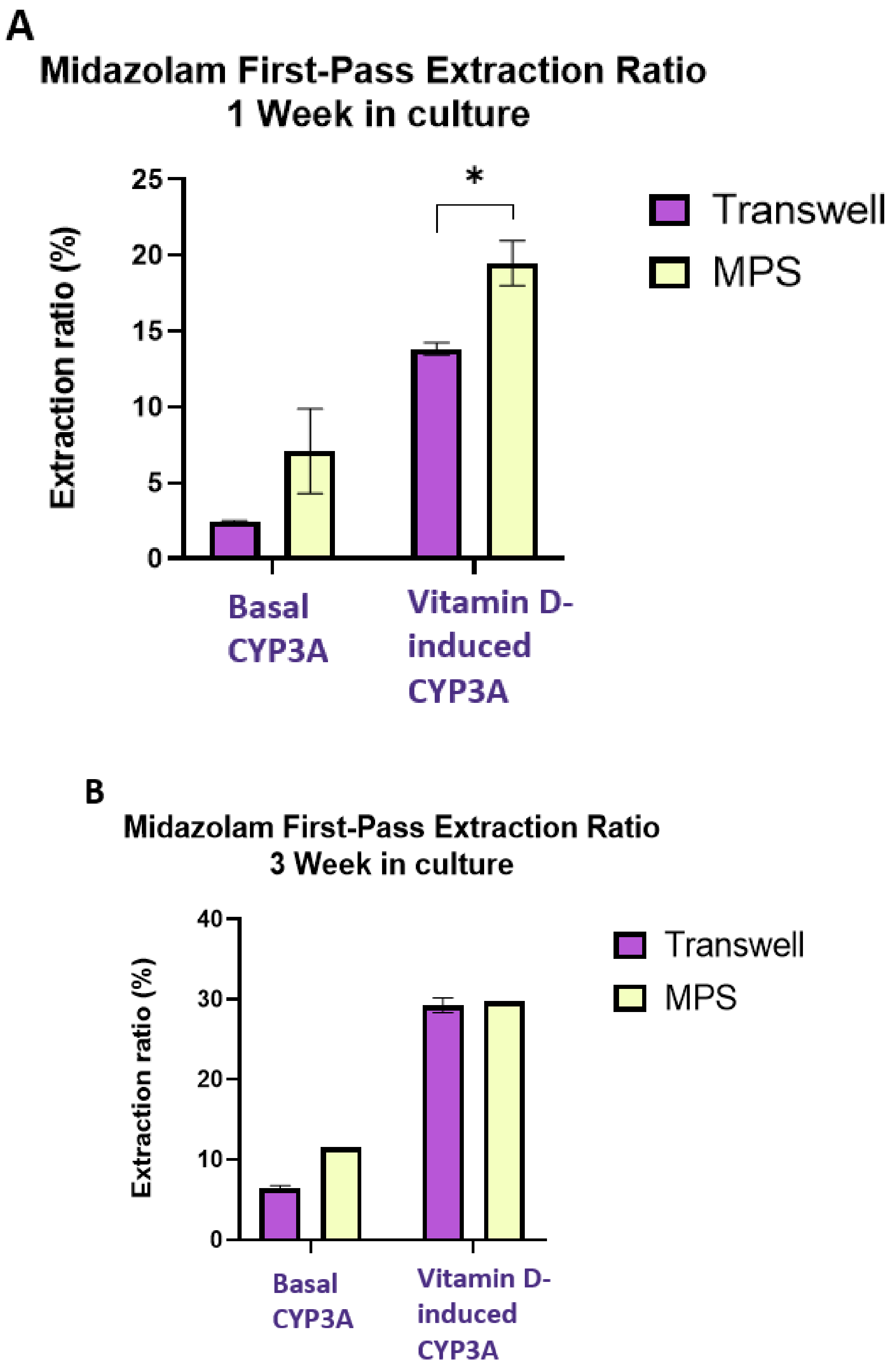

Figure 2.4. CYP3A activity

CYP3A activity, expressed as midazolam first-pass extraction ratio, for LS180 monolayers cultured in MPS and Transwell® in both the basal and vitamin D-induced states at 7 days in culture (A) and 21 days in culture (B). Bars represent the means of 3 culture replicates with standard deviation. MPS week 3 data is represented as the means of 2 culture replicates. * $P < 0.05$ and *** $P < 0.001$.

2.5. REFERENCES

Andrews S (2010) Babraham Bioinformatics - FastQC a quality control tool for high throughput sequence data, https://www.bioinformatics.babraham.ac.uk/projects/fastqc/.

Arian C, Mahony EO, MacDonald JW, Bammler TK, Donowitz M, Kelly EJ, and Thummel KE (2024) Human Enteroid Monolayers: A Novel, Functionally-Stable Model for Investigating Oral Drug Disposition. *Drug Metab Dispos*.

Arian CM, Imaoka T, Yang J, Kelly EJ, and Thummel KE (2022) Gutsy science: In vitro systems of the human intestine to model oral drug disposition. *Pharmacol Ther* **230:**107962.

Bein A, Shin W, Jalili-Firoozinezhad S, Park MH, Sontheimer-Phelps A, Tovaglieri A, Chalkiadaki A, Kim HJ, and Ingber DE (2018) Microfluidic Organ-on-a-Chip Models of Human Intestine. *Cellular and molecular gastroenterology and hepatology* **5:**659-668.

Benjamini Y and Hochberg Y (1995) Controlling the False Discovery Rate: A Practical and Powerful Approach to Multiple Testing. *Journal of the Royal Statistical Society: Series B (Methodological)* **57:**289-300.

Chang SY, Voellinger JL, Van Ness KP, Chapron B, Shaffer RM, Neumann T, White CC, Kavanagh TJ, Kelly EJ, and Eaton DL (2017) Characterization of rat or human hepatocytes cultured in microphysiological systems (MPS) to identify hepatotoxicity. *Toxicol In Vitro* **40:**170-183.

Drozdzik M, Groer C, Penski J, Lapczuk J, Ostrowski M, Lai Y, Prasad B, Unadkat JD, Siegmund W, and Oswald S (2014) Protein abundance of clinically relevant multidrug transporters along the entire length of the human intestine. *Mol Pharm* **11:**3547-3555.

Fisher JM, Wrighton SA, Calamia JC, Shen DD, Kunze KL, and Thummel KE (1999) Midazolam metabolism by modified Caco-2 monolayers: effects of extracellular protein binding. *J Pharmacol Exp Ther* **289:**1143-1150.

Heischmann S and Christians U (2018) Validation of the cell line LS180 as a model for study of the gastrointestinal toxicity of mycophenolic acid. *Xenobiotica* **48:**433-441.

Kasendra M, Luc R, Yin J, Manatakis DV, Kulkarni G, Lucchesi C, Sliz J, Apostolou A, Sunuwar L, Obrigewitch J, Jang KJ, Hamilton GA, Donowitz M, and Karalis K (2020) Duodenum Intestine-Chip for preclinical drug assessment in a human relevant model. *Elife* **9**.

Kim D, Paggi JM, Park C, Bennett C, and Salzberg SL (2019) Graph-based genome alignment and genotyping with HISAT2 and HISAT-genotype. *Nat Biotechnol* **37:**907-915.

Kim HJ, Huh D, Hamilton G, and Ingber DE (2012) Human gut-on-a-chip inhabited by microbial flora that experiences intestinal peristalsis-like motions and flow. *Lab Chip* **12:**2165-2174.

Liao Y, Smyth GK, and Shi W (2019) The R package Rsubread is easier, faster, cheaper and better for alignment and quantification of RNA sequencing reads. *Nucleic Acids Res* **47:**e47.

Lun AT, Chen Y, and Smyth GK (2016) It's DE-licious: A Recipe for Differential Expression Analyses of RNA-seq Experiments Using Quasi-Likelihood Methods in edgeR. *Methods Mol Biol* **1418:**391-416.

Marx U, Akabane T, Andersson TB, Baker E, Beilmann M, Beken S, Brendler-Schwaab S, Cirit M, David R, Dehne EM, Durieux I, Ewart L, Fitzpatrick SC, Frey O, Fuchs F, Griffith LG, Hamilton GA, Hartung T, Hoeng J, Hogberg H, Hughes DJ, Ingber DE, Iskandar A, Kanamori T, Kojima H, Kuehnl J, Leist M, Li B, Loskill P, Mendrick DL, Neumann T, Pallocca G, Rusyn I, Smirnova L, Steger-Hartmann T, Tagle DA, Tonevitsky A, Tsyb S, Trapecar M, Van de Water B, Van den Eijnden-van Raaij J, Vulto P, Watanabe K, Wolf A, Zhou X, and Roth A (2020) Biology-inspired microphysiological systems to advance patient benefit and animal welfare in drug development. *ALTEX* **37:**365-394.

McCarthy DJ and Smyth GK (2009) Testing significance relative to a fold-change threshold is a TREAT. *Bioinformatics* **25:**765-771.

McRae M, LaFratta LM, Nguyen BM, Paris JJ, Hauser KF, and Conway DE (2018) Characterization of cell-cell junction changes associated with the formation of a strong endothelial barrier. *Tissue Barriers* **6:**e1405774.

Paine MF, Hart HL, Ludington SS, Haining RL, Rettie AE, and Zeldin DC (2006) The human intestinal cytochrome P450 "pie". *Drug Metab Dispos* **34:**880-886.

Robinson MD, McCarthy DJ, and Smyth GK (2010) edgeR: a Bioconductor package for differential expression analysis of digital gene expression data. *Bioinformatics* **26:**139-140.

Robinson MD and Oshlack A (2010) A scaling normalization method for differential expression analysis of RNA-seq data. *Genome Biol* **11:**R25.

Shim KY, Lee D, Han J, Nguyen NT, Park S, and Sung JH (2017) Microfluidic gut-on-a-chip with three-dimensional villi structure. *Biomed Microdevices* **19:**37.

Trietsch SJ, Naumovska E, Kurek D, Setyawati MC, Vormann MK, Wilschut KJ, Lanz HL, Nicolas A, Ng CP, Joore J, Kustermann S, Roth A, Hankemeier T, Moisan A, and Vulto P (2017) Membrane-free culture and real-time barrier integrity assessment of perfused intestinal epithelium tubes. *Nat Commun* **8:**262.

Wikswo JP (2014) The relevance and potential roles of microphysiological systems in biology and medicine. *Experimental biology and medicine (Maywood, NJ)* **239:**1061-1072.

Yamaura Y, Chapron BD, Wang Z, Himmelfarb J, and Thummel KE (2016) Functional Comparison of Human Colonic Carcinoma Cell Lines and Primary Small Intestinal Epithelial Cells for Investigations of Intestinal Drug Permeability and First-Pass Metabolism. *Drug Metab Dispos* **44:**329-335.

Zushin PH, Mukherjee S, and Wu JC (2023) FDA Modernization Act 2.0: transitioning beyond animal models with human cells, organoids, and AI/ML-based approaches. *J Clin Invest* **133**.

CHAPTER 3. THE DEVELOPMENT OF A HUMAN ENTEROID MONOLAYER TO INVESTIGATE ORAL DRUG DISPOSITION

(Part of this chapter was published as an article “Human Enteroid Monolayers: A Novel, Functionally-Stable Model for Investigating Oral Drug Disposition” (2024) in *Drug Metabolism and Disposition*)

3.1. INTRODUCTION

Characterizing the efficiency of intestinal drug absorption and first-pass elimination for new molecular entities (NME) is a key step in the drug development pathway, often predicted pre-clinically with the use of *in vitro* models of human intestinal and hepatic functions. Strikingly, historically used *in vitro* models of the human intestine all have limitations which hinder broad and accurate predictions of the F_A and F_G components of oral bioavailability (Arian et al., 2022). The shortcomings of these models underscore the need for physiological *in vitro* models that can more accurately recapitulate drug absorption and metabolism processes that occur *in vivo*. A promising complex *ex vivo* system of the human intestine that can potentially fill this research need are adult intestinal stem cell-derived organoids, or enteroids, which are multicellular, 3-dimensional structures that recapitulate intestinal functions under appropriate culture conditions (Rossi et al., 2018).

The human adult intestinal stem cells, or LGR5$^+$ crypt-base columnar cells (CBCs), can be isolated and cultured within a Matrigel droplet in culture medium containing the key growth factors, Wnt3A, R-spondin-1, and Noggin (Barker et al., 2007). This high growth factor medium is necessary for the formation of 3-dimensional (3D) intestinal spheroids, which are undifferentiated enteroids (i.e., contain mostly LGR5$^+$ CBC and Paneth cells). Removal of the aforementioned growth factors, most notably Wnt3A, will cause the 3D intestinal spheroids in the Matrigel plugs to differentiate, giving rise to 3D differentiated enteroids (Sato et al., 2011). Due to the inside out nature of 3D enteroids (i.e., apical membrane is localized to the inside of the enteroids), the apical membrane can only be accessed via microinjecting the organoids or by flipping the membrane by treating with a chelating agent (e.g., EGTA) after Matrigel removal to mimic oral drug administration to the luminal membrane of the intestinal epithelium. To address this limitation, culturing protocols have been developed which dissociate the 3D undifferentiated intestinal spheroids so they can be plated as 2-dimensional (2D) monolayers atop Transwell® filters, and when growth factors are removed, monolayer differentiation can be achieved (Foulke-Abel et al., 2016; In et al., 2016). Complete removal of Wnt3A results in terminal differentiation, providing 5-12 days of viability before substantial cell death and loss of drug metabolizing enzyme and transporter (DMET) activity occurs. Using this protocol, groups have demonstrated robust activity of several highly expressed intestinal DMETs such as CYP3A4, CYP2C9, UGT1As, CES2, and P-glycoprotein (P-gp, *ABCB1*) (Vernetti et al., 2017; Kasendra et al., 2020; Michiba et al., 2022). While these results are exciting, the relatively short and dynamic culture period of roughly one week limits this model from use in protracted investigations, such as long-term toxicology studies, mechanism-based inactivator (MBI) studies, induction/deinduction time course studies, as well as the maturation time-course and inter-individual variability of constitutive DMET gene regulation.

This chapter reports on the characterization of extended culturing of human enteroid monolayers. In our hands, duodenal enteroid monolayers differentiated using a proprietary commercial medium which supports differentiation resulted in culture viability of at least 42 days. We used immunocytochemical (ICC) imaging, mRNA analysis, TEER measurements, and selective CYP3A probe disposition to confirm cell differentiation, monolayer barrier integrity/function, and retention CYP3A metabolic activity during the entire period.

3.2. METHODS

3.2.1. Chemicals and reagents

IntestiCult™ Organoid Growth Medium (Human), IntestiCult™ Organoid Differentiation Medium (Human), and Y-27632 (Dihydrochloride) were purchased from STEMCELL Technologies (Vancouver, BC, Canada). Advanced DMEM/F-12, DMEM, MEM, fetal bovine serum (FBS), Trypsin-EDTA (0.25%), Versene solution, Penicillin-Streptomycin (10,000 U/mL), Dulbecco's phosphate-buffered saline with calcium and magnesium (DPBS^{++}), DPBS without calcium and magnesium, HEPES buffer (1M), Hanks' Balanced Salt Solution with calcium and magnesium (HBSS^{++}), Tween-20, dextran 70, SlowFade™ Diamond Antifade mountant with DAPI, and ProLong™ Gold antifade reagent were purchased from Life Technologies (Carlsbad, CA). Gelatin-based coating solution (0.1%) and Complete Epithelial cell medium kit were purchased from Cell Biologics (Chicago IL). Midazolam, midazolam-d_4, 1-OH midazolam, and 1-OH midazolam-d_4 were purchased from Cerilliant (Round Rock, TX). Matrigel® Growth Factor Reduced (GFR) Basement Membrane Matrix (phenol red-free, LDEV-free), collagen IV, and Cell Recovery Solution were purchased from Corning (Corning, NY). Atenolol-d_7, digoxin-d_3, and 6',7'-dihydroxybergamottin were purchased from Cayman Chemical (Ann Arbor MI). Atenolol, digoxin, verapamil hydrochloride, rifampin, triton X-100, and sodium bicarbonate were purchased from Sigma-Aldrich (St. Louis, MO). RLT Lysis buffer was purchased from Qiagen (Germantown, MD). Normal goat serum (2.5%) was purchased from Vector Laboratories (Newark, CA). Human serum albumin (low endotoxin) was purchased from Gemini Bio (West Sacramento, CA). Paraformaldehyde (16%) was purchased from Electron Microscopy Sciences (Hatfield, PA). $1\alpha,25(OH)_2$ vitamin D_3 was purchased from Calbiochem (La Jolla, CA). Rabbit monoclonal antibody to Villin (ab130751), rabbit monoclonal antibody to Ki67 (ab16667), mouse monoclonal antibody to Occludin (ab242202), rabbit polyclonal antibody to MRP3 (ab204322), rabbit monoclonal antibody to Zonula Occludens protein 3 (ab181991), rabbit monoclonal antibody to ZO1 tight junction protein (ab221547), Alexa Fluor 647 goat polyclonal antibody to mouse IgG (ab150115), Alexa Fluor 488 goat polyclonal antibody to rabbit IgG (ab150077), and Alexa Fluor 647 goat polyclonal antibody to rabbit IgG (ab150079) were purchased from Abcam (Cambridge, UK).

3.2.2. Cell culture

Anonymized undifferentiated duodenal organoids from three donors (27 year old, female; 81 year old, female; 25 year old, male) derived via endoscopic biopsies during clinically indicated conditions, where upper GI tract was endoscopically normal, were kindly provided by Dr. Mark Donowitz, Johns Hopkins University, MD. The original biopsy samples were collected in accordance with the Institutional Review Board of John's Hopkins University (protocol numbers IRB-NA_00038329 and IRB-00044373). Experiments were conducted at passages 28 – 38. Undifferentiated organoids were suspended and grown in Matrigel droplets in the presence of Intesticult™ Intestinal Organoid Growth Medium (Human) containing 1% (v/v) penicillin-streptomycin. Undifferentiated organoids were passaged after 7-10 days in culture, or until they reached a large, cystic morphology, by the addition of 0.5 mL of cold Cell Recovery Solution followed by 30 minutes of shaking at 4^{o}C. Cells were then triturated until roughly 80% of the organoids were broken into small fragments followed by centrifugation for 10 minutes at 1200*g* at 4^{o}C. The resulting supernatant was discarded and the cell pellet was resuspended with Matrigel and plated onto a 24-well plate in 50 µL droplets. The plate was then placed into a 37^{o}C incubator for 10-15 minutes to allow for the Matrigel to polymerize, followed by the addition of 0.5 mL of Intesticult™ Growth Medium containing 10 µM Y-27632. Undifferentiated organoids were fed every two days with Intesticult™ Growth Medium without Y-27632. Cells were split from 1:3.

Enteroid monolayers were grown on polyester, 0.4 µm pore-size Transwell® filter inserts for 24-well plates (catalog no. 3470; Corning Inc., NY). The day before seeding, 50 µL of 34 µg/mL collagen IV was added to each Transwell® and allowed to polymerize overnight in a 37ºC incubator. The following day, undifferentiated organoids were removed from their Matrigel droplets (two Matrigel droplets per Transwell® insert plated) by the addition of 0.5 mL of cold Cell Recovery Solution followed by 30 minutes of shaking at 4ºC. Cells were then triturated on ice until roughly 95% of the organoids were broken into small fragments/single cells followed by centrifugation for 10 minutes at 1200*g* at 4ºC. The resulting supernatant was discarded and the cell pellet was resuspended with Intesticult™ Intestinal Organoid Differentiation Medium (Human) containing 1% (v/v) penicillin-streptomycin and 10 µM Y-27632. Buffer in the collagen IV-treated Transwell® inserts was then aspirated and the inserts washed with Advanced DMEM/F-12 before plating 100 µL of the cell suspension to each Transwell® insert (apical chamber) and addition of 0.5 mL of the Intesticult™ Differentiation Medium to the basolateral chamber of the 24-well plate. Enteroid monolayers were fed every two days by aspirating apical and basolateral media and replacing with 0.1 mL and 0.5 mL of Intesticult™ Differentiation Medium containing Y-27632 to the apical and basolateral chambers, respectively. For undifferentiated monolayers, the cell pellet was resuspended with Intesticult™ Growth Medium containing Y-27632, plated, and then fed every two days by aspirating apical and basolateral media and replacing with 0.1 mL and 0.5 mL with growth medium containing Y-27632 to the apical and basolateral chambers, respectively.

Cryopreserved human primary small intestinal epithelial cells (catalog no. H-6051, Cell Biologics Inc, IL) from a single donor were cultured as described by the vendor. Briefly, cells were thawed then cultured for two days in a gelatin-coated T25 flask containing Complete Epithelial cell medium (Cell Biologics Inc, IL). After two days, cells were washed with warm DPBS (without calcium and magnesium) then incubated with 2 mL 0.25% trypsin-EDTA solution for 3-6 minutes at room temperature to detach cells followed by washing with Complete Epithelial cell medium to neutralize the trypsin. Cells were then centrifuged at 500g for 6 minutes at room temperature. Supernatant was then removed and the cell pellet was resuspended in Complete Epithelial cell medium at a density of 350,000 cells/mL. Cell slurry (0.25 mL) was plated on a gelatin-coated 0.4 µm pore-size Transwell® filter inserts for 24-well plates and 1 mL of Complete Epithelial cell medium was added to the basolateral chamber. Cells were fed every two days by aspirating apical and basolateral medium and replacing with 0.25 mL and 1 mL of Complete Epithelial cell medium to the apical and basolateral chambers, respectively. Cells were grown for 7 days prior to CYP3A activity assessment.

LS180 cells (passage 38) were cultured in a T75 flask with MEM supplemented with 10% (v/v) FBS and 1% (v/v) penicillin-streptomycin. After 7 days in culture, cells were washed with warm DPBS (without calcium and magnesium) then incubated with Versene 1x for 5 minutes at room temperature. Suspended cells were then centrifuged at 1200g for 2 minutes. The resulting cell pellet was resuspended in MEM containing 10% FBS and 1% penicillin-streptomycin at a density of 167,000 cells/mL as determined by a hemocytometer. A 0.25 mL volume of the cell slurry was plated on a 0.4 µm pore-size Transwell® filter inserts for 24-well plates that were coated with 34 µg/mL collagen IV as described above. A 1 mL volume of MEM containing 10% FBS and 1% penicillin-streptomycin was then added to the basolateral chamber. Cells were fed every two days by aspirating apical and basolateral medium and replacing with 0.25 mL and 1 mL of MEM containing 10% FBS and 1% penicillin-streptomycin to the apical and basolateral chambers, respectively. Cells were grown for 7 days prior to CYP3A activity assessment.

Caco-2 cells (passage 29) were cultured in a T75 flask with DMEM supplemented with 10% (v/v) fetal bovine serum (FBS) and 1% (v/v) penicillin-streptomycin. After 7 days in culture, cells were washed with warm DPBS (without calcium and magnesium) then incubated with 3 mL of 0.25% trypsin-EDTA solution for 5 minutes at 37ºC for 5 minutes by washing with DMEM containing 10% FBS and 1% penicillin-streptomycin to neutralize the trypsin. Cells were then centrifuged at 1000g for 5 minutes at room temperature. Supernatant was then removed and the cell pellet was resuspended in DMEM containing 10% FBS and 1% penicillin-streptomycin at a density of 167,000 cells/mL as determined by a hemocytometer. 0.25 mL of the cell slurry was plated on a 0.4 µm pore-size Transwell® filter inserts for 24-well plates that were coated with 34 µg/mL collagen IV as described above. A 1 mL volume of DMEM containing 10% FBS and 1% penicillin-streptomycin was then added to the basolateral chamber. Cells were fed every two days by aspirating apical and basolateral medium and replacing with 0.25 mL and 1 mL of DMEM containing 10% FBS and 1% penicillin-streptomycin to the apical and basolateral chambers, respectively. Cells were grown for 21 days prior to CYP3A activity assessment.

For enteroid monolayer induction and inhibition experiments, differentiation medium was removed and the cells were washed three times with DPBS^{++} followed by addition of 0.1 mL and 0.5 mL of Intesticult™ Differentiation Medium containing compound or vehicle to the apical and basolateral chambers, respectively, for 48 hours. Stock solutions of 1α,25(OH)$_2$ vitamin D$_3$ (1 µM in ethanol), 6',7'-dihydroxybergamottin (50 mM in DMSO), or rifampin (50 mM in DMSO) were prepared and diluted 1000-fold in Intesticult™ Differentiation Medium containing Y-27632.

3.2.3. RNA-seq analysis for undifferentiated and differentiated organoids

Matched undifferentiated spheroids and differentiated enteroid monolayers cultured for 21 days from the same donor at the same passage number were lysed with 0.5 mL of RLT lysis buffer (Qiagen Sciences Inc., Germantown, Maryland) and stored at -80ºC until analysis. Samples were sent to Novogene America (Sacramento, California) where the RNA was isolated and messenger RNA was purified from total RNA using poly-T oligo-attached magnetic beads. mRNA was then fragmented and the first strand cDNA was synthesized using random hexamer primers, followed by second strand cDNA synthesis using dTTP for non-directional library and sequenced by a NovaSeq 6000 system (Illumina, San Diego, CA). Quality of the sequencing data was assessed using fastqc (Andrews, 2010), and then reads were aligned to the Ensembl GRCh38 p12 genome using the HiSat2 aligner (Kim et al., 2019). Counts/gene were generated using the Bioconductor Rsubread (Liao et al., 2019) package. Total aligned reads ranged between 14.5M – 18M per sample. Pathway analysis of the RNA-seq data was performed using the iPathwayGuide software from ADVAITA (Advaita Corporation, Ann Arbor, MI). Genes with FDR <0.05 were used for pathway analysis. Details for the statistical analysis of the RNA-seq data are provided in the section further down titled “Statistical analysis”.

3.2.4. Immunocytochemistry and confocal microscopy

Enteroid monolayers grown on Transwell® inserts for 21 or 42 days were washed twice with DPBS^{++}, fixed in 4% formaldehyde in DPBS^{++} for 15 minutes at room temperature, and then washed an additional three times with DPBS^{++}. Fixed monolayers were stored at 4ºC for no more than 7 days before protein imaging. Monolayers stained for Villin and Ki-67 were permeabilized for 5 minutes at room temperature with DPBS^{++} containing 0.1% Triton X-100. Permeabilized monolayers were then incubated in 0.05% Tween-20 and goat serum in DPBS^{++} (blocking solution) for 60 minutes and subsequently incubated with a 100-fold dilution of primary antibody in blocking solution for 60 minutes. Monolayers were thereafter washed three times with DPBS^{++} then incubated with a 1000-fold dilution of fluorescent-conjugated secondary antibody in blocking solution for 60 minutes. Monolayers were then washed an additional three times with DPBS^{++}.

After the fixing process, non-permeabilized monolayers were incubated with blocking solution for 60 minutes and subsequently incubated with a 100-fold dilution of primary antibody (anti-Occludin, MRP3, ZO-1, and ZO-3) in blocking solution overnight at 4ºC. Monolayers were thereafter washed three times with DPBS^{++} then incubated with a 1000-fold dilution of fluorescent-conjugated secondary antibody in blocking solution overnight at 4ºC. The following day, monolayers were washed an additional five times with DPBS^{++} while shaking.

Following the final washing step for both sets of monolayers, 50 µL of DAPI was added for 15 minutes and subsequently aspirated. Filters from each Transwell® insert were then cut out and mounted on glass microscope slides using ProLong Gold Antifade reagent. Images were captured and analyzed with a Nikon Eclipse Ti-S inverted microscope (Villin, Ki-67) using a 10x objective lens or with a Nikon A1R confocal microscope (Occludin, MRP3, ZO-1, and ZO-3) using a 40x oil immersion objective lens (Nikon, Melville, NY).

3.2.5. TEER measurement

Transepithelial electrical resistance was evaluated using an EVOM^2 epithelial voltohmmeter (World Precision Instruments, Sarasota, FL). Background resistance was determined for each set of cultures using a single Transwell® filter insert treated with collagen IV that was devoid of cells. The reported TEER values are a product of the background-corrected resistance and the surface area of the Transwell® insert.

3.2.6. Permeability assay

Cell monolayers were washed three times with blank apical transport buffer (10 mM HEPES in Hank's balanced salt solution, pH 6.5) and maintained at 37ºC until use. Stock solutions of the test compounds (midazolam, 3 mM in methanol; and atenolol, 60 mM in DMSO) were diluted in apical transport buffer to make their respective dosing solutions (final concentrations were 8 µM midazolam, 0.27% methanol; and 300 µM atenolol, 0.5% DMSO). Lucifer yellow dosing solution was made fresh for each assay by dissolving Lucifer yellow in apical transport buffer for a final concentration of 300 µM.

For the midazolam permeability measurement, 0.3 mL of the dosing solution was added to the filter insert and 0.7 mL of the receiver solution (10 mM HEPES in Hank's balanced salt solution, pH 7.4, containing 0.27% methanol) was added to the basolateral compartment. Cells were incubated for 60 minutes at 37ºC and the total volume from the apical and basolateral compartment were collected separately and stored at -80ºC until analysis. Midazolam was quantified using liquid chromatography coupled with tandem mass spectrometry on an Agilent 6410 QQQ equipped with a UPLC 1290 system. After thawing and vortexing, 200 µL of basolateral sample and 50 µL of apical sample (diluted 4-fold in blank apical buffer to a final volume of 200 µL) was mixed with 250 µL of sodium carbonate buffer (100 mM, pH 11.4) and 20 µL of internal standard (midazolam-d4, 150 ng/mL in methanol). A series of dilutions of midazolam standards were prepared in methanol and stored at -80ºC. The standard curve was prepared using 10 µL of each stock solution and 200 µL of blank transport buffer and mixing with 250 µL of sodium carbonate buffer and 20 µL of internal standard. 3 mL of ethyl acetate was then added to the unknown and standard curve samples followed by 20 minutes of shaking and centrifugation at 2000*g* for 20 minutes at room temperature. The top organic layer was then collected and samples were dried using a nitrogen evaporator. Dried samples were then resuspended in 100 µL of 1:1 formic acid solution (0.1% in water): methanol and analyzed via LC/MS-MS. Chromatographic separation following injection of 5 µL sample was achieved using a Zorbax SB-C18 narrow-bore, 5 µm, 2.1 x 150 mm column using 0.1% formic acid in water (A) and methanol (B) as a mobile phase. The flow rate was 0.25 mL/min with a gradient as follows: 50% B for 1 minute, increased to 90% B linearly over 2 minutes, held at 90% for 3 minutes, and then equilibrated back to 50% for 4 minutes. The following MRM transitions were monitored: *m/z* 326.0 > 291.2 for midazolam, and *m/z* 330.0 > 295.0 for midazolam-d_4 in the positive ion mode. For both compounds, dwell time was set to 100 ms, fragmentor was set to 159V, collision energy was set to 28 eV, and cell accelerator voltage was set to 7V.

For the atenolol permeability measurement, 0.3 mL of the dosing solution was added to the filter insert and 0.7 mL of the receiver solution (10 mM HEPES in Hank's balanced salt solution, pH 7.4, containing 0.5% DMSO) was added to the basolateral compartment. Cells were incubated for 90 minutes at 37ºC and the total volume from the apical and basolateral compartment were collected separately and stored at -80ºC until analysis. Atenolol was quantified using liquid chromatography coupled with tandem mass spectrometry on an Agilent 6410 QQQ equipped with a UPLC 1290 system. After thawing and vortexing, 50 µL of basolateral samples and 50 µL of diluted apical samples (diluted 300-fold in blank apical transport buffer) were mixed with 20 µL internal standard (1.25 µM in methanol) and 30 µL of methanol. A series of dilutions of atenolol standards were prepared in methanol and stored at -80ºC. The standard curve was prepared using 10 µL of each stock solution and 50 µL of blank transport buffer mixed with 20 µL of internal standard and 20 µL of methanol. Unknowns and standards were then centrifuged at 20,800*g* for 10 minutes at room temperature, and 75 µL of the supernatant was analyzed by LC/MS-MS. Chromatographic separation was achieved following injection of 5 µL of sample using a Zorbax SB-C18 narrow-bore, 5 µm, 2.1 x 150 mm column using 10 mM ammonium acetate (A) and methanol (B) as a mobile phase. The flow rate was 0.25 mL/min with a gradient as follows: 5% B for 1.5 minutes, then increased to 75% B linearly over 2 minutes, held at 75% for 4.5 minutes, and then equilibrated back to 5% for 4 minutes. The following MRM transitions were monitored: *m/z* 267.3 > 145.0 for atenolol, and *m/z* 274.3 > 145.2 for atenolol-d_7 in the positive ion mode. For both compounds, dwell time was set to 200 ms, collision energy was set to 29 eV, and cell accelerator voltage was set to 4 V. The fragmentor was set to 113 V for atenolol and 127 for atenolol-d_7.

For the Lucifer yellow permeability measurement, 0.3 mL of the dosing solution was added to the filter insert and 0.7 mL of the receiver solution (10 mM HEPES in Hank's balanced salt solution, pH 7.4) was added to the basolateral compartment. Cells were incubated for 60 minutes at 37°C and 300 µL of the basolateral compartment was collected. A series of dilutions of Lucifer yellow standards were prepared fresh during the 60-minute incubation period. The samples were analyzed by fluorescence detection using a Synergy HTX multi-mode reader (BioSPX, Netherlands) with excitation filter at 420 nm and emission filter at 528 nm.

3.2.7. Permeability coefficient calculation

The apparent cell monolayer permeability coefficient (P_{app}, cm/s) for midazolam was calculated using eq. 1 (Anoshchenko et al., 2021):

$$P_{app} = \frac{A_{MDZ,B}}{AUC_{MDZ,A} \cdot SA}$$

where $A_{MDZ,B}$ is the amount of unchanged midazolam (pmol) in the basolateral compartment under sink conditions (where less than 20% of the apically dosed midazolam was measured in the basolateral compartment), $AUC_{MDZ,A}$ is the area under the curve of unchanged midazolam concentration in the apical chamber versus time plot (pmol/mL*s), and SA is the surface area of the Transwell® filter insert (cm^2).

The apparent permeability coefficient for atenolol and Lucifer yellow was calculated using eq. 2:

$$P_{app} = \frac{dQ}{dt} \cdot \frac{1}{SA \cdot C_0}$$

where dQ/dt is the rate of compound appearance in the basolateral chamber (pmol/s) under sink conditions, SA is the surface area of the Transwell® filter insert (cm^2), and C_0 is the dosing concentration of compound in the apical compartment.

3.2.8. CYP3A activity assessment

Following experimental treatment as described above, monolayers were washed three times with blank apical transport buffer (10 mM HEPES in Hank's balanced salt solution, pH 6.5) and maintained at 37°C until use. A stock solution of midazolam (3 mM) was diluted in apical transport buffer to make the dosing solution (final concentration 8 µM midazolam, 0.27% methanol). Blank transport buffer was then removed, and 0.3 mL of the dosing solution was added to the filter insert and 0.7 mL of the receiver solution (10 mM HEPES in Hank's balanced salt solution, pH 7.4, containing 0.27% methanol) was added to the basolateral compartment. For HSA experiments, 1 g/dL of HSA was included in the receiver solution and 1 g/dL of dextran (70 kDa) was included in the apical chamber as an osmotic control. Cells were incubated for 60 minutes at 37°C and the total volume from the apical and basolateral compartment were collected separately and stored at -80°C until analysis. Parent midazolam and 1-OH midazolam was quantified as described above, with additional MRM transitions monitored: *m/z* 342 > 168.1 for 1-OH midazolam and *m/z* 346 > 168 for 1-OH midazolam-d_4. For both 1-OH midazolam and 1-OH midazolam-d_4, dwell time was set to 100 ms and cell accelerator voltage was set to 7 V. Fragmentor and collision energy was set to 143 V and 40 eV for 1-OH midazolam and 153 V and 44 eV for 1-OH midazolam-d_4. The 4-OH midazolam metabolite was not monitored during these experiments, as the dose of midazolam used in these incubation would not lead to significant formation of the 4-OH midazolam metabolite (Fisher et al., 1999a).

3.2.9. Total protein determination for CYP3A activity normalization

As part of the assessment of CYP3A activity in primary enterocytes, LS180 cells, and Caco-2 cells, cells were washed three times with ice-cold DPBS^{++}. After the final wash, DPBS^{++} was aspirated and 150 µL of 1M sodium hydroxide was added to the apical chamber of each Transwell® to lyse the cells at room temperature for 1 hour. While cells were incubating with sodium hydroxide, BCA standards (catalog no. 23208, Thermo Scientific, MA) were added to a 96-well plate and kept at 4ºC until cell lysing was complete. After the hour incubation, 150 µL of 1M HCl was added to each Transwell® insert to neutralize the sodium hydroxide. The neutralized cell lysate solution (25 µL) was added to the 96-well plate containing standards. BCA working reagent was prepared and 200 µL was added to each well containing BCA standards or cell lysate. The plate was then incubated at 37ºC for 30 minutes and then read on a Tecan SPARK multimode plate reader (Tecan Group Ltd., Switzerland), measuring an absorbance of 562 nm. The protein content of enteroid monolayers used for the CYP3A activity comparison experiment (i.e., monolayers of primary enterocytes, LS180, Caco-2 and differentiated enteroids) was not measured. As an alternative for activity normalization, we used the total protein content measured as described above in 208 different enteroid monolayers cultured under identical conditions; the coefficient of variation of that mean protein content (0.104 mg) was 16%.

3.2.10. Midazolam first-pass extraction ratio calculation

The midazolam first pass extraction ratio (ER) to assess CYP3A activity was calculated using eq. 3 (Fisher et al., 1999b):

$$ER = \frac{\Sigma(1 - OH\ MDZ)}{\Sigma(1 - OH\ MDZ) + MDZ_{Basolateral}}$$

where Σ(1-OH MDZ) is the amount of 1-OH midazolam measured in both the apical and basolateral compartments (pmol) and $MDZ_{Basolateral}$ is the amount of unchanged midazolam measured in the basolateral compartment. The impact of CYP3A5 expression on total activity was not assessed in this chapter – only one donor (donor 3) was heterozygous for the *CYP3A5*1* allele, and there was no obvious difference in catalytic activity between this donor and others.

3.2.11. P-gp activity assay

Cell monolayers were washed three times with blank transport buffer (10 mM HEPES in Hank's balanced salt solution, pH 7.4) and maintained at 37ºC until use. For the basal and rifampin-induced conditions, stock solutions of the test compound (digoxin, 10 mM in DMSO) was diluted in donor transport buffer (pH 7.4) to make the final dosing solution (final concentrations of digoxin was 10 μM, 0.1% DMSO). For the verapamil-inhibited condition, stock solutions of digoxin and verapamil (both 10 mM in DMSO) were diluted in donor transport buffer (pH 7.4) to make the final dosing solutions (final concentration of both digoxin and verapamil were 10 μM, 0.2% DMSO). For each condition, a matched vehicle control containing the same %DMSO was run in parallel.

For the apical digoxin dosing conditions, 0.3 mL of the dosing transport buffers prepared above were added to the filter insert and 0.72 mL of transport buffer (pH 7.4) containing a matched amount of DMSO (v/v) was added to the basolateral compartment. For the basolateral digoxin dosing conditions, 0.7 mL of the dosing transport buffers prepared above were added to the basolateral compartment and 0.32 mL of transport buffer (pH 7.4) containing a matched amount of DMSO (v/v) was added to the filter insert. Cells were incubated for 30 minutes at 37ºC and the total volume from all compartments were collected separately and stored at -80ºC until analysis.

Digoxin concentration in the donor and receiver transport buffer were measured using liquid chromatography coupled with tandem mass spectrometry on an Agilent 6410 QQQ equipped with a UPLC 1290 system. After thawing and vortexing, 50 µL of the receiver samples and 50 µL of diluted donor samples (diluted 25-fold in blank transport buffer) were mixed with 20 µL internal standard (3.75 ng/mL in methanol) and 30 µL of methanol. Samples were then centrifuged at 20,800*g* for 10 minutes at 4ºC, and 75 µL of the supernatant was analyzed by LC/MS-MS. Chromatographic separation was achieved following injections of 10 µL of sample using a Zorbax RX-C8 narrow bore, 5 µm, 2.1 x 150 mm column using 10 mM ammonium acetate, 1 mM ammonium chloride in water (A) and methanol (B) as mobile phase. The flow rate was 0.25 mL/min with a gradient as follows: 65% B for 1 minute, then increased to 100% linearly over 3 minutes, held at 100% for 3 minutes, and then equilibrated back to 65% for 2 minutes. The following SIM was monitored: *m/z* 815.5 for digoxin-chloride adduct, and *m/z* 818.5 for digoxin-d_3-chloride adduct in negative mode. For both compounds, dwell time was set to 100 ms, cell accelerator voltage was set to 7 V, and fragmentor was set to 200 V. Results are presented as the peak area ratio of the analyte (digoxin) to internal standard (digoxin-d_3).

3.2.12. Efflux ratio calculation

The efflux ratio of digoxin was calculated using eq. 3:

$$ER = \frac{P_{app,B \to A}}{P_{app,A \to B}}$$

Where P_{app} values for the basolateral and apical dosing conditions were calculated as described in equation 2.

3.2.13. Statistical analysis

Prior to making comparisons of results from RNA-Seq analysis, genes with very low expression levels were excluded, based on a mean log counts/million (logCPM) > 0, which reduced the number of genes from just over 70,000 to 13,728 genes. Normalization factors were estimated using the trimmed-mean of M-values (TMM) method (Robinson and Oshlack, 2010), and then comparisons were made between differentiated and undifferentiated cells using a quasi-likelihood F-test (Lun et al., 2016), with a blocking factor to control for sample donor. The analysis was performed using the Bioconductor edgeR package (Robinson et al., 2010). To restrict to those genes with a large change in expression, an additional 20%-fold change criterion was included (e.g., the null hypothesis was specified as $H_o: |\beta| < 1.2$), using the treat function (McCarthy and Smyth, 2009). Differentially expressed genes were selected using a false discovery rate (FDR)<0.05 (Benjamini and Hochberg, 1995).

Statistical significance ($\alpha = 0.05$) for the permeability and CYP3A metabolism studies was determined via linear mixed effect models (Bates et al., 2015). All statistical analyses were conducted using RStudio (R. Posit Software, PBC, Boston, MA).

3.3. RESULTS

3.3.1. Enteroid monolayer differentiation status and morphology

The effects of Wnt3A reduction on enteroid differentiation are shown in **Figure 3.1**. The mRNA expression of several of these genes, shown as Log_2CPM, is depicted in **Figure 3.1a**; there was a decrease in mRNA abundance of cell proliferation genes, PCNA and MKI67, and an increase in enterocyte and goblet cell associated gene transcripts, sucrase isomaltase and MUC13, respectively. Interestingly, mRNA for the stem cell marker, LGR5, did not change following differentiation, although there was significant inter-donor variability. Follow-up ICC experiments demonstrated the presence of a small population of proliferating cells, as shown by the nuclear stain of a prototypical proliferation marker, Ki67 (**Figure 3.1b**). As expected, ICC experiments confirmed the absence of an enterocyte marker, villin, after 1 day in culture with differentiation media (**Figure 3.1c**) and its presence after 7 days in culture (**Figure 3.1d**). Enteroid monolayers cultured for 21 days in differentiation media demonstrate a mixed-cobblestone morphology under brightfield microscopy and an undulating-like surface as seen in orthogonal images (**Figure 3.2a and 3.2b**). The presence and proper localization of prototypical apical- and basolateral-associated proteins, ZO-3 and MRP3 respectively, was confirmed via ICC experiments (**Figure 3.2c**).

3.3.2. Cell monolayer barrier integrity

TEER values for differentiated enteroid monolayers from three donors were measured during a 21-day culture period. As shown in **Figure 3.3a**, TEER values for the differentiated enteroid monolayers rose steadily, achieving an apparent plateau by day 11-15 for two donors; values ranged from approximately 200 to 600 $\Omega\cdot cm^2$. In contrast, TEER values for a representative undifferentiated organoid monolayer were substantially lower throughout the entire culture period, reaching a maximum of approximately 40 $\Omega\cdot cm^2$. A follow-up study assessing the stability of TEER values of a differentiated enteroid monolayer from a single representative donor over 42 days is shown in **Figure 3.3b**. The TEER values for this donor had a similar trajectory as the 21-day experiment, plateauing at approximately 400 $\Omega\cdot cm^2$ after 21-days in culture and remaining there through day 42.

A functional 21-day permeability study was conducted with differentiated enteroid monolayers from three donors utilizing the paracellular marker probe substrates, atenolol and Lucifer yellow, and the highly permeable transcellular marker probe, midazolam. As shown in **Figure 3.3c**, the apparent permeability (P_{app}) values for midazolam were approximately 17 x 10^{-6} cm/s on days 7 and 21. In contrast, the paracellular transport probe compounds atenolol and Lucifer yellow demonstrated P_{app} values comparable to the midazolam values on day 7 in culture but decreased to approximately 5 x 10^{-6} cm/s by day 21 in culture.

Barrier integrity was also assessed via ICC imaging of tight junction proteins (**Figure 3.4a-3.4c**). Occludin, ZO-1, and ZO-3 all demonstrated organized localization at the cell-cell boundaries in monolayers cultured for 21 days and ZO-3 in monolayers cultured for 42 days (**Figure 3.4d**).

3.3.3. RNA expression of various DMET genes

The abundances in undifferentiated spheroids and differentiated monolayers grown for 21 days of mRNA encoded by various DMET genes was compared (**Figure 3.5a and 3.5b**). The expression of most DMET genes increased following differentiation, including both phase I (*CYP3A4*) and phase II enzymes (*UGT1A1, SULT2B1*) and both SLC (*SLC15A1*, *SLCO2B1*) and ABC (*ABCB1*) transporters.

3.3.4. Midazolam extraction ratios in enteroid monolayers

A comparison of basal CYP3A activity, expressed as 1-OH midazolam formed per milligram of total protein, for enteroid monolayers grown for 7 and 21 days to primary enterocytes, LS180, and Caco-2 cells is shown in **Figure 3.6a**. These results demonstrate that differentiated enteroid monolayers have greater CYP3A activity than LS180 and Caco-2 cells, and enteroid monolayers grown for 21 days have greater CYP3A activity than primary enterocytes. A follow up study of CYP3A activity in enteroid monolayers cultured for 7 and 21 days was assessed by calculation of first-pass (A>B) midazolam extraction ratios, in basal, induced, and inhibited states (**Figure 3.6b**). Basal extraction ratios ranged from 4-15% at day 7 in culture and increased to 12-30% by day 21 in culture. Addition of the prototypical vitamin D receptor (VDR) ligand and CYP3A4 inducer, $1\alpha,25(OH)_2$ vitamin D_3, increased the midazolam extraction ratios at culture day 7 and day 21 to approximately 13-28% and 25-50%, respectively. The addition of a known mechanism-based inactivator of intestinal CYP3A4, 6’,7’-dihydroxybergamottin, decreased midazolam extraction ratios at day 7 and day 21 in culture to approximately 0-3% and 0-4% of basal control. An additional study assessing the enteroid monolayer midazolam extraction ratio under basal and CYP3A-induced conditions after 42 days in culture is shown in **Figure 3.6c**; values for basal and vitamin D-treated monolayers ranged from 6-42% and 19-52%, respectively.

Pharmacokinetic theory predicts that the presence of albumin in the vascular compartment of mucosal villi can affect both the permeability and metabolic extraction of orally administered CYP3A substrates, depending on albumin-drug binding affinity and the site of the rate-determining step in transcellular flux (Fisher et al., 1999a). The effect of human serum albumin (HSA) addition to the differentiated enteroid monolayer basolateral (i.e., vascular) compartment on apically dosed midazolam extraction ratios is shown in **Table 3.1**. The addition of HSA resulted in approximately a 25% decrease in midazolam extraction ratio for donor monolayers. The decrease in midazolam extraction ratio was accompanied by an increase in midazolam monolayer permeability; P_{app} was increased approximately 2-fold compared to no HSA control.

Of note, the rate of formation of 1’-hydroxymidazolam during the same 1-hr assessment period remained unchanged.

3.4. DISCUSSION

The development of a human intestinal enterocyte monolayer model to predict oral drug disposition is of particular importance to the field of pharmaceutical science and drug development. Stem-cell derived enteroid models have emerged as a promising new tool to address the scientific need, However, current reports utilizing intestinal organoids describe complete Wnt3A-removal to achieve terminal organoid differentiation, imparting limited viability of roughly one week and continuing dynamic changes in DMET functions (Michiba et al., 2022). Results presented in this chapter demonstrate that the use of a proprietary media formulation which promotes differentiation, provided by Intesticult, can elicit enterocyte differentiation, including functional barrier integrity and CYP3A enzyme activity, and that differentiation and cell viability is stable for an extended period of time (3-6 weeks). Under these conditions, enteroid monolayers showed a decline in mRNA for markers of cell proliferation (*PCNA* and *MKI67*) and an increase for cell type-specific markers for enterocytes and goblet cells (*SI* and *MUC13*, respectively), compared to undifferentiated intestinal spheroids. Pathway analysis of the RNA-Seq data supports these selected observations, as genes related to cell proliferation, intestinal absorptive/secretory processes, and xenobiotic metabolism/transport processes were differentially expressed between undifferentiated spheroids and enteroid monolayers. Interestingly, mRNA abundance of the stem cell marker, *LGR5*, in undifferentiated spheroids and differentiated enteroid monolayers was not statistically different (although a highly variable decreased trend apparent), suggesting that these monolayers contain a population of dividing cells that confers a self-renewing phenotype. Corroborating this interpretation was the identification of proliferating cells in the enteroid monolayer, as demonstrated by sporadic nuclear localization of Ki67 protein. Collectively, our results suggest that enteroid monolayers differentiated in this proprietary medium are amenable to long-term studies of the multiple processes affecting oral intestinal drug bioavailability.

Enteroid monolayers cultured for 21 days exhibited a mixed-cobblestone morphology under brightfield microscopy (**Figure 3.2A)** – a lack of uniformity in the monolayer is expected from a culture of a mixed population of cells, such as those found in the intestinal villi that are generated by the same crypt stem cell precursor (Barker et al., 2007). Interestingly, orthogonal imaging of DAPI stained nuclei in these monolayers demonstrated spontaneous formation of an undulating-like surface. Though not complete formation of a crypt-villus axis as seen *in vivo*, this observation suggests that the enteroid monolayers are self-organizing into an anatomically relevant structure. Monolayer morphology was further assessed by confirming the proper localization of prototypical apical and basolateral membrane-associated proteins, ZO-3 and MRP3, respectively, indicative of monolayer polarization.

We next explored the barrier function of intestinal monolayers. Measuring TEER allowed us to assess the maturation of the epithelial barrier during the entire study period. Results showed a time-dependent maturation of barrier function (10-14 days), but also relative stability in that function between 14-42 days. Permeability studies utilizing paracellular transport probe substrates corroborated TEER measurements. Importantly, the permeability of Lucifer yellow and atenolol were comparable to that of the highly permeable control, midazolam, on day 7 in culture, but were roughly 3-fold lower by day 21 in culture, demonstrating development of a functional barrier by this time. It should be noted that the P_{app} values calculated in this experiment are likely overestimated, given that the surface area used for these calculations was that of the Transwell® membrane but the true surface area of the cells was likely greater due to the undulations seen by microscopy and the potential presence of microvilli. ICC results confirmed the presence of inter-cellular tight junction proteins in enteroid monolayers, which is expected for a functioning paracellular barrier. Collectively, our study results suggest that enteroid monolayers differentiated using a proprietary differentiation medium maintain barrier integrity over an extended period and are amenable to repeated measurements of drug absorption across the intestinal mucosa under different experimental conditions.

As anticipated, the abundances of important DMET transcripts were increased in enteroid monolayers cultured for 21 days, compared to undifferentiated intestinal spheroids. Strikingly, the expression of both *CYP3A4* and *ABCB1* (P-glycoprotein) were among the most highly upregulated genes following differentiation, each with an approximately 60-fold mean increase in expression, although with high inter-donor variability. Following these findings, we characterized CYP3A activity in differentiated enteroid monolayers. We first compared the midazolam 1'-hydroxylation activity of enteroid monolayers to that of primary enterocytes, LS180 cells and Caco-2 cells cultured in the Transwell® system under similar conditions. Results demonstrated superior basal activity from the enteroid monolayer cultured for 21 days, compared to the other conventionally used intestinal cell models. In subsequent experiments, we found that enteroid monolayers were capable of first pass midazolam metabolic extraction (19-52%) that was comparable to that found *in vivo* (18-59%) (Paine et al., 1996), and the extraction was inducible and susceptible to mechanism-based inhibition. The strong agreement between the *in vivo* report and our *in vitro* data highlights the biochemical relevance of enteroid monolayers as a tool to predict oral first-pass drug metabolism. Indeed, our limited results from enteroid monolayers grown for 42 days in culture suggest stable metabolic function for at least 6 weeks, presumably because of self-replication during the treatment period, as occurs *in vivo*.

To further assess the utility of the enteroid monolayer model, we investigated a more physiologically relevant situation where binding proteins (HSA) are present in the basolateral chamber that might impact both midazolam permeability and extraction ratio. As hypothesized, basolateral HSA increased midazolam permeability by approximately 2-fold. Midazolam exhibits protein binding *in vivo* of around 97%, so the addition of abluminal HSA would produce a lower concentration of unbound midazolam in the basolateral chamber than in the absence of HSA, which could facilitate passive diffusion across the basolateral membrane by maintaining a high unbound midazolam concentration gradient. The increase in cell permeability was accompanied by a modest decrease in midazolam extraction ratio of about 25%, but no change in midazolam 1’-hydroxylation rate. This combination of results suggests that midazolam cell efflux across the basolateral membrane is rate-limiting, compared to uptake into the cell from the apical compartment. An equilibrium between apical and intracellular compartments is likely rapidly achieved and is unaffected by midazolam binding to basolateral HSA. The reduction in first-pass extraction is achieved by an increase in basolateral cell permeability and not a decrease in metabolism. These findings and conclusions may be applicable to other highly bound BCS Class 1 drugs.

A limitation of this study is the number of stem cell donors (n=3) utilized for experimentation. Future studies should look at a larger pool of donors to ascertain potential sources of interindividual variability in oral drug absorption and/or metabolism. An additional limitation is that only CYP3A activity was assessed. While it is well-established that CYP3A4 is the most abundant cytochrome P450 enzyme in the small intestine, other enzymes including both phase I and phase II are also present and should be assessed in future studies, including CYP2C9, CYP2C19, CES2, and UGT1A isoforms. Similarly, the activity of various efflux and uptake transporters, such as P-gp, PEPT1, OATP2B1, and various organic cation transporters, was not rigorously assessed in this work – future studies need to address this gap as transporters play an important role in modulating oral drug absorption and are a potential source of drug-drug/natural product-drug interactions. In this regard, a pilot experiment investigating P-gp function using digoxin as a probe substrate in enteroid monolayers grown for 7 days suggests that functional P-gp is present and that efflux activity increases in the presence of an inducer (rifampin) and decreases in the presence of an inhibitor (verapamil) (**Figure 3.7**). While encouraging, this study needs to be repeated across more donors and for enteroid monolayers grown for 21 days before firmer conclusions can be drawn. Moreover, this study did not assess changes in DMET mRNA abundance following treatment with $1\alpha,25(OH)_2$ vitamin D_3. While the CYP3A activity results suggest *CYP3A* transcription was increased, assessing the impact of $1\alpha,25(OH)_2$ vitamin D_3 on other DMET transcripts would help bolster the claim that enteroid monolayers respond appropriately to this stimulus. Additionally, this study did not assess differences in enteroid viability and function when enteroids were differentiated using a proprietary medium versus a medium that is completely devoid of Wnt3A. Furthermore, this publication did not fully investigate the differentiation stability between day 21 and day 42 enteroids – CYP3A activity data suggests stability, but additional metrics are needed to support this claim.

In summary, results from experiments detailed in this report support the use of human crypt stem cell derived enteroid monolayers as an *in vitro* model to study oral drug disposition. Cell culture with a proprietary differentiation medium imparted an extended viability that is not present for enteroid monolayers differentiated in a medium that is devoid of Wnt3A. Long term-cultured enteroids could have unique utility, compared to other *in vitro* models, for studying complex kinetic phenomena such as the time-course of perturbations in enzyme or transporter function/expression, as well as the interplay of intestinal transport and metabolism processes, such as P-gp and CYP3A (Benet et al., 1996), and *in vitro-in vivo* PBPK modeling. Moreover, this model might be more amenable for studying intestinal drug accumulation kinetics in the treatment of intestinal diseases, xenobiotic intestinal toxicity and the impact of chronic conditions such as microbial or disease-induced inflammation. Additional work is needed to explore these applications.

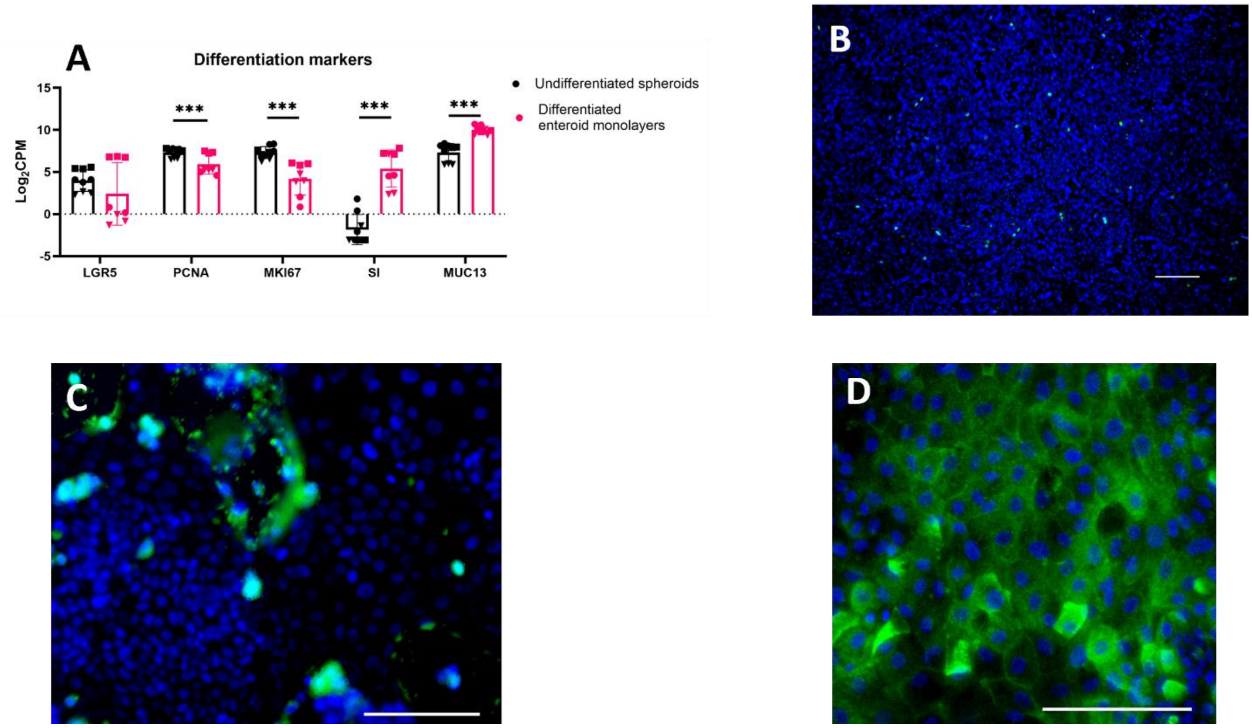

Figure 3.1. Enteroid differentiation status.

Effect of differentiation on gene expression of differentiation markers for undifferentiated spheroids and enteroid monolayers grown for 21 days expressed as the logarithm of counts per million reads (LogCPM) (a). Data points correspond to gene expression of an individual culture replicate, data point shape corresponds to organoid donor. Data represents means and SD of all culture replicates from three donors. ICC results are shown in figures 1b-d. Enteroids display a small population of Ki67 positive cells (green) by day 21 in culture (b). Enteroids lack robust staining of the enterocyte marker, Villin (green), at day 1 of culture (c) but demonstrate robust staining by day 7 (d). All scale bars represent 100 µm. *** $P < 0.001$.

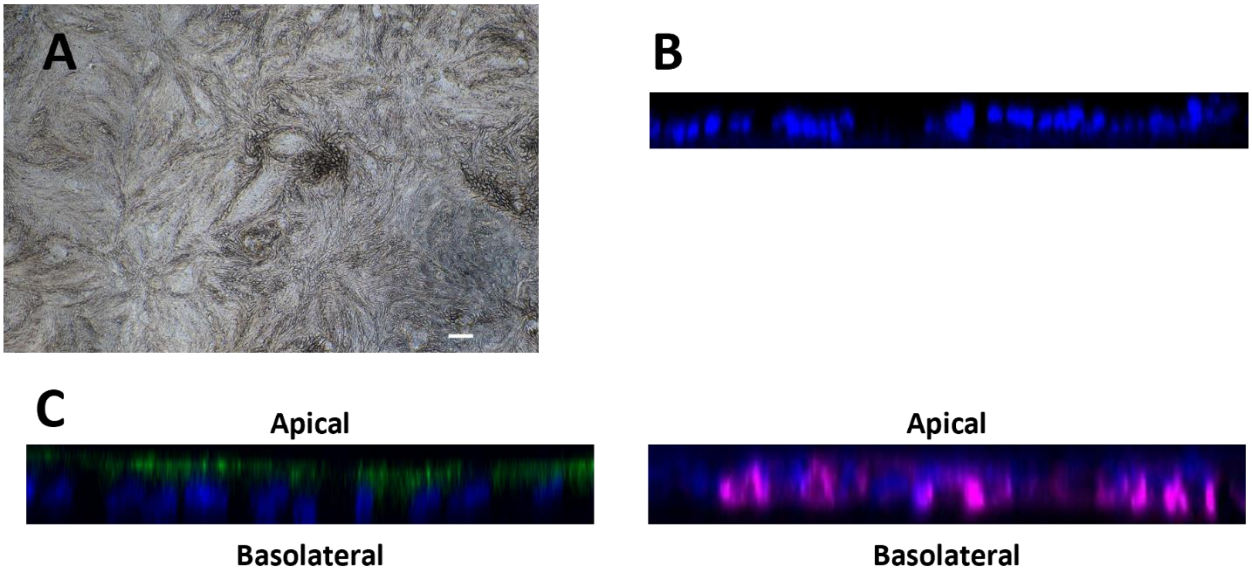

Figure 3.2. Enteroid morphology.

Enteroid monolayers under brightfield microscopy display a mixed-cobblestone morphology (a). Orthogonal images of DAPI (blue) stained nuclei show enteroids have an undulating morphology (b). Staining for ZO-3 (green) and MRP3 (magenta) confirm proper localization of apical and basolateral membrane proteins, respectively (c). All images are from enteroid monolayers grown for 21 days. The ZO-3 image in (c) is the same image as the orthogonal image in figure 4b. Scale bar represents 100 µm.

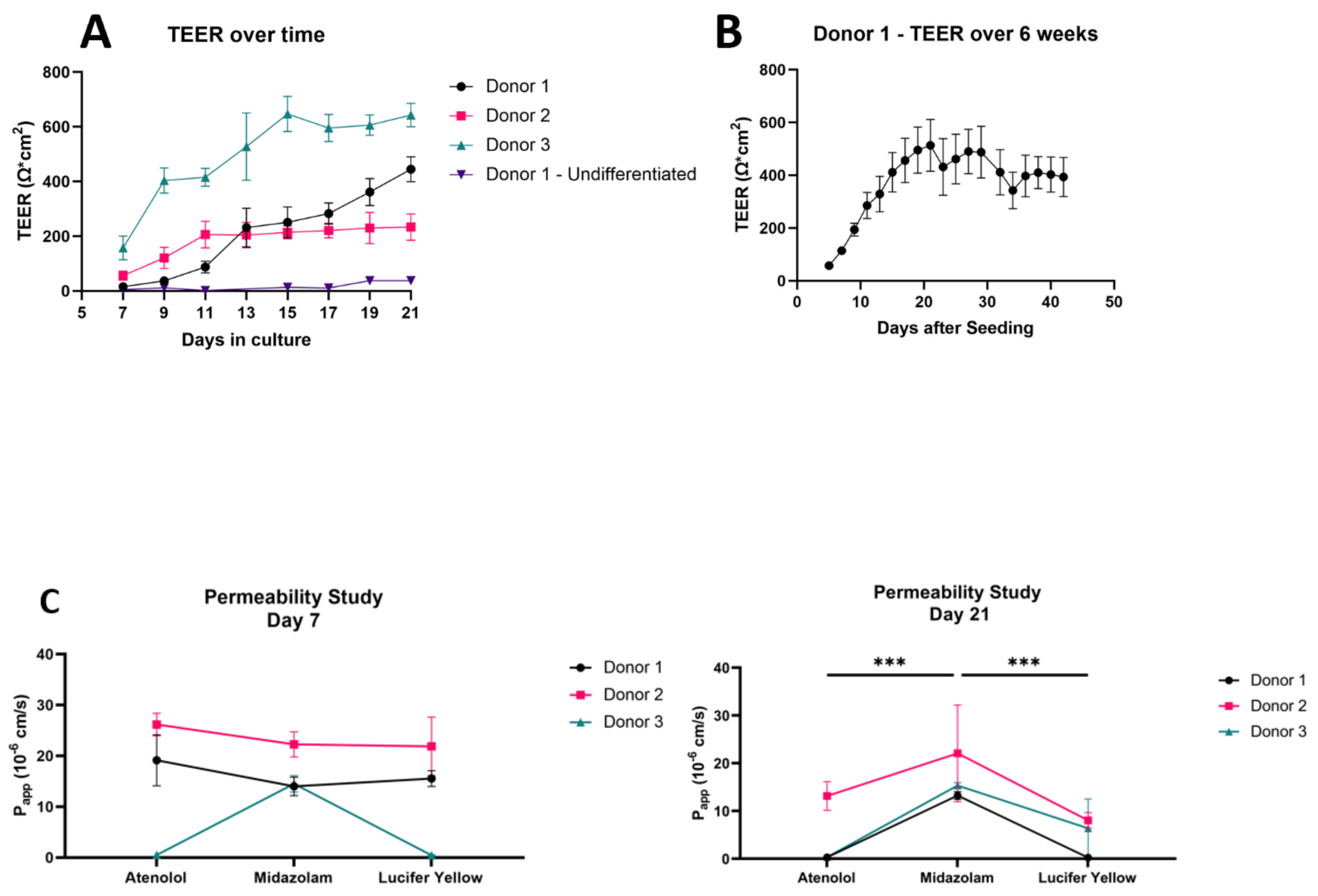

Figure 3.3. Barrier integrity.

Transepithelial electrical resistance (TEER) values over time for enteroid monolayers grown on Transwell® inserts for 21 days (a) and 42 days (b). Data represents means and SD for culture replicates (n = 6 for donor 1, n = 9 for donor 2 and donor 3, n = 3 for undifferentiated monolayers) for each donor. Permeability studies for cells grown on Transwell® inserts for 7 and 21 days are shown in figure c. Data represents means and SD for each donor with three culture replicates each. *** $P < 0.001$.

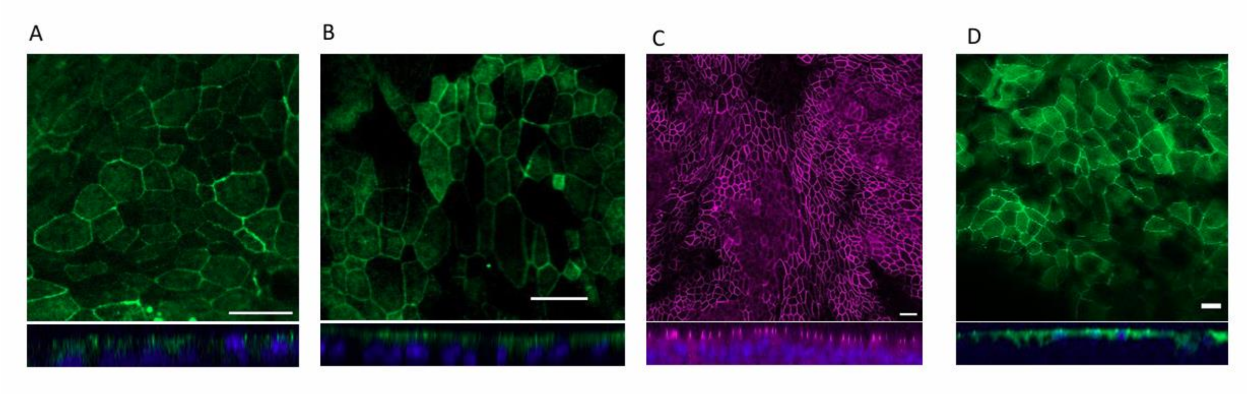

Figure 3.4. Tight junction proteins.

ICC imaging of tight junction proteins, ZO-1 (green), ZO-3 (green), and Occludin (magenta), are shown in (a), (b), and (c), respectively, for enteroid monolayers grown for 21 days. Figure 4d shows ICC imaging of ZO-3 for enteroid monolayers grown for 42 days. Orthogonal images of each stain are shown below, where nuclei were counterstained with DAPI (blue). The orthogonal image of the ZO-3 stain in (b) is the same image shown in figure 2c. Scale bars represent 20 µm.

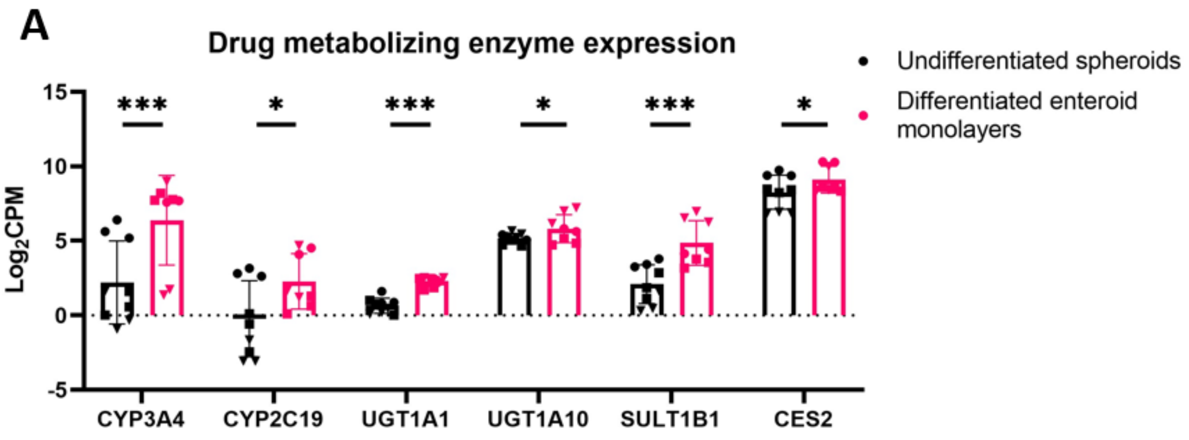

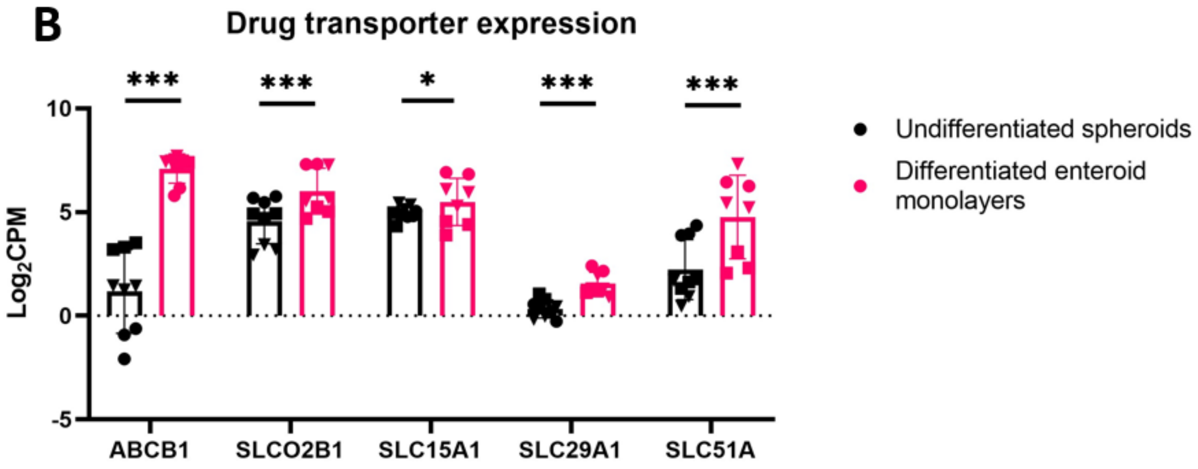

Figure 3.5. DMET RNA expression.

The RNA expression of drug metabolizing enzymes (a) and transporters (b) for undifferentiated spheroids and enteroid monolayers grown for 21 days. Data points correspond to gene expression of an individual culture replicate, data point shape corresponds to organoid donor. Data represents means and SD of all culture replicates from three donors. * $P < 0.05$, *** $P < 0.001$.

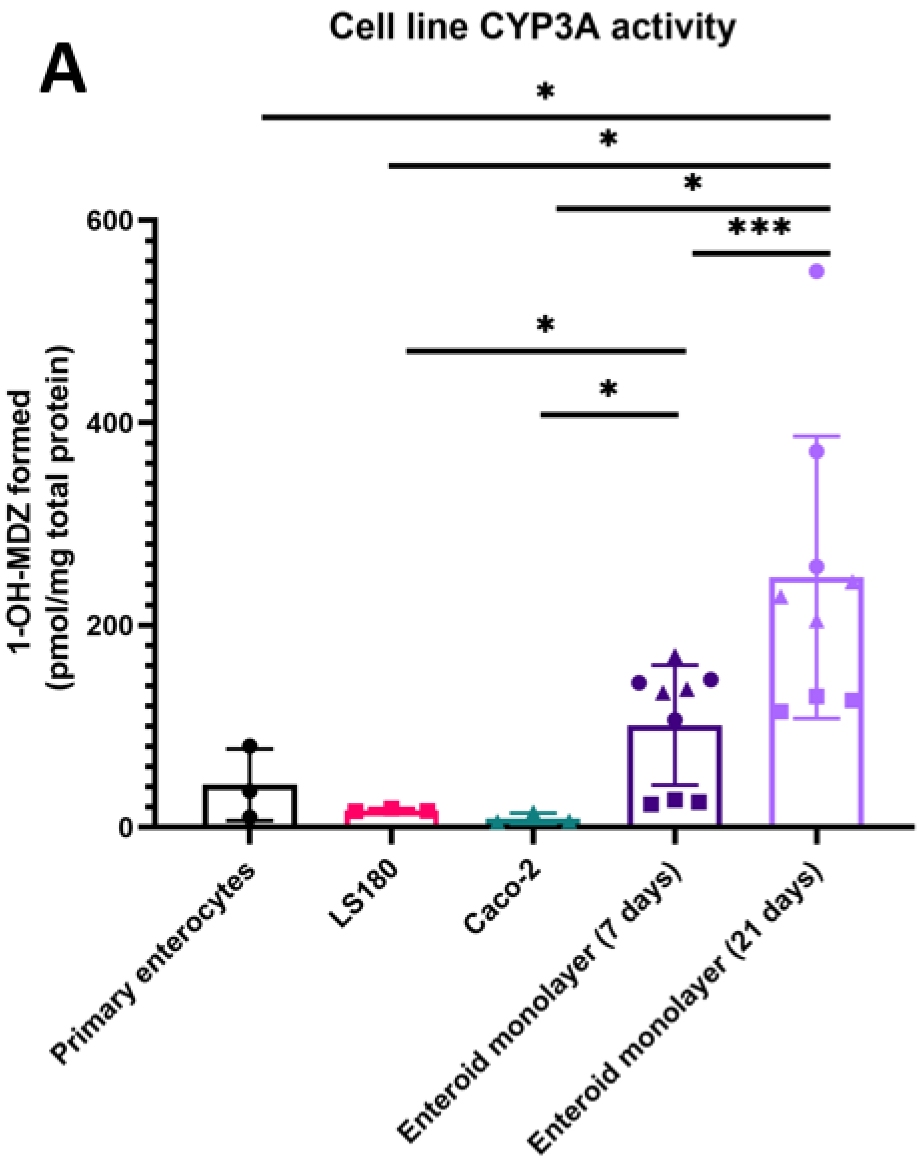
A
Cell line CYP3A activity
*
*
*
***
*
*
600
400
200
0
1-OH-MDZ formed (pmol/mg total protein)
Primary enterocytes
LS180
Caco-2
Enteroid monolayer (7 days)
Enteroid monolayer (21 days)

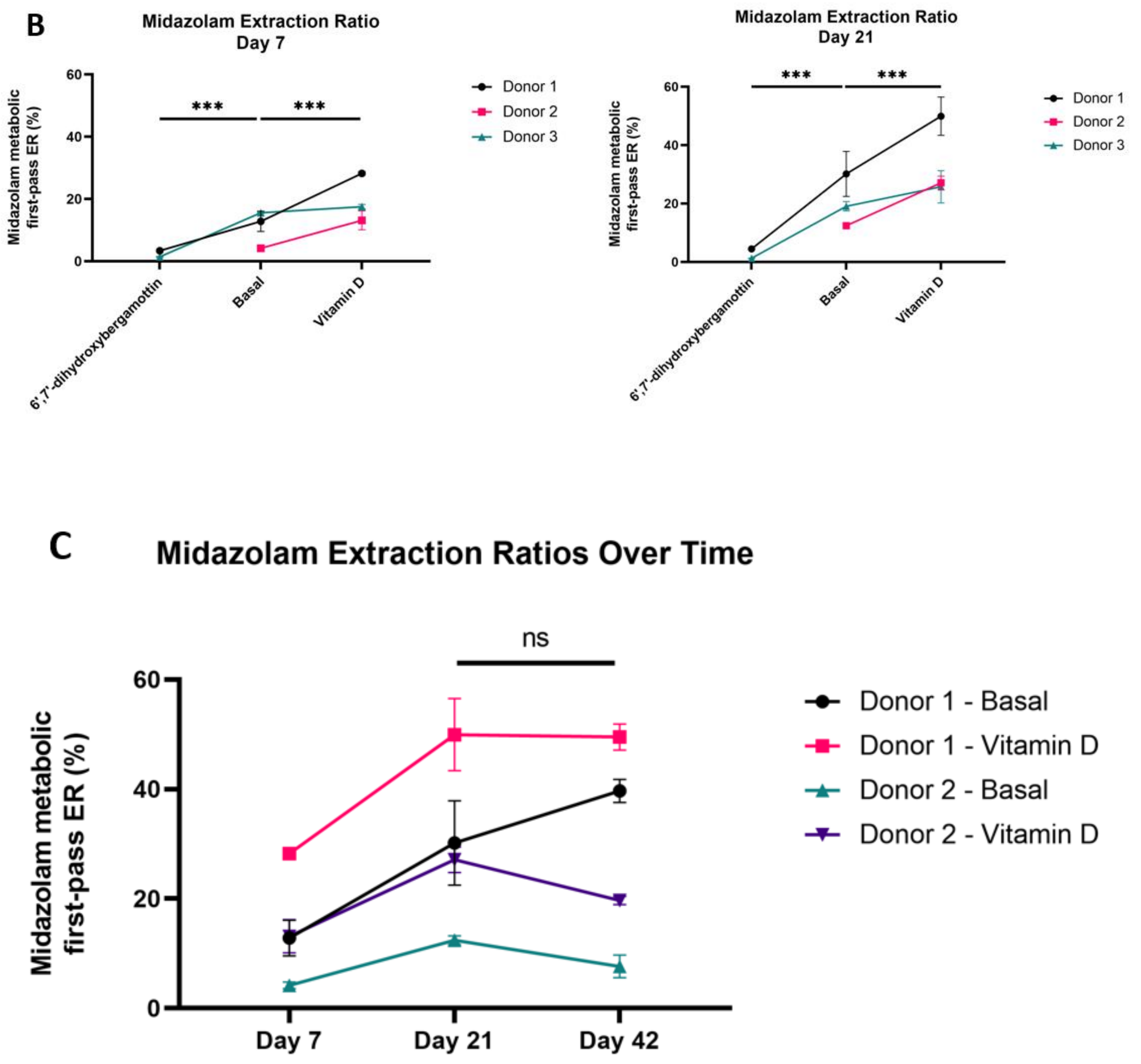

Figure 3.6. CYP3A activity.

A comparison of CYP3A activity, expressed as 1-OH midazolam formed per milligram of total protein, for primary enterocytes from a single donor, LS180 cells, Caco-2 cells, and enteroid monolayers grown for 7 and 21 days is shown in (a). CYP3A activity results, expressed as midazolam metabolic first pass extraction ratios (ERs), for enteroid monolayers grown for 7 and

21 days under basal, 6’,7’-dihydroxybergamottin, and vitamin D conditions are shown in (b), where the 6’,7’-dihydroxybergamottin treatment was conducted with only 2 of the 3 available stem cell donors. Midazolam metabolic first pass extraction ratio (ER) for enteroid monolayers grown for 42 days is compared to the 7 and 21 day results in (c). For (a), primary enterocytes from a single donor, LS180, and Caco-2 data represent means and SD of three culture replicates from a single source. For the enteroid monolayers, data represents means and SD of three donors combined, containing three culture replicates each. For (b) and (c), data represents means and SD for each donor with three culture replicates each. * $P < 0.05$, *** $P < 0.001$.

Table 3.1 HSA impact on midazolam disposition.

Effect of abluminal HSA on midazolam ER, permeability, and 1-OH midazolam formation for monolayers grown for 7 and 21 days is shown in Table 1. Data is represented as the mean and SD of three donors with three culture replicates each. P values, derived from linear mixed effect modeling, are listed for each comparison.

	Day 7				Day 21		
	(-)HSA	(+) HSA	(-)HSA vs (+)HSA		(-)HSA	(+) HSA	(-)HSA vs (+)HSA
	Mean (SD)	Mean (SD)	p-value		Mean (SD)	Mean (SD)	p-value
Midazolam First-Pass Extraction Ratio (%)				**Midazolam First-Pass Extraction Ratio (%)**			
Basal	10.2 (5.4)	5.5 (3.8)	4.3 x 10^{-6}	Basal	20.6 (9.3)	15.3 (11.9)	0.0055
Vitamin D	20.0 (7.3)	13.7 (7.2)	1.2 x 10^{-4}	Vitamin D	35.0 (13.3)	26.6 (12.8)	8.0 x 10^{-5}
Midazolam Permeability (10^{-6} cm/s)				**Midazolam Permeability (10^{-6} cm/s)**			
Basal	11.3 (3.0)	23.3 (3.7)	2.7 x 10^{-8}	Basal	14.2 (1.6)	27.7 (9.1)	7.1 x 10^{-5}
Vitamin D	11.5 (2.3)	19.2 (2.8)	1.7 x 10^{-6}	Vitamin D	14.7 (4.2)	23.5 (5.0)	1.4 x 10^{-5}
1-OH Midazolam formed (pmol)				**1-OH Midazolam formed (pmol)**			
Basal	10.1 (6.5)	10.3 (7.5)	0.61	Basal	26.4 (15.5)	31.5 (22.3)	0.23
Vitamin D	22.1 (12.1)	23.5 (14.5)	0.43	Vitamin D	54.0 (24.4)	57.9 (29.3)	0.18

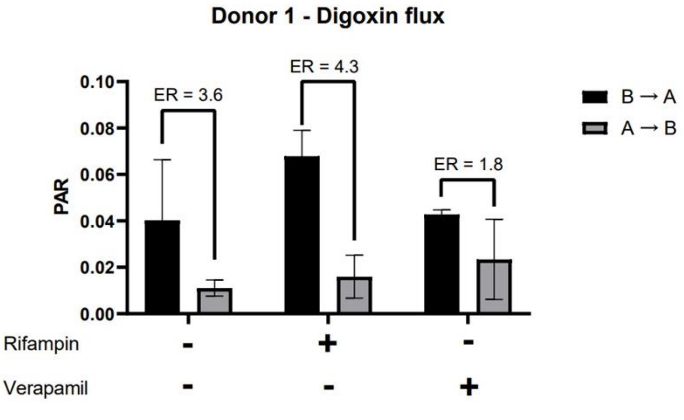

Figure 3.7. P-gp activity assay.

P-gp activity assay, expressed as an efflux ratio (ER), for enteroid monolayers from one donor grown for 7 days under basal, rifampin-induced, and verapamil inhibited conditions. Data is presented as the mean and SD peak area ratio (PAR) of digoxin to its internal standard (digoxin-d3) for three culture replicates from a single donor.

3.5. REFERENCES

Andrews S (2010) Babraham Bioinformatics - FastQC a quality control tool for high throughput sequence data, https://www.bioinformatics.babraham.ac.uk/projects/fastqc/.

Anoshchenko O, Storelli F, and Unadkat JD (2021) Successful Prediction of Human Fetal Exposure to P-Glycoprotein Substrate Drugs Using the Proteomics-Informed Relative Expression Factor Approach and PBPK Modeling and Simulation. *Drug Metab Dispos* **49:**919-928.

Arian CM, Imaoka T, Yang J, Kelly EJ, and Thummel KE (2022) Gutsy science: In vitro systems of the human intestine to model oral drug disposition. *Pharmacol Ther* **230:**107962.

Barker N, van Es JH, Kuipers J, Kujala P, van den Born M, Cozijnsen M, Haegebarth A, Korving J, Begthel H, Peters PJ, and Clevers H (2007) Identification of stem cells in small intestine and colon by marker gene Lgr5. *Nature* **449:**1003-1007.

Bates D, Mächler M, Bolker B, and Walker S (2015) Fitting Linear Mixed-Effects Models Using lme4. *Journal of Statistical Software* **67:**1 - 48.

Benet LZ, Wu C-Y, Hebert MF, and Wacher VJ (1996) Intestinal drug metabolism and antitransport processes: A potential paradigm shift in oral drug delivery. *Journal of Controlled Release* **39:**139-143.

Benjamini Y and Hochberg Y (1995) Controlling the False Discovery Rate: A Practical and Powerful Approach to Multiple Testing. *Journal of the Royal Statistical Society: Series B (Methodological)* **57:**289-300.

Fisher JM, Wrighton SA, Calamia JC, Shen DD, Kunze KL, and Thummel KE (1999a) Midazolam metabolism by modified Caco-2 monolayers: effects of extracellular protein binding. *J Pharmacol Exp Ther* **289:**1143-1150.

Fisher JM, Wrighton SA, Watkins PB, Schmiedlin-Ren P, Calamia JC, Shen DD, Kunze KL, and Thummel KE (1999b) First-pass midazolam metabolism catalyzed by 1alpha,25-dihydroxy vitamin D3-modified Caco-2 cell monolayers. *J Pharmacol Exp Ther* **289:**1134-1142.

Foulke-Abel J, In J, Yin J, Zachos NC, Kovbasnjuk O, Estes MK, de Jonge H, and Donowitz M (2016) Human Enteroids as a Model of Upper Small Intestinal Ion Transport Physiology and Pathophysiology. *Gastroenterology* **150:**638-649 e638.

In JG, Foulke-Abel J, Estes MK, Zachos NC, Kovbasnjuk O, and Donowitz M (2016) Human mini-guts: new insights into intestinal physiology and host-pathogen interactions. *Nat Rev Gastroenterol Hepatol* **13:**633-642.

Kasendra M, Luc R, Yin J, Manatakis DV, Kulkarni G, Lucchesi C, Sliz J, Apostolou A, Sunuwar L, Obrigewitch J, Jang KJ, Hamilton GA, Donowitz M, and Karalis K (2020) Duodenum Intestine-Chip for preclinical drug assessment in a human relevant model. *Elife* **9**.

Kim D, Paggi JM, Park C, Bennett C, and Salzberg SL (2019) Graph-based genome alignment and genotyping with HISAT2 and HISAT-genotype. *Nat Biotechnol* **37:**907-915.

Liao Y, Smyth GK, and Shi W (2019) The R package Rsubread is easier, faster, cheaper and better for alignment and quantification of RNA sequencing reads. *Nucleic Acids Res* **47:**e47.

Lun AT, Chen Y, and Smyth GK (2016) It's DE-licious: A Recipe for Differential Expression Analyses of RNA-seq Experiments Using Quasi-Likelihood Methods in edgeR. *Methods Mol Biol* **1418:**391-416.

McCarthy DJ and Smyth GK (2009) Testing significance relative to a fold-change threshold is a TREAT. *Bioinformatics* **25:**765-771.

Michiba K, Maeda K, Shimomura O, Miyazaki Y, Hashimoto S, Oda T, and Kusuhara H (2022) Usefulness of Human Jejunal Spheroid-Derived Differentiated Intestinal Epithelial Cells for the Prediction of Intestinal Drug Absorption in Humans. *Drug Metab Dispos* **50:**204-213.

Paine MF, Shen DD, Kunze KL, Perkins JD, Marsh CL, McVicar JP, Barr DM, Gillies BS, and Thummel KE (1996) First-pass metabolism of midazolam by the human intestine. *Clin Pharmacol Ther* **60:**14-24.

Robinson MD, McCarthy DJ, and Smyth GK (2010) edgeR: a Bioconductor package for differential expression analysis of digital gene expression data. *Bioinformatics* **26:**139-140.

Robinson MD and Oshlack A (2010) A scaling normalization method for differential expression analysis of RNA-seq data. *Genome Biol* **11:**R25.

Rossi G, Manfrin A, and Lutolf MP (2018) Progress and potential in organoid research. *Nat Rev Genet* **19:**671-687.

Sato T, Stange DE, Ferrante M, Vries RGJ, van Es JH, van den Brink S, van Houdt WJ, Pronk A, van Gorp J, Siersema PD, and Clevers H (2011) Long-term Expansion of Epithelial Organoids From Human Colon, Adenoma, Adenocarcinoma, and Barrett's Epithelium. *Gastroenterology* **141:**1762-1772.

Vernetti L, Gough A, Baetz N, Blutt S, Broughman JR, Brown JA, Foulke-Abel J, Hasan N, In J, Kelly E, Kovbasnjuk O, Repper J, Senutovitch N, Stabb J, Yeung C, Zachos NC, Donowitz M, Estes M, Himmelfarb J, Truskey G, Wikswo JP, and Taylor DL (2017) Functional Coupling of Human Microphysiology Systems: Intestine, Liver, Kidney Proximal Tubule, Blood-Brain Barrier and Skeletal Muscle. *Sci Rep* **7:**42296.

CHAPTER 4. UTILIZING SINGLE CELL RNA-SEQ DECONVOLUTION TO ASCERTAIN CELL TYPE PROPORTIONS IN DIFFERENTIATED AND UNDIFFERENTIATED ENTEROID MONOLAYER CULTURES

4.1. INTRODUCTION

In the previous chapter, the development and characterization of human enteroid monolayers as an *in vitro* model of the human intestine was explored. However, a question remains – what cell types are present within our differentiated enteroid monolayer cultures and what are their proportions. To answer a question like this, researchers may opt towards a flow cytometry approach – which utilizes fluorophore conjugated antibodies against specific cell antigens to identify and quantify cell types present within a sample (McKinnon, 2018). While a powerful and highly utilized technique, the reliance on antigen-based identification faces challenges including: 1. Reliance on known antigen markers (i.e., biased against rare or unknown cell types), 2. Treatment-driven changes in antigen expression, 3. *In vivo* antigen expression not aligning with *in vitro* antigen expression, and 4. Cell-type limitations in antibody multiplexing and gating strategy (Drescher et al., 2021).

Another approach to identify and quantify cell types present within a sample is single cell RNA sequencing (scRNA-seq) which utilizes RNA-seq technology on isolated single cells from a sample to identify the transcriptome of individual cells within a sample. Subsequent data analysis and bioinformatics allows researchers to identify cell clusters based on gene expression patterns and these clusters can be identified based on marker gene analysis (Andrews et al., 2021). This approach identifies cell clusters without the *a priori* knowledge of cell-specific antigens – allowing researchers to identify rare or previously unknown cell types (Haque et al., 2017). Additionally, cell-specific transcriptional responses to a treatment can be ascertained using this technique, providing unique insight on the cellular dynamics of a given treatment. While scRNA-seq methods are advancing (Svensson et al., 2018), they generally include a loss of 40% or greater of input cells, can create biases based on cell size, require a cell number that may exceed *in vitro* sample cell number, and are significantly more expensive than other techniques (Li and Wang, 2021). To overcome these limitations, researchers have developed cellular deconvolution pipelines, which utilize published reference scRNA-seq datasets to ascertain the cell types present within a bulk RNA-seq sample and quantify their proportions based on transcriptome contribution (Nguyen et al., 2024). An important assumption in deconvolution techniques is that all cell types express the same amount of RNA, such that if the deconvolved transcriptome is reported to be 50% cell X and 50% cell Y, the sample would be 50% cells of cell-type X and 50% cells of cell-type Y. However, it is more accurate to report that 50% of the transcriptome is from cell-type X and 50% of the transcriptome is from cell type Y. This may be important in contextualizing finding from diverse cell samples – as different cells may not express the same amount of RNA (Hippen et al., 2023).

The general steps of reference-based cellular deconvolution are; (1) scRNA-seq data processing and cell type identification through clustering and manual annotation; (2) generation of a signature matrix that represents the transcriptome of each cell type; and (3) bulk sample deconvolution to ascertain cell types and relative abundance in unknown samples of interest.

The first step in the deconvolution pipeline involves processing the published raw scRNA-seq counts datasets so they can be utilized for cell type identification. In general, this step is performed as the authors of the reference data performed their analysis to eliminate potential biases. Following dataset QC, count normalization, and data scaling, cell types are identified based on variable gene analysis and marker gene expression. An important aspect of scRNA-seq datasets is the large numbers of technical zeros or “dropouts”, leading to upwards of 90% of a given dataset containing zeros which can make further data analysis challenging (Qiu, 2020). Dropouts refer to when an expressed transcript is not detected in a given cell and are distinct from true biological zeros, where a gene is not expressed and thus is not measured. To deal with this phenomenon, several “imputation” methods have been developed which aim to reduce technical zeros in a scRNA-seq dataset while maintaining true biological zeroes (Hou et al., 2020). The imputation methods fall under three general categories to impute dropout gene expression: (1) those which model scRNA-seq data sparsity with probabilistic models (e.g., SAVER) (Huang et al., 2018); (2) those which adjust values by smoothing/diffusing gene expression values for cells with similar expression profiles (e.g., MAGIC) (van Dijk et al., 2018); and (3) those which utilize low rank approximations of data followed by adaptive thresholding to restore biological zeros (e.g., ALRA) (Linderman et al., 2022).

The second step of deconvolution involves generating a signature gene matrix for each cell type. Typically, this incorporates specific marker genes for each cell type based on variable gene expression analysis and averaging those gene expression values for each cell in a given cell type (Im and Kim, 2023). Following the generation of a signature matrix, deconvolution can be achieved by utilizing the signature matrix compared to the bulk RNA-seq to estimate cell type proportions within a given sample. This can be represented mathematically as the following equation:

$$M\alpha = b$$

where M is an n x m signature matrix of cell-type specific gene expression averages with n genes and m cell types. The term α is an m-length vector of the relative proportions of cell types within a bulk RNA-seq dataset, where the sum of the elements of α is one. The term b is an m-length vector of gene expression from the bulk RNA-seq dataset. Given M and b, the goal of deconvolution is to estimate α (Nguyen et al., 2024). There are several different deconvolution algorithms available to achieve the estimate of α. All algorithms discussed in this chapter generally use linear models to estimate α by minimizing the total squared absolute error, including ordinary least squared (OLS) approach, a dampened weighted least squares (DWLS) approach, and support vector regression (SVR and v-SVR) approach (Newman et al., 2019; Tsoucas et al., 2019).

This chapter will explore the utility of cellular deconvolution to predict the cell type proportions in our established human enteroid monolayer cultures. It will focus on enterocytes, goblet cells and proliferating cells, as these hold the greatest interest for DMET applications of our *in vitro* model. Three publicly available human adult intestine scRNA-seq datasets were utilized for this analysis. The impact of scRNA-seq dataset imputation using two imputation methods (ALRA and SAVER) compared to non-imputed datasets was assessed by running cellular deconvolution on pseudobulk data, where cell type proportions were known. Along with the various imputation methods, four deconvolution methods (OLS, DWLS, SVR, and v-SVR – using CIBERSORTx) were compared with respect to their accuracy to deconvolute pseudobulk sample data with known cell proportions. Following benchmarking, a cellular deconvolution pipeline was run on the bulk RNA-seq samples from undifferentiated intestinal organoids and 21-day differentiated monolayers generated in the previous chapter.

4.2. METHODS

4.2.1. Bulk RNA-seq datasets for intestinal organoids.

The bulk RNA-seq sample processing for intestinal organoids was described in our recent publication (Arian et al., 2024) and was submitted through Gene expression omnibus (GEO) repository and is publicly accessible through the access number GSE253641. The dataset consists of matched undifferentiated and 21-day differentiated enteroid samples from 3 donors (Donor 1 - 27 year old, female; Donor 2 - 81 year old, female; Donor 3 - 25 year old, male) derived from the duodenum.

4.2.2. Adult human intestine scRNA-seq datasets.

Three scRNA-seq datasets were utilized for deconvolution. The first scRNA-seq dataset from Elmentaite et al., termed paper 1, was accessed via the Gut Cell Axis (https://www.gutcellatlas.org/) (Elmentaite et al., 2021). The original dataset consisted of samples from 41 subjects from 6-weeks to 75 years of age and encompassed samples from the small intestine and large intestine from healthy subjects and pediatric subjects with Crohn's disease. The dataset was filtered to remove all fetal and pediatric subjects and to only include healthy adult samples from the small intestine, leading to a final demographic of 5 subjects (1 female, 4 male) from 20-70 years of age.

The second dataset from Burclaff et al., termed paper 2, was accessed through the GEO repository under the access number GSE185224 (Burclaff et al., 2022). The dataset consisted of 3 male adult donors from 29-53 years of age and encompassed samples from the small intestine and colon.

The third dataset from Zwick et al., termed paper 3, was accessed through CELLxGENE (https://cellxgene.cziscience.com/collections) (Zwick et al., 2024). The dataset used for analysis consisted of one adult donor aged 30 and encompassed samples from the small intestine.

A summary of the demographic information from each dataset is supplied in **Table 4.1**.

4.2.3. scRNA-seq dataset processing.

All data processing was performed as each reference described in their publication to eliminate potential biases. Data processing for all sample sets was performed utilizing Seurat (Hao et al., 2024) in RStudio (R. Posit Software, PBC, Boston, MA). In general, cells with too few genes/counts were excluded as low-quality cells (or empty droplets) will have few genes. Additionally, cells with too many genes/counts are excluded as this may indicate that more than one cell is in a droplet for sequencing – these are referred to as "doublets" or "multiplets". The percentage of mitochondrial genes are filtered out because cells with a high proportion of mitochondrial gene reads relative to non-mitochondrial gene reads indicate dying cells.

The data processing for paper 1 was performed as described in the publication (Elmentaite et al., 2021). Briefly, genes that were expressed in 3 or less cells were excluded from subsequent analysis. Additionally, cells that contained less than 500 genes, contained a doublet score of more than 25%, and had a >50% mitochondrial reads were excluded from subsequent analysis. These filtering steps decreased the total number of cells present in the dataset from 16,692 cells to 16,613 cells. The resulting dataset was normalized using the NormalizeData function using the "LogNormalize" method and a scale factor of 1×10^6. Variable features were then identified using the FindVariableFeatures function using the "vst" selection method. The data was scaled using the ScaleData function with the following variables regressed: cell cycle score, the percentage of mitochondrial genes, and unique molecular identifiers (UMIs). Data from samples processed in different batches were then merged with the harmony R package (Korsunsky et al., 2019) to eliminate batch effects. Cells were then clustered using the FindNeighbors and FindClusters functions and marker genes were then identified using the FindMarkers function. Cell types were identified via marker genes noted from the source paper and the identification was compared to the source paper's cell identification. Following cell type identification, CPM normalized data was calculated by using the NormalizeData function on the counts data using the "RC" normalization method and a scale factor of 1 x 10^6 – the CPM data was used for subsequent analysis.

The data processing for paper 2 was performed as described in the publication (Burclaff et al., 2022). Briefly, for donors 1 and 3, cells that contained less than 500 genes, more than 75% mitochondrial reads, less than 3000 counts, or more than 50000 counts were filtered out of subsequent analysis. For donor 2, cells that contained less than 800 genes, more than 50% mitochondrial reads, and less than 1000 counts or more than 30000 counts were filtered out of subsequent analysis. These filtering steps decreased the total number of cell from 7,815 cells to 5,595 cells for donor 1, from 9,389 cells to 8,748 cells for donor 2, and from 5,981 cells to 4,816 cells for donor 3. The resulting filtered datasets were then combined and normalized using the NormalizeData function using the "LogNormalize" method and a scale factor of 1 x 10^6. Variable features were then identified using the FindVariableFeatures function using the "vst" selection method. The data was scaled using the ScaleData function with the following variables regressed: gene expression count, percent mitochondrial reads, and cell cycle score. Data from samples processed in different batches were then merged with the harmony R package to eliminate batch effects (Korsunsky et al., 2019). Cells were then clustered using the FindNeighbors and FindClusters functions and marker genes were then identified using the FindMarkers function. Cell types were identified via marker genes noted from the source paper and the identification was compared to the source paper's cell identification. Following cell type identification, CPM normalized data was calculated by using the NormalizeData function on the counts data using the “RC” normalization method and a scale factor of 1 x 10^6 – the CPM data was used for subsequent analysis.

The data for paper 3 was available pre-processed by the authors of the publication (Zwick et al., 2024) with cell types identified. CPM normalized data was calculated by using the NormalizeData function on the counts data using the “RC” normalization method and a scale factor of 1 x 10^6 – the CPM data was used for subsequent analysis.

A summary of the cell count and cell proportion information for each dataset is provided in **Table 4.2.**

4.2.4. scRNA-seq imputation.

ALRA imputation was performed for each dataset in R using the ALRA package as described in their publication (Linderman et al., 2022). Briefly, the CPM dataset for each paper was transposed and the alra function was used on the transposed data using the default settings.

SAVER imputation was performed for each dataset in R using the SAVER package as described in their publication (Huang et al., 2018). Prior to running saver imputation, the datasets were randomly down sampled to 1/3rd of their size due to computational limitations. SAVER was run on CPM data using default parameters with size.factor set to 1.

4.2.5. Cell reference matrix and pseudobulk sample generation.

Cell reference matrices were generated from each paper and each imputation method for a total of 9 cell reference matrices (3 cell reference matrices per paper). A total of 5 pseudobulk samples, with varying known cell proportions, were generated from each paper and each imputation method, utilizing cells that were not used for the cell reference matrices, for a total of 45 pseudobulk samples (15 pseudobulk samples per paper).

A total of 300 cells from each cell type were used for cell reference matrix generation and were randomly sampled from the CPM dataset. If a given cell type did not have 300 total cells for the reference matrix generation, the total number of cells in that cell type was included to generate the cell reference matrix. The cells pulled for the cell reference matrix were then removed from the original dataset so they would not be included in the pseudobulk sample generation. The final cell reference matrix was a data matrix with the rows as gene names and columns as cell types and data entered as CPM.

Pseudobulk generation was performed on the dataset with cell reference matrix cells removed by randomly sampling a set number of cells from each cell type to generate a mixture of cells with known cell type proportions. The CPM expression for each gene was then averaged to generate a dataset that mimics a bulk RNA-seq dataset. For the five pseudobulk samples created from each dataset and each imputation method, the proportion of enterocytes varied as follows: 10%, 25%, 50%, 75%, and 90%. The proportion of other cell types varied for each dataset based on the number of each cell type present in each dataset.

4.2.6. Signature matrix generation.

For CIBERSORTx deconvolution, signature matrix generation was achieved using the CIBERSORTx online tool (https://cibersortx.stanford.edu/index.php) based on the publication from Newman et al. (Newman et al., 2019). Signature matrices were generated from each cell reference matrix utilizing the default options on the CIBERSORTx analysis.

For DWLS, OLS, and SVR deconvolution, signature matrix generation was achieved using the DWLS package in R (Tsoucas et al., 2019). Signature matrices were generated using the buildSignatureMatrixMAST function using Log_2CPM data from the previously generated cell reference matrices. The maximum number of genes used in generating the signature matrices set was to 300.

4.2.7. Cellular deconvolution.

For CIBERSORTx deconvolution, signature matrices and pseudobulk samples were input into CIBERSORTx. For deconvolution on pseudobulk samples and signature matrices generated from the same dataset, deconvolution was run without enabling batch correction and permutations were set to 500 for significance. For deconvolution on pseudobulk samples and signature matrices generated from separate datasets, deconvolution was run with S-mode batch corrections enabled and permutations were set to 500 for significance. For deconvolution on organoid RNA-seq bulk samples and signature matrices generated from each dataset, deconvolution was run with S-mode batch corrections enabled and permutations were set to 500 for significance. For DWLS, OLS, and SVR, pseudobulk and bulk sample data was deconvoluted using the solveDampenedWLS, solveOLS, and solveSVR functions, respectively, using the signature matrices prepared as described above.

4.3. RESULTS

4.3.1. Imputation of scRNA-seq datasets.

The impact of two imputation methods, ALRA and SAVER, on scRNA-seq datasets is shown in **Figure 4.1** and **Table 4.3**. Both imputation methods resulted in a marked decrease in the percentage of total zero values in the scRNA-seq datasets, which ranged from 92-81% for non-imputed data, 69-56% for ALRA-imputed data, and 31-1% in SAVER-imputed data. Cell marker gene analysis for enterocytes, goblet cells, and proliferating cells demonstrates that specific marker genes for each cell type display a decrease in the percentage of zero values following imputation. Importantly, the genes that were not marker genes for each cell type did not have a similar decrease in the percentage of zero values following imputation.

4.3.2. Cellular deconvolution of pseudobulk sample datasets.

The results of cellular deconvolution on pseudobulk samples using signature matrices derived from the same datasets as the pseudobulk samples are shown in **Figure 4.2** and **Table 4.4.** Results include four different deconvolution methods (CIBERSORTx, DWLS, OLS, and SVR) for non-imputed, ALRA-imputed, and SAVER-imputed datasets to predict enterocyte, goblet cell, and proliferating cell proportions. The proportion of enterocytes was well predicted by most methods, with DWLS deconvolution on ALRA-imputed data performing the best with a mean absolute percent error (MAPE) of approximately 6%. CIBERSORTx with SAVER-imputed data performed the best for the prediction of goblet cells, with a MAPE of approximately 3%. Interestingly, the proportion of proliferating cells was predicted poorly across all deconvolution and imputation methods – with DWLS deconvolution on ALRA-imputed data performing the best with a MAPE of approximately 38%.

The results of cellular deconvolution on pseudobulk sample datasets using signature matrices derived from different datasets than the pseudobulk samples are shown in **Figure 4.3** and **Table 4.5**. In general, all cell types were predicted with lower accuracy when using signature matrices from different datasets than the pseudobulk samples. The methods that had the best accuracy for enterocyte deconvolution were DWLS with ALRA-imputation and OLS with ALRA-imputation with MAPE values of approximately 19.8% and 21.1%, respectively. Both DWLS with ALRA-imputation and OLS with ALRA-imputation performed the best for goblet cell deconvolution with MAPE values of approximately 22.4% and 17.9%, respectively. All methods performed poorly for proliferating cell deconvolution, with all MAPE values above 95%.

A representative example of deconvolution results for a pseudobulk sample made with complete scRNA-seq dataset from paper 2 is shown in **Figure 4.4** and **Table 4.6**. The DWLS deconvolution method with ALRA imputation was chosen for this example, as this model performed the best for predicting enterocytes and performed well for predicting goblet cells. Similar to the results above, the proportions of enterocytes and goblet cells were well predicted – with percent error values of 6.7% and 0.6%, respectively. The proportions of proliferating cells and other cells (which include enteroendocrine cells, tuft cells, BEST4 cells, Paneth cells, and M cells) had substantially greater error – with percent error values of 515% and 42.3%, respectively.

4.3.3. Intestinal organoid RNA-seq deconvolution.

The cellular deconvolution to predict the enterocyte and goblet cell proportions of undifferentiated intestinal organoid and differentiated enteroid monolayers cultured for 21-days is shown in **Figure 4.5**. Proliferating cells are not reported due to a lack of accuracy in the pseudobulk sample deconvolution benchmarking analysis. However, they were included as a cell type category (along with “other” cell types) when deconvolution was performed, such that total cell abundances at the end of a computational step always added up to 100%. Results that are presented utilize the DWLS deconvolution methods with ALRA-imputed signature matrices from the three scRNA-seq datasets. They indicate that the proportion of enterocytes increased from undifferentiated organoids to differentiated enteroid monolayers by approximately 7-fold for donors 1 and 3 (from approximately 2% to 14% enterocytes) and 2-fold for donor 2 (from approximately 2% to 4% enterocytes), which corroborates single transcript and enzyme activity results from our earlier publication (Arian et al., 2024). Interestingly, deconvolution results using the signature matrix derived from the paper 3 dataset resulted in 0% enterocytes in all samples – which is unlikely, due to functional results from our previous publication. Of note, RNA-Seq data in this paper was generated from a single tissue donor. Thus, deconvolution results without the paper 3 dataset were generated and are shown in **Figure 4.6**. These results show a higher proportion of enterocytes in both the undifferentiated (ranging from approximately 1% to 3%) and differentiated states (ranging from approximately 2% to 20%) and a lower standard deviation for enterocytes across all samples, but little to no change in goblet cell proportions or standard deviation.

4.4. DISCUSSION

The development of cellular deconvolution methods to garner cellular information from available bulk RNA-seq data is an exciting prospect for researchers, as there is an abundance of publicly available bulk RNA-seq datasets to which these methods can be applied without encumbering the cost of scRNA-seq studies. Work in this chapter explores the utility of cellular deconvolution, utilizing three publicly available scRNA-seq datasets, to extract cell type information from bulk RNA-seq datasets of undifferentiated intestinal organoids and differentiated enteroid monolayers cultured for 21-days. The scRNA-seq datasets used for these analyses encompassed data from 9 total donors over a wide range of ages from 20-70 years of age, which relatively closely matched the age ranges of the intestinal organoid donors, which ranged from 25-81 years of age. Interestingly, the cell type proportions had substantial variation across the three organoid monolayer datasets – for example, the proportion of enterocytes to total cells ranged from 33% to 58% and the proportion of goblet cells ranged from 1.5% to 30%. Variability in the *in vivo* cell proportions across different datasets and donors is not unexpected given the impact of certain factors, such as diet (Cheng et al., 2019), on intestinal cell type differentiation.

We next assessed the impact of scRNA-seq imputation on subsequent deconvolution results. Imputation of scRNA-seq datasets allows for the recovery of technical zeros, or “dropouts”, while maintaining true biological zeros in scRNA-seq datasets. To achieve this, we utilized two highly utilized imputation methods, ALRA and SAVER (Huang et al., 2018; Linderman et al., 2022). Highlighting the high proportion of zeros in scRNA-seq datasets, the non-imputed datasets had high percentages of the datasets with zero values, ranging from 81% to 92%. Following ALRA-imputation, the percentage of zero values dropped substantially, ranging from 56% to 69%. SAVER-imputation resulted in a further decrease in the proportion of zero values, ranging from 1% to 31%. The extremely low proportion of zero values for the SAVER-imputed datasets suggests that true biological zeros were imputed to have expression values above zero. To explore this, we assessed the expression of cell type specific genes for enterocytes, goblet cells, and proliferating cells along with the expression of genes that are not expected to be expressed in these cell types in imputed and non-imputed datasets. These analyses demonstrate that ALRA- and SAVER-imputation results in a decreased proportion of zero values for cell type specific genes for enterocytes, goblet cells, and proliferating cells while maintaining zero values for genes that are not expected to be expressed in these cell types.

To benchmark the deconvolution methods, we performed cellular deconvolution on pseudobulk samples derived from the three scRNA-seq datasets. These pseudobulk samples had known cell type proportions and were created with varying proportions of cell types. For this analysis, we focused on varying the proportion of enterocytes in each pseudobulk sample from each paper – with cell proportions of 10%, 25%, 50%, 75%, and 90% – where other cell types varied based on the cell abundance in each dataset using each imputation method (no imputation, ALRA-imputation, SAVER-imputation) and four deconvolution methods (CIBERSORTx, DWLS, OLS, and SVR). The signature matrices used for these analyses were also derived from the three scRNA-seq datasets, but importantly did not utilize the same cells that were used for the generation of pseudobulk samples. Again, we focused on the prediction accuracy of enterocytes, goblet cells, and proliferating cells, as these cell types are of the most interest for DMET applications of our intestinal organoid model. Deconvolution results using signature matrices derived from the same datasets as the pseudobulk samples yielded relatively good predictions for enterocytes and goblet cells for most imputation and deconvolution methods, resulting in MAPE values of 6% and 3%, respectively. The deconvolution and imputation methods that performed the best for enterocytes and goblet cells were DWLS deconvolution on ALRA-imputed datasets and CIBERSORTx deconvolution on SAVER-imputed datasets, respectively. Interestingly, the prediction of proliferating cells was substantially worse for all methods, with all methods resulting in MAPE values greater than 35%.

To further benchmark the deconvolution pipeline, we performed deconvolution on pseudobulk samples utilizing signature matrices derived from different datasets than the pseudobulk samples. This is an important benchmarking step, as this assessment more closely matches the deconvolution process we expect from the intestinal organoid RNA-seq datasets, given that the signature matrices are derived from cells that are completely independent of the bulk samples. While the deconvolution results from these had lower accuracy than the previous deconvolution results, the prediction of enterocytes and goblet cells still displayed acceptable accuracy for the DWLS and OLS deconvolution on ALRA imputed datasets, all of which had MAPE values below 25%. Similar to the previous results, the prediction of proliferating cells was substantially worse – with MAPE values above 95% for all deconvolution and imputation methods. These findings suggest that the DWLS and OLS deconvolution methods using ALRA-imputed signature matrices provide the best accuracy for predicting enterocyte and goblet cell proportions in our intestinal organoid RNA-seq datasets.

As a final benchmark, we performed deconvolution on a pseudobulk sample, generated from paper 2, which contained all cells from the scRNA-seq dataset, excluding the cells used to generate the signature matrix for this dataset. The DWLS deconvolution method using ALRA imputed data was chosen for this deconvolution, as this model provided the best prediction for enterocyte proportions and good predictions for goblet cell proportions. Results were consistent with the previous benchmarking, where enterocyte and goblet cell proportions were predicted with high accuracy (6.7% and 0.6% error, respectively), while proliferating cells and other cells had substantially worse predictions (515% and 42.3% error, respectively).

A potential explanation for the poor prediction of proliferating cell abundances lies in the common practice in scRNA-seq workflow to regress out cell cycle phase prior to clustering and subsequent cell identification and deconvolution – this is of note, as all of our reference scRNA-seq datasets employed this step in their data processing workflow. The rationale behind the practice is to remove any variation that results from cell cycle status. While this may be appropriate for cells with low rates of division/quiescent cells, like enterocytes, this may not be appropriate for cells that are rapidly dividing, like intestinal stem cells and transit amplifying cells. Future applications of deconvolution should explore the impact of removing this step from the scRNA-seq data analysis workflow on the subsequent prediction of proliferating cell proportions in pseudobulk/bulk sample analysis. The rationale for including these cells is based on the fact that we can maintain enteroid monolayers for over 6 weeks while also achieving cellular differentiation. Given the relatively short lifespan of an enterocyte, our cultures must retain proliferating crypt cells to support self-renewal of enterocytes.

Due to the low prediction accuracy throughout the benchmarking of these methods, proliferating cell proportions were not included in the subsequent table of enteroid monolayer RNA-seq deconvolution results. Additionally, other cells were not included as these cells are not the focus of our model. Deconvolution results demonstrated that undifferentiated intestinal organoids have a low proportion of enterocytes, of less than 2%, that increased approximately 7-fold following differentiation for donors 1 and 3 and 2-fold for donor 2, with donor 2 showing the lowest abundance of enterocytes. These results corroborate the CYP3A activity results from our previous study (Arian et al., 2024), where donor 2 had substantially lower CYP3A activity compared to the other two donors, which is reflective of the proportion of enterocytes between the three donors. Interestingly, the fold increase in enterocytes based on deconvolution does not match the fold increase in CYP3A4 mRNA from our RNA-seq analysis (Arian et al., 2024), which resulted in a 16-fold increase in expression following differentiation. This is likely due to the large number of genes (300) used in the signature matrices for each cell type. This means that the increase in enterocytes represents an average increase in expression for these signature genes – where some signature genes (such as CYP3A4) may display greater fold changed than other signature genes from undifferentiated to differentiated states, resulting in this discrepancy.

Curiously, there was substantial variability in the prediction of enterocytes proportions between the three signature matrices used in the deconvolution. Notably, the deconvolution results utilizing the signature matrix derived from paper 3 resulted in a prediction of 0% enterocytes for all organoid monolayer samples. These results are unlikely given the CYP3A activity and RNA-seq results from our previous publication (Arian et al., 2024). Removing paper 3 scRNA results from our analysis yields less variable and moderately higher enterocyte proportions – where enterocyte proportions for undifferentiated organoids and differentiated enteroid monolayers were approximately 2.5% and 20%, respectively for donors 1 and donor 3. The proportion of enterocytes did not change following differentiation for donor 2, remaining at approximately 3%.

Additionally, the proportion of goblet cells did not change when the paper 3 scRNA results were removed from the analysis and remained consistent across all samples.

The proportion of enterocytes in the differentiated enteroid monolayer culture was lower than the proportion of enterocytes in the *in vivo* scRNA-seq datasets. This result is not unexpected, given that our enteroid differentiation protocol utilizes a differentiation medium that contains a low amount of the WNT3A growth factor – which could cause incomplete differentiation of stem cells into enterocytes. One would expect a higher proportion of enterocytes in enteroid monolayer cultures that were differentiated utilizing media that is completely devoid of WNT3A, though this differentiation protocol was not explored in our previous study. Despite a lower proportion of enterocytes in our culture relative to the *in vivo* (3-20% in differentiated enteroid monolayers compared to 33-58% in the scRNA-seq datasets), our differentiation protocol fits our purposes – as we have demonstrated pharmacokinetically appropriate drug metabolism while maintaining culture longevity of up to 6 weeks. However, the sub-physiological proportions of enterocytes in this model may impact the ability for this model to provide accurate predictions of pharmacokinetic parameters for *in vitro* to *in vivo* extrapolation using static or physiologically based pharmacokinetic (PBPK) models.

A limitation of this study is that we did not fully explore the ability of the various deconvolution methods to predict the proportion of rare cell types – such as tuft cells, enteroendocrine cells, Paneth cells, and M cells – in our culture. These cell types are important for normal intestinal physiology and response to pathogens but are not the focus of our model or our drug metabolism and transport studies to date, and thus were not explored. However, to fully assess the utility of the model, future studies should explore the predictions of these cell types, which would entail addressing the poor prediction results for proliferating cells. Another important limitation of our study is that the true proportions of cell types in our organoid monolayer culture were not known and thus the deconvolution results could not be benchmarked against the true cell proportion values. Future studies should employ flow cytometry or scRNA-seq to ascertain cell type proportions and compare these results to the predicted cell proportions from deconvolution.

In summary, results from the studies outlined in this chapter suggest that deconvolution of bulk RNA-seq samples utilizing publicly available scRNA-seq datasets may be a useful tool for predicting cell type abundances in complex intestinal *in vitro* cultures, but further validation is required. The DWLS deconvolution method, paired with ALRA-imputed signature matrices, imparted the best cell proportion predictions across all methods. Deconvolution of the intestinal organoid monolayer RNA-seq data confirmed the differentiation status of our enteroid monolayer cultures. Additional work is needed to refine the deconvolution methods to improve the cell proportion prediction of proliferating cells in our cultures. Additionally, the ability of these methods to predict the proportion of rare cell types requires further exploration.

Table 4.1. Dataset demographic information

Dataset	**Number of donors**	**Age (years)**	**Sex**	**Sample type**
Paper 1 (Elmentaite et al., 2021)	5	20-70	1 Female, 4 Male	Small intestine
Paper 2 (Burclaff et al., 2022)	3	29-53	3 Male	Small intestine and colon
Paper 3 (Zwick et al., 2024)	1	30	Male	Small intestine

Table 4.2. Cell proportions in dataset

Dataset	Total cell #	Enterocyte %	Goblet cells %	Proliferating cells %	EECs %	Paneth cells %	Tuft cells %	BEST 4 cells %	Other cells %
Paper 1	16,613	57.7%	1.5%	19.6%	0.2%	15.7%	0.5%	3.7%	1.1%
Paper 2	19,159	48.8%	13.6%	3.0%	1.1%	3.0%	5.6%	2.4%	22.4%
Paper 3	19,200	33.4%	19.8%	29.9%	4.1%	0.7%	4.4%	5.1%	2.6%

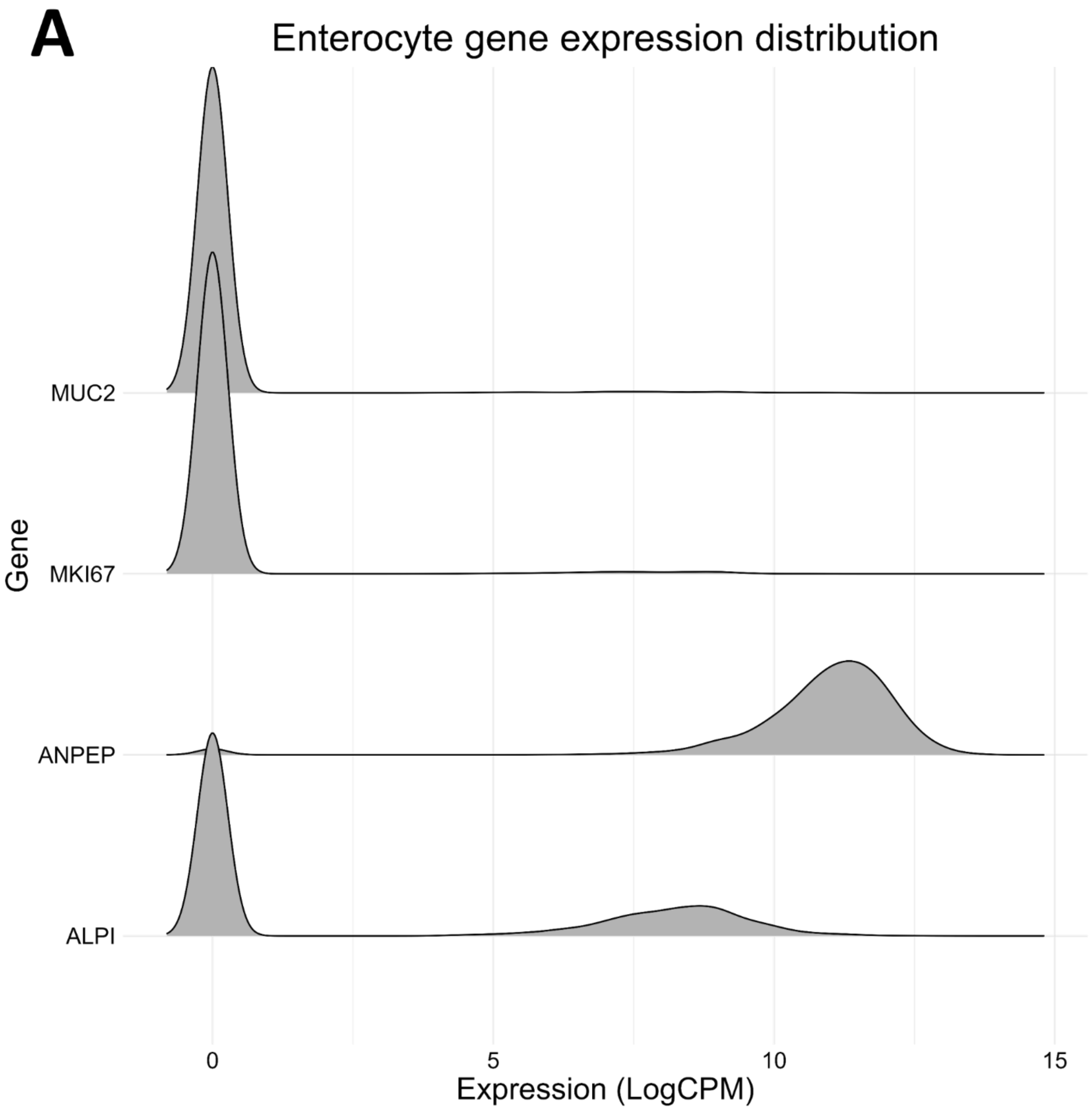
A
Enterocyte gene expression distribution
Gene
MUC2
MKI67
ANPEP
ALPI
0
5
10
15
Expression (LogCPM)

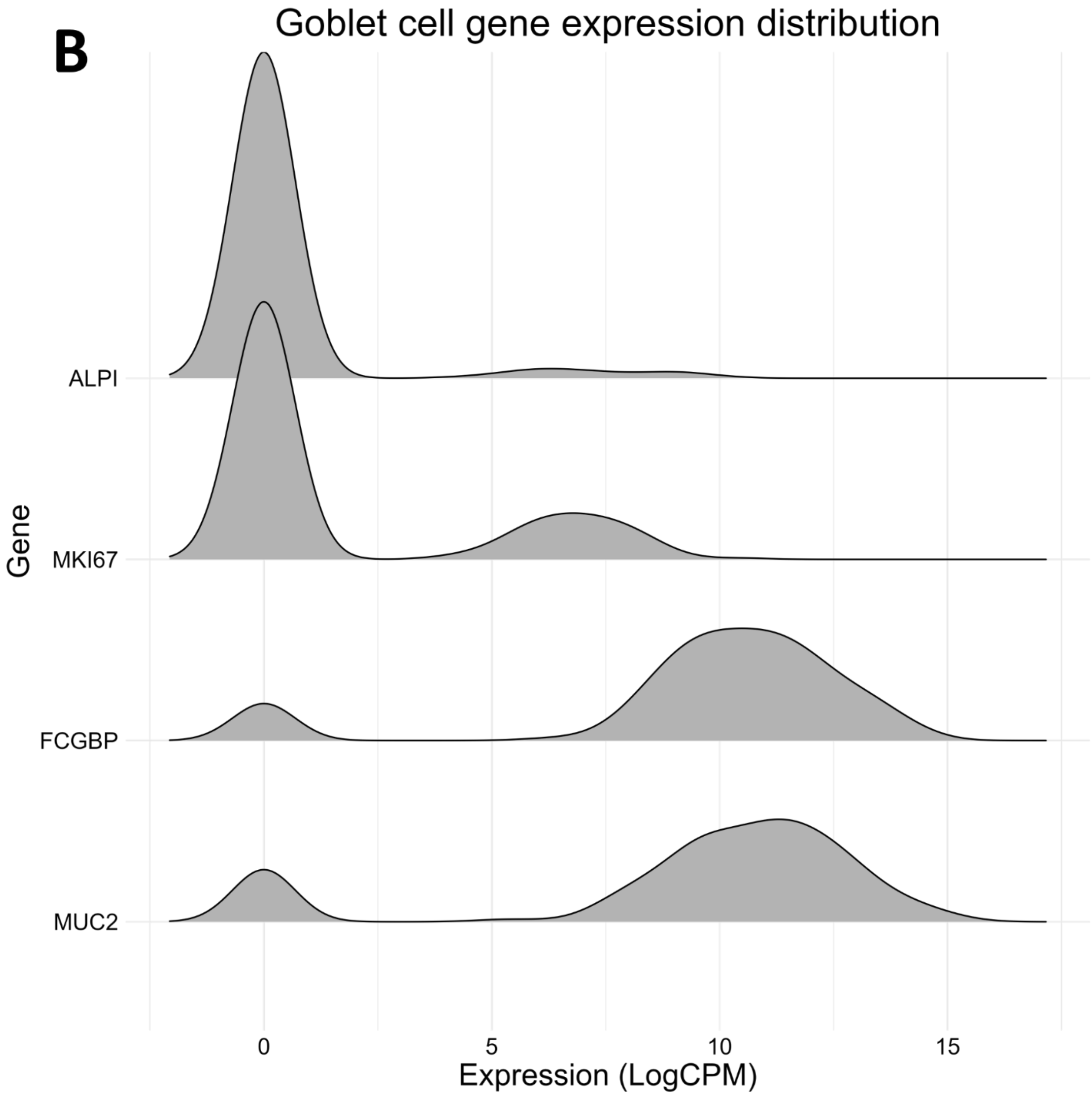
B
Goblet cell gene expression distribution
Gene
ALPI
MKI67
FCGBP
MUC2
0
5
10
15
Expression (LogCPM)

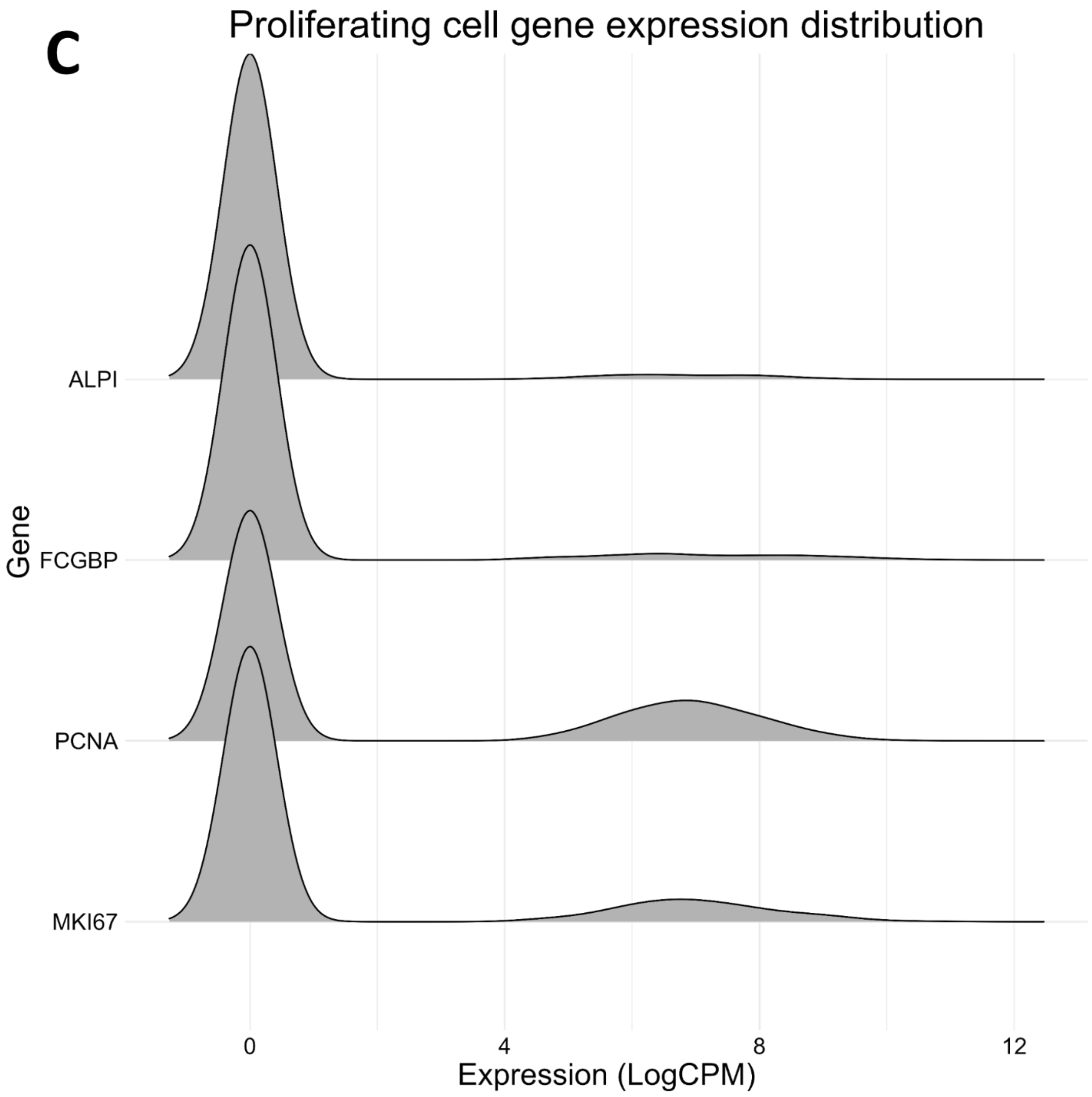
C
Proliferating cell gene expression distribution
Gene
ALPI
FCGBP
PCNA
MKI67
0
4
8
12
Expression (LogCPM)

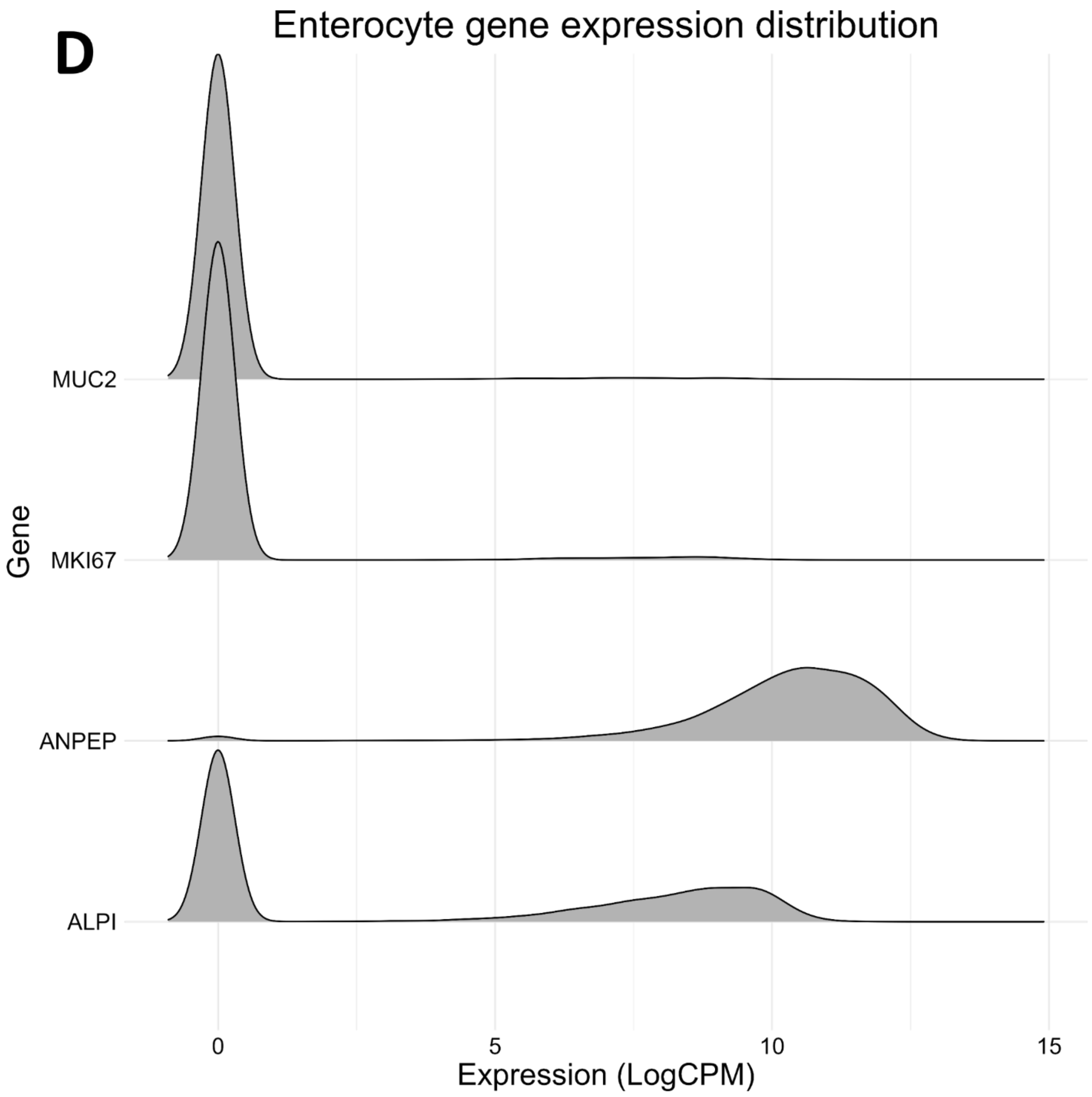
D
Enterocyte gene expression distribution
MUC2
MKI67
ANPEP
ALPI
Gene
0
5
10
15
Expression (LogCPM)

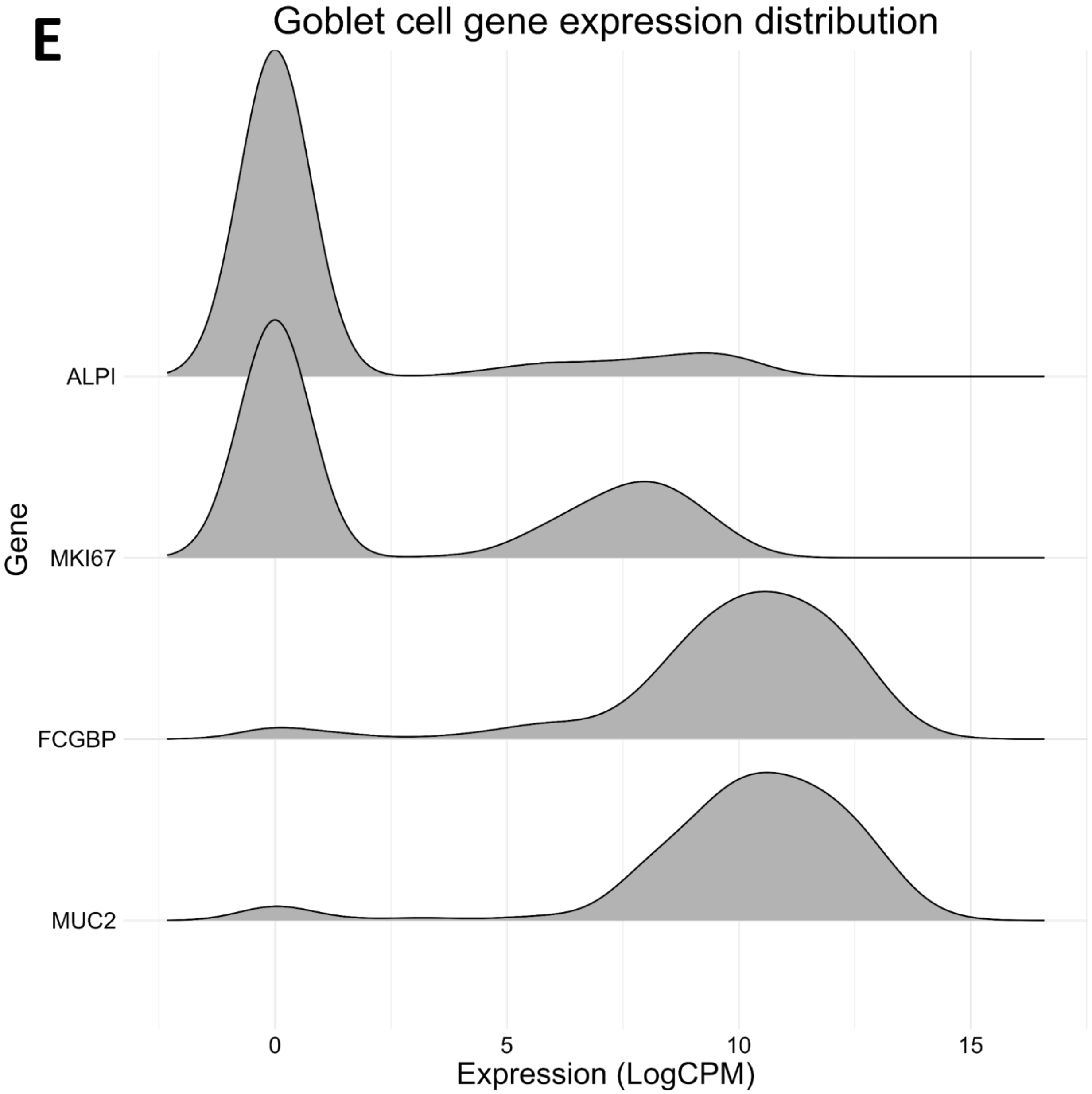
E
Goblet cell gene expression distribution
ALPI
MKI67
FCGBP
MUC2
Gene
0
5
10
15
Expression (LogCPM)

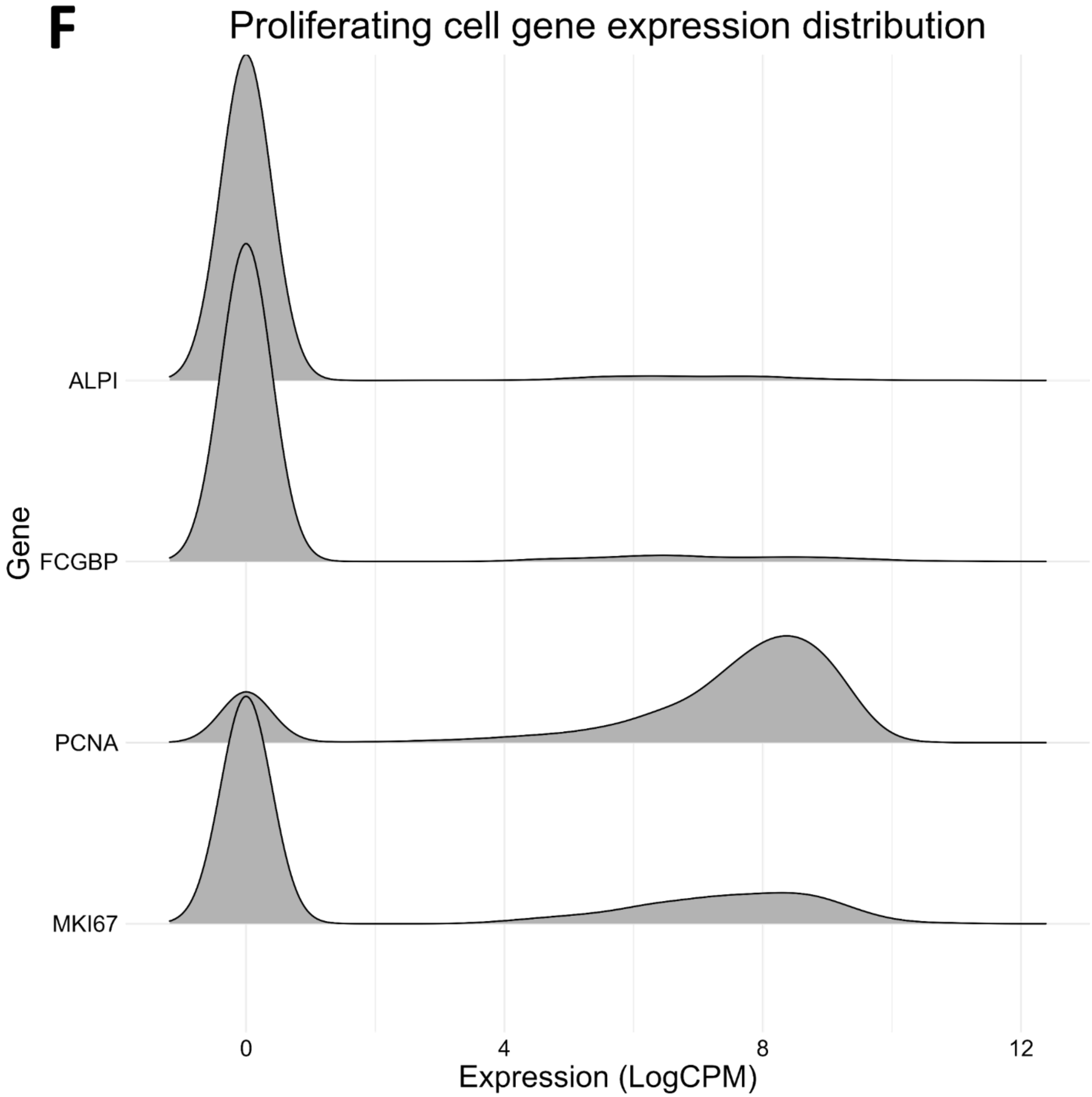
F
Proliferating cell gene expression distribution
Gene
ALPI
FCGBP
PCNA
MKI67
0
4
8
12
Expression (LogCPM)

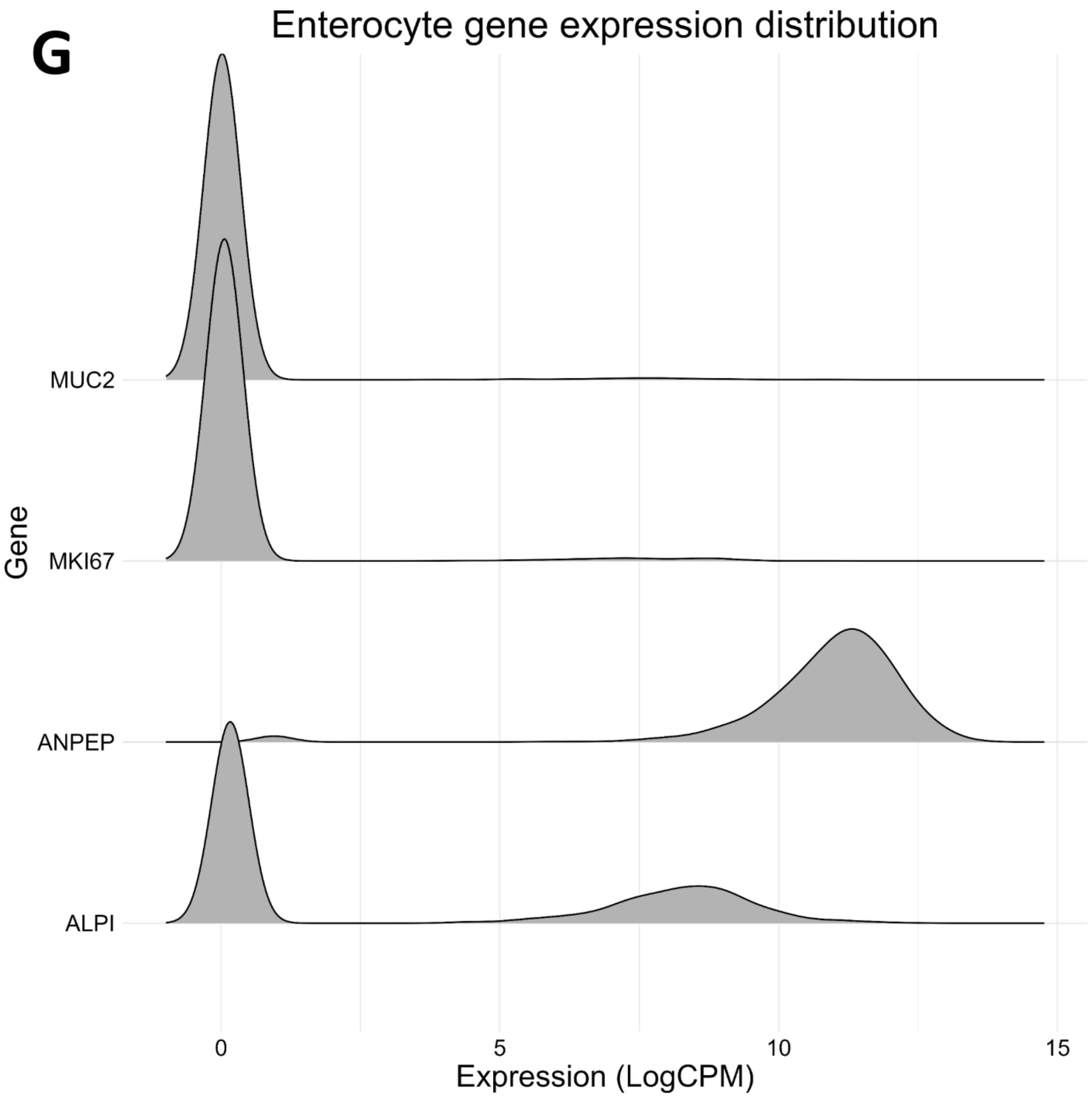
G
Enterocyte gene expression distribution
Gene
MUC2
MKI67
ANPEP
ALPI
0
5
10
15
Expression (LogCPM)

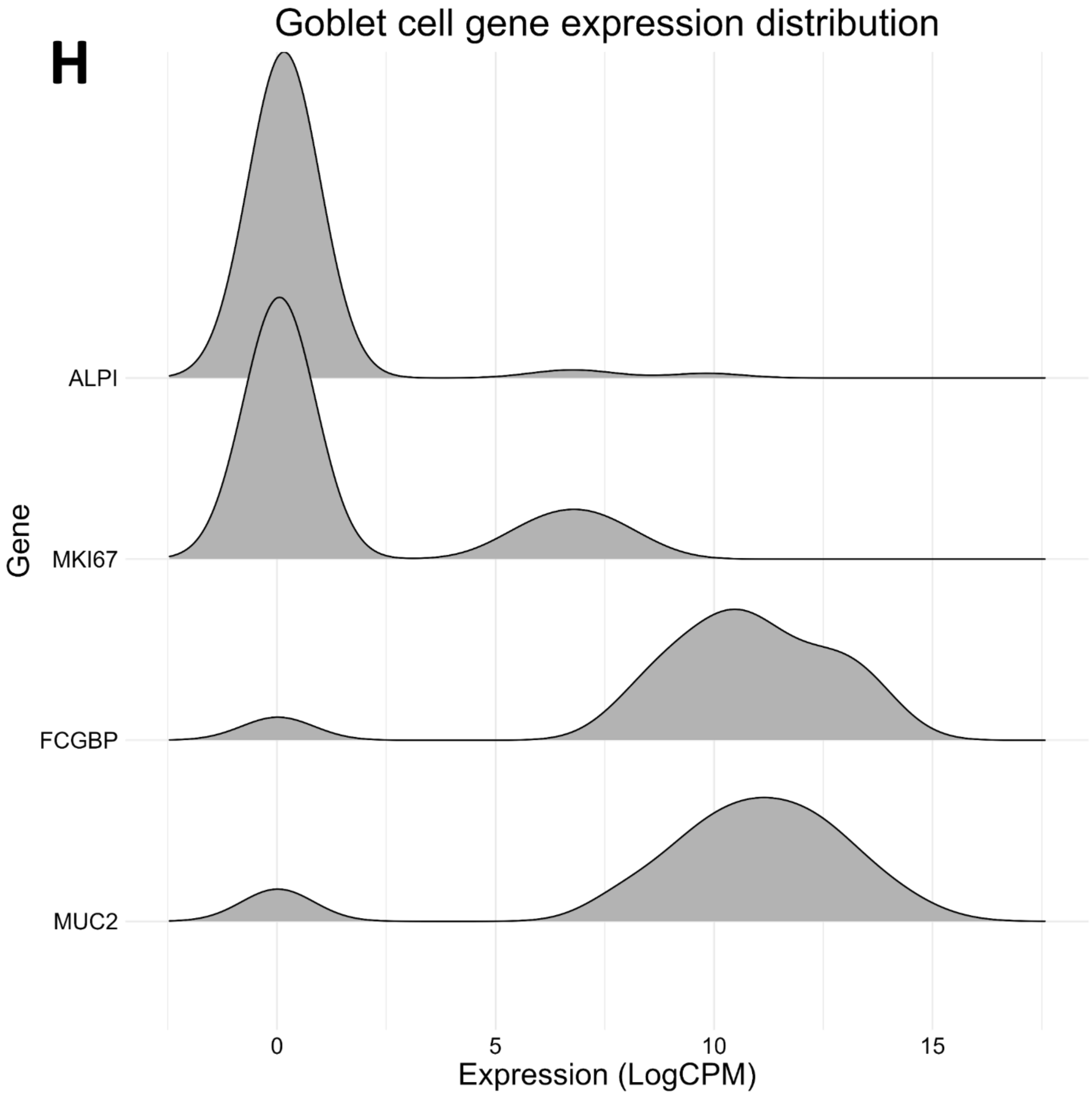
H
Goblet cell gene expression distribution
Gene
ALPI
MKI67
FCGBP
MUC2
0
5
10
15
Expression (LogCPM)

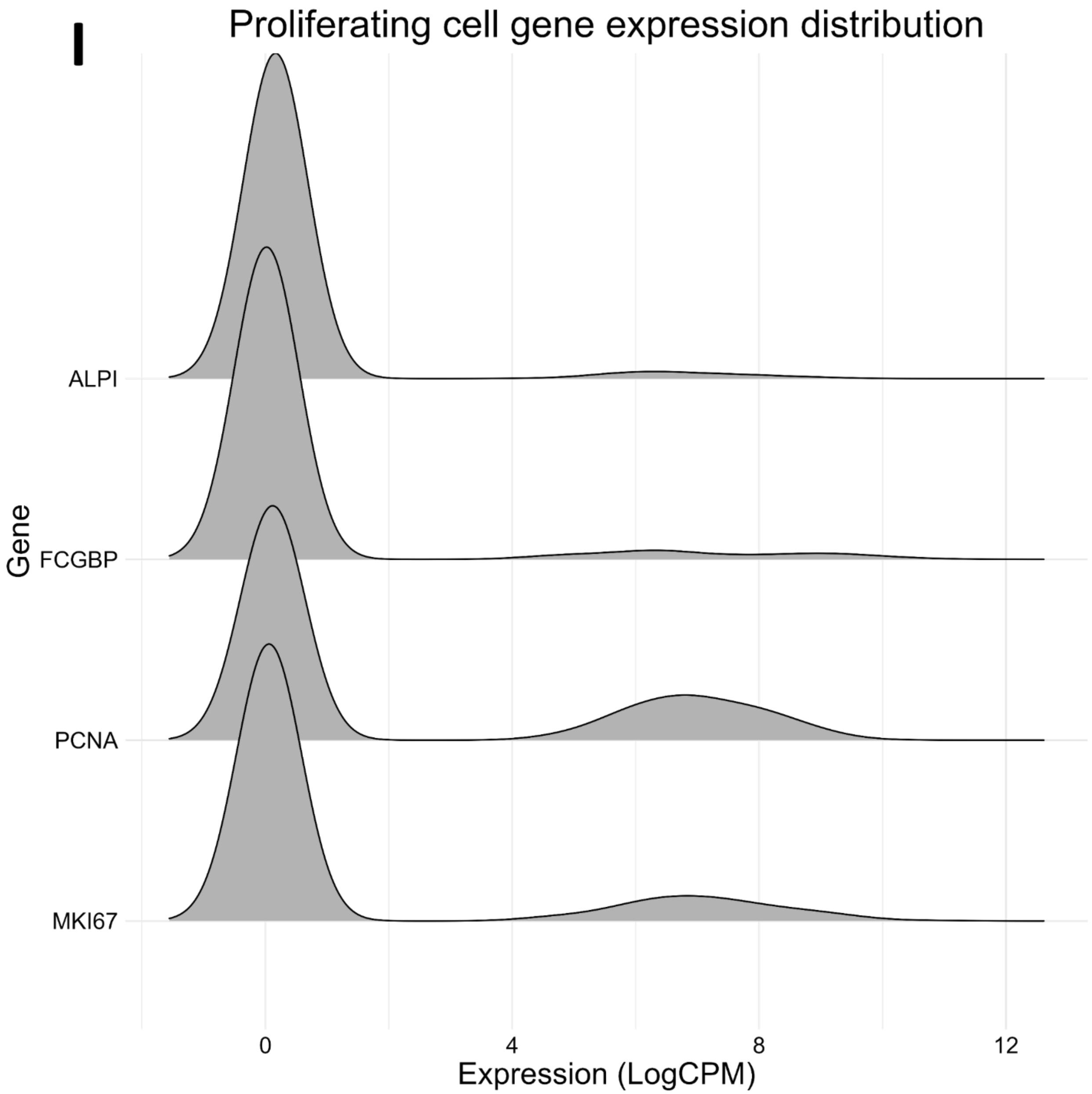

Figure 4.1. Imputation results on cell specific gene expression.

The distribution of cell specific gene expression for enterocytes, goblet cells, and proliferating cells for non-imputed (A-C), ALRA-imputed (D-F), and SAVER-imputed (G-I) datasets. Enterocyte results include enterocyte specific gene markers, ALPI and ANPEP, with non-enterocyte markers, MUC2 and MKI67. Goblet cell results include goblet cell specific gene markers, MUC2 and FCGBP, with non-goblet cell markers, ALPI and MKI67. Proliferating cell results include proliferating cell specific gene markers, MKI67 and PCNA, with non-proliferating cell markers, ALPI and FCGBP.

Table 4.3. Imputation results

Dataset	**No imputation %zeros**	**ALRA imputation %zeros**	**SAVER imputation %zeros**
Paper 1	92.2	61.8	2.3
Paper 2	92.2	68.9	30.8
Paper 3	81.3	55.6	0.62

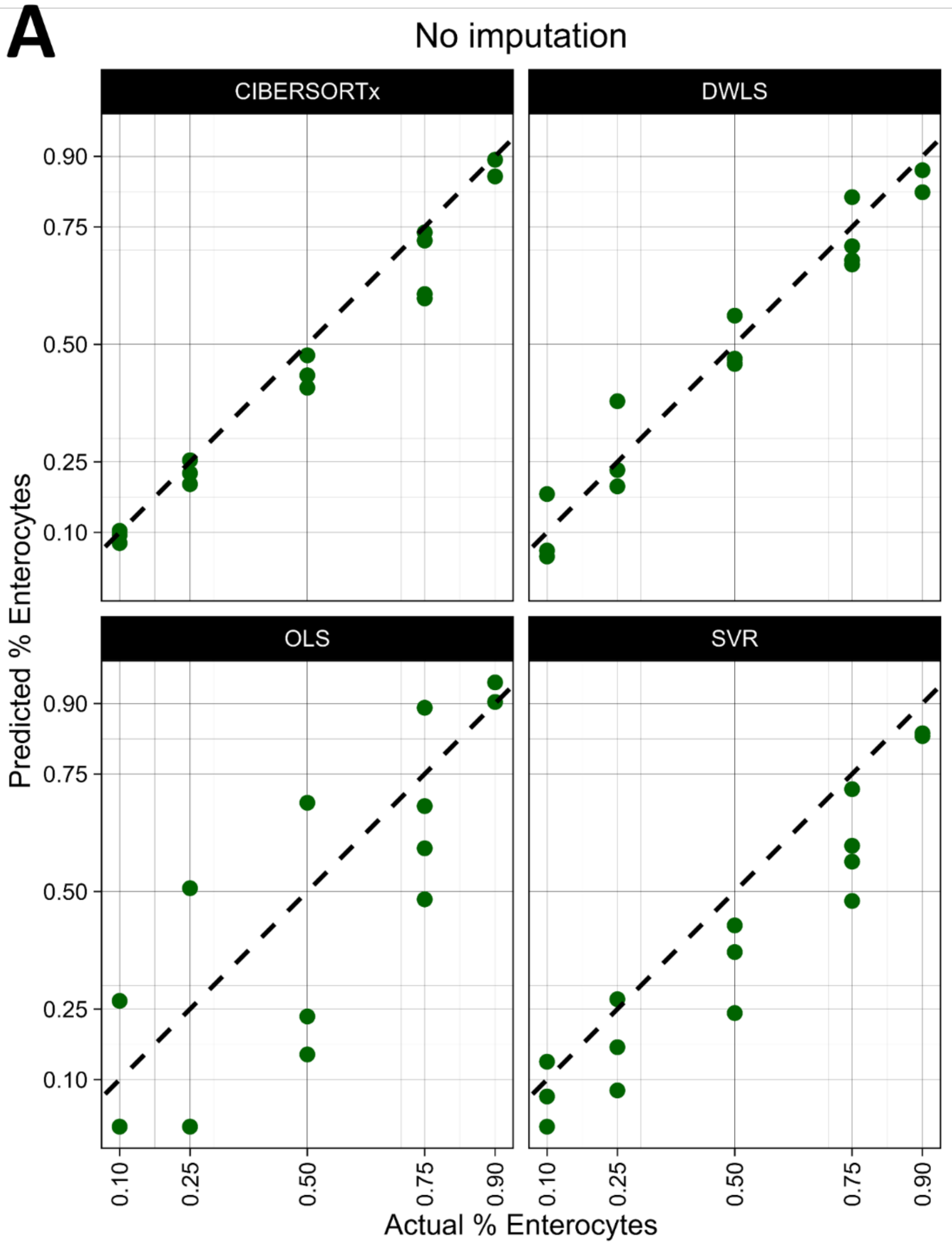
A
No imputation
CIBERSORTx
DWLS
OLS
SVR
Predicted % Enterocytes
0.90
0.75
0.50
0.25
0.10
Actual % Enterocytes
0.10
0.25
0.50
0.75
0.90

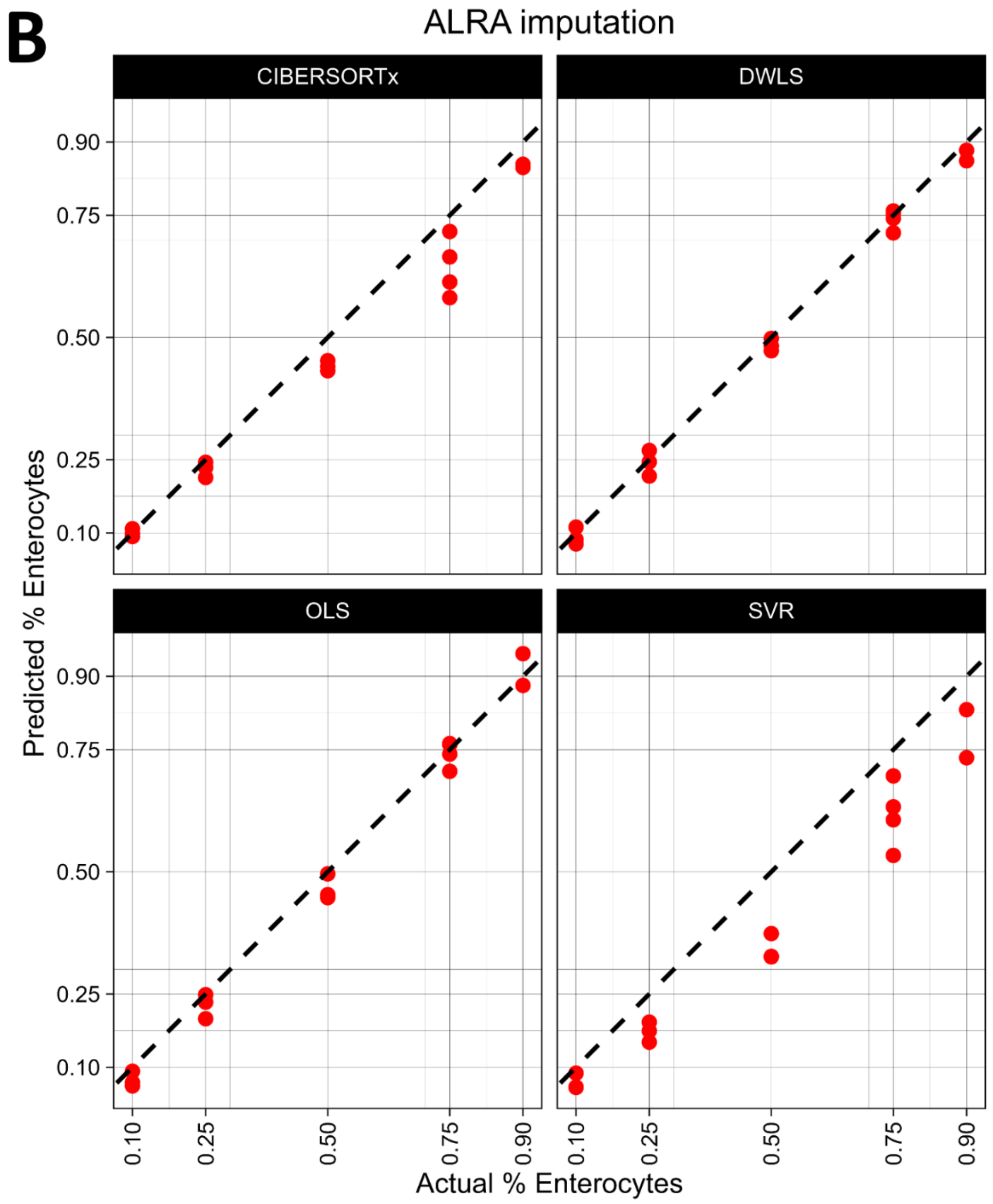
B
ALRA imputation
CIBERSORTx
DWLS
OLS
SVR
Predicted % Enterocytes
0.90
0.75
0.50
0.25
0.10
Actual % Enterocytes
0.10
0.25
0.50
0.75
0.90

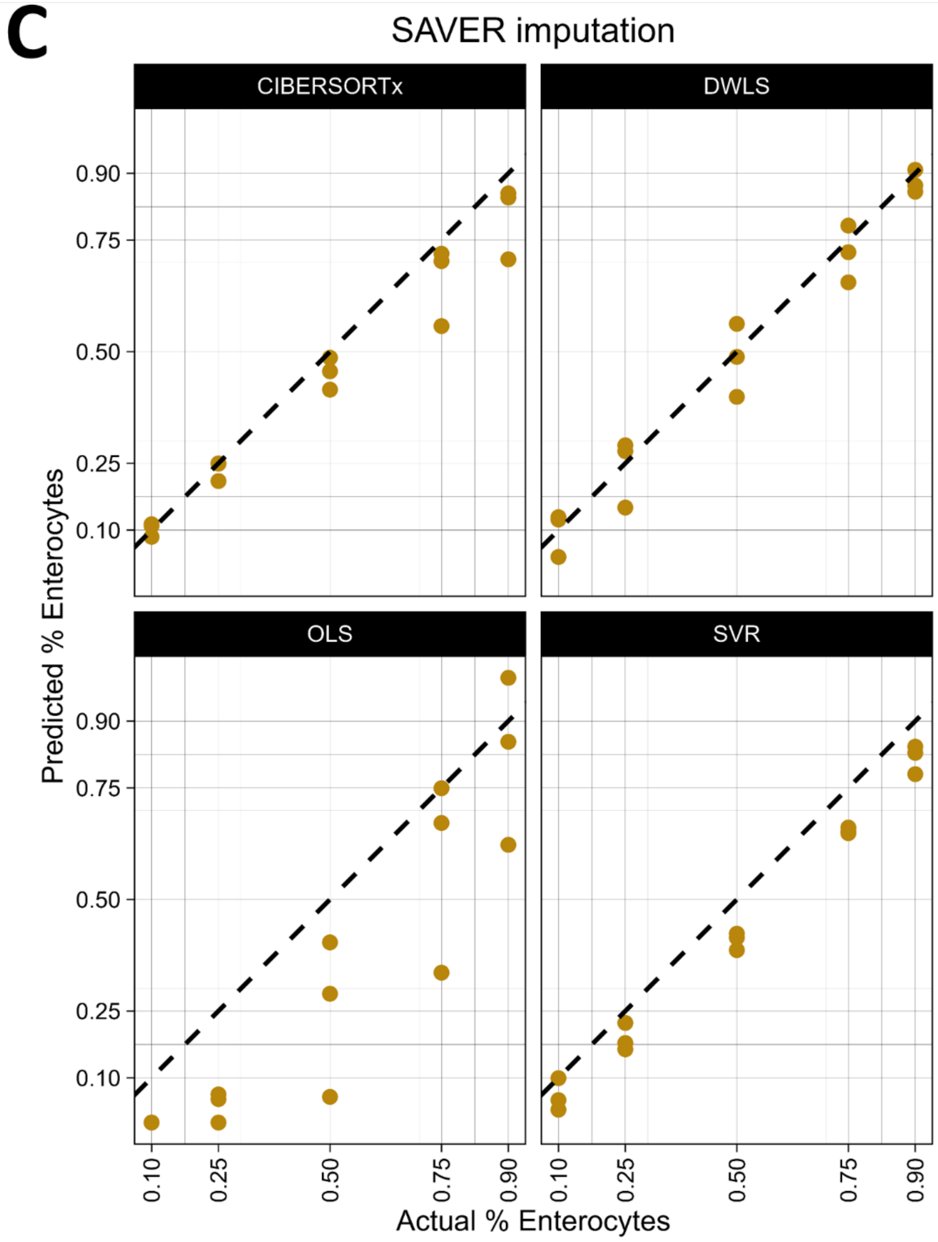

Figure 4.2 Deconvolution results for enterocytes using signature matrices from the same datasets as pseudobulk samples.

The deconvolution results to predict enterocyte cell proportion across 15 pseudobulk samples with varying proportions of enterocytes. Results include four different deconvolution methods (CIBERSORTx, DWLS, OLS, and SVR) for non-imputed (A), ALRA-imputed (B), and SAVER-imputed (C) dataset. Data points corresponding to the predicted portion of enterocytes for each individual pseudobulk sample. Enterocyte proportions varied from 10%, 25%, 50%, 75%, and 90%. The dotted line corresponds to the line of unity between the predicted and actual enterocyte proportions.

Table 4.4. Deconvolution results using signature matrices from the same datasets as pseudobulk samples

Deconvolution method	Imputation method	Enterocyte prediction MAPE (%)	Goblet cell prediction MAPE (%)	Proliferating cell prediction MAPE (%)
CIBERSORTx	No imputation	9.9	4.0	58.0
CIBERSORTx	ALRA	9.5	18.7	104.3
CIBERSORTx	SAVER	10.1	2.7	38.8
DWLS	No imputation	21.5	18.3	74.0
DWLS	ALRA	6.2	7.6	38.0
DWLS	SAVER	16.3	23.4	59.2
OLS	No imputation	61.4	69.3	100
OLS	ALRA	9.5	5.0	46.1
OLS	SAVER	54.4	79.7	87.7
SVR	No imputation	31.7	31.2	72.5
SVR	ALRA	25.2	23.6	38.8
SVR	SAVER	21.1	41.9	83.1

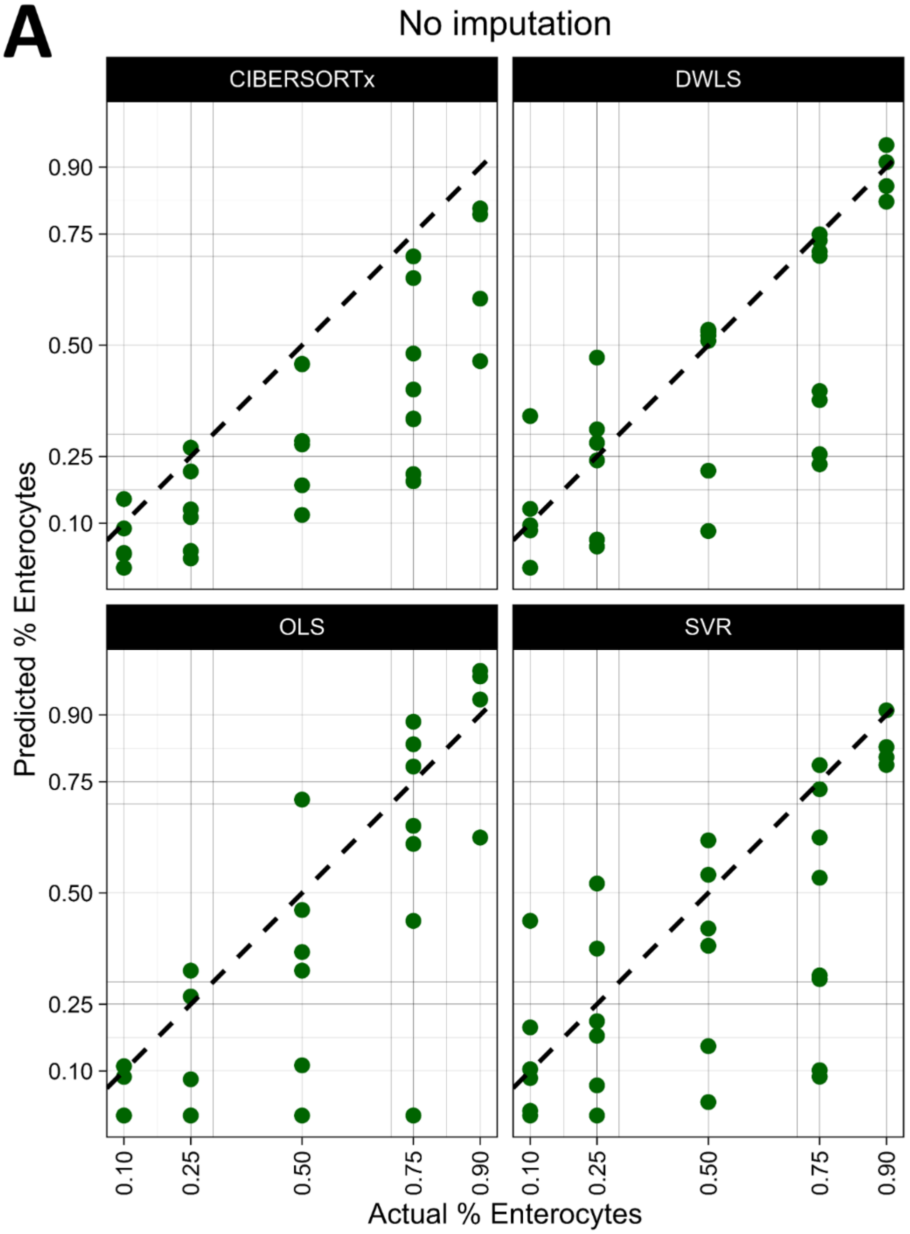
A
No imputation
CIBERSORTx
DWLS
OLS
SVR
Predicted % Enterocytes
0.10
0.25
0.50
0.75
0.90
Actual % Enterocytes
0.10
0.25
0.50
0.75
0.90

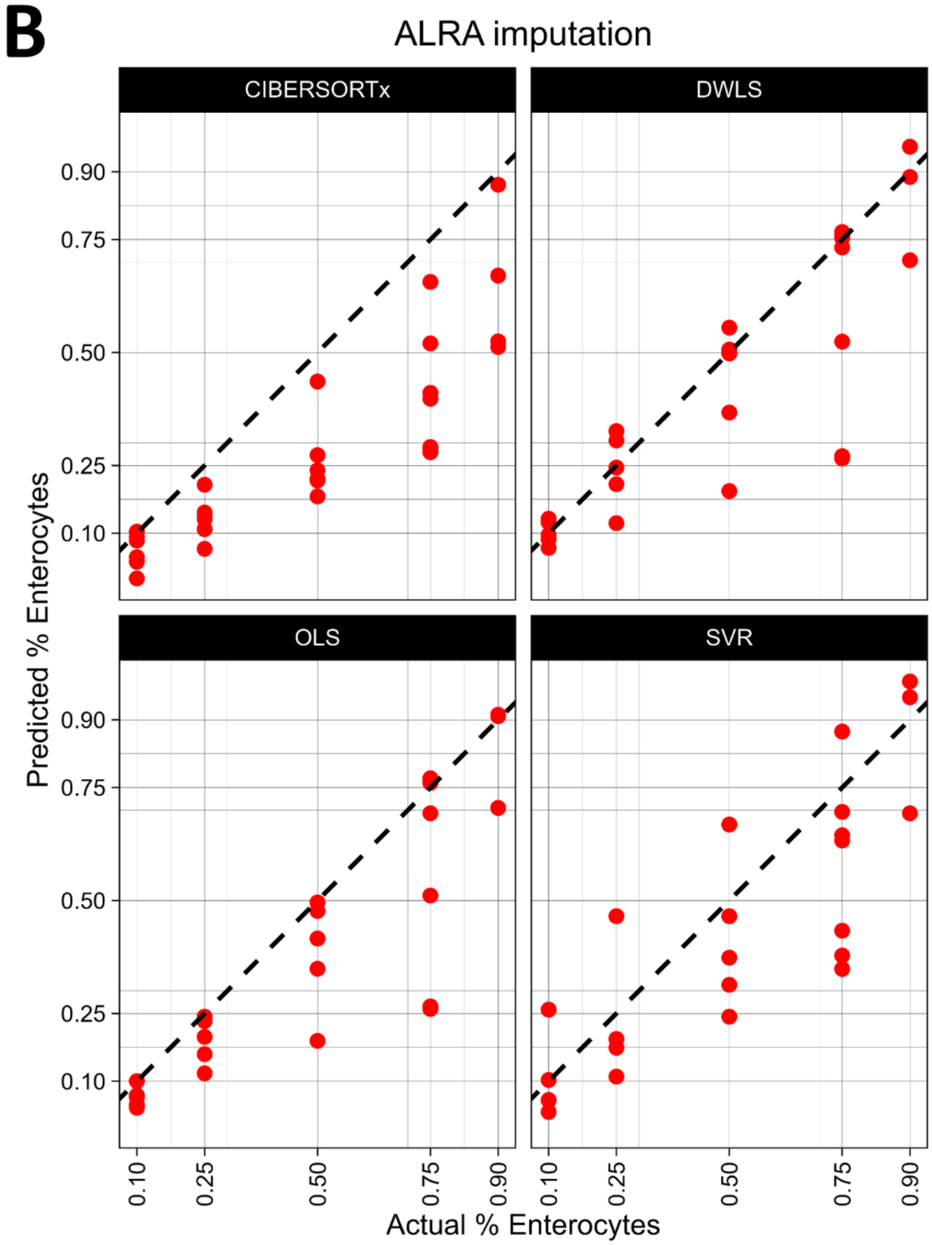
B
ALRA imputation
CIBERSORTx
DWLS
OLS
SVR
Predicted % Enterocytes
0.10
0.25
0.50
0.75
0.90
Actual % Enterocytes
0.10
0.25
0.50
0.75
0.90

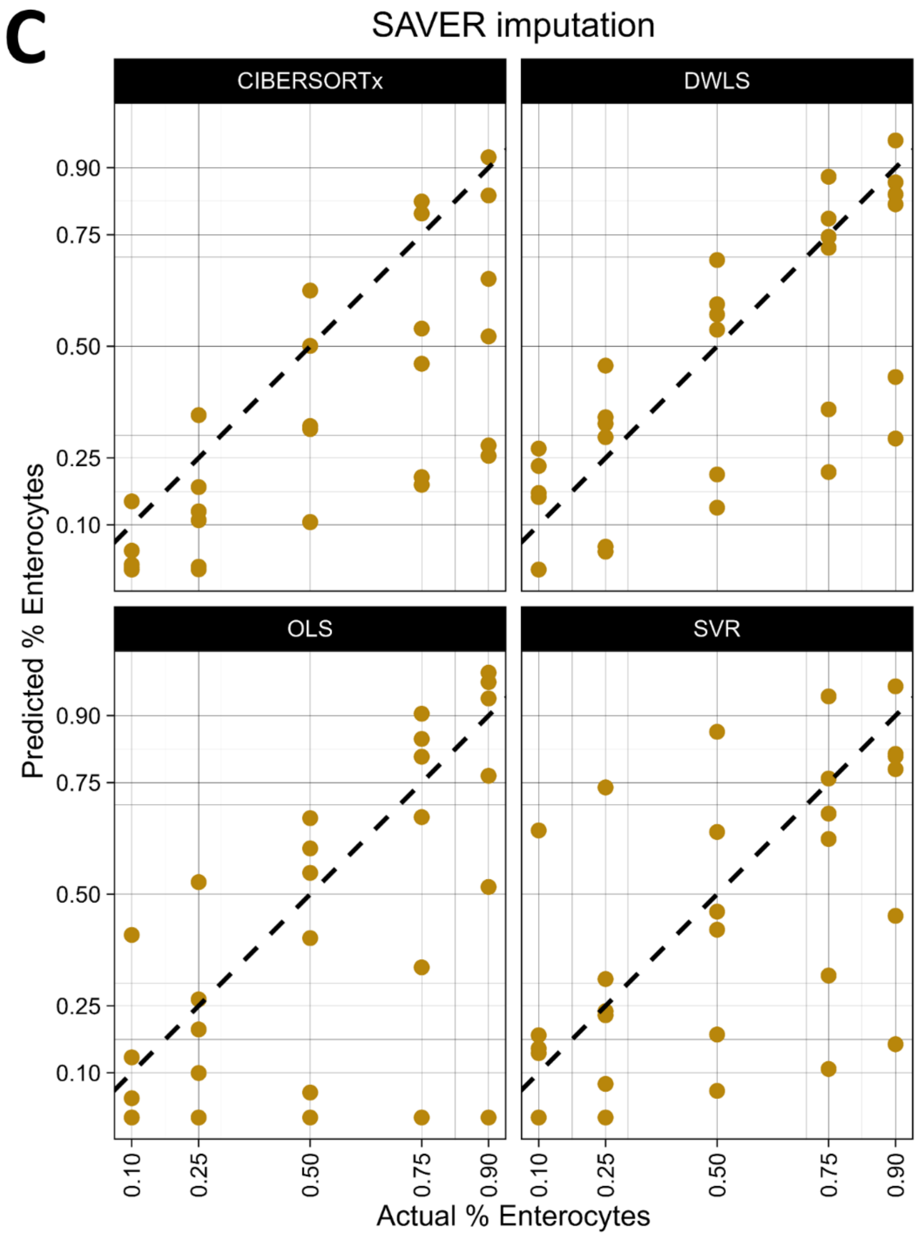

Figure 4.3 Deconvolution results for enterocytes using signature matrices from different datasets as pseudobulk samples.

The deconvolution results to predict enterocyte cell proportion across 15 pseudobulk samples using with varying proportions of enterocytes. The signature matrices used to deconvolute these pseudobulk samples were from different datasets, resulting in 30 total datapoints per plot. Results include four different deconvolution methods (CIBERSORTx, DWLS, OLS, and SVR) for non-imputed (A), ALRA-imputed (B), and SAVER-imputed (C) dataset. Data points corresponding to the predicted portion of enterocytes for each individual pseudobulk sample and each signature matrix. Enterocyte proportions varied from 10%, 25%, 50%, 75%, and 90%. The dotted line corresponds to the line of unity between the predicted and actual enterocyte proportions.

Table 4.5. Deconvolution results using signature matrices from different datasets than pseudobulk samples

Deconvolution method	Imputation method	Enterocyte prediction MAPE (%)	Goblet cell prediction MAPE (%)	Proliferating cell prediction MAPE (%)
CIBERSORTx	No imputation	46.9	30.1	174
CIBERSORTx	ALRA	43.6	60.8	281
CIBERSORTx	SAVER	52.2	53.7	103
DWLS	No imputation	40.1	86.3	100
DWLS	ALRA	19.8	22.4	174
DWLS	SAVER	49.1	65.1	117
OLS	No imputation	49.3	98.8	96.5
OLS	ALRA	21.1	17.9	167
OLS	SAVER	58.6	70.9	98.7
SVR	No imputation	54.4	98.8	99.2
SVR	ALRA	40.9	22.6	153
SVR	SAVER	65.7	86.7	123

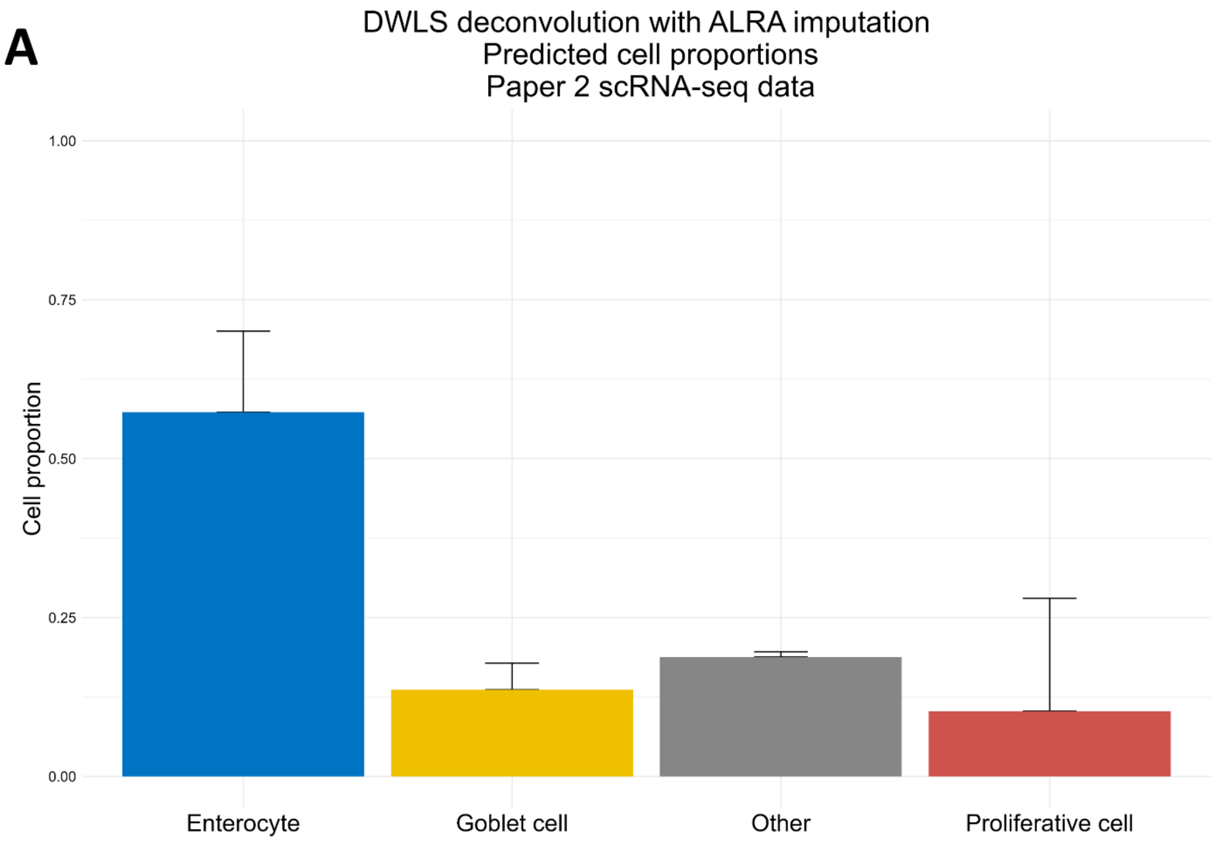
A
DWLS deconvolution with ALRA imputation
Predicted cell proportions
Paper 2 scRNA-seq data
Cell proportion
1.00
0.75
0.50
0.25
0.00
Enterocyte
Goblet cell
Other
Proliferative cell

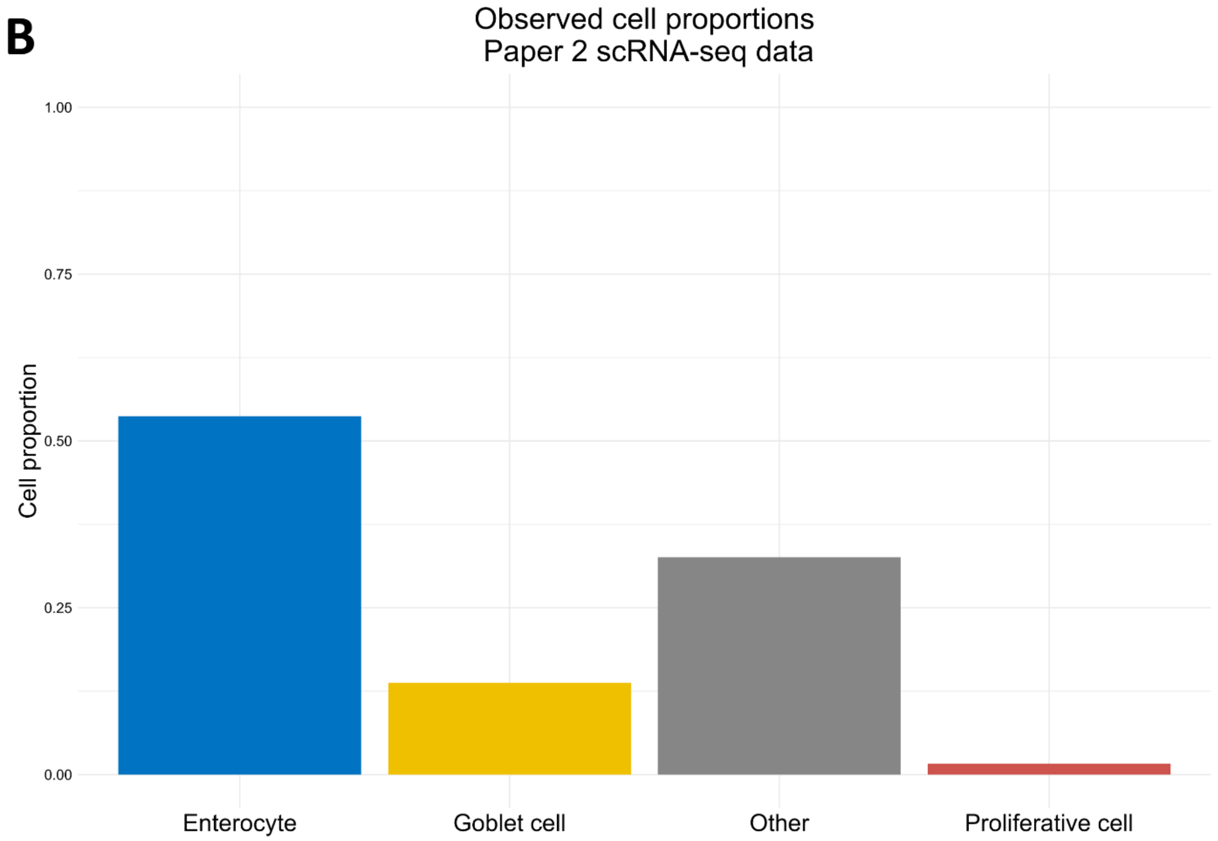

Figure 4.4. Deconvolution results for a pseudobulk sample generated using all cells in the paper 2 scRNA-seq dataset.

The deconvolution results to predict enterocytes, goblet cells, other cells, and proliferative cells for a pseudobulk sample generated using all cells from the paper 2 scRNA-seq dataset (A) compared to the observed values (B). The DWLS deconvolution method was used on ALRA imputed data. Other cells refer to enteroendocrine cells, tuft cells, BEST4 cells, Paneth cells, and M cells. Bars and error bars represent the mean prediction ± SD from three signature matrices made from each scRNA-seq dataset.

Table 4.6. Comparison of predicted versus observed cell proportions for the deconvolution of a pseudobulk generated using all cells from the paper 2 scRNA-seq dataset.

Cell type	Predicted proportion (SD)	Observed proportion	% error
Enterocyte	0.57 (0.12)	0.54	6.6%
Goblet cell	0.14 (0.04)	0.14	0.6%
Proliferating cell	0.10 (0.18)	0.017	515%
Other	0.19 (0.01)	0.33	42.3%

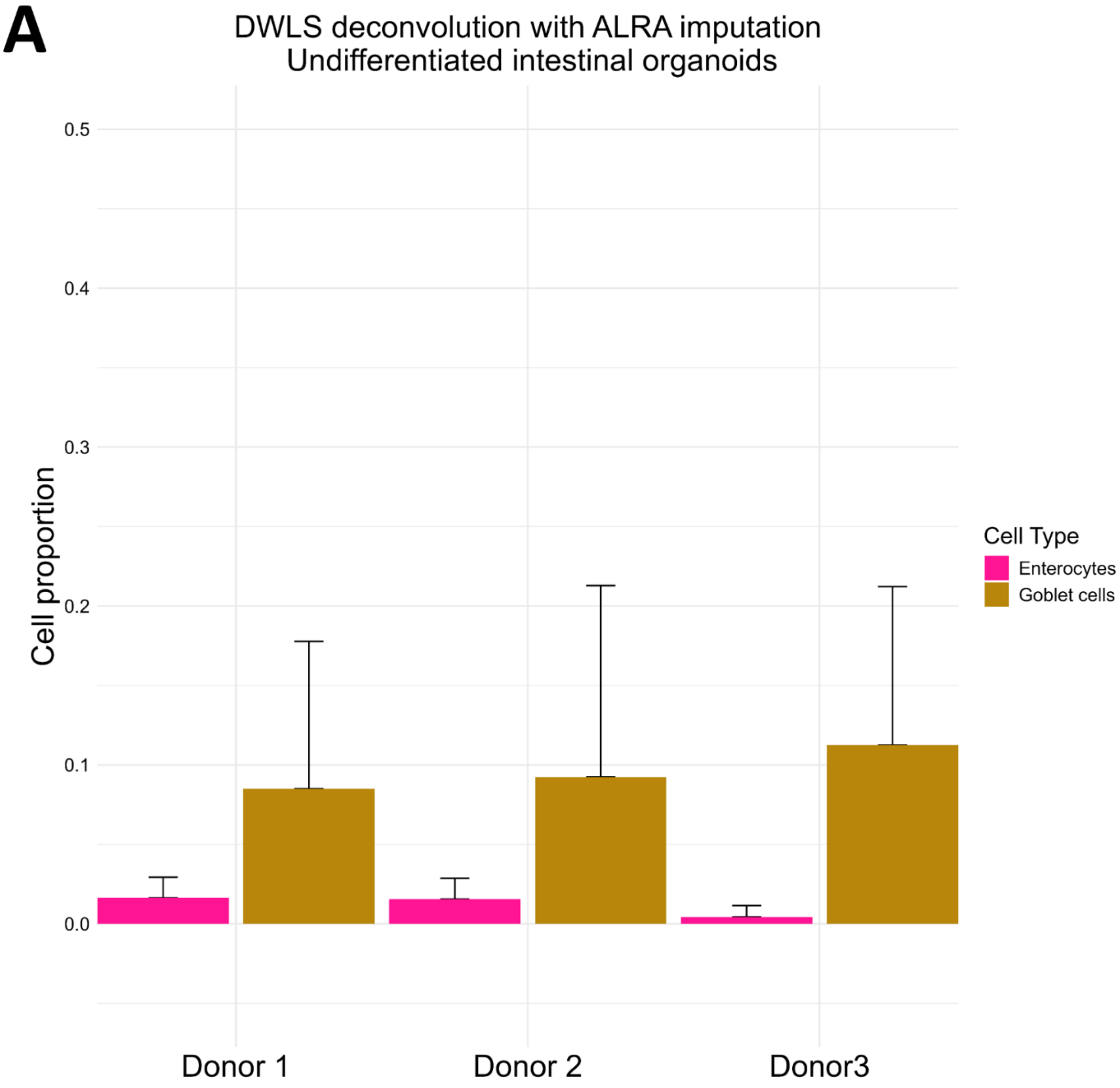

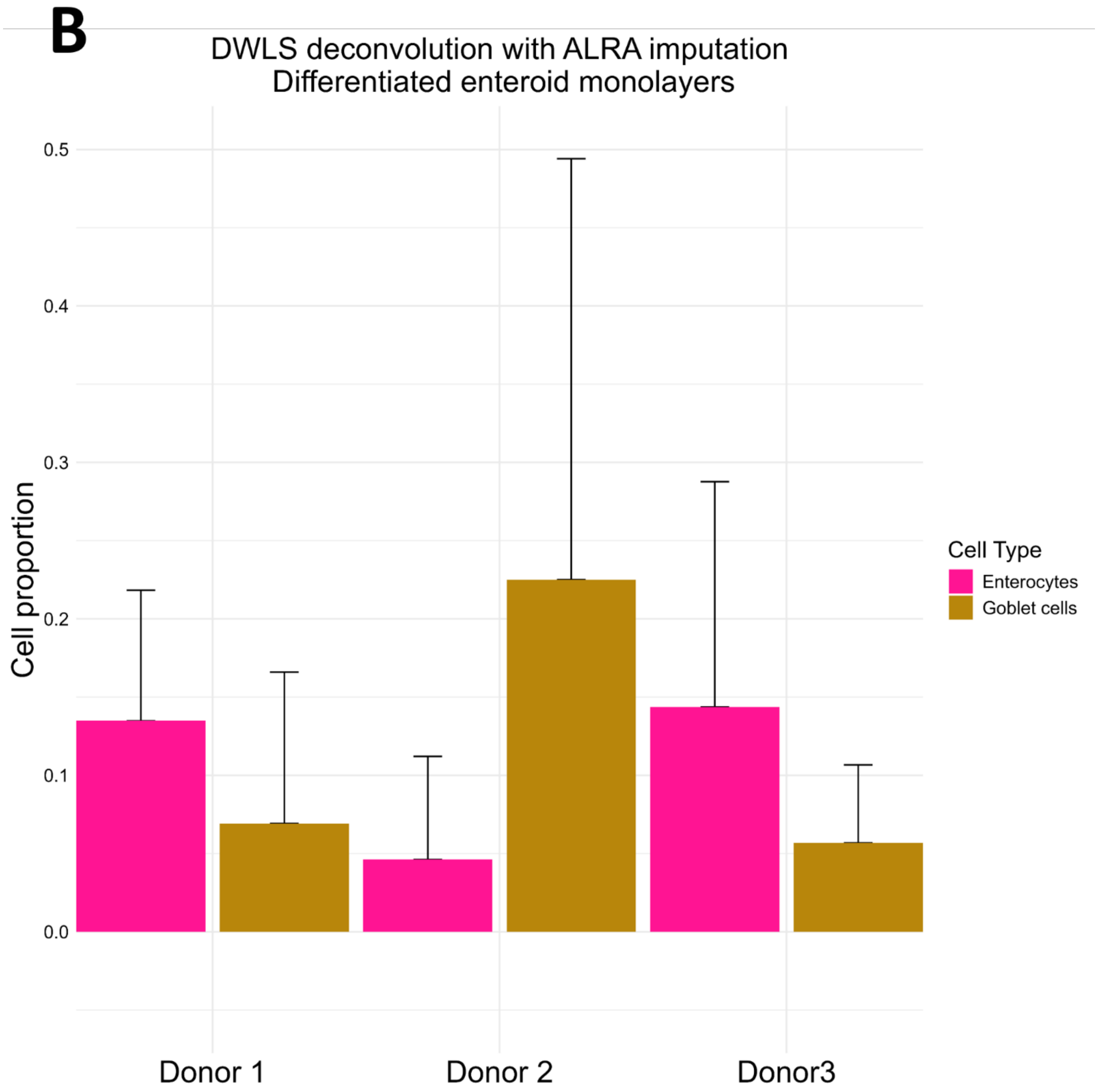

Figure 4.5. Deconvolution results of undifferentiated intestinal organoids and differentiated enteroid monolayers using signature matrices from all scRNA-seq datasets.

The results of deconvolution using the DWLS deconvolution method on undifferentiated intestinal organoids (A) and differentiated enteroid monolayers cultured for 21-days (B). Bars represent mean ± standard deviation of the deconvoluted cell proportions from three culture replicates for each donor/differentiation condition using three ALRA-imputed signature matrices derived from the three scRNA-seq datasets.

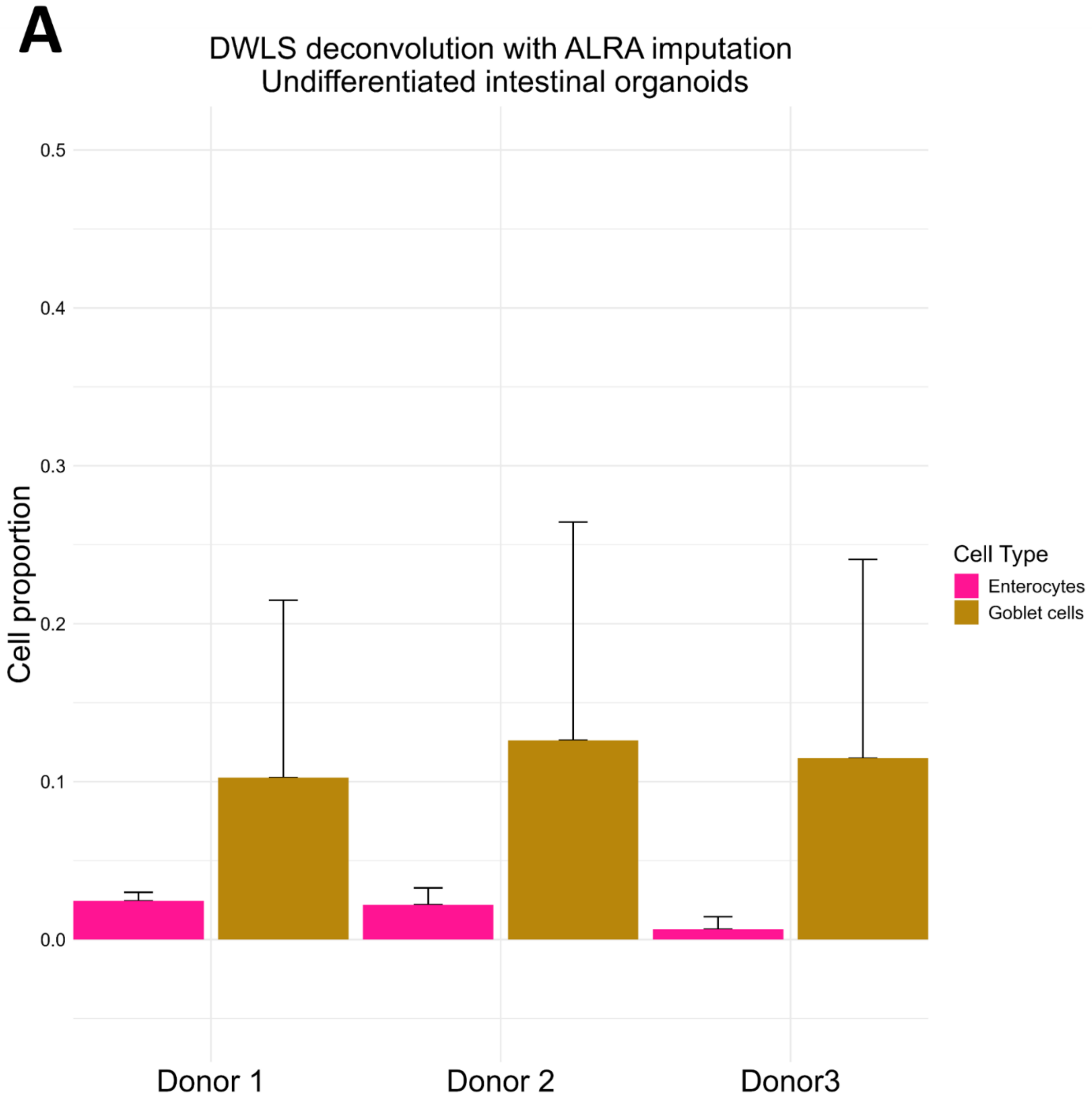

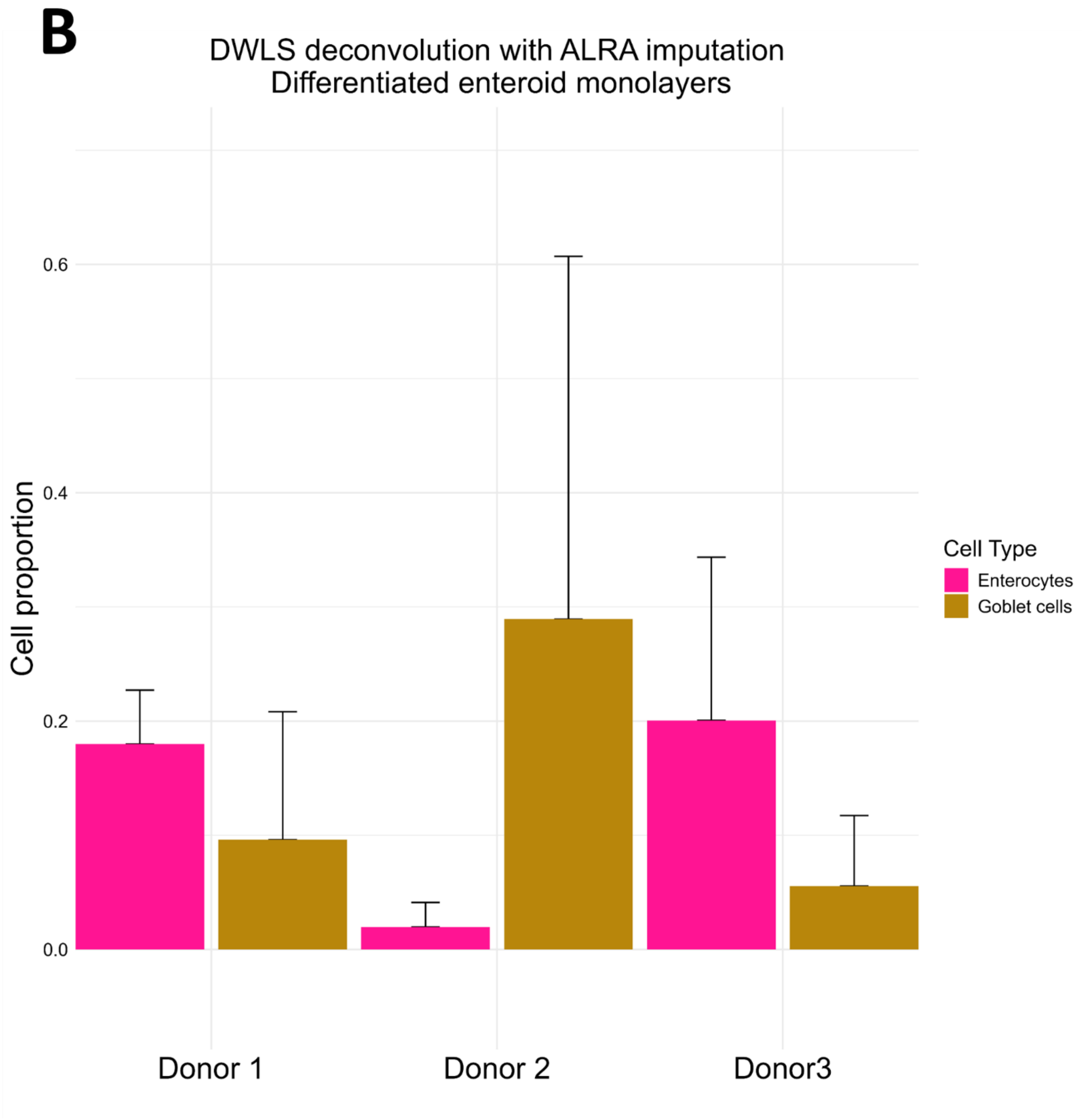

Figure 4.6. Deconvolution results of undifferentiated intestinal organoids and differentiated enteroid monolayers using signature matrices from paper 1 and paper 2 scRNA-seq datasets.

The results of deconvolution using the DWLS deconvolution method on undifferentiated intestinal organoids (A) and differentiated enteroid monolayers cultured for 21-days (B). Bars represent mean ± standard deviation of the deconvoluted cell proportions from three culture replicates for each donor/differentiation condition using two ALRA-imputed signature matrices derived from paper 1 and paper 2 scRNA-seq datasets.

4.5. REFERENCES

Andrews TS, Kiselev VY, McCarthy D, and Hemberg M (2021) Tutorial: guidelines for the computational analysis of single-cell RNA sequencing data. *Nature Protocols* **16:**1-9.

Arian C, Mahony EO, MacDonald JW, Bammler TK, Donowitz M, Kelly EJ, and Thummel KE (2024) Human Enteroid Monolayers: A Novel, Functionally-Stable Model for Investigating Oral Drug Disposition. *Drug Metab Dispos*.

Burclaff J, Bliton RJ, Breau KA, Ok MT, Gomez-Martinez I, Ranek JS, Bhatt AP, Purvis JE, Woosley JT, and Magness ST (2022) A Proximal-to-Distal Survey of Healthy Adult Human Small Intestine and Colon Epithelium by Single-Cell Transcriptomics. *Cell Mol Gastroenterol Hepatol* **13:**1554-1589.

Cheng CW, Biton M, Haber AL, Gunduz N, Eng G, Gaynor LT, Tripathi S, Calibasi-Kocal G, Rickelt S, Butty VL, Moreno-Serrano M, Iqbal AM, Bauer-Rowe KE, Imada S, Ulutas MS, Mylonas C, Whary MT, Levine SS, Basbinar Y, Hynes RO, Mino-Kenudson M, Deshpande V, Boyer LA, Fox JG, Terranova C, Rai K, Piwnica-Worms H, Mihaylova MM, Regev A, and Yilmaz Ö H (2019) Ketone Body Signaling Mediates Intestinal Stem Cell Homeostasis and Adaptation to Diet. *Cell* **178:**1115-1131.e1115.

Drescher H, Weiskirchen S, and Weiskirchen R (2021) Flow Cytometry: A Blessing and a Curse. *Biomedicines* **9**.

Elmentaite R, Kumasaka N, Roberts K, Fleming A, Dann E, King HW, Kleshchevnikov V, Dabrowska M, Pritchard S, Bolt L, Vieira SF, Mamanova L, Huang N, Perrone F, Goh Kai'En I, Lisgo SN, Katan M, Leonard S, Oliver TRW, Hook CE, Nayak K, Campos LS, Domínguez Conde C, Stephenson E, Engelbert J, Botting RA, Polanski K, van Dongen S, Patel M, Morgan MD, Marioni JC, Bayraktar OA, Meyer KB, He X, Barker RA, Uhlig HH, Mahbubani KT, Saeb-Parsy K, Zilbauer M, Clatworthy MR, Haniffa M, James KR, and Teichmann SA (2021) Cells of the human intestinal tract mapped across space and time. *Nature* **597:**250-255.

Hao Y, Stuart T, Kowalski MH, Choudhary S, Hoffman P, Hartman A, Srivastava A, Molla G, Madad S, Fernandez-Granda C, and Satija R (2024) Dictionary learning for integrative, multimodal and scalable single-cell analysis. *Nature Biotechnology* **42:**293-304.

Haque A, Engel J, Teichmann SA, and Lonnberg T (2017) A practical guide to single-cell RNA-sequencing for biomedical research and clinical applications. *Genome Med* **9:**75.

Hippen AA, Omran DK, Weber LM, Jung E, Drapkin R, Doherty JA, Hicks SC, and Greene CS (2023) Performance of computational algorithms to deconvolve heterogeneous bulk ovarian tumor tissue depends on experimental factors. *Genome Biology* **24:**239.

Hou W, Ji Z, Ji H, and Hicks SC (2020) A systematic evaluation of single-cell RNA-sequencing imputation methods. *Genome Biol* **21:**218.

Huang M, Wang J, Torre E, Dueck H, Shaffer S, Bonasio R, Murray JI, Raj A, Li M, and Zhang NR (2018) SAVER: gene expression recovery for single-cell RNA sequencing. *Nature Methods* **15:**539-542.

Im Y and Kim Y (2023) A Comprehensive Overview of RNA Deconvolution Methods and Their Application. *Mol Cells* **46:**99-105.

Korsunsky I, Millard N, Fan J, Slowikowski K, Zhang F, Wei K, Baglaenko Y, Brenner M, Loh P-r, and Raychaudhuri S (2019) Fast, sensitive and accurate integration of single-cell data with Harmony. *Nature Methods* **16:**1289-1296.

Li X and Wang C-Y (2021) From bulk, single-cell to spatial RNA sequencing. *International Journal of Oral Science* **13:**36.

Linderman GC, Zhao J, Roulis M, Bielecki P, Flavell RA, Nadler B, and Kluger Y (2022) Zero-preserving imputation of single-cell RNA-seq data. *Nature Communications* **13:**192.

McKinnon KM (2018) Flow Cytometry: An Overview. *Curr Protoc Immunol* **120:**5 1 1-5 1 11.

Newman AM, Steen CB, Liu CL, Gentles AJ, Chaudhuri AA, Scherer F, Khodadoust MS, Esfahani MS, Luca BA, Steiner D, Diehn M, and Alizadeh AA (2019) Determining cell type abundance and expression from bulk tissues with digital cytometry. *Nature Biotechnology* **37:**773-782.

Nguyen H, Nguyen H, Tran D, Draghici S, and Nguyen T (2024) Fourteen years of cellular deconvolution: methodology, applications, technical evaluation and outstanding challenges. *Nucleic Acids Res* **52:**4761-4783.

Qiu P (2020) Embracing the dropouts in single-cell RNA-seq analysis. *Nature Communications* **11:**1169.

Svensson V, Vento-Tormo R, and Teichmann SA (2018) Exponential scaling of single-cell RNA-seq in the past decade. *Nat Protoc* **13:**599-604.

Tsoucas D, Dong R, Chen H, Zhu Q, Guo G, and Yuan G-C (2019) Accurate estimation of cell-type composition from gene expression data. *Nature Communications* **10:**2975.

van Dijk D, Sharma R, Nainys J, Yim K, Kathail P, Carr AJ, Burdziak C, Moon KR, Chaffer CL, Pattabiraman D, Bierie B, Mazutis L, Wolf G, Krishnaswamy S, and Pe’er D (2018) Recovering Gene Interactions from Single-Cell Data Using Data Diffusion. *Cell* **174:**716-729.e727.

Zwick RK, Kasparek P, Palikuqi B, Viragova S, Weichselbaum L, McGinnis CS, McKinley KL, Rathnayake A, Vaka D, Nguyen V, Trentesaux C, Reyes E, Gupta AR, Gartner ZJ, Locksley RM, Gardner JM, Itzkovitz S, Boffelli D, and Klein OD (2024) Epithelial zonation along the mouse and human small intestine defines five discrete metabolic domains. *Nature Cell Biology* **26:**250-262.

CHAPTER 5. RECAPITULATING THE OBSERVED GOLDENSEAL-METFORMIN NATURAL PRODUCT DRUG INTERACTION IN ENTEROID MONOLAYERS

(A version of this chapter is currently a draft manuscript "A Gut Response: Utilizing Human Enteroid Monolayers to Uncover the Mechanism of Goldenseal-Mediated Inhibition of Metformin's Intestinal Absorption" (2024) with planned submission to *Biochemical Pharmacology*)

5.1. INTRODUCTION

The limitations of historically used *in vitro* models of the human intestine hinders accurate prediction of orally administered drug pharmacokinetics under mono- and polytherapy dosing conditions (Arian et al., 2022). This is particularly evident for the prediction of natural product-drug interactions (NPDIs), as these interactions take place preferentially in the intestinal mucosa, where exposure concentrations of drug and natural product (NP) are uncertain and where currently used *in vitro* models often fail to quantitatively replicate *in vivo* enzyme and transporter functions (Nguyen et al., 2021).

In an effort to improve patient safety by investigating the potential for NPDIs to occur, the Center of Excellence for Natural Product-Drug Interaction Research has established a set of recommended approaches to study NPDIs (Paine et al., 2018) and applied these approaches to study several high priority natural products (Tian et al., 2018; Bansal et al., 2022; Tanna et al., 2023). One such high priority NP is goldenseal (*Hydrastis canadenis*) – a perennial plant native to eastern North America. The roots of the goldenseal plant are formulated to produce medicines that are utilized to self-treat respiratory tract infections, digestive issues, and skin irritation (NCCIH, 2021). A recent clinical study demonstrated goldenseal inhibits intestinal organic cation uptake transporters, leading to decreased exposure and C_{max} of a subtherapeutic dose (50 mg) of oral metformin (Nguyen et al., 2021). Interestingly, the observed interaction did not affect the renal clearance of metformin, suggesting that the interaction occurred preferentially in the intestinal mucosa. This observation is of particular note, as the initial *in vitro* models used to predict *in vivo* interactions did not suggest goldenseal would cause a clinically significant inhibition of intestinal organic cation uptake transporters, highlighting the need for a more physiologically relevant model of the human intestine that can accurately recapitulate drug transporter functions.

A follow-up study sought to assess the impact of goldenseal on metformin pharmacokinetics (PK) and pharmacodynamics (PD) in well-managed type II diabetic patients taking clinically relevant doses of metformin (unpublished data, Mary Paine). When results from all subjects were analyzed together, there was no significant pharmacokinetic interaction between metformin and goldenseal. However, when metformin dosing groups were stratified into low, medium, and high dosing groups there was a clear metformin dose-dependent effect on the magnitude of inhibition, where low doses of metformin corresponded to greater magnitudes of a goldenseal effect, decreasing metformin exposure and C_{max} by ~20%. Of note, again, the renal clearance and half-life of all metformin dosing groups remained unchanged, suggesting that goldenseal inhibits a saturable transport process in the intestine that precipitates a greater magnitude of effect at lower doses of metformin.

A mechanistic study was conducted by Oyanna et al. to elucidate the transporters involved in the goldenseal-metformin interaction, which utilized both transfected cell lines (HEK-293) and mouse models (Oyanna et al., 2023). Results from this study implicated OCT3, PMAT, and ThTR-2 as the major intestinal transporters involved in the metformin-goldenseal interaction. While these are valuable results, the use of overexpressing cell systems does not take into account physiologically relevant protein abundances of intestinal transporters, where the *in vivo* expression and abundance of these transporters may be too low to be clinically significant, and as such, may overestimate the importance of certain transporters to the NP-drug interaction. Additionally, the availability of certain transporter-expressing cell lines may be limited – as mentioned by the authors, who were unable to utilize SERT-expressing cell lines and where SERT has been implicated as an important transporter mediating metformin absorption (Han et al., 2015).

Development of a more advanced *in vitro* system, such as an adult stem cell-derived intestinal organoid (enteroid) monolayer, may significantly improve the prediction of NP-drug interactions and allow for the elucidation of their mechanisms, such as the goldenseal-metformin interaction, leading to more informed clinical decisions affecting patient safety. Human enteroids represent an appealing model as they are multicellular constructs that recapitulate DMET functions of the intestinal mucosal barrier, maintain the genetic identity of the donor, and demonstrate improved viability over primary enterocytes (Rossi et al., 2018). Work outlined in Chapter 3 of this dissertation work characterized human enteroid monolayers for use in pharmaceutical science research – demonstrating proper cell differentiation and morphology, RNA expression of clinically relevant drug metabolizing enzymes and transporters, high intercellular barrier integrity, physiologically relevant CYP3A activity, and extended culture viability of up to 6-weeks (Arian et al., 2024). Importantly, the presence of high intercellular barrier integrity and RNA expression of several drug transporters may be critical for mechanistic understanding of the metformin-goldenseal interaction, making human enteroid monolayers an appealing model to recapitulate the observed interaction and elucidate the transporter(s) involved.

Thus, the goal of this study was to assess the utility of human enteroid monolayers as a model to predict the goldenseal-metformin interaction observed in the clinic and identify the mechanism of the interaction. Using enteroid monolayers derived from the duodenum of 3-4 adult donors cultured on Transwell® inserts, we characterized the kinetics of metformin uptake from the apical chamber into the cells and overall metformin flux from the apical to basolateral chamber. We then performed goldenseal-metformin interaction studies using both a sub-clinical metformin concentration and physiologically relevant metformin dosing concentrations derived from the two *in vivo* clinical studies. To identify the transporters involved in the goldenseal-metformin interaction, we measured RNA expression of select transporters and performed inhibition experiments utilizing metformin and transporter selective inhibitors. Finally, we assessed the susceptibility of SERT and ThTr-2/ThTr-1 inhibition by goldenseal utilizing serotonin and thiamine, respectively, as probe substrates. Our results demonstrate that metformin uptake from the apical chamber into epithelial cells was saturable and strongly inhibited by goldenseal at subtherapeutic concentrations of metformin (≤ 1.5 mM),), but not at therapeutic concentrations (> 1.5 mM), and likely involved ThTR-2. However, transcellular metformin flux from apical to basolateral chamber was inhibited by goldenseal for all clinically relevant doses of metformin (1.5-70 mM) and involves an as of yet unidentified cation transporter. Although not fully consistent with the observed clinical data, our findings with the enteroid monolayer suggest a more complicated NPDI than that revealed by previous *in vitro* studies, demonstrating the utility of the model.

5.2. METHODS

5.2.1. Chemicals and reagents

IntestiCult™ Organoid Growth Medium (Human), IntestiCult™ Organoid Differentiation Medium (Human), and Y-27632 (Dihydrochloride) were purchased from STEMCELL

Technologies (Vancouver, BC, Canada). Advanced DMEM/F-12, Streptomycin (10,000 U/mL), Dulbecco's phosphate-buffered saline with calcium and magnesium (DPBS++), HEPES buffer (1M), and Hanks' Balanced Salt Solution with calcium and magnesium (HBSS++) were purchased from Life Technologies (Carlsbad, CA). Matrigel® Growth Factor Reduced (GFR) Basement Membrane Matrix (phenol red-free, LDEV-free), collagen IV, and Cell Recovery Solution were purchased from Corning (Corning, NY). RLT Lysis buffer was purchased from Qiagen (Germantown, MD). Lucifer Yellow CH dilithium salt, metformin hydrochloride, thiamine hydrochloride, paroxetine hydrochloride, desipramine hydrochloride, and MPP^+ iodide were purchased from Sigma-Aldrich (St. Louis, MO). Mannitol [^{3}H] and 5-hydroxytrptamine [^{3}H] trifluoroacetate were purchased from American Radiolabeled Chemicals (St. Louis, MO). Metformin [^{14}C] hydrochloride and thiamine [^{3}H] were purchased from Moravek (Brea, CA). SLC6A4 (Hs00984349_m1), SLC19A3 (Hs00228858_m1), SLC19A2 (Hs00949693_m1), SLC29A4 (Hs00928283_m1), SLC22A3 (Hs01009571_m1), SLC22A1 (Hs00427552_m1), and GAPDH (Hs02786624_g1) Taqman probes were purchased from Thermo Fisher Scientific (Waltham, MA). Goldenseal extracts were kindly provided by Dr. Nadja Cech and Dr. Nicholas Oberlies (University of North Carolina at Greensboro, NC).

5.2.2. Cell culture

Anonymized undifferentiated duodenal organoids from four donors (HDO01 – 64 year old female; HDO03 – 68 year old male; HDO05 – 40 year old male; HDO07 – 70 year old female), derived via biopsies obtained from NW BioTrust, a core service for patient consenting, and NWBioSpecimen, a core service for procurement and annotation of research biospecimens, were kindly provided by Dr. Jason Smith, University of Washington, WA. Experiments were conducted at passages 10-15 on HDO03, HDO05, and HDO07 and passages 20-24 on HDO01.

Cell maintenance, passaging, and plating protocols are described in depth in the following report from our group (Arian et al., 2024). Briefly, undifferentiated organoids were suspended and grown in Matrigel droplets plated in a 24-well plate with 0.5 mL of Intesticult™ Intestinal Organoid Growth Medium (Human) containing 1% (v/v) penicillin-streptomycin. Cells were passaged when undifferentiated organoids reached a large, cystic, morphology by the addition of 0.5 mL of cold Cell Recovery Solution followed by shaking at 4ºC and subsequent trituration until ~80% of the whole organoids were broken into smaller fragments. The cells were then centrifuged and the resulting cell pellet was resuspended in Matrigel and 50 µL of the suspension was plated in each well of a 24-well plate along with Intesticult™ Growth Medium containing 10 µM Y-27632. Cells were split from 1:2 to 1:4 depending on cell density. Undifferentiated organoids were fed every other day with Intesticult™ Growth Medium without Y-27632. Enteroid monolayers were derived from undifferentiated organoids following a similar protocol as cell passaging – with additional trituration until ~95% of the organoids were broken into single cells prior to centrifugation. Following centrifugation, the resulting pellet was resuspended with Intesticult™ Intestinal Organoid Differentiation Medium (Human) containing 1% (v/v) penicillin-streptomycin and 10 µM Y-27632. The cell suspension (100 µL) was then plated atop 0.4 µm pore-size Transwell® filter inserts for 24-well plates (catalog no. 3470; Corning Inc., NY) overlaid first with 34 µg/mL collagen IV. Intesticult™ Differentiation Medium (0.5 mL) was then added to the basolateral chamber of the 24-well plate. Enteroid monolayers were fed every other day with Intesticult™ Differentiation Medium in both the apical and basolateral chamber, 0.1 mL and 0.5 mL, respectively. Enteroid monolayers were grown for 21 days prior to experimentation, as this timepoint was determined to be suitable in previous work shown by our group (Arian et al., 2024).

5.2.3. Metformin uptake time linearity assays

Enteroid monolayers were moved from their original 24-well plate ("experiment plate") to a blank 24-well ("wash plate") and washed three times with blank apical transport buffer (10 mM HEPES in Hank's balanced salt solution, pH 6.5) and maintained at 37ºC until use. Stock solutions of radiolabeled [^{14}C] metformin (1.7 mM, in water) and radiolabeled [^{3}H] mannitol (50 mM, in ethanol) were diluted in apical transport buffer to a final concentration of 2 µM and 50 µM for metformin and mannitol, respectively (containing 0.1% ethanol v/v). A 4 µL volume of the dosing solution was added to an appropriately labeled scintillation vial to serve as the calibrator for the radioactivity analysis. A 0.7 mL volume of basolateral transport buffer (10 mM HEPES in Hank's balanced salt solution, pH 7.4, containing 0.1% ethanol v/v) was added to the basolateral compartment of the "experiment plate". Wash buffer was aspirated from each Transwell® insert and 0.3 mL of the dosing solution prepared above was added to the filter inserts and the filters were moved to the experiment plate. Cells were incubated at 37ºC for the following timepoints: 15, 30, 45, 60, 90, and 120 minutes. Following the timepoints, Transwell® inserts were moved to a 24-well plate placed on ice containing 0.5 mL of ice cold DPBS++ in each well. 40 µL of the apical dosing media from each insert was collected and placed in an appropriately labeled scintillation vial for subsequent analysis. Following collection of apical samples, the inserts were then aspirated and then cells were washed three times with DPBS++. After the third wash, inserts were aspirated and 150 µL of 1M sodium hydroxide was added to each Transwell® insert and the plate was moved off ice to allow for cells to lyse at room temperature for 1 hour. During the 1-hour incubation, 200 µL of the basolateral transport buffer from each well was placed in an appropriately labeled scintillation vial for subsequent analysis. Additionally, BCA standards (catalog no. 23208, Thermo Scientific, MA) were added to a 96-well plate and kept at 4ºC until cell lyses was complete. After the hour incubation, 150 µL of 1M hydrochloric acid was added to each Transwell® insert to neutralize the cell lysate solution. A 200 µL volume of the neutralized cell lysate solution was placed in an appropriately labeled scintillation vial for subsequent analysis and 25 µL was added to the 96-well plate containing BCA standards prepared earlier. BCA working reagent was prepared and 200 µL of the solution was added to each well of the 96-well plate containing BCA standards or cell lysate. The plate was then incubated at 37ºC for 30 minutes and then read on a Tecan SPARK multimode plate reader (Tecan Group Ltd., Switzerland), measuring an absorbance of 562 nm. Scintillation vials containing radioactive samples were analyzed using a Tri-Carb Liquid Scintillation Counter (Perkin Elmer, Waltham, MA, USA). Results for these studies are shown in **Figure 5.1**.

5.2.4. Serotonin and thiamine uptake time linearity assay

Enteroid monolayers were moved from their original 24-well plate ("experiment plate") to a blank 24-well ("wash plate") and washed three times with blank apical transport buffer (10 mM HEPES in Hank's balanced salt solution, pH 6.5) and maintained at 37ºC until use. Stock solutions of test compounds; radiolabeled [^{3}H] serotonin (12.5 mM) in water:ethanol:TFA:mercaptoethanol (98:2:0.1:0.2, v/v); and radiolabeled [^{3}H] thiamine (10 mM) in water:ethanol (1:1, v/v) were diluted in apical transport buffer to make their respective dosing solutions (final concentrations of 3 µM and 5 µM, respectively). Each dosing solution contained Lucifer Yellow at a final concentration of 300 µM, prepared from a 60 mM stock solution in water, to serve as the barrier integrity control. A series of 4 µL volumes of the dosing solutions were added to appropriately labeled scintillation vials to serve as the calibrators for the radioactivity analysis. A volume of 0.7 mL of basolateral transport buffer (10 mM HEPES in Hank's balanced salt solution, pH 7.4, containing a matched % organic to the dosing solution) was added to the basolateral compartment of the "experiment plate". Wash buffer was aspirated from each Transwell® insert and 0.3 mL of the dosing solution prepared above was added to the filter inserts and the filters were moved to the experiment plate. Cells were incubated at 37ºC for the following timepoints: 2, 5, 10, 15, 30, and 45 minutes. Following the timepoints, Transwell® inserts were moved to a 24-well plate placed on ice containing 0.5 mL of ice cold DPBS++ in each well. A 40 µL volume of the apical dosing media from each insert was collected and placed in an appropriately labeled scintillation vial for subsequent analysis. Following collection of apical samples, the inserts were then aspirated and then cells were washed three times with DPBS++. After the third wash, inserts were aspirated and 150 µL of 1M sodium hydroxide was added to each Transwell® insert and the plate was moved off ice to allow for cells to lyse at room temperature for 1 hour. During the 1-hour incubation, 200 µL of the basolateral transport buffer from each well was placed in an appropriately labeled scintillation vial for subsequent analysis. For lucifer yellow analysis, a series of Lucifer Yellow standards were prepared during the 60-minute time period and added to a 96-well plate along with 200 µL of the basolateral transport buffer. The standards and samples were analyzed by fluorescence detection using a Synergy HTX multi-mode reader (BioSPX, Netherlands) with excitation filter at 420 nm and emission filter at 528 nm. BCA standards (catalog no. 23208, Thermo Scientific, MA) were added to a 96-well plate and kept at 4ºC until cell lyses was complete. After the hour incubation, 150 µL of 1M hydrochloric acid was added to each Transwell® insert to neutralize the cell lysate solution. 200 µL of the neutralized cell lysate solution was placed in an appropriately labeled scintillation vial for subsequent analysis and 25 µL was added to the 96-well plate containing BCA standards prepared earlier. BCA working reagent was prepared and 200 uL of the solution was added to each well of the 96-well plate containing BCA standards or cell lysate. The plate was then incubated at 37ºC for 30 minutes and then read on a Tecan SPARK multimode plate reader (Tecan Group Ltd., Switzerland), measuring an absorbance of 562 nm. Scintillation vials containing radioactive samples were analyzed using a Tri-Carb Liquid Scintillation Counter (Perkin Elmer, Waltham, MA, USA). Results for these studies are shown in **Figure 5.7**.

5.2.5. Metformin uptake kinetics assay

Enteroid monolayers were moved from their original 24-well plate (“experiment plate”) to a blank 24-well (“wash plate”) and washed three times with blank apical transport buffer (10 mM HEPES in Hank’s balanced salt solution, pH 6.5) and maintained at 37ºC until use. Eight dosing solutions were created in apical transport buffer with the final cold (nonradiolabeled) metformin concentrations of 10, 50, 250, 750, 1000, 3000, 6000, and 9000 μM. Stock solutions of radiolabeled [^{14}C] metformin (1.7 mM, in water) and radiolabeled [^{3}H] mannitol (50 mM, in ethanol) were diluted into each dosing solution to a final concentration of 10 μM and 50 μM for radiolabeled metformin and mannitol, respectively (containing 0.1% ethanol v/v). A volume of 0.7 mL of basolateral transport buffer (10 mM HEPES in Hank’s balanced salt solution, pH 7.4, containing 0.1% ethanol v/v) was added to the basolateral compartment of the “experiment plate”. Wash buffer was aspirated from each Transwell® insert and 0.3 mL of the dosing solution prepared above was added to the filter inserts and the filters were moved to the experiment plate. Cells were incubated at 37ºC for the linear time range of uptake determined for each donor in the metformin uptake linearity experiment detailed above. The sample collection, Transwell® wash, BCA assay, and radioactive sample analysis was performed as described above. Metformin uptake kinetics were determined in R Studio (R. Posit Software, PBC, Boston, MA) using the drc package (Ritz et al., 2015).

5.2.6. Metformin inhibition experiments

For the sub-clinical metformin dose experiments, enteroid monolayers were moved from their original 24-well plate ("experiment plate") to a blank 24-well ("wash plate") and washed three times with blank apical transport buffer (10 mM HEPES in Hank's balanced salt solution, pH 6.5) and maintained at 37ºC until use. A stock solution of decynium-22 (2 mM, in DMSO) was diluted in apical transport buffer to a final dosing concentration of 2 µM (0.1% DMSO, v/v). A matched vehicle control for the decynium-22 condition was created by diluting blank DMSO in apical transport buffer to a final %DMSO of 0.1% (v/v). Goldenseal dosing buffer was created by directly dissolving goldenseal extract in apical transport buffer, with sonication to aid in dissolution of the product, to a final dosing concentration of 1.2 mg/mL. This dose of goldenseal was chosen as it is close to the expected intestinal luminal concentration of goldenseal following a 1 gram dose (approximately 4 mg/mL) while maintaining goldenseal extract solubility. A matched vehicle control for the goldenseal condition was pure apical transport buffer without the addition of organic solvents. For experimental conditions where goldenseal was present in the basolateral chamber, goldenseal extract was dissolved in basolateral transport buffer (10 mM HEPES in Hank's balanced salt solution, pH 7.4), with sonication to aid in dissolution of the product, to a final dosing concentration of 1.2 mg/mL. A small aliquot of the inhibitor dosing solutions was set aside for the inhibitor preincubation. Wash buffer was aspirated from each Transwell® insert and 100 µL of inhibitor dosing solution was added to the apical chamber of the appropriate wells and 0.5 mL of blank basolateral buffer was added to the basolateral chamber. For experimental conditions with goldenseal present in the basolateral chamber, 0.5 mL of the goldenseal dosing solution dissolved in basolateral transport buffer was added to the basolateral chamber. Cells were incubated at 37ºC for 15 minutes with their respective inhibitor solutions. During the 15-minute preincubation, stock solutions of radiolabeled [^{14}C] metformin

(1.7 mM, in water) and radiolabeled [^{3}H] mannitol (50 mM, in ethanol) were diluted into each inhibitor dosing solution to a final concentration of 2 µM and 50 µM for radiolabeled metformin and mannitol, respectively (containing 0.1% ethanol v/v). 0.7 mL of basolateral transport buffer (10 mM HEPES in Hank's balanced salt solution, pH 7.4, containing 0.1% ethanol v/v) was added to the basolateral compartment of the "experiment plate". For experimental conditions with basolateral goldenseal, the basolateral transport buffer contained 1.2 mg/mL goldenseal. Following the 15-minute preincubation period, inhibitor preincubation solutions was aspirated from each Transwell® insert and 0.3 mL of the dosing solution prepared above was added to the filter inserts and the filters were moved to the experiment plate. Cells were incubated at 37ºC for the linear time range of uptake determined for each donor in the metformin uptake linearity experiment detailed above. The sample collection, Transwell® wash, BCA assay, and radioactive sample analysis was performed as described above.

For the goldenseal-metformin inhibition experiment using clinically relevant metformin doses, enteroid monolayers were moved from their original 24-well plate ("experiment plate") to a blank 24-well ("wash plate") and washed three times with blank apical transport buffer (10 mM HEPES in Hank's balanced salt solution, pH 6.5) and maintained at 37ºC until use. Goldenseal dosing buffer was created by directly dissolving goldenseal extract in apical transport buffer, with sonication to aid in dissolution of the product, to a final dosing concentration of 1.2 mg/mL. A matched vehicle control for the goldenseal condition was pure apical transport buffer without the addition of organic solvents. A small aliquot of the inhibitor dosing solutions was set aside for the inhibitor preincubation. Additionally, four dosing solutions were created in blank apical transport buffer with the final cold (nonradiolabeled) metformin concentrations of 1.5, 17.5, 35, and 70 mM. An additional four dosing solutions were created in apical transport buffer containing 1.2 mg/mL goldenseal with the final cold (nonradiolabeled) metformin concentrations of 1.5, 17.5, 35, and 70 mM. Wash buffer was aspirated from each Transwell® insert and 100 μL of inhibitor dosing solution was added to the apical chamber of the appropriate wells and 0.5 mL of blank basolateral buffer was added to the basolateral chamber. During the 15-minute preincubation, stock solutions of radiolabeled [^{14}C] metformin (1.7 mM, in water) and radiolabeled [^{3}H] mannitol (50 mM, in ethanol) were diluted into each inhibitor dosing solution to a final concentration of 10 μM and 50 μM for radiolabeled metformin and mannitol, respectively (containing 0.1% ethanol v/v). A volume of 0.7 mL of basolateral transport buffer (10 mM HEPES in Hank's balanced salt solution, pH 7.4, containing 0.1% ethanol v/v) was added to the basolateral compartment of the "experiment plate". Following the 15-minute preincubation, inhibitor preincubation solutions were aspirated from each Transwell® insert and 0.3 mL of the dosing solution prepared above was added to the filter inserts and the filters were moved to the experiment plate. Cells were incubated at 37°C for the linear time range of uptake determined for each donor in the metformin uptake linearity experiment detailed above. The sample collection, Transwell® wash, BCA assay, and radioactive sample analysis was performed as described above.

For the cation specific inhibitor experiment, enteroid monolayers were moved from their original 24-well plate ("experiment plate") to a blank 24-well ("wash plate") and washed three times with blank apical transport buffer (10 mM HEPES in Hank's balanced salt solution, pH 6.5) and maintained at 37°C until use. Stock solutions of the inhibitors, corticosterone (37.5 mM in DMSO), desipramine (50 mM in DMSO), thiamine (50 mM in water), were diluted in apical transport buffer to a final concentration of 150 μM, 200 μM, and 100 μM for corticosterone, desipramine, and thiamine, respectively. Paroxetine and MPP^{+} powder were dissolved directly in apical transport buffer to final concentrations of 0.1 μM and 5 mM, respectively. DMSO was added to the thiamine, paroxetine, and MPP$^+$ dosing solutions to a final concentration of 0.4% (v/v) to keep the %DMSO consistent across all dosing solutions. Vehicle control dosing solution was prepared by diluting DMSO in apical transport buffer to a final concentration of 0.4% (v/v). A stock solution of thiamine (50 mM in water) was added to blank basolateral transport buffer (10 mM HEPES in Hank's balanced salt solution, pH 7.4) to a final concentration of 100 μM. A small aliquot of the inhibitor dosing solutions was set aside for the inhibitor preincubation. Wash buffer was aspirated from each Transwell® insert and 100 μL of inhibitor dosing solution was added to the apical chamber of the appropriate wells and 0.5 mL of blank basolateral buffer was added to the basolateral chamber. For the thiamine experimental condition wells, 0.5 mL of the basolateral transport buffer containing thiamine is added to the basolateral chamber. During the 15-minute preincubation, stock solutions of radiolabeled [^{14}C] metformin (1.7 mM, in water) and radiolabeled [^{3}H] mannitol (50 mM, in ethanol) were diluted into each apical inhibitor dosing solution to a final concentration of 10 μM and 50 μM for radiolabeled metformin and mannitol, respectively (containing 0.1% ethanol v/v). 0.7 mL of basolateral transport buffer (containing 0.1% ethanol, v/v, and 0.4% DMSO, v/v) was added to the basolateral compartment of the "experiment plate". For the thiamine experimental condition wells, 0.7 mL of the basolateral transport buffer containing thiamine (with 0.1% ethanol, v/v, and 0.4% DMSO, v/v) is added to the basolateral chamber. Following the 15-minute preincubation, inhibitor preincubation solutions were aspirated from each Transwell® insert and 0.3 mL of the dosing solutions prepared above was added to the filter inserts and the filters were moved to the experiment plate. Cells were incubated at 37ºC for the linear time range of uptake determined for each donor in the metformin uptake linearity experiment detailed above. The sample collection, Transwell® wash, BCA assay, and radioactive sample analysis was performed as described above.

5.2.7. Serotonin and thiamine inhibition experiments

Enteroid monolayers were moved from their original 24-well plate ("experiment plate") to a blank 24-well ("wash plate") and washed three times with blank apical transport buffer (10 mM HEPES in Hank's balanced salt solution, pH 6.5) and maintained at 37ºC until use. A stock solution of nonradiolabed ("cold thiamine") was diluted in apical transport buffer to a final concentration of 100 µM. Goldenseal and paroxetine dosing buffers were created by directly dissolving goldenseal extract or paroxetine powder in apical transport buffer, with sonication to aid in dissolution of the product, to a final dosing concentration of 1.2 mg/mL and 0.1 µM, respectively. Pure apical transport buffer without the addition of organic solvents was used as the matched vehicle control. Small aliquots of the inhibitor dosing solutions and vehicle control were set aside for the inhibitor preincubation. Wash buffer was aspirated from each Transwell® insert and 100 µL of inhibitor dosing solution was added to the apical chamber of the appropriate wells and 0.5 mL of blank basolateral buffer was added to the basolateral chamber. Cells were incubated at 37ºC for 15 minutes with their respective inhibitor solutions. Stock solutions of test compounds; radiolabeled [^{3}H] serotonin (12.5 mM) in water:ethanol:TFA:mercaptoethanol (98:2:0.1:0.2, v/v); and radiolabeled [^{3}H] thiamine (10 mM) in water:ethanol (1:1, v/v) were diluted in apical transport buffer to make their respective dosing solutions (final concentrations of 3 µM and 5 µM, respectively). Each dosing solution contained Lucifer Yellow at a final concentration of 300 µM, prepared from a 60 mM stock solution in water, to serve as the barrier integrity control. 4 µL of the dosing solutions were added to appropriately labeled scintillation vials to serve as the calibrators for the radioactivity analysis. 0.7 mL of basolateral transport buffer (10 mM HEPES in Hank's balanced salt solution, pH 7.4, containing a matched % organic to the dosing solution) was added to the basolateral compartment of the "experiment plate". Following the 15-minute inhibitor preincubation, wash buffer was aspirated from each Transwell® insert and 0.3 mL of the dosing solution prepared above was added to the filter inserts and the filters were moved to the experiment plate. Cells were incubated at 37ºC for the linear time range of uptake determined for each donor in the serotonin and thiamine uptake linearity experiment detailed above. The sample collection, Transwell® wash, BCA assay, and radioactive sample analysis was performed as described above.

5.2.8. Permeability coefficient calculation

The apparent permeability of coefficient for metformin, serotonin, thiamine, mannitol, and Lucifer Yellow was calculated as described in a previous report by our group using equation 1:

$$P_{app} = \frac{dQ}{dt} \cdot \frac{1}{SA \cdot C_0}$$

where dQ/dt is the rate of compound appearance in the basolateral chamber (pmol/s) under sink conditions, SA is the surface area of the Transwell® filter insert (cm^2), and C_0 is the dosing concentration of compound in the apical compartment. If the paracellular marker compounds, mannitol or Lucifer Yellow, P_{app} values exceeded our predefined cutoff of 1×10^{-6} cm/s, transcellular flux data from these wells were not included in the final analysis, as these wells did not have an appropriate barrier to accurately determine test compound permeability.

5.2.9. RNA analysis.

Cells were lysed in each insert using 0.25 mL of RLT Lyses buffer and brought up to a final volume of 0.5 mL of RLT Lyses buffer and stored at -80ºC until further analysis. Total RNA was isolated according to the manufacturer-supplied protocol for RNeasy Mini Kit (Qiagen –

Germantown, MD). Isolated RNA concentration was determined using a Nanodrop spectrophotometer ND-1000 (Thermo Scientific, Wilmington, DE). Reverse transcription was performed according to the manufacturer-supplied protocol for Applied Biosystems High-Capacity cDNA Reverse Transcription Kit. Each reaction contained 2 µL of 10X RT Buffer, 0.8 µL of 25× dNTP Mix (100 nM), 2 µL of 10× Random Primer mix, 1 µL of MultiScribeTM Reverse Transcriptase, 4.2 µL of nuclease-free water, and 10 µL of the isolated RNA for a final volume of 20 µL. The reverse transcription condition was set as 25°C for 10 minutes, 37°C for 120 minutes, 85°C for 5 minutes, and held at 4°C until sample retrieval using a C1000 Touch(TM) Thermal Cycler (Bio-Rad, Hercules, CA). Following reverse transcription, cDNA samples were diluted with nuclease-free water to obtain a concentration of 2.5 ng/µL. qPCR was performed using TaqMan assays and the TaqMan Fast Advanced Master Mix with a QuantStudio 3 system (Applied Biosystems, Bedford, MA). Each PCR mixture consisted of 10 µL of TaqMan Fast Advanced Master Mix, 5 µL of nuclease-free water, 1 µL of TaqMan Gene Expression Assay, and 4 µL of cDNA. The qPCR conditions were as follows: a denaturation step at 50°C for 2 minutes followed by 95°C for 10 minutes, 40 cycles of PCR (denaturation at 95°C for 15 seconds and annealing and extension at 60°C for 1 minute). All tested gene products were quantified using comparative ΔCt calculation for relative quantification of gene expression to the endogenous housekeeping gene product glyceraldehyde-3-phosphate dehydrogenase (GAPDH).

5.2.10. Statistical analysis.

Statistical significance ($\alpha = 0.05$) for inhibition studies was determined via generalized estimating equations using the “gee” package (Carey, 2024) in RStudio (R. Posit Software, PBC, Boston, MA), which applies a generalized linear model to the data to determine coefficients of interaction. Models were run using an exchangeable correlation structure.

5.3. RESULTS

5.3.1. Metformin uptake kinetics across enteroid monolayers.

The concentration-dependent kinetics of metformin uptake from the apical chamber into monolayer cells and from the apical to basolateral chamber are shown in **Figure 5.2**. Metformin uptake from the apical chamber into cells displayed saturating kinetics, with a V_{max} ranging from 0.092 to 0.48 nmol/min/mg total protein and a K_m ranging from 3.9 to 14.6 mM. Strikingly, the flux of metformin from the apical to basolateral chamber exhibited concentration-proportional linear kinetics across all concentrations tested.

5.3.2. Goldenseal-mediated inhibition of sub-clinical metformin doses

The effect of apically-dosed goldenseal on intracellular uptake and transcellular flux of a sub-saturating metformin dose (2 µM), which is much lower than the measured K_m, is shown in **Figure 5.3a-b**. Decynium-22 was included in this experiment as a positive control, as it is a known inhibitor of OCT1, OCT3, PMAT, and SERT (Horton et al., 2013; Fraser-Spears et al., 2019). Both goldenseal and decynium-22 inhibited intracellular metformin uptake, by approximately 70% and 30%, respectively. However, the apical to basolateral flux of metformin was not changed following treatment with either inhibitor, though a trend of modestly decreased flux was seen with 3 of the 4 donors.

5.3.3. Goldenseal-mediated inhibition of clinically relevant metformin doses

The effects of goldenseal on intracellular uptake and transcellular flux of clinically relevant metformin doses are shown in **Figure 5.4**. The metformin dosing concentration used in this study corresponded to a subtherapeutic dose (1.5 mM), a low dose (17.5 mM), a medium dose (35 mM), and a high dose (70 mM). The dose concentrations chosen mimic expected intestinal luminal concentrations from four different dosing groups in the completed *in vivo* clinical studies (unpublished data, Mary Paine, 2024). Results show that goldenseal inhibited the intracellular uptake of a subtherapeutic dose of metformin by approximately 30% but had no effect on cell uptake of the low, medium, or high doses of metformin. Interestingly, goldenseal decreased the apical to basolateral flux of metformin for all dosing groups, by ~20% on average.

5.3.4. RNA expression of transporters that may play a role in metformin uptake

The qPCR results for the gene products of solute carrier (SLC) transporters that may play a role in the transport of metformin across apical and basolateral membranes are shown in **Figure 5.5**. Transporters investigated were *SLC19A2* (ThTr-1), *SLC19A3* (ThTr-2), *SLC22A1* (OCT1), *SLC22A3* (OCT3), *SLC29A4* (PMAT), and *SLC6A4* (SERT). All SLC transporters had quantifiable expression, with PMAT, ThTr-1, and ThTr2 having the highest expression levels relative to the housekeeping gene, GAPDH.

Effect of specific inhibitors on metformin uptake. The impact of specific cation transporter inhibitors on metformin uptake are shown in **Figure 5.6**. The inhibitors included; corticosterone (150 μM) to inhibit OCT1 and OCT3; desipramine (200 μM) to inhibit OCT1, OCT3, and PMAT; paroxetine (0.1 μM) to inhibit SERT; thiamine (100 μM) to inhibit ThTr-1 and ThTr-2; and MPP^+ (5 mM) to inhibit all carrier-mediated transport processes. The inhibitor dosing concentrations were adapted from a similar study assessing metformin uptake transporters in Caco-2 cells (Han et al., 2015). Intracellular uptake of metformin was 45% by thiamine and 70% by MPP^+. Interestingly, metformin apical to basolateral flux was only inhibited by MPP^+, by approximately 20%.

Goldenseal-mediated inhibition of SERT, ThTr-1, and ThTr-2. The effect of goldenseal on the uptake of radiolabeled serotonin and radiolabeled thiamine, SERT and ThTr-1/ThTr-2 probes, respectively, is shown in **Figure 5.8**. Goldenseal treatment resulted in no significant change in intracellular uptake of serotonin but resulted in decreased apical to basolateral flux of serotonin by approximately 40%. The transcellular flux results closely mimic that of the positive control for SERT inhibition, paroxetine. Similarly, goldenseal treatment resulted in a decreased intracellular uptake of thiamine by approximately 65% and decreased apical to basolateral flux of thiamine by approximately 20%. The intracellular uptake results closely mimic that of the positive control for ThTr-2 inhibition, non-radiolabeled thiamine, while goldenseal resulted a greater magnitude of inhibition of apical to basolateral flux than non-radiolabeled thiamine.

5.4. DISCUSSION

With the sale and use of NPs on the rise, there is an increased need for more physiologically relevant *in vitro* models of the human intestine to predict the potential for these products to precipitate NPDIs before they arise in the clinic. Results presented in this article investigated the utility of human enteroid monolayers, derived from the duodenum of four adult donors, cultured on Transwell® inserts as a model to predict the metformin-goldenseal interaction seen *in vivo*. Our initial studies sought to elucidate the kinetics of metformin uptake from the apical chamber into cells and from apical to basolateral chamber. Metformin uptake followed single transporter Michaelis-Menten kinetics for a relatively low affinity process. Considering the doses used in the *in vivo* metformin-goldenseal clinical studies, this suggests that only the subtherapeutic metformin dose would result in intestinal luminal concentrations of metformin below the reported K_m value – further suggesting that at higher doses there would be an attenuated effect of goldenseal on the uptake of metformin intracellularly due to saturation of the uptake mechanisms. That is what occurred but, curiously, the flux of metformin from the apical to basolateral chamber was linear with respect to the dosing concentration at all concentrations tested. Those results suggest that most of the A > B metformin flux involves a basolateral process(es) that is rate-determining under all therapeutic and sub-therapeutic metformin dosing conditions tested. For the proportion that is transporter dependent, it may involve a saturable basolateral process(es) that is rate-determining with respect to apical membrane transport under all metformin dosing conditions. The basolateral transporter-dependent A > B flux can be inhibited by goldenseal and other cation transport inhibitors (e.g., MPP^+), if present at a sufficiently high enough concentration to outcompete metformin for binding to the basolateral transporter(s). The fact that the A > B metformin flux is proportional to the apical metformin dosing concentration and largely (~80%) not inhibited by goldenseal or MPP^+ suggest that there is substantial paracellular transport, as other investigators have suggested (Proctor et al., 2008).

Following the elucidation of metformin intracellular uptake and transcellular flux kinetics, we performed a preliminary inhibition experiment utilizing decynium-22, a known inhibitor of OCT1, OCT3, PMAT, and SERT, and goldenseal. The apical metformin dose used in this experiment, 2 μM, was far below the measured K_m values. Both goldenseal and decynium-22 inhibited metformin intracellular uptake; the greater magnitude of inhibition seen with goldenseal-treated monolayers indicates that goldenseal is inhibiting other transporters, either separately or in conjunction with those inhibited by decynium-22. Curiously, the transcellular A > B flux of metformin was not inhibited by either goldenseal or decynium-22, though there was a modest trend of decreased flux seen with goldenseal and three of the donors used in this study. Again, these results suggest that basolateral transporters are not significantly important to transcellular flux at this low concentration of metformin and that, again, passive paracellular transport of the highly charged metformin molecule dominates transepithelial absorption, as others have speculated in studies with Caco-2 cells (Han et al., 2015; Shirasaka et al., 2022).

We next performed a metformin-goldenseal inhibition experiment using metformin dosing concentrations from the *in vivo* clinical studies, which were calculated by taking the doses used in the clinical study divided by 250 mL, representing gastric fluid volume (Grimm et al., 2023). This approach assumes each subject in the clinical studies administered their metformin dose with 240 mL of water – which may not be true, particularly for the second goldenseal clinical study as these subjects self-administered their metformin in a nonclinical setting throughout the study. Lower volumes of water administered with the metformin doses would lead to higher intestinal concentrations than we have predicted, exacerbating the potential for saturation of the apical transporters. Additionally, the administered volume of water may not necessarily be the volume of water that reaches the small intestine (Mudie et al., 2014). Nevertheless, the 250 mL volume is a commonly used approach often used in bioavailability/bioequivalence studies and was chosen for this study. The *in vitro* concentrations used corresponded to a subtherapeutic dose (1.5 mM), low dose (17.5 mM), medium dose (35 mM), and high dose (70 mM). Results demonstrate that goldenseal inhibits metformin uptake into cells for the subtherapeutic dosing condition by approximately 30%, but does not inhibit uptake for the low, medium, or high dosing condition. These results corroborate the metformin uptake kinetics results, which yielded a K_m value that was approximately 4-fold higher than the subtherapeutic dosing concentration, but approximately 2- to 8-fold lower than the low to high metformin dosing concentration. Additionally, the decreased magnitude of inhibition of the intracellular uptake of metformin from the subtherapeutic dose (1.5 mM), compared to the subclinical dose (2 µM), is consistent with a subtherapeutic metformin concentration approaching the K_m value of metformin intracellular uptake, while the sub-clinical dose is >1000-fold lower than the measured K_m. Moreover, the observation that goldenseal inhibited A > B flux at the 1.5 mM – 70 mM dose concentrations and not at the 2 µM dose concentration suggests that basolateral transporters involved in A > B metformin flux under clinical conditions are different from those involved at the very low, sub-saturating (cell uptake) metformin dose concentration.

The effect of goldenseal on metformin transcellular flux following a range of metformin dosing conditions is in apparent conflict with results from the *in vivo* goldenseal clinical study in well managed type II diabetic patients, where there was an attenuated effect of goldenseal for the higher doses of metformin. However, the clinical study did show interindividual variability for the effect of goldenseal on metformin exposure, where some of the subjects in the medium and high dose groups displayed decreased metformin exposure when metformin was co-administered with goldenseal compared to control. Limited sample size and inter-individual variability might explain the apparent discrepancy.

To identify the transporters involved in metformin intracellular uptake and transcellular flux, we employed specific inhibitors of several cation transporters and a subclinical dose of metformin (10 μM). The design of this study was adapted from a similar study conducted in Caco-2 cells by Han et al. (ref), which implicated OCT1, PMAT, SERT, and CHT as the transporters involved in metformin intracellular uptake in Caco-2 cells. While these results are valuable, the Caco-2 cell line is a colorectal adenocarcinoma cell line, where there is known aberrant transporter expression (Sun et al., 2002) which may not accurately reflect the *in vivo* transporter expression in the small intestine. For example, there is no evidence of RNA expression or protein abundance of CHT in the human small intestine (Oyanna et al., 2023). Our RT-qPCR results demonstrated robust expression of the PMAT, ThTr-1, and ThTr-2 genes in the enteroid monolayer model, consistent with our prior RNA-Seq findings (Arian et al., 2024). Using enteroid monolayers we showed that metformin intracellular accumulation was inhibited approximately 45% by thiamine and 70% by MPP^+– which are inhibitors of ThTr-2 and all carrier mediated transport processes, respectively. Unlike the results from Han et al., we did not observe inhibition of metformin intracellular uptake when cells were treated with corticosterone (OCT1 and OCT3 inhibitor), desipramine (OCT1, OCT3, and PMAT inhibitor), or paroxetine (SERT), suggesting that individually these transporters do not play a substantial role in intracellular uptake of metformin in human enteroid monolayers. The difference between the thiamine and MPP$^+$ inhibition suggest that there may an appreciable collective contribution or that additional transporter(s) mediate metformin intracellular uptake. More importantly from a clinical perspective, among the panel of transporter-selective inhibitors tested, only MPP$^+$ inhibited metformin transcellular A > B flux, with a modest inhibition of 20% compared to control, suggesting that a basolateral transporter outside of OCT1 and ThTr-1 is involved in the transport of metformin from the cells into the basolateral chamber. An important caveat to this conclusion is the fact only a sub-saturating metformin dose concentration (10 μM) was used to test the effect of selective inhibitors; the study was designed to identify the cell uptake transporter(s).

To further investigate the susceptibility of SERT and ThTr-1/2 to inhibition by goldenseal, we performed an inhibition experiment using the endogenous substrates of these transporters, serotonin and thiamine, respectively. Goldenseal treatment resulted in a decreased intracellular uptake and transcellular flux relative to control of thiamine, closely mimicking the inhibition seen with the positive inhibitor control (cold thiamine). Interestingly, goldenseal treatment imparted a greater magnitude of inhibition on thiamine flux than the positive control non-radiolabeled thiamine, which could be due to non-radiolabeled thiamine being dosed in the apical chamber only, which only reached substantial inhibitory concentrations at the apical ThTr-2 transporter binding site. Goldenseal treatment decreased serotonin transcellular flux but did not impact serotonin intracellular uptake, unlike the positive control inhibitor, paroxetine, which inhibited both transcellular flux and intracellular uptake. These results suggest that goldenseal does not inhibit SERT, which is localized to the apical membrane of the absorptive enterocytes, though there is a trend of decrease seen with two of the enteroid donors. Overall, these results indicate that goldenseal inhibits the thiamine transporters and further investigation in a larger number of donors is needed to confirm goldenseal's impact on SERT transport.

Our findings that ThTr-2 mediates metformin uptake across the apical enterocyte membrane is in line with a previous report from Oyanna et al, as is its inhibition by goldenseal (Oyanna et al., 2023). However, our collective results suggest that the *in vivo* goldenseal – metformin interactions (clinical and sub-clinical) involves an as yet unknown basolateral transporter and not ThTR-2 to any significant degree. This new hypothesis which we propose highlights the utility of enteroid monolayers in predicting NPDIs. Enteroid monolayers express various transporters *in vitro* that are present in the *in vivo* small intestine, allowing for broad screening for the potential for these transporters to be inhibited by NPs and drugs. While we were able to identify the apical transporter involved in the intracellular uptake of sub-saturating metformin doses that are inhibited by goldenseal, we were unable to identify the goldenseal-inhibitable, basolateral transporter(s) involved in the transcellular A > B flux of higher doses (≥ 1.5 mM) metformin. OCT1 or ThTr-1 would be obvious choices, but would require further study using selective inhibitors and higher doses of metformin.

While there is a discrepancy between the goldenseal-mediated inhibition from our *in vitro* A>B flux results and the *in vivo* pharmacokinetic results for clinically relevant metformin doses, these *in vitro* results are still informative. The *in vivo* study was not powered to assess differences in the goldenseal inhibition effect across the different metformin dosing groups, so the metformin dose-dependent impact of goldenseal-mediated inhibition *in vivo* requires additional study.

Additionally, the modest effects (10-30% decrease) of goldenseal-mediated inhibition on metformin A>B flux for clinically relevant metformin doses *in vitro* is not completely out of line with the observed *in vivo* data. Although only small decreases in metformin exposure and C_{max} were seen in the low and medium metformin dosing groups, there was inter-individual variability in the effect. The lack of statistical significance may be due to chance and the small number of subjects in each dosing group (n = 4 and n = 8, respectively).

One limitation of this report is the small number of stem cell donors (n=3 or 4) used in our experiments. Future studies can utilize a larger number of donors to account for potential interindividual variability in the natural product-drug interaction. Additionally, this report utilized stem cells obtained from the duodenum, which generated enteroids with a duodenal phenotype. The more distal segments of the small intestine, such as the jejunum and ileum, may play a large role for certain drugs due to their increased length and surface area, relative to the short duodenum, particularly for poorly absorbed drugs such as metformin. It is known that transporter expression patterns change along the length of the intestine (Drozdzik et al., 2014), which may impact experimental results and interpretation. Moreover, this study did not investigate the protein abundance of various cation transporters in the enteroid monolayers. While we investigated the mRNA expression of these transporters, the mRNA abundance does not always correspond to protein abundance, and as such protein abundance, particularly the abundance of transporters at the cell membrane, would be more informative.

In summary, these results suggest that metformin intracellular uptake is mediated predominately by ThTr-2, and that this transporter is inhibited by goldenseal, but that the goldenseal-inhibitable rate-limiting step in A > B metformin flux resides at the basolateral membrane, mediated by an as yet unknown cation transporter. Inhibition of this process can account for the observed goldenseal-metformin interaction *in vivo*. Our results also suggest that metformin transcellular flux is mediated predominately by paracellular transport. Collectively, our results suggest that enteroid monolayers are a promising model to study NPDIs and to understand the mechanisms that precipitate these interactions, though additional study is required to assess the accuracy of this model.

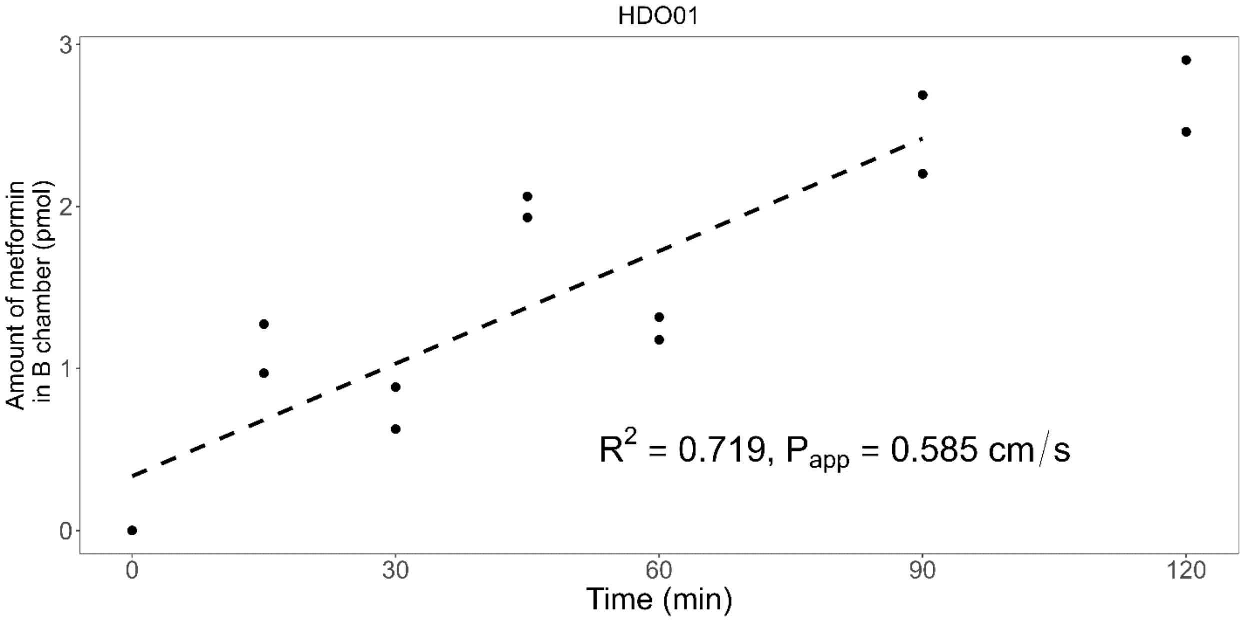

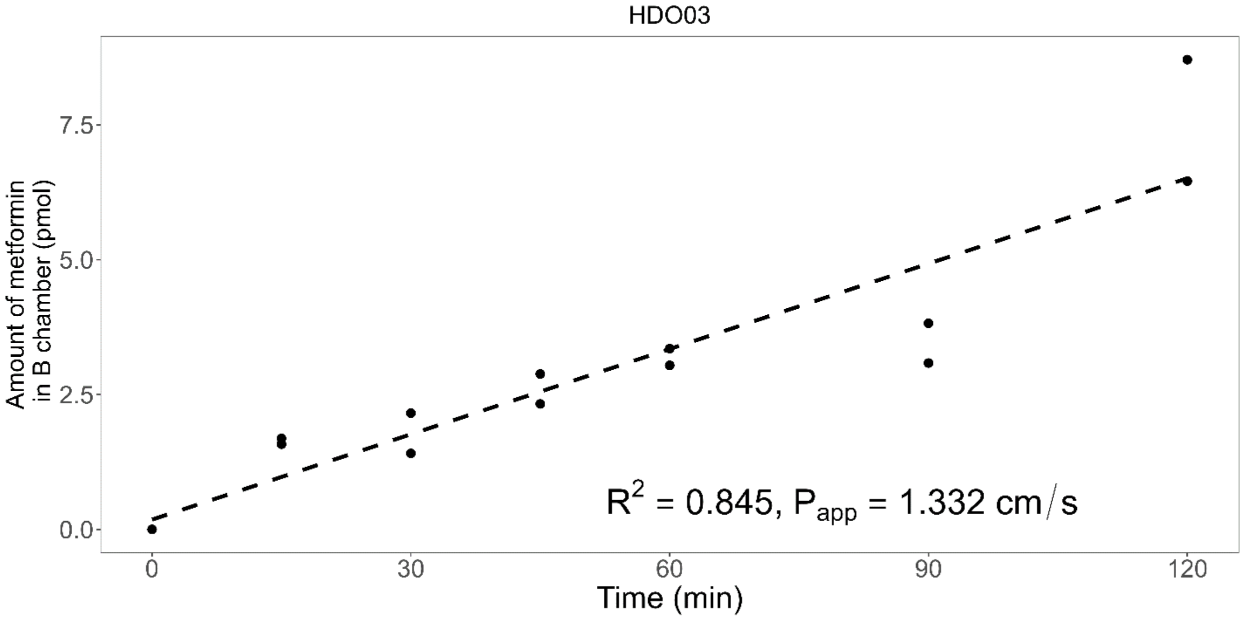
HDO03
Amount of metformin in B chamber (pmol)
0.0
2.5
5.0
7.5
0
30
60
90
120
Time (min)
R^2 = 0.845, P_{app} = 1.332 cm/s

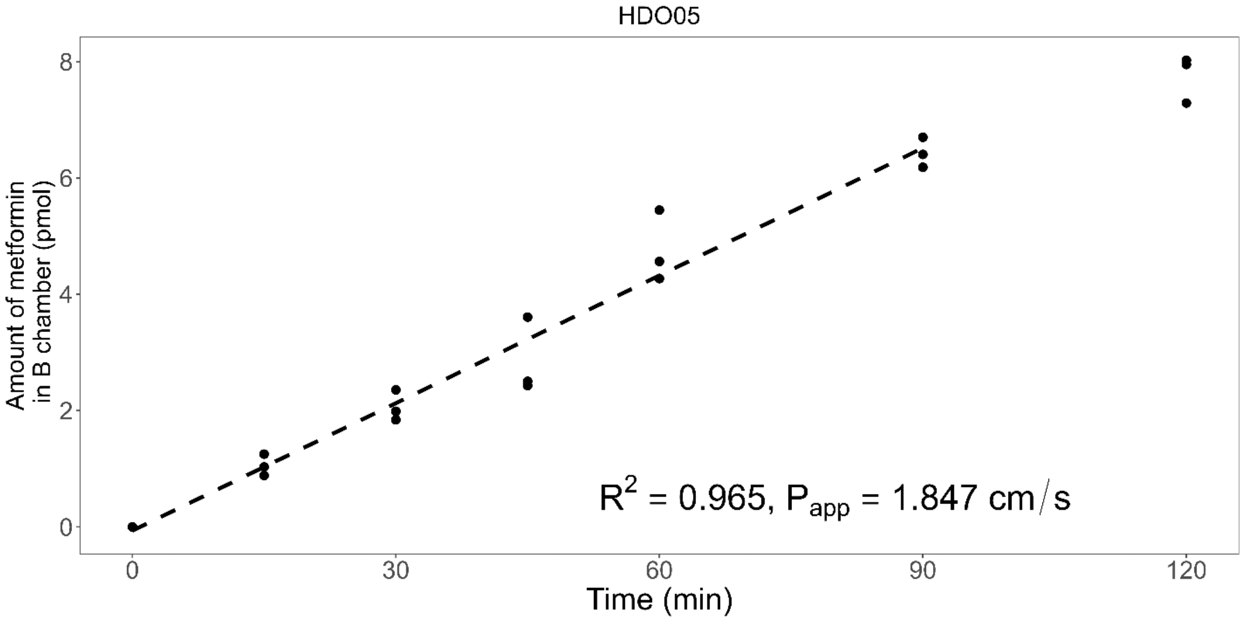
HDO05
Amount of metformin in B chamber (pmol)
0
2
4
6
8
0
30
60
90
120
Time (min)
R^2 = 0.965, P_{app} = 1.847 cm/s

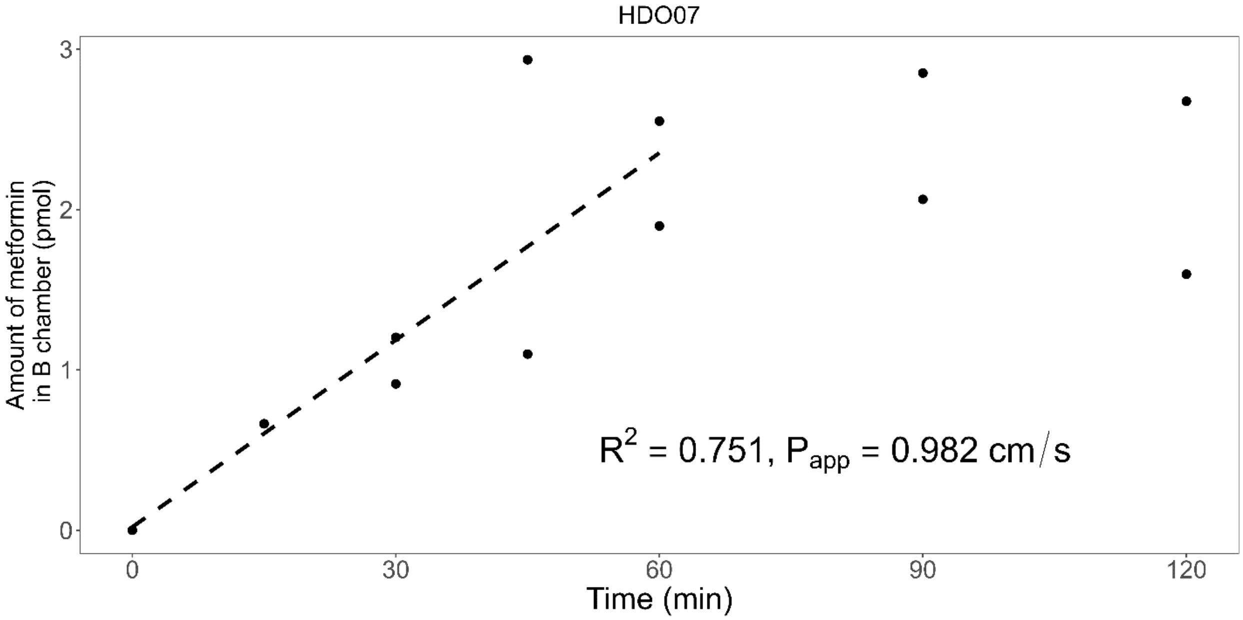

Figure 5.1. Metformin transcellular flux time linearity.

The transcellular flux linearity of metformin from A > B across enteroid monolayers for four donors. Dotten lines represent linear range up metformin transcellular flux. Goodness of fit and P_{app} values for each donor are presented on each plot.

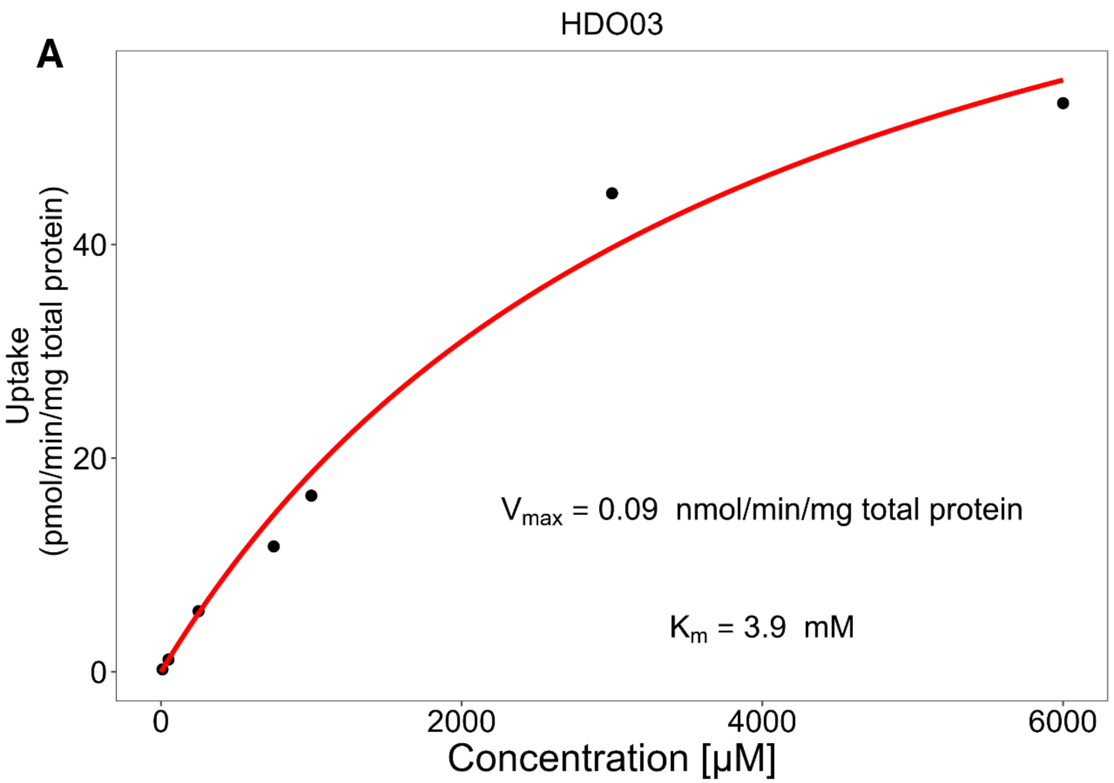
A
HDO03
Uptake
(pmol/min/mg total protein)
0
20
40
0
2000
4000
6000
Concentration [μM]
V_{max} = 0.09 nmol/min/mg total protein
K_m = 3.9 mM

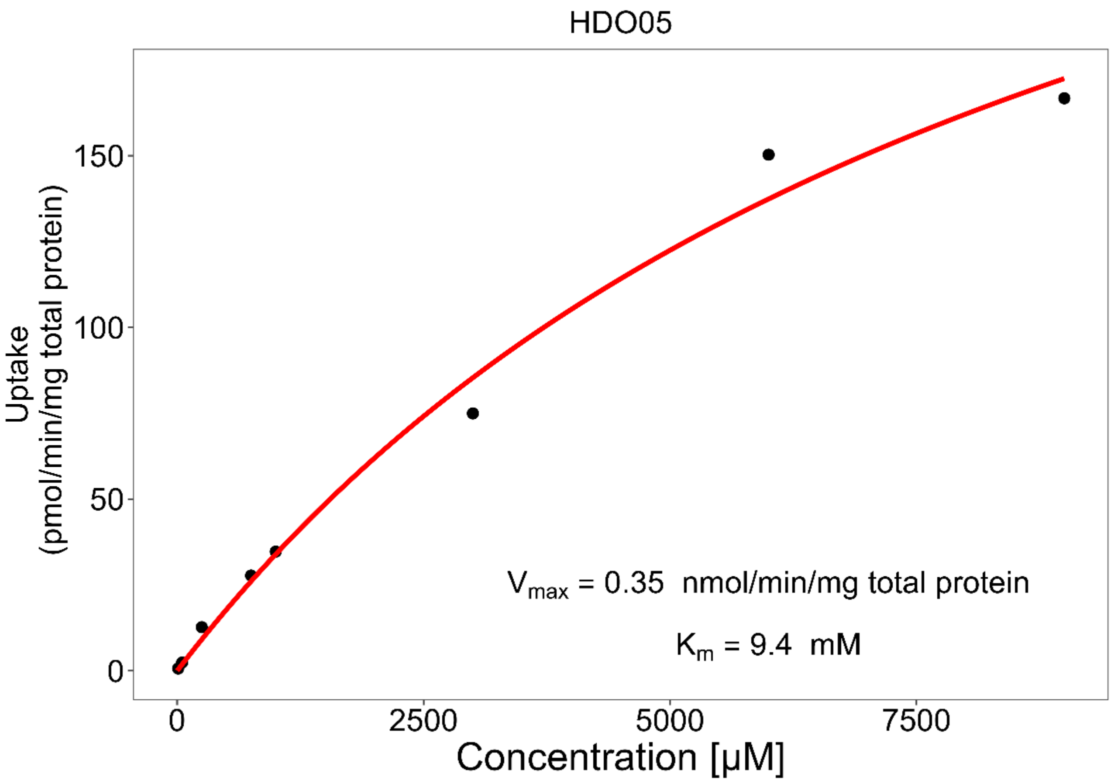
HDO05
Uptake
(pmol/min/mg total protein)
0
50
100
150
0
2500
5000
7500
Concentration [μM]
V_{max} = 0.35 nmol/min/mg total protein
K_m = 9.4 mM

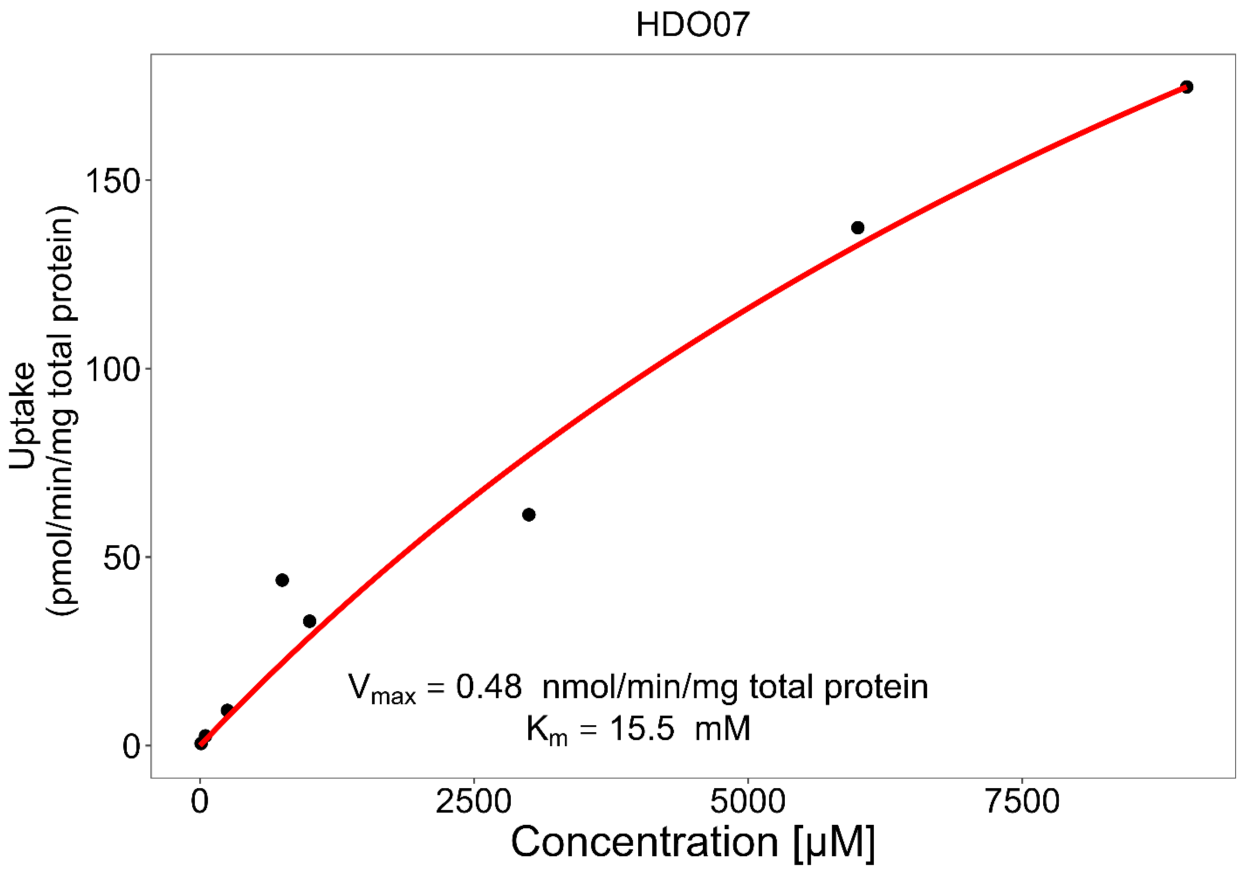
HDO07
Uptake
(pmol/min/mg total protein)
150
100
50
0
0
2500
5000
7500
Concentration [µM]
V_{max} = 0.48 nmol/min/mg total protein
K_m = 15.5 mM

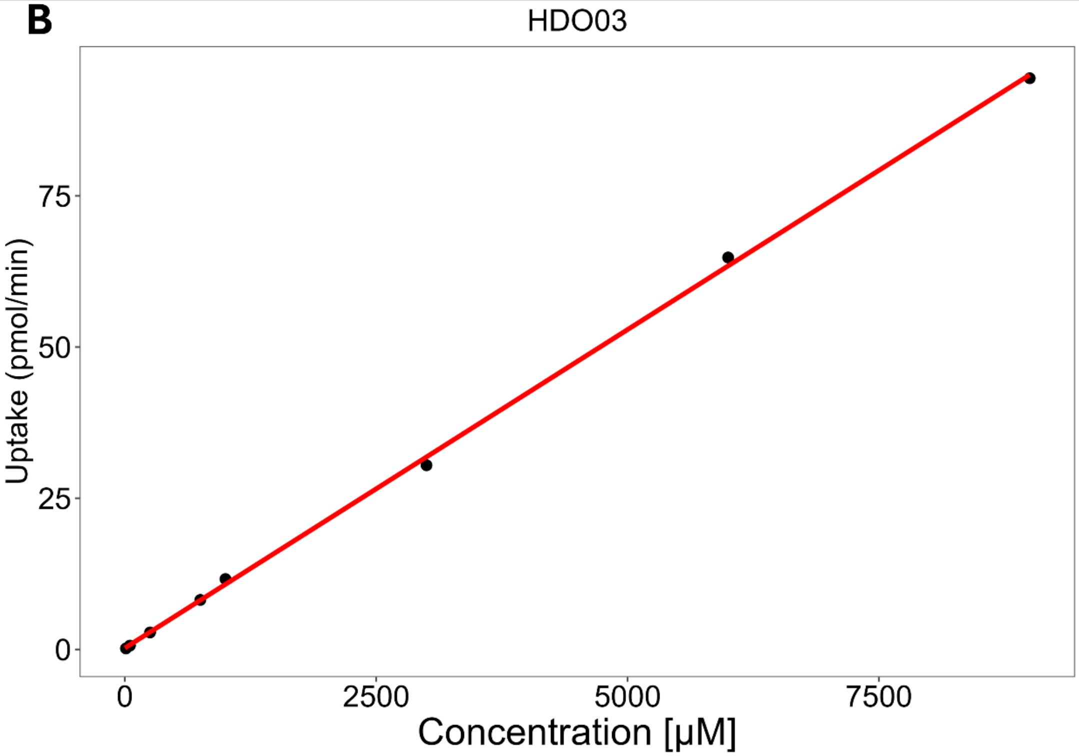
B
HDO03
Uptake (pmol/min)
0
25
50
75
0
2500
5000
7500
Concentration [μM]

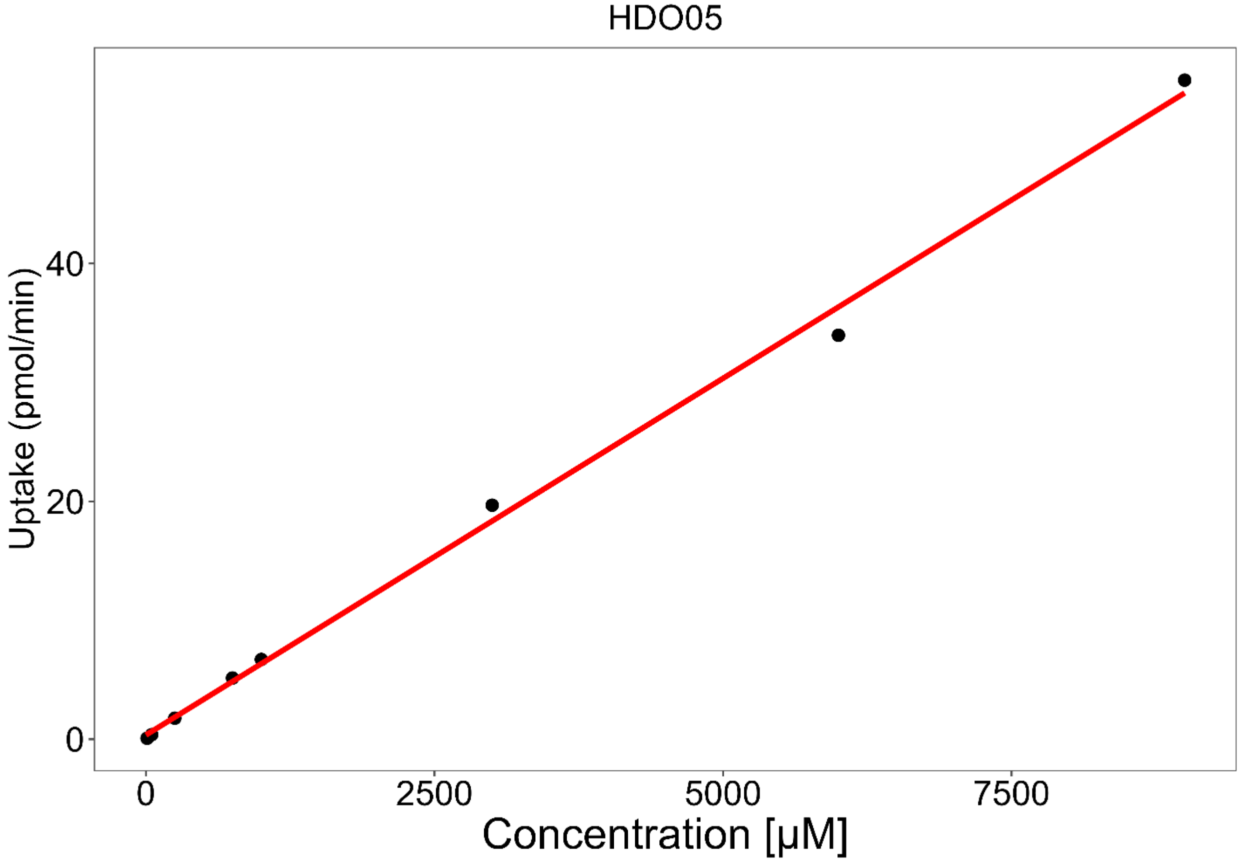
HDO05
Uptake (pmol/min)
0
20
40
0
2500
5000
7500
Concentration [μM]

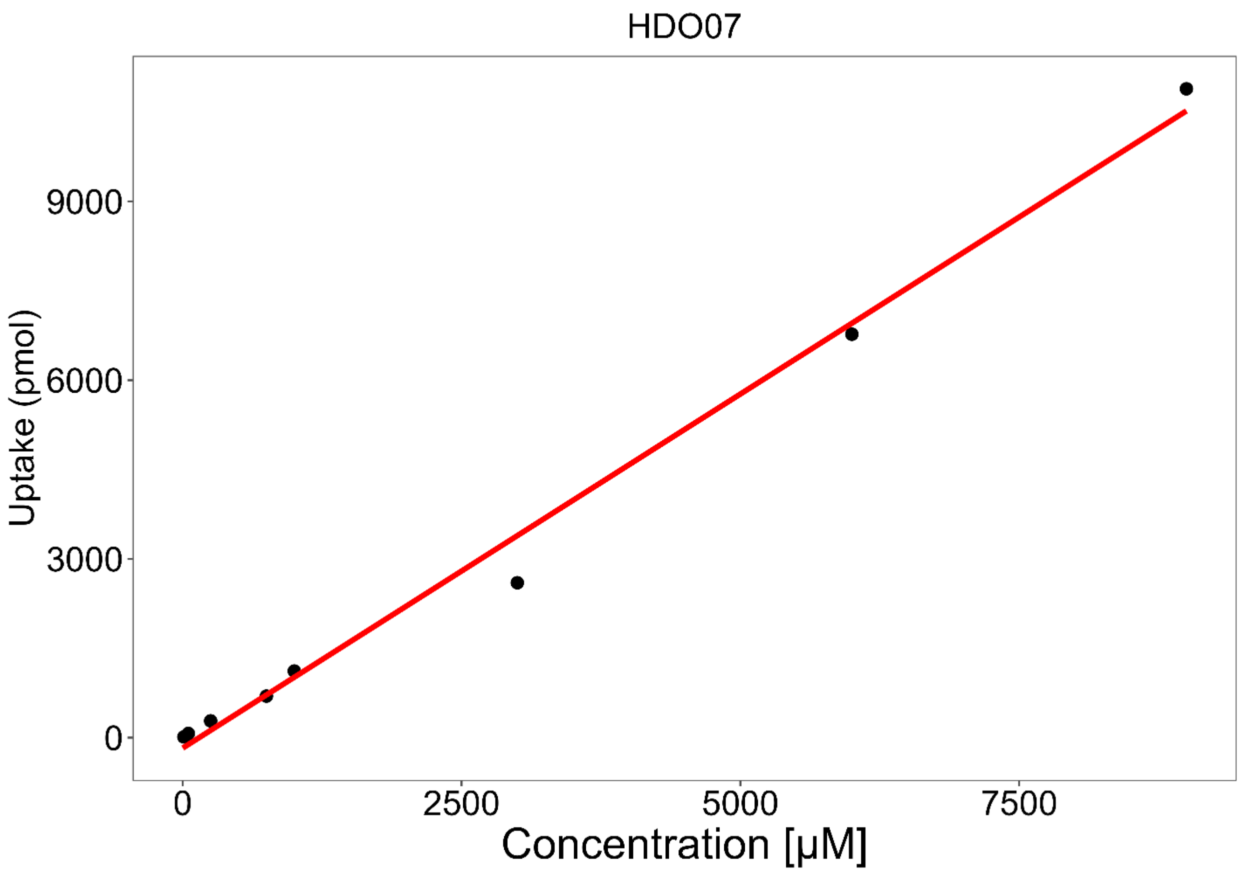

Figure 5.2. Metformin uptake kinetics.

Metformin concentration-depended kinetics for metformin intracellular uptake (a) and transcellular flux (b) across enteroid monolayers for three donors. Data points correspond to uptake values for individual culture replicates. The red lines correspond to the fit of a Michaelis-Menten model (a) or linear model (b) to the data. Individual donor K_m and V_{max} estimates are presented on the plots.

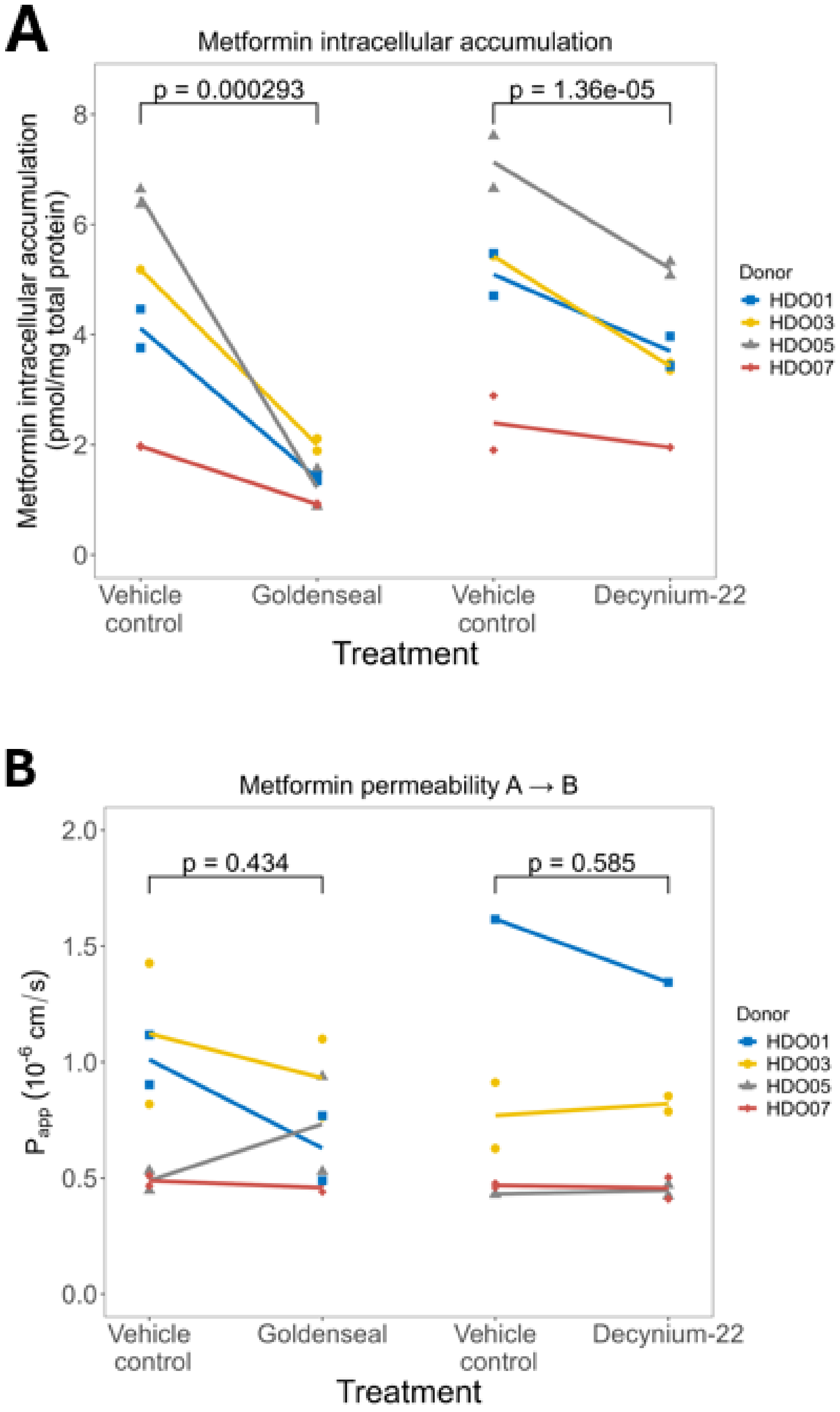
A
Metformin intracellular accumulation
Metformin intracellular accumulation (pmol/mg total protein)
p = 0.000293
p = 1.36e-05
0
2
4
6
8
Vehicle control
Goldenseal
Vehicle control
Decynium-22
Treatment
Donor
HDO01
HDO03
HDO05
HDO07
B
Metformin permeability A → B
P_{app} (10^{-6} cm/s)
p = 0.434
p = 0.585
0.0
0.5
1.0
1.5
2.0
Vehicle control
Goldenseal
Vehicle control
Decynium-22
Treatment
Donor
HDO01
HDO03
HDO05
HDO07

Figure 5.3. Goldenseal-mediated inhibition of a sub-clinical metformin dose. Intracellular uptake (a) and transcellular flux (b) of a sub-clinical dose of metformin (2 μM) across enteroid monolayers for four donors with and without the presence of goldenseal or decynium-22. Data points correspond to uptake values of individual culture replicates. Solid lines connect the mean uptake values across culture replicates for each donor. P values for each comparison are presented on the plots and were calculated via generalized estimating equations modeling.

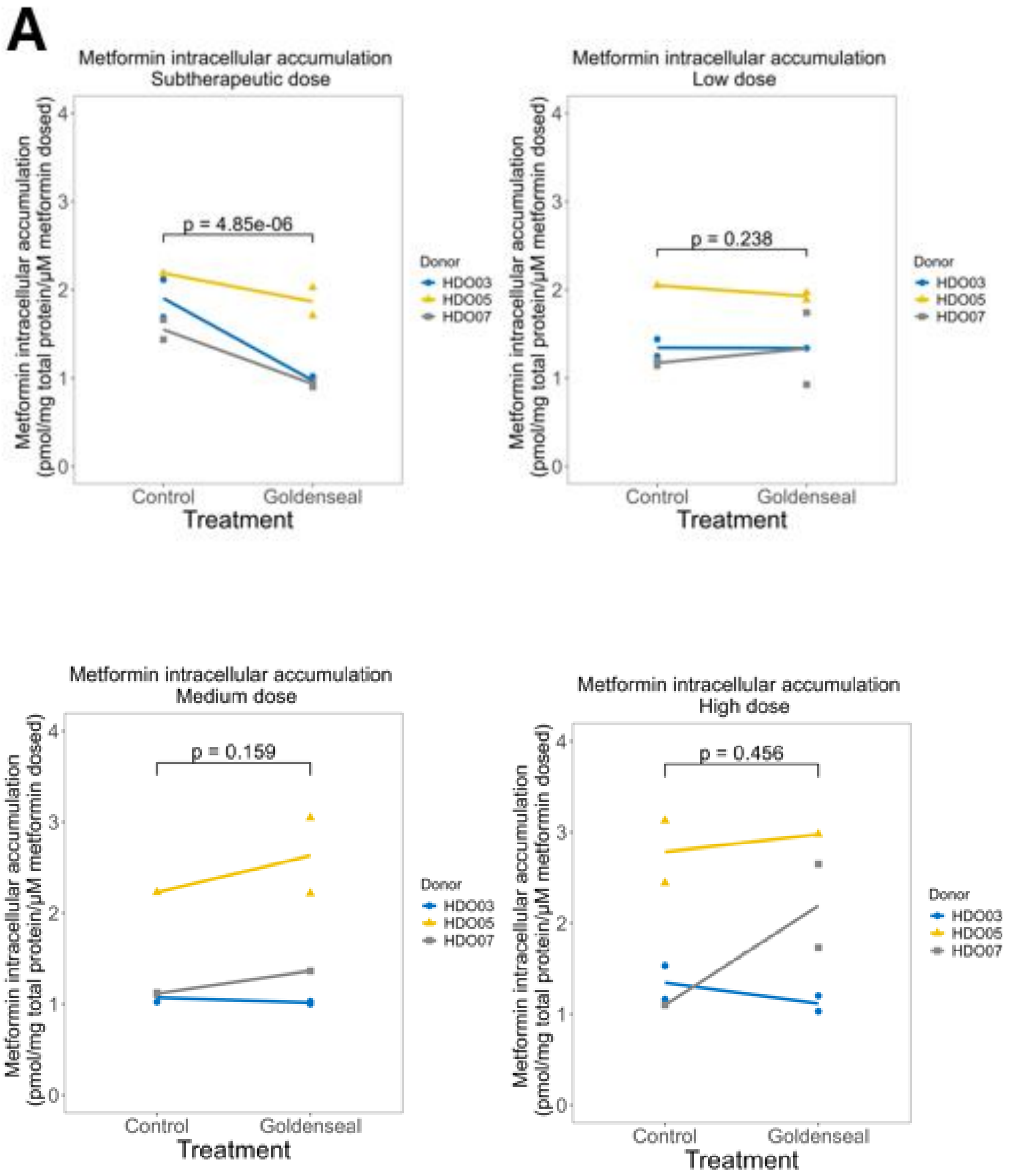
A
Metformin intracellular accumulation
Subtherapeutic dose
p = 4.85e-06
Metformin intracellular accumulation
Low dose
p = 0.238
Metformin intracellular accumulation
Medium dose
p = 0.159
Metformin intracellular accumulation
High dose
p = 0.456
Metformin intracellular accumulation (pmol/mg total protein/µM metformin dosed)
0
1
2
3
4
Control
Goldenseal
Treatment
Donor
HDO03
HDO05
HDO07

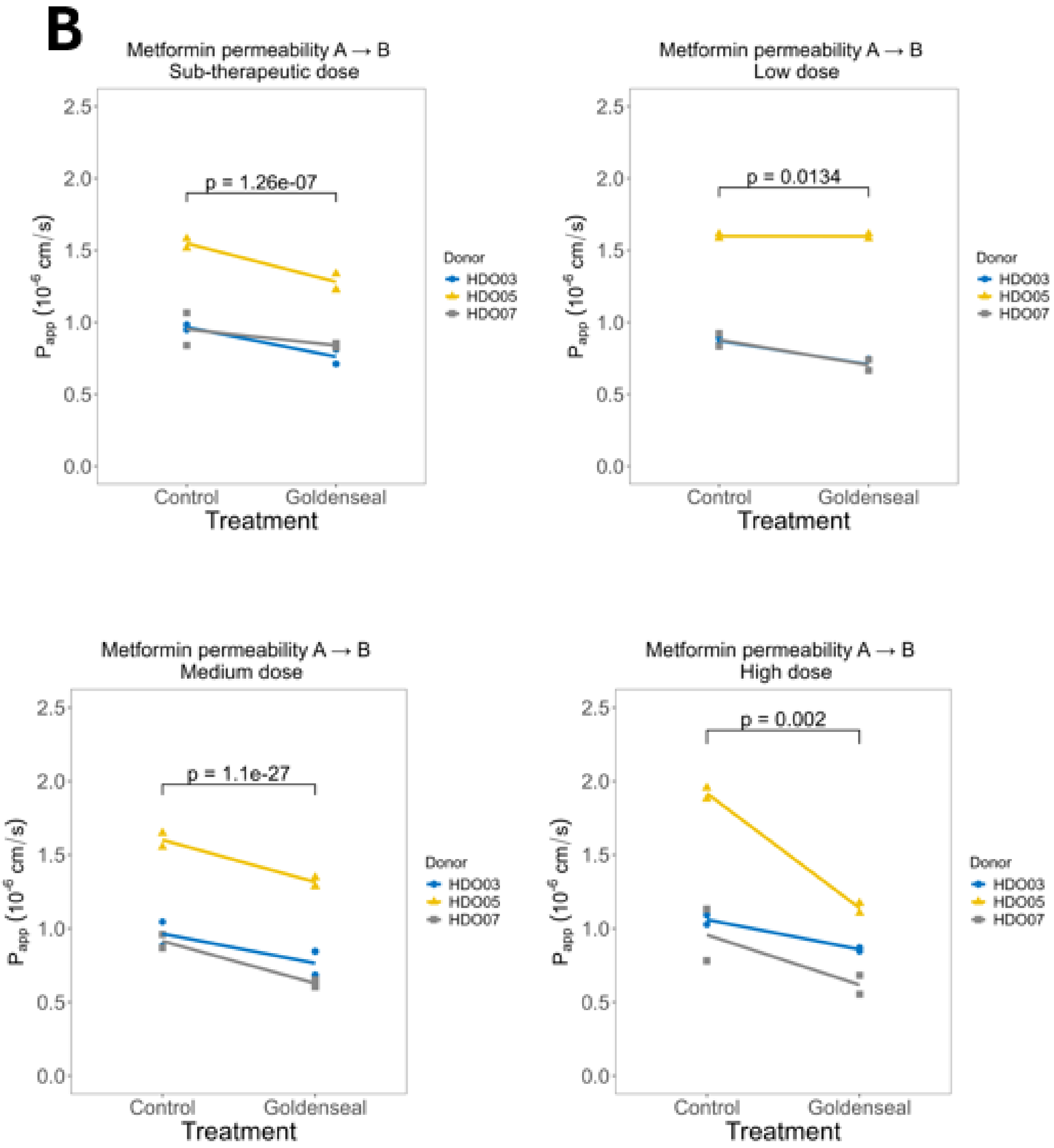

Figure 5.4. Goldenseal-mediated inhibition of clinical metformin doses.

Intracellular uptake (a) and transcellular flux (b) of a clinical doses of metformin derived from two *in vivo* clinical trials across enteroid monolayers for three donors. Data points correspond to uptake values of individual culture replicates. Solid lines connect the mean uptake values across culture replicates for each donor. P values for each comparison are presented on the plots and were calculated via generalized estimating equations modeling.

Figure 5.5. SLC transporter mRNA expression.

The expression of several transporters thought to be involved in metformin A > B flux. Transporters investigated were SLC19A2 (ThTr-1), SLC19A3 (ThTr-2), SLC22A1 (OCT1), SLC22A3 (OCT3), SLC29A4 (PMAT), and SLC6A4 (SERT). Expression was quantified using comparative ΔCt calculation for relative quantification of gene expression normalized to GAPDH. Individual datapoints correspond to individual culture replicates from each donor.

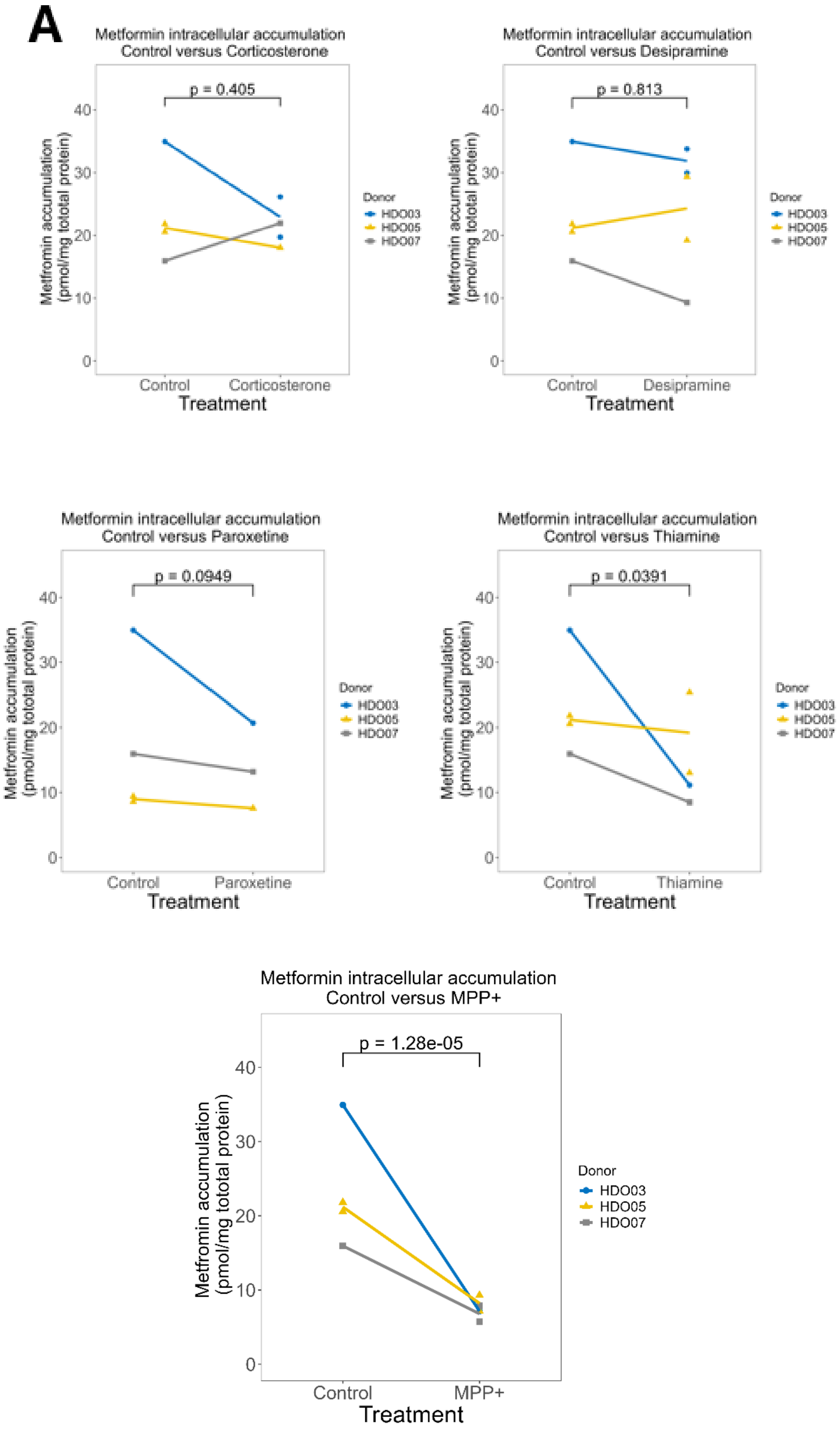
A
Metformin intracellular accumulation
Control versus Corticosterone
p = 0.405
Metformin accumulation (pmol/mg tototal protein)
0
10
20
30
40
Control
Corticosterone
Treatment
Donor
HDO03
HDO05
HDO07
Metformin intracellular accumulation
Control versus Desipramine
p = 0.813
Control
Desipramine
Metformin intracellular accumulation
Control versus Paroxetine
p = 0.0949
Control
Paroxetine
Metformin intracellular accumulation
Control versus Thiamine
p = 0.0391
Control
Thiamine
Metformin intracellular accumulation
Control versus MPP+
p = 1.28e-05
Control
MPP+

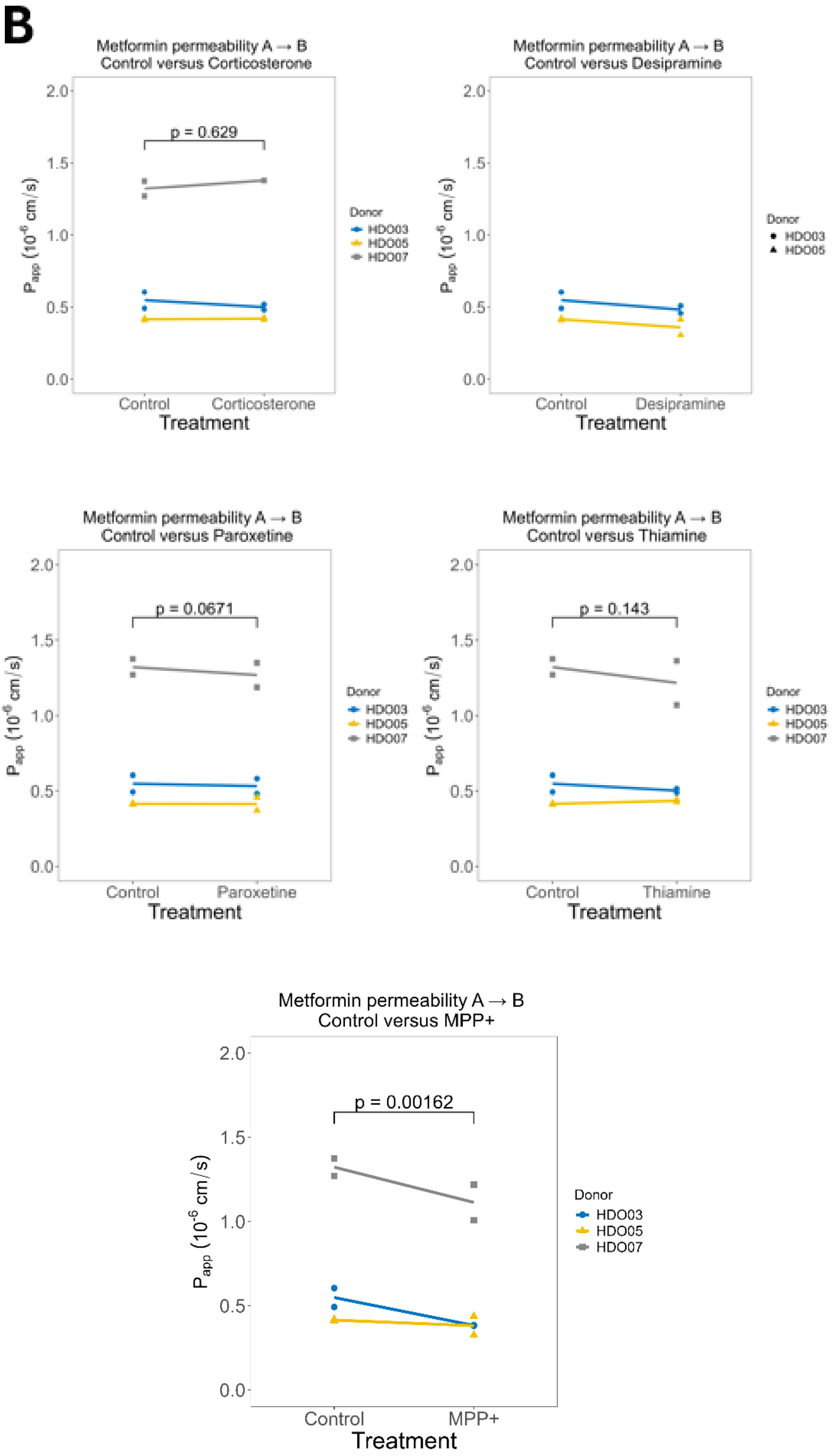
B
Metformin permeability A → B
Control versus Corticosterone
p = 0.629
P_{app} (10^{-6} cm/s)
2.0
1.5
1.0
0.5
0.0
Control
Corticosterone
Treatment
Donor
HDO03
HDO05
HDO07
Metformin permeability A → B
Control versus Desipramine
P_{app} (10^{-6} cm/s)
2.0
1.5
1.0
0.5
0.0
Control
Desipramine
Treatment
Donor
HDO03
HDO05
Metformin permeability A → B
Control versus Paroxetine
p = 0.0671
P_{app} (10^{-6} cm/s)
2.0
1.5
1.0
0.5
0.0
Control
Paroxetine
Treatment
Donor
HDO03
HDO05
HDO07
Metformin permeability A → B
Control versus Thiamine
p = 0.143
P_{app} (10^{-6} cm/s)
2.0
1.5
1.0
0.5
0.0
Control
Thiamine
Treatment
Donor
HDO03
HDO05
HDO07
Metformin permeability A → B
Control versus MPP+
p = 0.00162
P_{app} (10^{-6} cm/s)
2.0
1.5
1.0
0.5
0.0
Control
MPP+
Treatment
Donor
HDO03
HDO05
HDO07

Figure 5.6. Effect of specific cation transporter inhibitors on metformin absorption. Intracellular uptake (a) and transcellular flux (b) of a sub-clinical dose of metformin (10 µM) across enteroid monolayers for three donors with and without the presence of specific cation transporter inhibitors. Data points correspond to uptake values of individual culture replicates. Solid lines connect the mean uptake values across culture replicates for each donor. Control values are the same across all inhibitor conditions and are repeated for clarity. P values for each comparison are presented on the plots and were calculated via generalized estimating equations modeling.

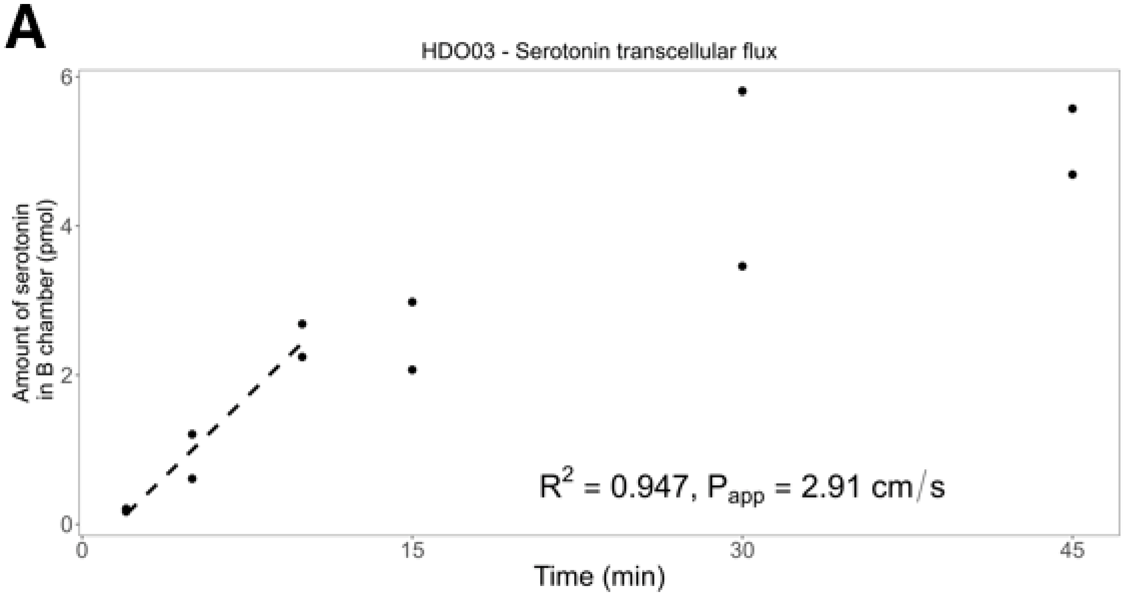

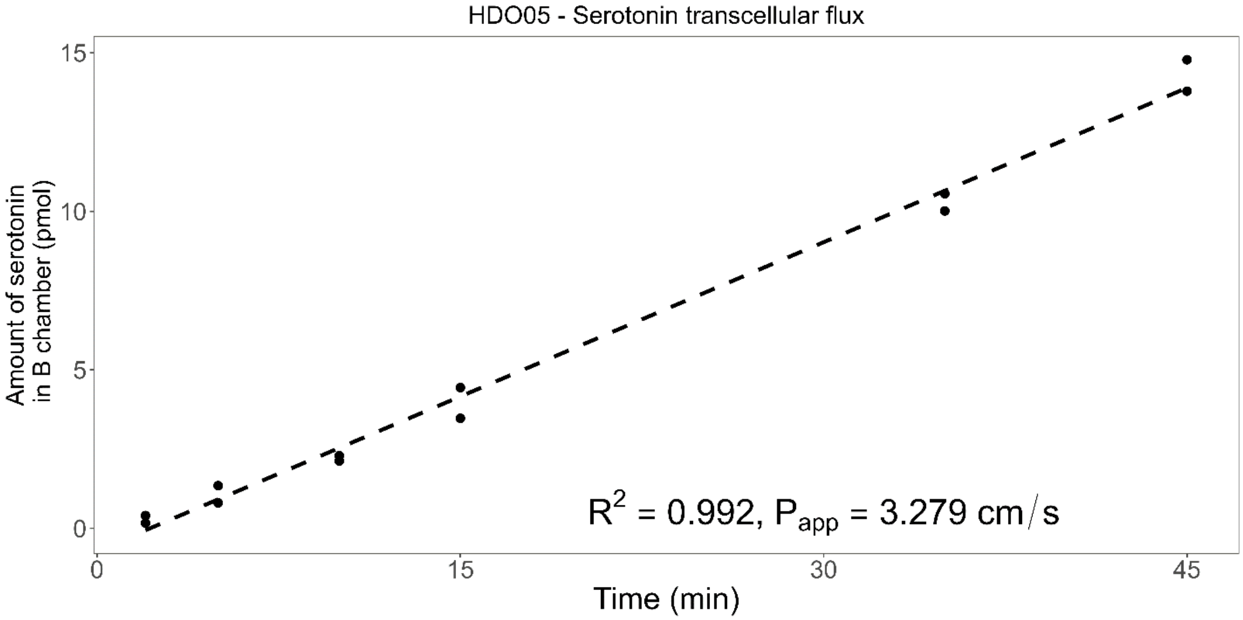

HDO05 - Serotonin transcellular flux
Amount of serotonin in B chamber (pmol)
15
10
5
0
0
15
30
45
Time (min)
R^2 = 0.992, P_{app} = 3.279 cm/s

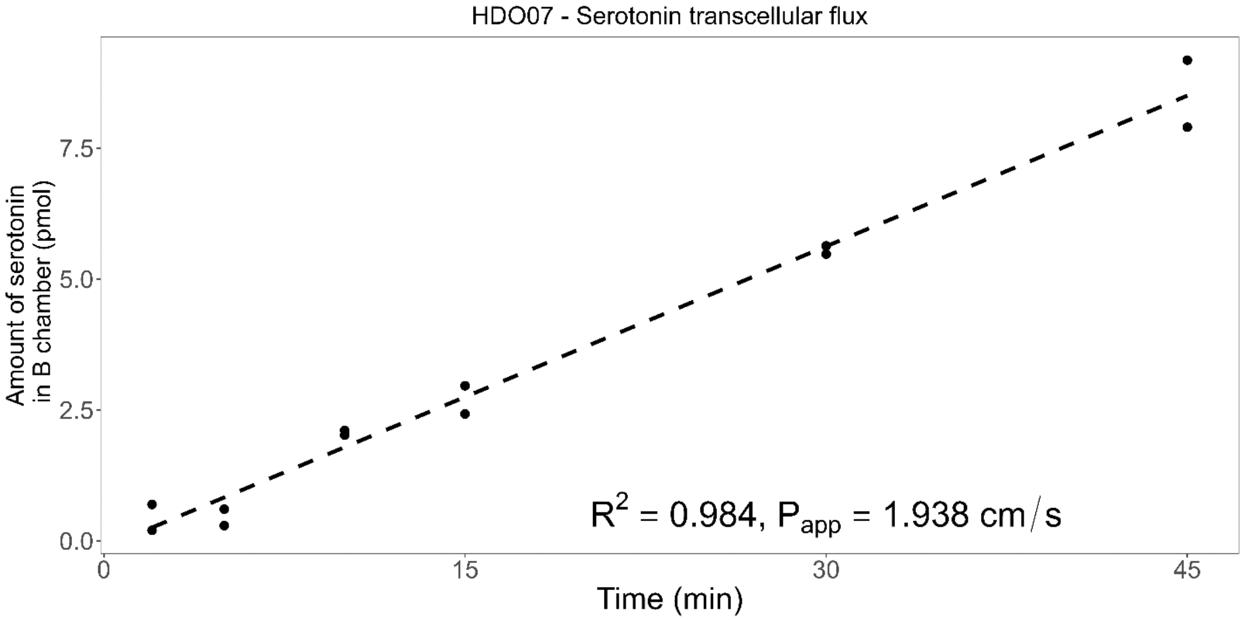

HDO07 - Serotonin transcellular flux
Amount of serotonin in B chamber (pmol)
7.5
5.0
2.5
0.0
0
15
30
45
Time (min)
R^2 = 0.984, P_{app} = 1.938 cm/s

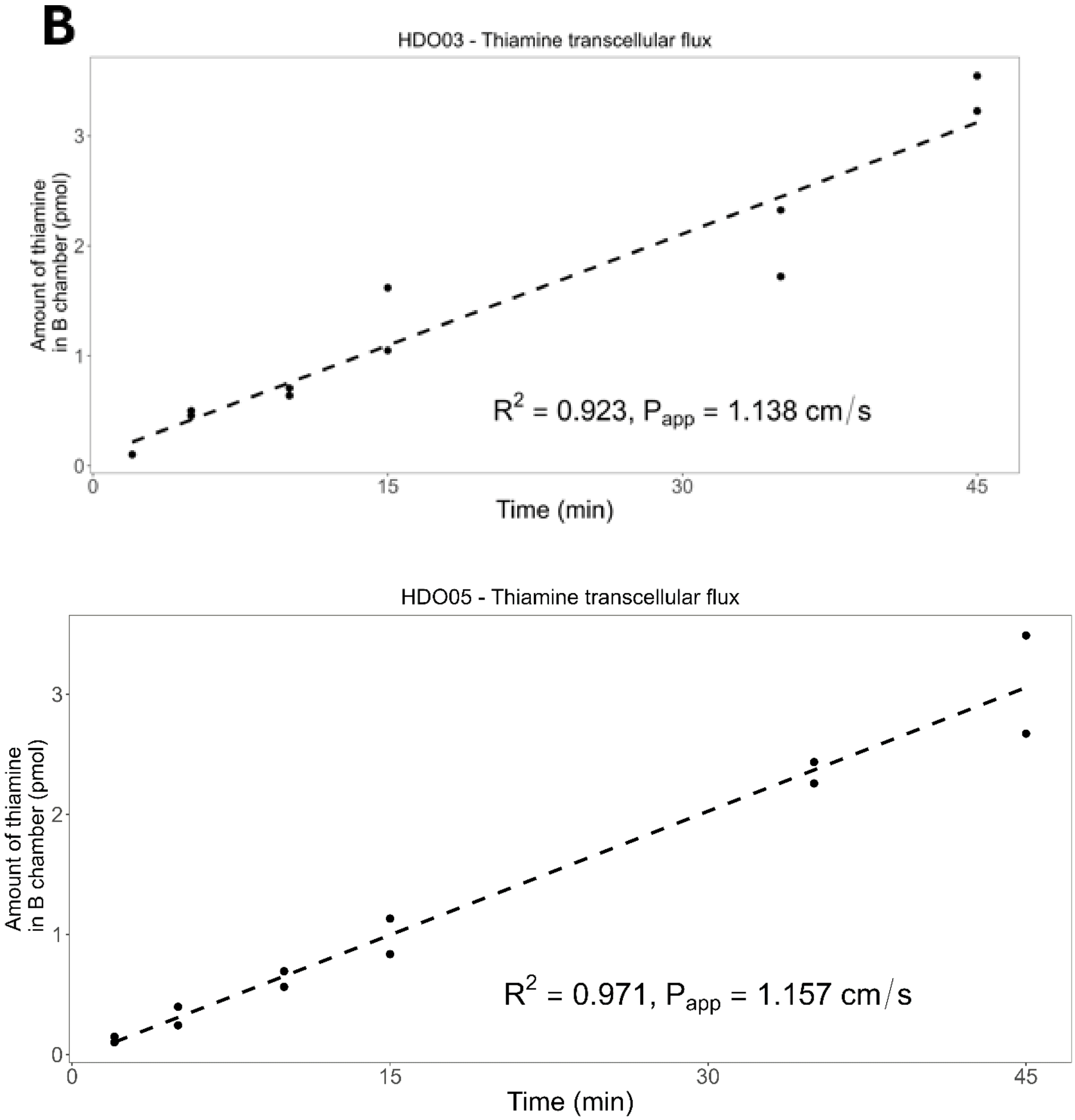
B
HDO03 - Thiamine transcellular flux
Amount of thiamine in B chamber (pmol)
0
1
2
3
0
15
30
45
Time (min)
R^2 = 0.923, P_{app} = 1.138 cm/s
HDO05 - Thiamine transcellular flux
Amount of thiamine in B chamber (pmol)
0
1
2
3
0
15
30
45
Time (min)
R^2 = 0.971, P_{app} = 1.157 cm/s

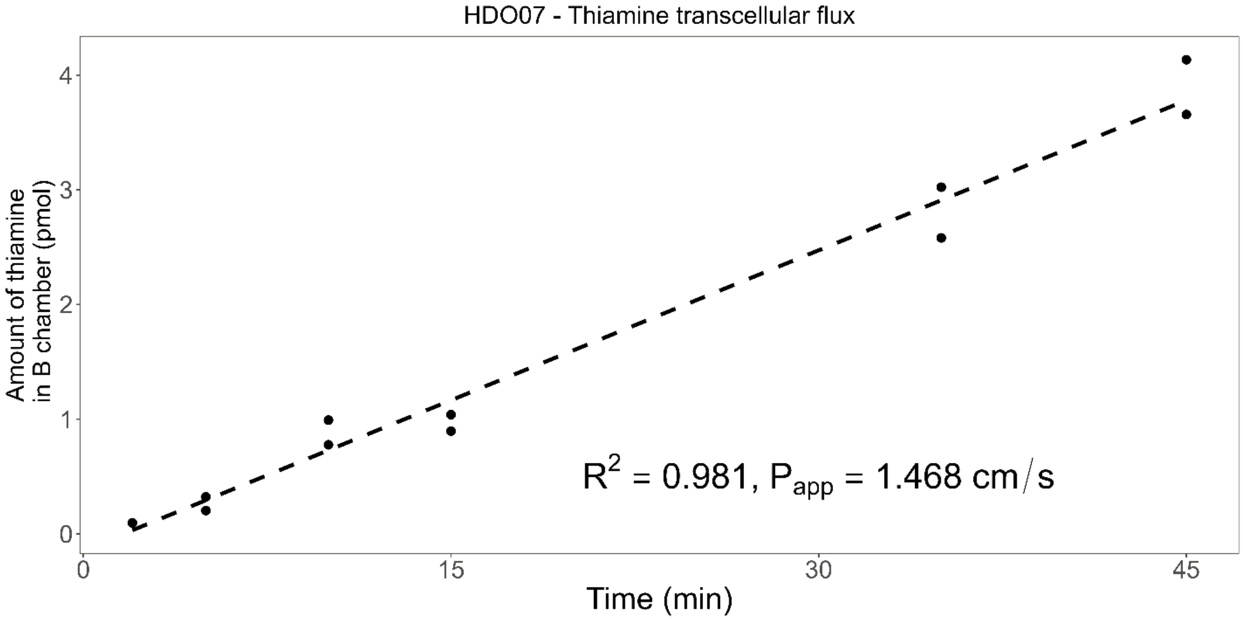

Figure 5.7. Serotonin and thiamine transcellular flux time linearity.

The transcellular flux linearity of serotonin (a) and thiamine (b) from A > B across enteroid monolayers for three donors. Dotten lines represent linear range up metformin transcellular flux. Goodness of fit and P_{app} values for each donor are presented on each plot.

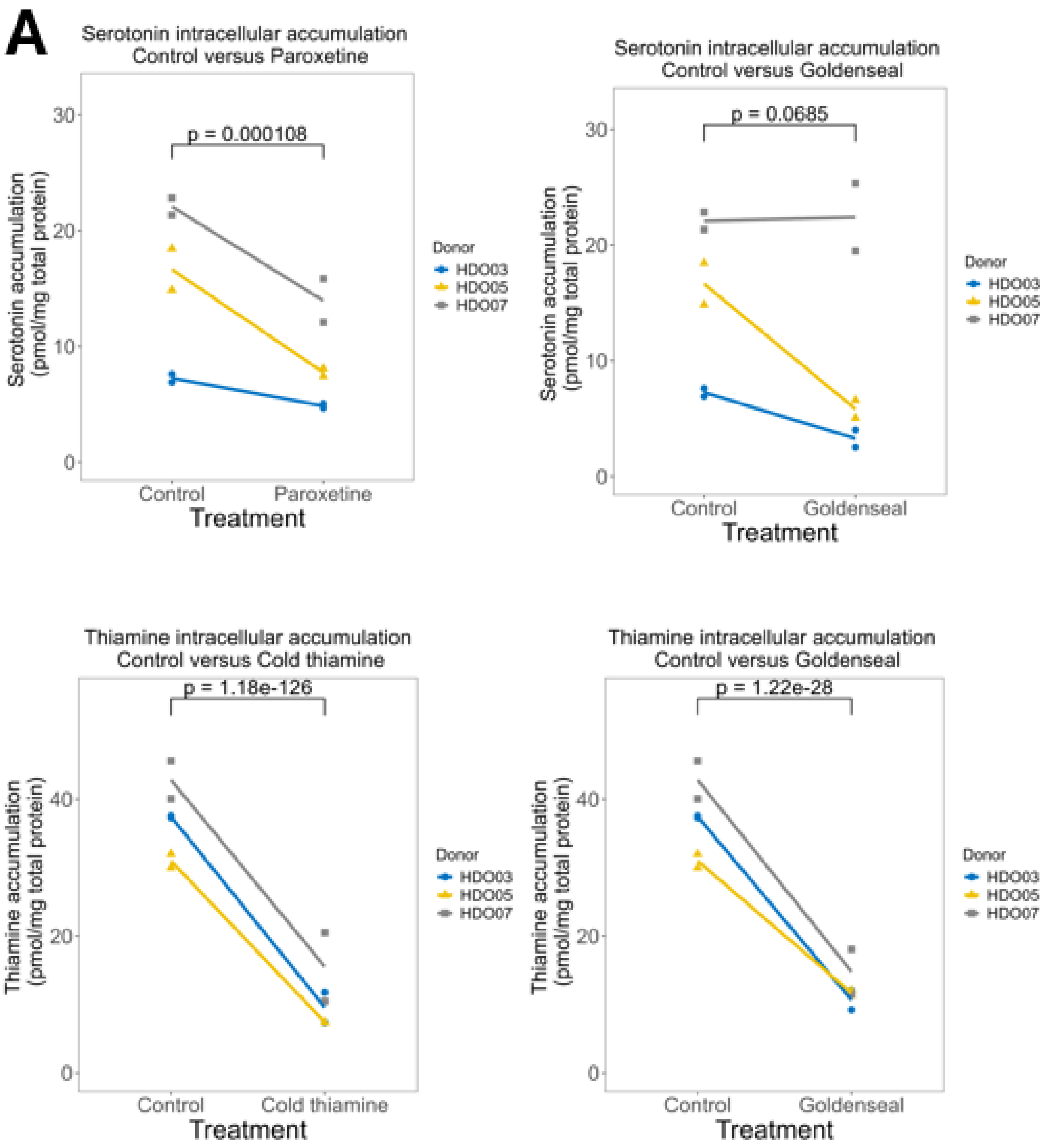

Serotonin intracellular accumulation Control versus Paroxetine

Serotonin intracellular accumulation Control versus Goldenseal

Thiamine intracellular accumulation Control versus Cold thiamine

Thiamine intracellular accumulation Control versus Goldenseal

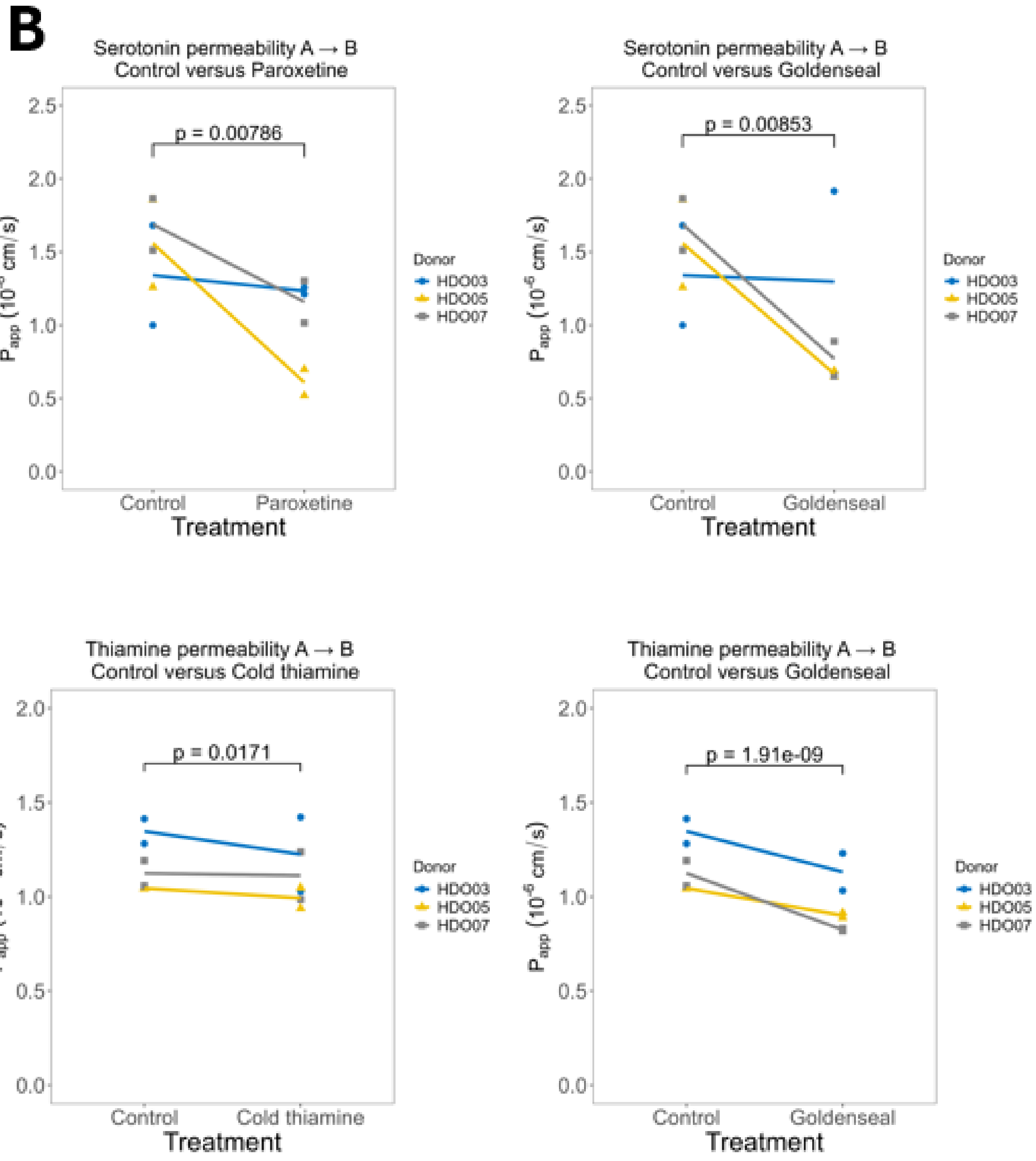

Figure 5.8. Goldenseal inhibition of SERT and ThTr-2/ThTr-1.

Intracellular uptake (a) and transcellular flux (b) of radiolabeled serotonin and radiolabeled thiamine across enteroid monolayers for three donors with and without the presence of goldenseal or specific inhibitors. Data points correspond to uptake values of individual culture replicates. Solid lines connect the mean uptake values across culture replicates for each donor.

Control values for are the same across all inhibitor conditions for serotonin and thiamine and are repeated for clarity. P values for each comparison are presented on the plots and were calculated via generalized estimating equations modeling.

5.5. REFERENCES

Arian C, Mahony EO, MacDonald JW, Bammler TK, Donowitz M, Kelly EJ, and Thummel KE (2024) Human Enteroid Monolayers: A Novel, Functionally-Stable Model for Investigating Oral Drug Disposition. *Drug Metab Dispos*.

Arian CM, Imaoka T, Yang J, Kelly EJ, and Thummel KE (2022) Gutsy science: In vitro systems of the human intestine to model oral drug disposition. *Pharmacol Ther* **230:**107962.

Bansal S, Paine MF, and Unadkat JD (2022) Comprehensive Predictions of Cytochrome P450 (P450)-Mediated In Vivo Cannabinoid-Drug Interactions Based on Reversible and Time-Dependent P450 Inhibition in Human Liver Microsomes. *Drug Metab Dispos* **50:**351-360.

Carey V (2024) Generalized Estimation Equation solver

CRAN.

Drozdzik M, Groer C, Penski J, Lapczuk J, Ostrowski M, Lai Y, Prasad B, Unadkat JD, Siegmund W, and Oswald S (2014) Protein abundance of clinically relevant multidrug transporters along the entire length of the human intestine. *Mol Pharm* **11:**3547-3555.

Fraser-Spears R, Krause-Heuer AM, Basiouny M, Mayer FP, Manishimwe R, Wyatt NA, Dobrowolski JC, Roberts MP, Greguric I, Kumar N, Koek W, Sitte HH, Callaghan PD, Fraser BH, and Daws LC (2019) Comparative analysis of novel decynium-22 analogs to inhibit transport by the low-affinity, high-capacity monoamine transporters, organic cation transporters 2 and 3, and plasma membrane monoamine transporter. *Eur J Pharmacol* **842:**351-364.

Grimm M, Aude P, Feldmuller M, Kessler R, Scheuch E, Tzvetkov MV, Koziolek M, and Weitschies W (2023) Comparing the gastric emptying of 240 mL and 20 mL water by MRI and caffeine salivary tracer technique. *Eur J Pharm Biopharm* **184:**150-158.

Han TK, Proctor WR, Costales CL, Cai H, Everett RS, and Thakker DR (2015) Four cation-selective transporters contribute to apical uptake and accumulation of metformin in Caco-2 cell monolayers. *J Pharmacol Exp Ther* **352:**519-528.

Horton RE, Apple DM, Owens WA, Baganz NL, Cano S, Mitchell NC, Vitela M, Gould GG, Koek W, and Daws LC (2013) Decynium-22 enhances SSRI-induced antidepressant-like effects in mice: uncovering novel targets to treat depression. *J Neurosci* **33:**10534-10543.

Mudie DM, Murray K, Hoad CL, Pritchard SE, Garnett MC, Amidon GL, Gowland PA, Spiller RC, Amidon GE, and Marciani L (2014) Quantification of gastrointestinal liquid volumes and distribution following a 240 mL dose of water in the fasted state. *Mol Pharm* **11:**3039-3047.

NCCIH (2021) Goldenseal.

Nguyen JT, Tian DD, Tanna RS, Hadi DL, Bansal S, Calamia JC, Arian CM, Shireman LM, Molnar B, Horvath M, Kellogg JJ, Layton ME, White JR, Cech NB, Boyce RD, Unadkat JD, Thummel KE, and Paine MF (2021) Assessing Transporter-Mediated Natural Product-Drug Interactions Via In vitro-In Vivo Extrapolation: Clinical Evaluation With a Probe Cocktail. *Clin Pharmacol Ther* **109:**1342-1352.

Oyanna VO, Garcia-Torres KY, Bechtold BJ, Lynch KD, Call MR, Horvath M, Manwill PK, Graf TN, Cech NB, Oberlies NH, Paine MF, and Clarke JD (2023) Goldenseal-Mediated

Inhibition of Intestinal Uptake Transporters Decreases Metformin Systemic Exposure in Mice. *Drug Metab Dispos* **51:**1483-1489.

Paine MF, Shen DD, and McCune JS (2018) Recommended Approaches for Pharmacokinetic Natural Product-Drug Interaction Research: a NaPDI Center Commentary. *Drug Metab Dispos* **46:**1041-1045.

Proctor WR, Bourdet DL, and Thakker DR (2008) Mechanisms underlying saturable intestinal absorption of metformin. *Drug Metab Dispos* **36:**1650-1658.

Ritz C, Baty F, Streibig JC, and Gerhard D (2015) Dose-Response Analysis Using R. *PLoS One* **10:**e0146021.

Rossi G, Manfrin A, and Lutolf MP (2018) Progress and potential in organoid research. *Nat Rev Genet* **19:**671-687.

Shirasaka Y, Seki M, Hatakeyama M, Kurokawa Y, Uchiyama H, Takemura M, Yasugi Y, Kishimoto H, Tamai I, Wang J, and Inoue K (2022) Multiple Transport Mechanisms Involved in the Intestinal Absorption of Metformin: Impact on the Nonlinear Absorption Kinetics. *J Pharm Sci* **111:**1531-1541.

Sun D, Lennernas H, Welage LS, Barnett JL, Landowski CP, Foster D, Fleisher D, Lee KD, and Amidon GL (2002) Comparison of human duodenum and Caco-2 gene expression profiles for 12,000 gene sequences tags and correlation with permeability of 26 drugs. *Pharm Res* **19:**1400-1416.

Tanna RS, Nguyen JT, Hadi DL, Layton ME, White JR, Cech NB, Oberlies NH, Rettie AE, Thummel KE, and Paine MF (2023) Clinical Assessment of the Drug Interaction Potential of the Psychotropic Natural Product Kratom. *Clin Pharmacol Ther* **113:**1315-1325.

Tian DD, Kellogg JJ, Okut N, Oberlies NH, Cech NB, Shen DD, McCune JS, and Paine MF (2018) Identification of Intestinal UDP-Glucuronosyltransferase Inhibitors in Green Tea (Camellia sinensis) Using a Biochemometric Approach: Application to Raloxifene as a Test Drug via In Vitro to In Vivo Extrapolation. *Drug Metab Dispos* **46:**552-560.

CHAPTER 6. CONCLUSIONS AND FUTURE DIRECTIONS.

6.1. CONCLUSIONS

The intestine has important gate-keeping functions that can profoundly impact the systemic blood exposure and efficacy/safety of orally administered drugs. Thus, accurately predicting the rate of drug absorption and absolute oral bioavailability of new molecular entities from *in vitro* experimentation can enhance the preclinical and clinical development process and potentially increase the likelihood of bringing a new drug to market. Unfortunately, currently used *in vitro* models of the human intestine have limitations that hinder accurate prediction of drug pharmacokinetics under mono- and polytherapy dosing conditions (Arian et al., 2022). Due to these shortcomings, there has been a concerted effort to develop physiologically relevant advanced *in vitro* models of the human intestine. The recently passed FDA Modernization Act 2.0, which has authorized the use of alternatives to animal testing in the drug development pipeline, highlights the growing interest in the development of advanced complex *in vitro* models to predict drug disposition (Zushin et al., 2023). Studies presented in this dissertation sought to develop and characterize the utility of two such models for use in pharmaceutical research: an intestinal microphysiological system (MPS) and human intestinal organoids.

Chapter 2 describes the development and evaluation of a dual channel MPS, where one channel was cultured with LS180 cells, an intestinal cell line derived from colorectal adenocarcinoma, and an adjacent channel was cultured with primary human umbilical vein endothelial cells (HUVECs). The design of this MPS allows for the study of vectorial transport and the determination of drug permeability and metabolic extraction ratios. We compared global mRNA expression, barrier integrity, and CYP3A activity for LS180 cells cultured in MPS versus Transwell®. While DMET characteristics of LS180 cells cultured in a 3-dimensional MPS were not substantially different from LS180 cells cultured in 2-dimensions in a Transwell® device, the effort led to the development of a high-fidelity, dual channel MPS preparation protocol, with an established high success rate. This protocol, when used with a more physiologically relevant cell system than the LS180 cell line, could produce a model that has significant utility in the prediction of orally administered drug disposition.

One such physiologically relevant cell system, human enteroids, is an excellent candidate for culture in the MPS protocol outlined in Chapter 2. Stem cell-derived human enteroid models are a relatively novel *in vitro* system for replicating functions of the human intestine, developed within the past 15 years. Most of the research conducted to date using these systems has focused on intestinal physiology/pathophysiology (Sato et al., 2011; Rossi et al., 2018). While the use of human enteroid models in pharmaceutical research remains relatively uncommon, groups have demonstrated robust expression and activity of several key drug metabolizing enzymes and transporters using a culturing protocol that imparts a short culture viability of roughly one week (Michiba et al., 2022).

Studies in Chapter 3 described the development of and characterization of a long-term human enteroid monolayer model, cultured in the Transwell® device. Using human enteroid monolayers derived from three donors, we were able to establish a robust long-term culturing protocol that demonstrates proper cell differentiation and monolayer morphology, including polarized membrane localization of key DMET proteins, confirmed by RNA-seq and immunocytochemical (ICC) analysis. Additionally, our enteroid monolayer model maintains barrier integrity and robust inducible and inhibitable CYP3A activity for up to 6-weeks in culture. Indeed, basal and induced CYP3A-dependent first-pass metabolic extraction of midazolam dosed in the Transwell® apical compartment was on par with drug extraction ratios observed *in vivo* (Paine et al., 1996). Moreover, drugs such as atenolol and compounds such as mannitol and lucifer yellow, that are known to be relatively impermeable to the intestinal mucosal barrier, exhibited low transcellular fluxes as a consequence of the proper localization of tight-junction proteins such as ZO-1, ZO-3, and Occludin. In addition, although exploratory, the model showed an expected P-glycoprotein-mediated efflux activity towards the drug digoxin across the apical organoid monolayer membrane. The long-term viability of this functional cell culture model represents a significant advantage over other culture methods for the study of time-dependent phenomena, such as robust induction/de-induction studies and long-term toxicology studies.

Further characterization of the long-term organoid monolayer model was achieved in Chapter 4 – where we explored the utility of bulk RNA-seq deconvolution using publicly available scRNA-seq datasets to determine the proportion of enterocytes and goblet cells in our differentiated and undifferentiated organoid culture. Initial studies described in this chapter systematically evaluated several deconvolution and scRNA-seq imputation methods for their ability to accurately predict cell type proportions in "pseudobulk" datasets, where cell proportions were known. Using this benchmarking approach, we determined that the DWLS deconvolution method in conjunction with the ALRA scRNA-seq imputation method as the best method for accurately predicting enterocyte and goblet cell proportions in an artificial or real complex cell mixture. Applying this method to the RNA-seq data presented in Chapter 3, we were able to determine that differentiated enteroid monolayers have an increased proportion of enterocytes relative to undifferentiated organoids, with a range of 2% to 20% enterocytes in differentiated enteroid monolayers compared to 1% to 3% in undifferentiated organoids. This finding is consistent with observations in Chapter 3, showing a marked increase in *CYP3A4* gene transcription and substantially enhanced midazolam hydroxylation activity upon cell differentiation (presumably derived from newly formed enterocytes).

In Chapter 5 we assessed the utility of the enteroid monolayer model to recapitulate the natural product-drug interaction seen *in vivo* between the herbal supplement, goldenseal, and metformin (Nguyen et al., 2021). Studies in this chapter demonstrated that goldenseal inhibits metformin intracellular accumulation, and that this inhibition is ameliorated at higher doses of metformin, suggesting that intracellular uptake occurs via a saturable processes. Interestingly, goldenseal only inhibited metformin transcellular A>B flux at clinical doses of metformin (>1.5 mM) but not at subclinical doses, suggesting that goldenseal inhibits a low affinity basolateral transporter. Additionally, we were able to confirm the mRNA expression of several intestinal organic cation transporter genes, such as *SLC22A1* (OCT1), *SLC22A3* (OCT3), *SLC29A4* (PMAT), *SLC19A2* (ThTr-1), *SLC19A3* (ThTr-2), and *SLC6A4* (SERT) – corroborating our previous RNA-seq results in three separate enteroid donors. Further studies confirmed the activity of SERT, ThTr-1, and ThTr-2 towards metformin – the latter of which was determined to be the apical transporter that is inhibited by goldenseal. More importantly, from a quantitative drug disposition perspective, results produced by the model suggest that ~80% of the transcellular A>B flux of metformin is mediated by a non-saturable, possibly paracellular, process. This has been proposed earlier investigators working with Caco-2 cell monolayers (Proctor et al., 2008).

6.2. FUTURE DIRECTIONS

A major limitation of the studies outlined in this dissertation is the small number of donors used for experimentation – with no more than four donors used in Chapter 3 or Chapter 5. A larger number of donors utilized for future studies will allow for a more thorough assessment of interindividual variability in drug metabolism/transport phenomena. Additionally, our studies only utilized enteroids derived from the duodenum of healthy human donors. While the duodenum is undoubtedly important for the metabolism and transport of highly soluble and permeable compounds (i.e., BCS class I drugs), the duodenum is a relatively short segment of the small intestine where the bulk of the small intestine length and surface area resides in the jejunum and ileum. The inclusion of enteroids derived from these regions could allow for more comprehensive studies of a given drug's oral disposition, particularly for drugs that undergo transporter-mediated absorption/efflux, as transporter expression is known to change along the length of the intestine (Drozdzik et al., 2014).

A limitation of our enteroid culture protocol is the relatively low proportion of enterocytes in differentiated enteroids, which ranged from approximately 3% to 20%, which is lower than the proportion of enterocytes in published scRNA-seq datasets of the human intestine, which ranged from 33% to 58%. This difference could be an artifact of the deconvolution methodology used to determine relative cell abundances or it could appropriately reflect the continually replicating state of the organoid monolayer when cultured with some WNT3A. While we still have robust expression and activity of several DMET proteins, the lower number of enterocytes in our model could lead to mispredictions of drug disposition using static or physiologically-based pharmacokinetic models (PBPK) that utilize pharmacokinetic parameters derived from our model. Future studies should systematically assess the impact of partial WNT3A withdrawal to determine the WNT3A concentration that is most beneficial for enteroid DMET expression/function that produces a physiologically relevant proportion of enterocytes while maintaining a population of proliferating cells that allows for a self-renewing system.

Future studies using enteroid monolayers should also include the incorporation of enteroids in the MPS developed in Chapter 2. Other groups have demonstrated that human duodenal enteroids cultured in MPS display DMET mRNA expression and protein abundance that more closely matches that of the *in vivo* human duodenum than other models such as Caco-2 cells cultured in MPS (Kasendra et al., 2020). The inclusion of our long-term cultured enteroid model in an MPS which incorporates flow of media could impact the DMET function and cell differentiation and could potentially change the proportion of enterocytes in culture relative to Transwell® culture. Additionally, the use of a more physiologically relevant endothelial cell line could impart additional benefits on the DMET expression/function and cell phenotype, as cell-cell communication is known to be an important aspect of normal cell physiology (Armingol et al., 2021).

In summary, the studies presented in this dissertation suggest that human enteroid monolayers represent a promising *in vitro* model to predict orally administered drug disposition. Future studies will work towards refining this model so it can be further improved as a tool used in the preclinical space of the drug development pipeline.

6.3. REFERENCES

Arian CM, Imaoka T, Yang J, Kelly EJ, and Thummel KE (2022) Gutsy science: In vitro systems of the human intestine to model oral drug disposition. *Pharmacol Ther* **230:**107962.

Armingol E, Officer A, Harismendy O, and Lewis NE (2021) Deciphering cell–cell interactions and communication from gene expression. *Nature Reviews Genetics* **22:**71-88.

Drozdzik M, Groer C, Penski J, Lapczuk J, Ostrowski M, Lai Y, Prasad B, Unadkat JD, Siegmund W, and Oswald S (2014) Protein abundance of clinically relevant multidrug transporters along the entire length of the human intestine. *Mol Pharm* **11:**3547-3555.

Kasendra M, Luc R, Yin J, Manatakis DV, Kulkarni G, Lucchesi C, Sliz J, Apostolou A, Sunuwar L, Obrigewitch J, Jang KJ, Hamilton GA, Donowitz M, and Karalis K (2020) Duodenum Intestine-Chip for preclinical drug assessment in a human relevant model. *Elife* **9**.

Michiba K, Maeda K, Shimomura O, Miyazaki Y, Hashimoto S, Oda T, and Kusuhara H (2022) Usefulness of Human Jejunal Spheroid-Derived Differentiated Intestinal Epithelial Cells for the Prediction of Intestinal Drug Absorption in Humans. *Drug Metab Dispos* **50:**204-213.

Nguyen JT, Tian DD, Tanna RS, Hadi DL, Bansal S, Calamia JC, Arian CM, Shireman LM, Molnar B, Horvath M, Kellogg JJ, Layton ME, White JR, Cech NB, Boyce RD, Unadkat JD, Thummel KE, and Paine MF (2021) Assessing Transporter-Mediated Natural Product-Drug Interactions Via In vitro-In Vivo Extrapolation: Clinical Evaluation With a Probe Cocktail. *Clin Pharmacol Ther* **109:**1342-1352.

Paine MF, Shen DD, Kunze KL, Perkins JD, Marsh CL, McVicar JP, Barr DM, Gillies BS, and Thummel KE (1996) First-pass metabolism of midazolam by the human intestine. *Clin Pharmacol Ther* **60:**14-24.

Proctor WR, Bourdet DL, and Thakker DR (2008) Mechanisms underlying saturable intestinal absorption of metformin. *Drug Metab Dispos* **36:**1650-1658.

Rossi G, Manfrin A, and Lutolf MP (2018) Progress and potential in organoid research. *Nat Rev Genet* **19:**671-687.

Sato T, Stange DE, Ferrante M, Vries RGJ, van Es JH, van den Brink S, van Houdt WJ, Pronk A, van Gorp J, Siersema PD, and Clevers H (2011) Long-term Expansion of Epithelial Organoids From Human Colon, Adenoma, Adenocarcinoma, and Barrett's Epithelium. *Gastroenterology* **141:**1762-1772.

Zushin PH, Mukherjee S, and Wu JC (2023) FDA Modernization Act 2.0: transitioning beyond animal models with human cells, organoids, and AI/ML-based approaches. *J Clin Invest* **133**.

VITA

Christopher Arian was born and raised in Cleveland, Ohio. He received his Bachelor Science in Pharmaceutical Sciences and Bachelor of Arts in Italian from the Ohio State University, Columbus in 2018.